Non-linear GNSS signal processing applied to land observation with high-rate airborne reflectometry

Hamza Issa

PhD Thesis

Major : Information and Communication Sciences and Technologies
Specialty : Signal and Image Processing

presented to the Doctoral School in Science, Technology and Health (ED 585)

of the l'Université du Littoral Côte d'Opale

by

Hamza ISSA

to obtain the degree of Doctor of Philosophy from the Université du Littoral Côte d'Opale

Non-linear GNSS Signal Processing Applied to Land Observation with High-rate Airborne Reflectometry

Defended on March 10, 2022, after the approval of the reviewers, in front of the examining board :

Ms. Sylvie LE HEGARAT-MASCLE, Professor, Polytech Paris-Saclay	**President**
Mr. Pierre-Olivier AMBLARD, Research Director, CNRS GIPSA-lab	**Reviewer**
Mr. Thierry CHONAVEL, Professor, IMT Atlantique	**Reviewer**
Mr. Manuel MARTIN-NEIRA, Engineer, ESA	**Examiner**
Mr. Jens WICKERT, Professor, Technische Universität Berlin	**Examiner**
Mr. Mohamad RAAD, Senior Lecturer, Lebanese International University	**Examiner**
Mr. Georges STIENNE, Senior Lecturer, Université du Littoral Côte d'Opale	**Examiner**
Mr. Serge REBOUL, Professor, Université du Littoral Côte d'Opale	**Thesis director**
Mr. Ghaleb FAOUR, Head of Research HDR, CNRS Lebanon	**Thesis director**

Thèse de Doctorat

Mention : Sciences et technologies de l'information et de la communication
Spécialité : Traitement du signal et des images

présentée à *l'École Doctorale en Sciences Technologie et Santé (ED 585)*

de l'Université du Littoral Côte d'Opale

par

Hamza ISSA

pour obtenir le grade de Docteur de l'Université du Littoral Côte d'Opale

Traitement non linéaire du signal GNSS appliqué à l'observation de la terre par réflectométrie GNSS aéroportée

Soutenue le 10 Mars 2022, après avis des rapporteurs, devant le jury d'examen :

M^{me}. Sylvie LE HEGARAT-MASCLE, Professeur, Polytech Paris-Saclay	**Présidente**
M. Pierre-Olivier AMBLARD, Directeur de Recherche, CNRS GIPSA-lab	**Rapporteur**
M. Thierry CHONAVEL, Professeur, IMT Atlantique	**Rapporteur**
M. Manuel MARTIN-NEIRA, Ingénieur, ESA	**Examinateur**
M. Jens WICKERT, Professeur, Technische Universität Berlin	**Examinateur**
M. Mohamad RAAD, Maître de Conférences, Lebanese International University	**Examinateur**
M. Georges STIENNE, Maître de Conférences, Université du Littoral Côte d'Opale	**Examinateur**
M. Serge REBOUL, Professeur, Université du Littoral Côte d'Opale	**Directeur de thèse**
M. Ghaleb FAOUR, Chargé de Recherche HDR, CNRS Lebanon	**Directeur de thèse**

This dissertation is dedicated to my mentor, Serge Reboul. You are and forever will be a great source of inspiration for me. I owe it all to you.

Acknowledgements

The end of the thesis work must be the occasion to thank all the people who, at one time or another, made it possible or contributed in its fulfillment. First and foremost, I would like to thank my mentor and thesis director Mr. Serge Reboul. I am extremely grateful to his continuous guidance and supervision for the past three years. His insightful feedbacks pushed me to sharpen my thinking and brought my work to a higher level. His valuable expertise, motivation, patience, availability, humanity and his trust in my work were all essential to me. During these three years, I would always reach Mr. Reboul who was able, at each key step, to place me in the best conditions to continue my work, whenever faced by major challenges that would have hurdled the research progress. For this, and for the continuous support that he provided to me both professionally and personally, I will be forever in his debt.

I would like to express my deep sense of thanks and gratitude to my thesis co-director Mr. Georges Stienne whose continuous support, patience and availability are sincerely appreciated. His competences and guidance through the past three years were so valuable to the research work. I would like to thank him because he would always let me pursue my own ideas and had the patience and care to discuss it with me. Mr. Stienne is a remarkable advisor and an even more exceptional person whose friendliness made these three years a lot more exciting. I would like to extend my sincere thanks to Mr. Ghaleb Faour for directing my work and allowing this thesis to take place. His trust and persistence to choose me for this topic are forever appreciated. His availability and guidance were vital for the continuation of the research work. I would also like to thank Mr. Mohmmad Raad for his valuable contributions and support to the research work.

I would like to thank all the members of my thesis jury. Special thanks to Ms. Sylvie Le Hégarat-Mascle for chairing the jury with cordiality and proficiency. I would also like to express my special thanks to Mr. Pierre-Olivier Amblard and Mr. Thierry Chonavel for their precious time and effort to review my work, and to Mr. Manuel Martin-Neira and Mr. Jens Wickert who

were also able to judge and improve this thesis document with discernment.

I would like to thank all the people who have supported, helped and advised me during this thesis in the Laboratoire d'Informatique Signal et Image de la Côte d'Opale (LISIC). I address my gratitude to its current director Mr. Sébastien Verel and his predecessor Mr. Christophe Renaud for allowing me to integrate myself as part of the lab, as well as the lab secretary, Mrs. Gaëlle Compiègne, for her dedication and support in the administrative procedures. I also thank all my research colleagues and friends in LISIC with whom we spent good times together, and in particular my friend Williams Kouassi, whose thesis started and ended at the same time as mine. Many thanks to Mr. Maximilian Semmling and Mr. Mario Moreno of Deutsches Zentrum für Luft- und Raumfahrt (DLR) for their valuable support and contributions.

Special thanks to Université du Littoral Côte d'Opale (ULCO), and the National Council For Scientific Research in Lebanon (CNRS-L) for supporting this work with a scholarship grant.

It can't go without saying that this thesis would not have been done without all the support of my friends and family in Lebanon and France. I would like to express my gratitude and love to my family for being there every moment, showering me with love, support, encouragement, sincere prayers, and care. This thesis gave me the opportunity to meet new people with whom I established life long friendships. I would like to thank in this occasion my friend Hassan Yassine who is also a doctoral student in ULCO for his continuous support and encouragement especially during the writing of the thesis manuscript. Finally, I would like to thank my partner and supporter Layal Al Rifai. Thank you for your love and support during this journey. It would have never been the same without you.

HAMZA ISSA

Abstract

Soil moisture remote sensing has been an active area of research over the past few decades due to its essential role in agriculture and in the prediction of some natural disasters. GNSS-Reflectometry (GNSS-R) is an emerging bi-static remote sensing technique that uses the L-band GNSS signals as sources of opportunity to characterize Earth surface. In this passive radar system, the amplitudes of the GNSS signal reflected by soil and the GNSS signal received directly from the GNSS satellites can be used to derive measurements of reflectivity from which the soil moisture content of the surface is determined. The study of soil moisture content using reflectivity measurements can also be applied for the detection of in-land water body surfaces.

In this dissertation, we propose in the first step a non-linear estimate of the GNSS signal amplitude. This estimate is based on a statistical model that we develop for the coherent detection of a GNSS signal quantized on 1 bit. We show with experimentations on synthetic and real data that the proposed estimator is more accurate than reference approaches and provide measurements of the Signal-to-Noise Ratio (SNR) at a higher rate. When the reflected GNSS signal is obtained in an airborne experiment, its evolution as a function of time is piecewise stationary. The different stationary parts are associated to different kinds of reflecting surfaces. We propose in a second step a change point detector that takes into account the radar signal characteristics in order to segment the signal. We show on synthetic data that the proposed change point detector can detect and localize changes more accurately than reference approaches present in the literature. This work is applied to airborne GNSS-R observation of Earth. We propose in the third step, a new GNSS-R sensor with its implementation on a lightweight airborne carrier. We also propose a new front-end receiver architecture, a software radio implementation of the receiver, and the complete instrumentation of the airborne carrier.

A real flight experimentation has taken place in the North of France obtaining reflections from different landforms. We show using the airborne GNSS measurements obtained, that the proposed radar technique detects different surfaces along the flight trajectory, and in particular in-land water bodies, with high temporal and spatial resolution. We also show that we can localize the edges of the detected water body surfaces at meter accuracy.

Keywords: GNSS signal processing; GNSS amplitude estimation; signal segmentation; GNSS-Reflectometry; passive radar; airborne observation

Résumé

L'estimation du taux d'humidité des sols par télédétection est un domaine de recherche très actif car ses applications concernent l'agriculture et les catastrophes naturelles. La réflectométrie GNSS (GNSS-R) est une nouvelle technique d'observation de la terre basée sur un système radar bi-statique qui utilise le signal GNSS en bande L comme source d'opportunité. Dans ce système radar passif, le signal GNSS réfléchi par le sol est utilisé pour estimer le taux d'humidité de la surface de réflexion. Il peut aussi être utilisé pour détecter et localiser les zones humides.

Dans ce travail de thèse nous proposons dans un premier temps un estimateur non linéaire de l'amplitude du signal GNSS. Cet estimateur est basé sur un modèle statistique que nous proposons pour la détection cohérente du signal GNSS quantifié sur 1 bit. On montre, grâce à une expérimentation sur données synthétiques et sur données réelles, que l'estimateur proposé permet d'estimer le rapport signal à bruit d'un signal GNSS, avec une fréquence et une précision plus importante que les techniques de références. Quand le signal GNSS réfléchi est obtenu dans un vol aéroporté celui-ci est composé de zones stationnaires qui représentent les différents types de surfaces de réflexion. Nous proposons dans un deuxième temps un détecteur de rupture qui prend en compte la nature du signal radar pour découper celui-ci en zones stationnaires. On montre grâce à une expérimentation sur données synthétiques que le détecteur proposé offre une meilleure détection et localisation des ruptures que les méthodes de références. Ce travail est appliqué à l'observation GNSS-R aéroportée. Nous proposons dans une troisième partie l'étude et la mise en œuvre originale du capteur GNSS-R que nous avons développé. Cette étude porte à la fois sur la conception du capteur, la réalisation du récepteur génie logiciel qui traite les données et l'implantation du capteur sur un porteur de type autogyre.

Une expérimentation aéroportée, qui a été réalisée dans le nord de la France, nous a permis d'obtenir des réflexions du signal GNSS pour différents types de sol. On montre que les traitements du signal et la technique radar proposés permettent de détecter différents types de surfaces de réflexion avec une résolution spatiale et temporelle importante. On montre aussi que l'on peut localiser avec une précision métrique les zones en eau.

Keywords: Traitement du Signal GNSS; Segmentation du Signal; Réflectométrie GNSS; Radar Passif; Observation Aéroportée

Contents

List of Figures

List of Tables

List of Abbreviations

ADC	**A**nalog-to-**D**igital **C**onversion
AGC	**A**utomatic **G**ain **C**ontrol
AIEM	**A**dvanced **I**ntegral **E**quation **M**odel
AMSR	**A**dvanced **M**icrowave **S**canning **R**adiometer
ASAR	**A**dvanced **S**ynthetic **A**perture **R**adar
ASCAT	**A**dvanced **SCAT**terometer
AWGN	**A**dditive **W**hite **G**aussian **N**oise
BL	**B**eau**l**ieu's Method
BPSK	**B**inary **P**hase **S**hift **K**eying
BW	Normalized noise equivalent **b**and**w**idth of the receiver RF front end
C/A	**C**oarse/**A**cquisition code
CC	**C**orrelator **C**omparison
CDMA	**C**ode **D**ivision **M**ultiple **A**ccess
CDTI	**C**entro para el **D**esarrollo **T**eccnologico **I**ndustrial
cGNSS-R	**c**onventional **GNSS-R**
C/N$_0$	**C**arrier-to-**N**oise Ratio
CNES	**C**entre **N**ational d'**E**tudes **S**patiales
CUSUM	**Cu**mulative **Sum** change detection algorithm
CyGNSS	**Cy**clone **GNSS**
DDM	**D**elay **D**oppler **M**ap
DLL	**D**elay **L**ock **L**oop
ECV	**E**ssential **C**limate **V**ariable
EKF	**E**xtended **K**alman **F**ilter
ERS	**E**uropean **R**emote **S**ensing
ESA	**E**uropean **S**pace **A**gency
FLL	**F**requency **L**ock **L**oop
FoV	**F**ield **o**f **V**iew
GLORI	**GLO**bal navigation satellite system **R**eflectometry **I**nstrument
GLR	**G**eneralized **L**ikelihood **R**atio
GNSS	**G**lobal **N**avigation **S**atellite **S**ystem
GNSS-R	**GNSS-R**eflectometry
GOM	**G**eometric **O**ptic **M**odel
GPS	**G**lobal **P**ositioning **S**ystem
GREOS	**G**NSS **RE**flectometry Radio **O**ccultation and **S**catterometry
H-Pol	**H**orizontal **Pol**arization
IEM	**I**ntegral **E**quation **M**odel

iGNSS-R	**i**nterferometric **G**NSS-**R**
IPT	**I**nterference **P**attern **T**echnique
LHCP	**L**eft-**H**and **C**ircular **P**olarized
L-MEB	**L**-band **M**icrowave **E**mission of the **B**iosphere
LNA	**L**ow **N**oise **A**mplifier
MAP	**M**aximum **A** **P**osteriori probability
MIR	**M**icrowave **I**nterferometer **R**eflectometer
MIRAS	**M**icrowave **I**maging **R**adiometer with **A**perture **S**ynthesis
ML	**M**aximum **L**ikelihood SNR estimator
MLLE	**M**aximum **L**ikelihood **L**ocalization **E**stimate
MM	**M**oments **M**ethod
MML	**M**odified **M**aximum **L**ikelihood estimator
MMSE	**M**inimum **M**ean **S**quared **E**rror
NASA	**N**ational **A**eronautics and **S**pace **A**dministration
NWPR	**N**arrowband-**W**ideband **P**ower **R**atio
PARIS	**P**assive **R**eflectometry and **I**nterferometry **S**ystem
PLL	**P**hase **L**ock **L**oop
POM	**P**hysical **O**ptic **M**odel
PRN	**P**seudo-**R**andom **N**oise
PSD	**P**ower **S**pectral **D**ensity
RF	**R**adio **F**equency
RHCP	**R**ight-**H**and **C**ircular **P**olarized
RSCN	**R**eal **S**ignal-**C**omplex **N**oise
RTE	**R**adiative **T**ransfer **E**quation
RTM	**R**adiative **T**ransfer **M**odel
SAR	Synthetic Aperture Radar
SCA	**S**ingle-**C**hannel **A**lgorithm
SE	**S**tandard **E**stimate
SMAP	**S**oil **M**oisture **A**ctive and **P**assive
SMC	**S**oil **M**oisture **C**ontent
SMOS	**S**oil **M**oisture and **O**cean **S**alinity
SNR	**S**ignal-to-**N**oise **R**atio
SNV	**S**ignal-to-**N**oise **V**ariance
SPM	**S**mall **P**erturbation **M**odel
SSA	**S**mall **S**lope **A**pproximation
SSM	**S**urface **S**oil **M**oisture
SSS	**S**eas **S**urface **S**alinity
TDS-1	**T**ech**D**emo**S**at-1
UAV	**U**nmanned **A**erial **V**ehicle
UK-DMC	**UK** - **D**isaster **M**onitoring **C**onstellation
V-Pol	**V**ertical **Pol**arization
VS	**V**ariance **S**ummation method

List of Symbols

L-band emissions

ε	soil dielectric constant
m_{v}	volumetric soil moisture
E	emissivity
Γ	Fresnel surface reflectivity
R_{P}	Fresnel reflection coefficient
γ	incidence angle
R_{P}^{R}	rough surface reflection coefficient
Γ^{R}	rough surface reflectivity
λ	signal wavelength

Passive remote sensing

τ	vegetation optical depth
ω	single scattering albedo
T_{s}	effective (physical) soil temperature
T_{v}	vegetation temperature
T_{∞}	deep soil temperature
T_{surf}	surface temperature
T_{b}	brightness temperature

Active remote sensing

σ^{0}	backscattering coefficient
h_{rms}	surface root mean square height
d_{m}	distance from a radar to a target
P_{r}	received signal power
P_{t}	transmitted signal power
σ	scattering cross section

GNSS-R

a	semi-major axis of the first Fresnel ellipse
b	semi-minor axis of the first Fresnel ellipse
h	receiver height

δ	differential phase change across the surface
γ	incidence angle
θ	elevation angle of a GNSS satellite
pq	polarizations for the incident and scattered signals
P^r_{pq}	bistatic radar total scatter power
P^c_{pq}	bistatic radar coherent component power
P^i_{pq}	bistatic radar incoherent component power
Γ_{LR}	cross-polarization Fresnel reflectivity
Γ_{RR}	right hand co-polarization Fresnel reflectivity
P^c_{LR}	cross-polarized coherent component power
P^i_{RR}	co-polarized incoherent component power
G^t	transmitter antenna gain
G^r	receiver antenna gain
d_1	distance between the specular point and the receiver
d_2	distance between the specular point and the satellite
d_3	distance between the receiver and the satellite
σ_{LR}	cross-polarization bistatic radar scattering cross section
σ_{RR}	co-polarization bistatic radar scattering cross section

GNSS signals

t	instant of time
$s^d(t)$	direct GNSS signal
$s^r(t)$	reflected GNSS signal
$CA(t)$	C/A code replica generated by the receiver
A	GNSS signal amplitude
T_c	coherent integration time
τ	code delay
f	carrier frequency
f^D	Doppler frequency
ϕ	phase delay
K^r	number of non-coherent integrations
Y^r_c	amplitude of correlation corresponding to cross-correlating $s^r(t)$ with $CA(t)$ using cGNSS-R
Y^r_i	amplitude of correlation corresponding to cross-correlating $s^r(t)$ and $s^d(t)$ using iGNSS-R
I	in-phase component of the signal
Q	quadrature-phase component of the signal
$s^R(t)$	GNSS signal sensed by an antenna
η	noise term
f_{LO}	local oscillator frequency
f_{IF}	intermediate frequency
$s(t)$	down-converted GPS C/A signal
K	AGC gain

f_s	sampling frequency
$ci_{v,i}$	in-phase component of the digitized local replica for satellite v
$cq_{v,i}$	quadrature-phase component of the digitized local replica for satellite v
s_i	digitized signal
P_d	signal data power
P_n	noise power
P_r	total received signal power
P_W	Wideband power
P_N	Narrowband power
$P_{N/W}$	Narrow-to-Wideband power ratio
N	number of samples used to produce one SNR estimate
$r_C[n]$	sampled signal at the output of the prompt correlator
$c_{v,i}$	digitized local replica for satellite v
A^r_{LHCP}	amplitude of the reflected LHCP antenna signal
A^d_{RHCP}	amplitude of the direct RHCP antenna signal
Δ_f	delay introduced by the delay line
l_f	length of the fiber optic coil
Δ_d	delay due to the path difference between the direct and reflected GNSS signals
Δ_r	total delay due to the path difference and delay line

Kalman Filter

k	time instant
x_k	state vector
y_k	measurement vector
F_k	state transition matrix
H_k	noiseless measurement matrix
w_k	state noise vector
v_k	measurement noise vector
R_k	covariance matrix of the measurement noise vector
Q_k	covariance matrix of the state noise vector
f_k	non-linear state transition function
h_k	non-linear measurement function
ϵ_k	innovation of the EKF
S_k	covariance of the innovation
P_k	state covariance
$P_{k/k-1}$	predicted state covariance
$\hat{x}_k$	state estimate
$\hat{x}_{k/k-1}$	predicted state estimate

Change Detection

ν	change dynamic
λ	detection threshold
t	starting instant of a transition
Δt	duration of a transition
$\hat{.}$	estimate of a parameter
$t^a_{l,i}$	i^{th} instant of change detected by the Kalman-CUSUM detector for satellite l
$n^c_{l,i}$	i^{th} localized change instant by CUSUM localization approach for satellite l
$n^e_{l,i}$	i^{th} localized change instant by MLLE localization approach for satellite l
N	number of samples in a working window for localization
m_1	mean estimate of a segment before a change
m_2	mean estimate of a segment after a change
f_n	sampling line that models the evolution of reflectivity from m_1 to m_2
$\hat{\sigma}^2$	empirical variance
μ^m	true mean value of a segment
m	mean estimate of a segment
E_i	maximum error of a mean estimate
s^f_i	unbiased sample standard deviation of a segment
n^f_i	number of samples in a segment
α	significance level
$\alpha/2$	area in one tail for a confidence interval
$t_{\alpha/2,i}$	t-score
λ^m	merging threshold
p^f	percentage of overlapping
p^s	degree of symmetry
λ^s	symmetry threshold
$\tilde{n}^e_{l,j}$	j^{th} localized change instant after merging for satellite l
Nbr	number of detected changes

General Introduction

Soil moisture is one of the key parameters in the hydrological cycle, i.e. the continuous circulation of water between oceans, atmosphere and land in a never-ending process [1, 2]. It directly influences the amount of evaporation, infiltration, and the amount of water uptake by plants and was recognized as an Essential Climate Variable (ECV) [3, 4]. In this context, measuring the soil moisture content on a global scale can be of a great benefit for a large number of applications. Disciplines such as hydrology, climatology, and agriculture, require estimating the soil moisture content for prediction of potential flood and drought hazards, understanding land–atmosphere energy balance, and crop yield expectation [5–7]. The study of soil moisture content can be applied to observe the distribution of in-land water body surfaces.

Floodplains and in-land water body surfaces cover at least $12.1 \times 10^6\ km^2$ (8%) of landscapes on Earth [8, 9]. They play a significant role in the water cycle through river flow variability, flood mitigation, groundwater recharge and water quality improvement [10]. Despite its important role, little knowledge has been acquired concerning the water stored in floodplains and wetlands as well as its temporal variations from regional to global scales until remote sensing techniques emerged as potential instruments for soil moisture and water body detection.

In this regard, soil moisture and water content remote sensing on a global and regional scale has been an active area of research over the past few decades. It has been proven that the microwave band that is optimal for soil moisture remote sensing lies within the L-band [11, 12]. It is shown that the soil dielectric constant value that governs the surface reflectivity can be determined from only the top 0-5 cm of soil [12].

The Global Navigation Satellite Systems (GNSS) have been used as an effective tool for remote sensing, due to its unique characteristics. It uses the

radio navigation signals as opportunistic bistatic radar transmissions, providing precise, continuous, free 24 hours detections and positioning capabilities. The use of GNSS signals for remote sensing applications is referred to as GNSS-Reflectometry (GNSS-R).

GNSS-R is an emerging bistatic remote sensing technique that uses the GNSS signals (mainly GPS signals) as sources of opportunity to characterize Earth surface. GNSS systems continuously transmit signals to Earth surface at different L-bands ranging between 1 and 2 GHz. A GNSS-R sensor receives the direct GNSS signals from the satellites as well as those reflected from Earth surface. The reflected signals carry information about the reflecting surface such as its height, shape and moisture content. GNSS-R platforms offer dedicated applications for Earth surface remote sensing on a local scale using ground-based experiments, a regional scale using airborne campaigns, and recently extending to a global scale using GNSS-R based space-borne missions.

In GNSS-R, the soil moisture content can be derived from the reflectivity measurements. These measurements are directly linked to the amplitudes of the GNSS signals. In this regard, the ratio of the received carrier power level to the noise power level can be used to observe the GNSS signal amplitude. This ratio is referred to as the Carrier-to-Noise ratio (C/N_0) when the noise power is defined for a unit of bandwidth. It is seen as the normalized measure of the Signal-to-Noise Ratio (SNR). C/N_0 observations have been utilized for remote sensing applications by the GNSS-R community. The C/N_0 of the direct and reflected GNSS signals are compared to retrieve some geophysical parameters of the reflecting surface [13–16].

This dissertation is dedicated to the study of airborne GNSS-R techniques for soil moisture and water body detection using a low-altitude airborne carrier. We estimate the amplitudes of the direct and reflected GNSS signals at high rate, from which the surface reflectivity of different reflecting surfaces is derived. We develop a GNSS-R setup on-board a lightweight airborne carrier that can achieve the high temporal and spatial resolution requirements of our application. The GNSS signals are segmented into stationary parts based on the changes in the reflectivity measurements associated to different areas of reflection. The general aims and contributions of this work can be summarized as follows:

- Development of GNSS signal processing techniques for airborne reflectometry. These techniques involve the acquisition, tracking and dating of the raw GNSS data in classical and master/slave configurations.
- Development of a novel probabilistic model that makes use of dedicated GNSS signal processing techniques for on-line estimation of the GNSS signal amplitudes and consequently the C/N_0.
- Development of a novel GNSS signal segmentation system that makes use of pre-existing tools and merge them with proposed models for differentiating water body surfaces in landforms.
- Assessment of the proposed systems and methodologies on real data. The data are recorded using an original GNSS sensor designed specifically for this work.
- Implementation of a novel quantitative analysis for water body detection and edge localization using the proposed radar technique over the data collected along the whole flight trajectory.

The developed techniques will be presented through five chapters. The first two chapters are mainly bibliographical, while the last three chapters are dedicated for the presentation of the research work. In the first chapter, we present a brief review of soil dielectric constant and emissions models that allow to derive the soil moisture content of land using remote sensing techniques. These techniques are classified as active and passive remote sensing techniques, and thus are presented in this chapter, and in particular, remote sensing using GNSS-R radar techniques. The principle of GNSS-R is highlighted in this chapter. The different geometric configurations of the reflectometry system in the modeling of the signal reflection on Earth surface are thoroughly discussed. We conclude this chapter by presenting various applications that have emerged and the main signal processing methods used in the context of GNSS-R.

The second chapter presents a literature review of different carrier-to-noise estimation techniques and its application to soil moisture retrieval using GNSS-R. This chapter introduces the GNSS signal model, in particular, the GNSS front end processing that leads to the derivation of the GNSS

carrier-to-noise expression. This chapter also investigates various C/N_0 estimation algorithms for digital communications channels that have been published in the literature over the last few decades. By evaluating the performance of the C/N_0 estimators presented, we select one particular estimator to use in assessing the performance of the proposed C/N_0 estimator that is presented in this work. Soil moisture retrieval algorithms from the Signal-to-Noise-Ratio (SNR) under different GNSS-R antenna configurations are detailed in this chapter.

In the third chapter, we propose a model that estimates C/N_0 at high rate in order to maximize the time resolution of the observations. We show in this chapter that in a 1-bit quantization receiver, the in-phase component of the signal can provide a direct observation of the signal amplitude, and therefore of the carrier-to-noise ratio. The non-linear expression that links the maximum value of the in-phase correlation component to the signal amplitude is derived. In order to estimate the time varying amplitudes of the signals, we propose an Extended Kalman Filter to reverse the non-linear expression with the noisy observations of correlation provided by the tracking loop. The proposed model and filter inversion method are assessed on synthetic and real data. We show that the proposed GNSS amplitude estimator performs coherently with an existing GNSS receiver and with much higher data rate which is essential in multi-path and dynamic GNSS-R applications.

In the fourth chapter, we propose a segmentation model that divides the GNSS signals into stationary parts associated to different areas of reflection. The amplitudes of the reflected GNSS signals change significantly with the displacement of the satellites footprints from one area to another. In this chapter, we define the model that characterizes such displacement. We detect the changes in the reflected GNSS signal levels using an already proven change point detector. Then, we propose an algorithm that localizes these changes in an optimal working window. We also propose a merging algorithm in order to decrease the number of false change detections. Signal segmentation is implemented based on the different processing steps. This chapter concludes by assessing the performance of the proposed system on synthetic data and evaluating its performance on real GNSS airborne data. We show in this chapter the feasibility of the proposed segmentation model to segment real GNSS airborne signals.

The fifth chapter is dedicated to the GNSS-R airborne experiment that took place in the context of this work and its findings. In this chapter, we introduce the airborne GNSS-R configuration adapted and the techniques used for localizing the GNSS measurements. Then, the airborne experimental setup is described along with the utilized sensors and GNSS-R receiver hardware. In this chapter, we demonstrate the architecture of our self-built software receiver for processing the GNSS data acquired during the flight experimentation. We make use of the developed models and systems in the preceding chapters to apply a real radar signal segmentation on the airborne GNSS measurements. This chapter concludes by providing a detailed analysis of the proposed radar technique and its application to water body detection and edge localization as well as its feasibility to detect other surfaces in landforms. We expose in this analysis the capacity of the proposed approach to detect in-land water body surfaces. We also show that we can localize at meter accuracy the edges of the detected water body surfaces.

Finally, a general conclusion is presented which takes stock of the work described in this thesis and proposes future perspectives to further advance in the topic.

Publications

This thesis work is valorized in 3 journals (1 of which is a collaborative work on GNSS signal processing), 2 international conference with proceedings, 3 international conferences without proceedings, 2 national communications and 1 invited talk.

Publications in a journal

1. **Issa, H.**, Stienne, G., Reboul, S., Raad, M., & Faour, G. (2021). Airborne GNSS Reflectometry for Water Body Detection. Remote Sensing, 14(1), 163.

2. **Issa, H.**, Stienne, G., Reboul, S., Semmling, M., Raad, M., Faour, G., & Wickert, J. (2021). A probabilistic model for on-line estimation of the GNSS carrier-to-noise ratio. Signal Processing, 183, 107992.

3. Kouassi, H. K. W., **Issa, H.**, Stienne, G., & Reboul, S. (2021). A linear-circular regression estimate for data fusion: Application to GNSS carrier-phase signal processing. Digital Signal Processing, 117, 103172.

International conferences with proceedings

1. **Issa, H.**, Stienne, G., Reboul, S., Raad, M., & Faour, G. (2021, September). High-Rate GNSS Reflectometry for Water Body Detection Using Low Altitude Airborne Carrier. In 2021 IEEE Specialist Meeting on Reflectometry using GNSS and other Signals of Opportunity (GNSS+ R) (pp. 9-12). IEEE.

2 **Issa, H.**, Stienne, G., Reboul, S., Raad, M., & Faour, G.. In-land Water Body Monitoring using Airborne GNSS- Reflectometry. In 2022 International Geoscience and Remote Sensing Symposium (IGARSS).

International conferences without proceedings

1. **Issa, H.**, Stienne, G., Reboul, S., Semmling, M., Raad, M., Faour, G., and Wickert, J.: High-rate GNSS Reflectometry Estimates for Airborne Soil-moisture Detection, EGU General Assembly 2021, online, 19–30 Apr 2021, EGU21-11577, https://doi.org/10.5194/egusphere-egu21-11577, 2021

2. **Issa, H.**, Stienne, G., Reboul, S., Semmling, M., Raad, M., Faour, G., and Wickert, J.: Airborne Experiment for Soil Moisture Retrieval using GNSS Reflectometry, EGU General Assembly 2020, Online, 4–8 May 2020, EGU2020-16032, https://doi.org/10.5194/egusphere-egu2020-16032, 2020

3. **Issa, H.**, Stienne, G., Reboul, S., Raad, M., & Faour, G. (2021). High-rate Airborne GNSS-R for land observation: Application to Water Body Detection. 10th ESA-China GNSS-R Workshop.

National communications

1. **Issa, H.**, Stienne, G., Reboul, S., Raad, M., & Faour, G. (2021). High-rate Airborne Experiment for Water Body Detection using GNSS Reflectometry. Recherches Marines et Littorales en Côte d'Opale (MARCO 2021).

2. **Issa, H.**, Stienne, G., Reboul, S., Raad, M., & Faour, G. (2021). Nonlinear GNSS Signal Processing Applied to Land Observation with High-rate Airborne Reflectometry. 7ème Journée Régionale des Doctorants en Automatique (JRDA 2021).

Invited talks

1. **Issa, H.**, Stienne, G., Reboul, S., Raad, M., & Faour, G. (2021). Airborne Experiment for Soil Moisture Retrieval using GNSS Reflectometry. Regional Center for Space Science and Technology Education for West Asia / United Nations (RCSSTEWA 2021).

Chapter 1

Remote Sensing of Soil Moisture

1.1 Introduction

Knowledge of distributed surface Soil Moisture Content (SMC) has been studied over the years, however it originally lacked observations of global data over large surface areas and had to recur to numerical models [12]. Even though in situ soil moisture sensors have been widely available, estimating the soil moisture content of large surface areas using in situ observations is generally impractical due to its complex installment procedure and equipment relocation, expensive cost, and most importantly the relatively small scanned surface area per use.

Remote sensing of soil moisture has been investigated using ground-based, airborne and spaceborne radiometers and radars. In this regard, active and passive sensors including radiometers, monostatic and bistatic radars have been used for soil moisture estimation. The emitted electromagnetic radiation (in passive remote sensing) or the reflected microwave radiation (in active remote sensing) from the soil surface to the sensor represents the only measurement for studying the soil properties remotely. This emitted or reflected radiation from a covered soil surface to the remote sensor no longer represent the actual soil surface emission because part of the emitted / reflected radiation might be either absorbed or enhanced by the soil cover. Different active and passive models have been developed to take into account the surface reflectivity, the effects of surface roughness, the soil physical temperature, the effect of vegetation and all other factors that contribute to the proper derivation of the soil moisture content.

GNSS-R is a method of remote sensing which uses GNSS navigation signals as "Signals of Opportunity" in a bistatic radar system. Its main principle is to receive and further extract information from the GNSS signals which

were reflected off Earth surface. GNSS-R remote sensing provides numerous advantages over other active and passive approaches. It offers the ability to estimate land surface parameters (such as SMC) on a local, regional and global scale. GNSS-R techniques use GNSS satellites as free source signal transmitters with 24 hours on-line global coverage and detection capabilities providing precise localization and dating of the received data [17]. Such systems are considered to be cost-effective compared to other techniques. In addition, GNSS-R sensors are generally light weight and thus can be mounted on spacecrafts, aircrafts, Unmanned Aerial Vehicles (UAVS) or can be simply fixed on the ground. Since the GNSS satellites provide global coverage, combining it with a dynamic GNSS-R receiver provides the ability to scan large surface areas on a regional scale and quickly reach the area to monitor at a reasonable time, which is the case in this dissertation where the GNSS-R receiver is mounted on an aircraft.

This chapter addresses the fundamentals of soil moisture remote sensing from L-band emissions. The differences between active and passive soil moisture remote sensing techniques are highlighted and remote sensing using GNSS-R is introduced. Since this dissertation focuses on soil moisture remote sensing using GNSS-R, the GNSS-R principles, geometry, methodologies, and applications are thoroughly investigated.

1.2 L-band emissions of land covers

Soil moisture remote sensing has been examined mainly in the microwave region of the electromagnetic spectrum. Short wavelengths (e.g. X-band; $\sim$ 3 cm, $\sim$ 10 GHz) reflect information from the vegetation canopy, while medium wavelengths (e.g. C-band; $\sim$ 6 cm, $\sim$ 5 GHz) reflects information from both the soil and the vegetation canopy. Long wavelengths (e.g. L-band; $\sim$ 30 cm, $\sim$ 1 GHz), on the other hand, can penetrate the canopy and obtain signals reflected solely from the soil surface.

Consequently, the microwave band that works best for soil moisture remote sensing lies within the L-band (1-2 GHz) [12, 18–20] because at these frequencies: (1) the atmosphere is nearly transparent to electromagnetic waves, (2) vegetation is semi-opaque allowing observations of the surface, (3) the microwave measurement is strongly dependent on soil moisture, because the sensitivity to changes in the dielectric constant, and hence in soil moisture, is

very large, and (4) the measurements are independent of solar illumination [12, 21]. Soil moisture affects the dielectric constant of the soil, and therefore can be retrieved from measurements of the reflectivity or emissivity of the surface [5].

Recent studies [22, 23] have exploited the use of the P-band ($\sim$ 30 cm wavelength) which could potentially provide soil moisture information for the top $\sim$ 10 cm layer of soil. However, this band is not broadcasted by the "free-source" GNSS systems. In addition, questions over the ionospheric effects on this and other low frequency radars have not been completely resolved [24]. The P-band would also require the use of larger antennas in order to maintain the same spatial resolution as L-band at the same height. Nevertheless, more satellite missions are expected to use the P-band in the future for remote sensing of the vegetation biomass.

1.2.1 Soil dielectric constant model

The soil dielectric constant ε is an electrical property that determines the response of the soil to an incident electromagnetic wave [25]. This response is composed of a real ε' and imaginary ε'' part, which is negligible at low frequencies (L, C, and X bands), and can be expressed as:

$$\varepsilon = \varepsilon' + j\varepsilon'' \tag{1.1}$$

ε' determines the wave velocity and ε'' determines the energy losses.

The soil dielectric constant depends on the volumetric SMC parameter. For instance, the dielectric properties of water ($\varepsilon \approx 80$) is much different than that of soil ($\varepsilon \approx 4$) [26]. However, the relationship between the soil dielectric constant and the soil physical properties is not straightforward. In this context, a large number of studies have been conducted over the past few decades to determine the relationship between SMC and the dielectric constant of the soil [27–29]. Most studies have used a semi-empirical approach that contains a model of the complex dielectric constant and the volume fraction of each of the soil components [26]. One of the most widely used models is presented in [27]. This model starts by expressing the dielectric mixing model as:

$$\varepsilon^{\alpha} = V_s {\varepsilon_s}^{\alpha} + V_a {\varepsilon_a}^{\alpha} + V_{fw} {\varepsilon_{fw}}^{\alpha} + V_{bw} {\varepsilon_{bw}}^{\alpha} \tag{1.2}$$

where V represents the volume fraction and the subscripts s, a, fw and bw refer to solid soil, air, free water, and bound water in the soil, respectively. α is a constant geometric factor. Since the complex dielectric constant of bound water is not well known, the following approximation is made [27]:

$$m_v{}^{\beta}\varepsilon_{fw}{}^{\alpha} = V_{fw}\varepsilon_{fw}{}^{\alpha} + V_{bw}\varepsilon_{bw}{}^{\alpha} \tag{1.3}$$

where m_v is the volumetric soil moisture. The value of the empirical constant β depends on the textural composition of the soil. The value of the shape factor α is established by using the soil model presented earlier to apportion the soil water into bound and free volume fractions and to provide estimates of ε_{fw}. According to [27], inserting these estimates and optimizing ε' and ε'' over all frequencies and soils yields $\alpha = 0.65$ as a constant. The expression (1.2) can be written as a function of a given soil bulk density ρ_b and particle density ρ_s as [27]:

$$\varepsilon^{\alpha} = 1 + \frac{\rho_b}{\rho_s}(\varepsilon_s^{\alpha} - 1) + V_{fw}\varepsilon_{fw}^{\alpha} + V_{bw}\varepsilon_{fw}^{\alpha} - m_v \tag{1.4}$$

The final expression of the semi-empirical model is then expressed as:

$$\varepsilon = \left(1 + \frac{\rho_b}{\rho_s}(\varepsilon_s^{\alpha} - 1) + m_v^{\beta}\varepsilon_{fw}^{\alpha} - m_v\right)^{1/\alpha} \tag{1.5}$$

Using $\alpha = 0.65$, the values of the soil-texture-dependent coefficient β are optimized for each of the five soils ranging from sandy loam to silty clay as in [27]. The resultant values are related to the soil texture of the five soils by :

$$\beta_{\epsilon}{}' = (127.48 - 0.519S - 0.152C)/100 \tag{1.6}$$

$$\beta_{\epsilon}{}'' = (1.33797 - 0.603S - 0.166C)/100 \tag{1.7}$$

where S and C are the percentages of sand and clay, respectively.

1.2.2 Soil emissions

The emissivity E of land covers does not only depend on the soil moisture content , but also on the surface roughness [30] , soil temperature [31], vegetation canopy [32, 33] and snow cover [34]. Emissivity is inversely related to the soil dielectric constant. For homogeneous and smooth surfaces, soil emissivity can be approximated from the soil reflectivity Γ of a plane surface as [35]:

$$E = 1 - \Gamma = 1 - |R_{\mathrm{P}}(\varepsilon, \gamma)|^2 \tag{1.8}$$

where the surface reflectivity of the soil can be computed from the Fresnel reflection coefficient R_{P} as a function of the soil dielectric constant ε and the incidence angle γ relative to the nadir using the horizontal $R_H(\varepsilon, \gamma)$ and vertical $R_V(\varepsilon, \gamma)$ Fresnel reflection coefficients defined as [36]:

$$R_H(\varepsilon, \gamma) = \frac{\cos\gamma - \sqrt{\varepsilon - \sin^2\gamma}}{\cos\gamma + \sqrt{\varepsilon - \sin^2\gamma}} \tag{1.9}$$

$$R_V(\varepsilon, \gamma) = \frac{\varepsilon\cos\gamma - \sqrt{\varepsilon - \sin^2\gamma}}{\varepsilon\cos\gamma + \sqrt{\varepsilon - \sin^2\gamma}} \tag{1.10}$$

However, for a rough surface, the surface normals at all points are not parallel as in the case of smooth surfaces, and thus the surface reflectivity may no longer be obtained from the Fresnel equations. Assuming that the radiation in a polarization state for a rough surface may be expressed as a linear combination of the radiations in horizontal and vertical polarizations for a smooth surface, the horizontal $R^{\mathrm{R}}_{\mathrm{H}}(\varepsilon, \gamma)$ and vertical $R^{\mathrm{R}}_{\mathrm{V}}(\varepsilon, \gamma)$ reflection coefficients for a rough surface may be written as:

$$R^{\mathrm{R}}_{\mathrm{H}}(\varepsilon, \gamma) = \left[(1 - Q)R_{\mathrm{H}}(\gamma) + QR_{\mathrm{V}}(\gamma)\right] e^{-h_{\mathrm{s}}\cos^{N_{\mathrm{s}}}\gamma} \tag{1.11}$$

$$R^{\mathrm{R}}_{\mathrm{V}}(\varepsilon, \gamma) = \left[(1 - Q)R_{\mathrm{V}}(\gamma) + QR_{\mathrm{H}}(\gamma)\right] e^{-h_{\mathrm{s}}\cos^{N_{\mathrm{s}}}\gamma} \tag{1.12}$$

where Q is a parameter for polarization mixing due to surface roughness, and $e^{-h_{\mathrm{s}}\cos^{N_{\mathrm{s}}}\gamma}$ is the factor by which the smooth surface reflectivity is lowered with h_{s} being a parameter characterizing height and often accounts for the intensity of the roughness effects. N_{s} is a parameter that accounts for multi-angular and dual-polarization measurements [37]. In the initial study of [38], N_{s} was set to 2. For low-frequency bands like the L-band, N_{s} can be set to 0, and Q can be disregarded [35, 37]. Therefore, at L-band, the emissivity can be corrected from surface roughness as:

$$E^R = 1 - \Gamma^{\mathrm{R}} = 1 - \Gamma e^{-h_{\mathrm{s}}} \tag{1.13}$$

where Γ^{R} corresponds to the reflectivity of a rough surface. This means that for a smooth surface ($h_{\mathrm{s}} = 0$), the emissivity is governed only by the specular Fresnel reflectivity Γ. h_{s} can be expressed as a function of the wavelength of the signal λ and the standard deviation of the surface σ_s as:

$$h_{\mathrm{s}} = 4\,k^2\sigma_s^2 \tag{1.14}$$

where $k = \frac{2\pi}{\lambda}$ is the wave number.

The volumetric soil moisture m_{v} decreases monotonically with the increase of the emissivity E of bare soil. In this regard, if the surface roughness conditions do not change much during the observations, this function can be well approximated by a linear equation of the type [35, 38]:

$$E = -a_0 m_{\mathrm{v}} + a_1 \tag{1.15}$$

Moreover, soil emission is attenuated by the covered vegetation and its contribution to the emitted radiation must be taken into consideration. For low frequency bands such as the L-band, this effect can be approximated by by a simple Radiative Transfer Model (RTM), referred to as the $\tau - \omega$ model [35, 39]. This basic model accounts for vegetation optical depth τ and the single scattering albedo ω to parameterize, respectively, the vegetation attenuation properties and the scattering effects within the canopy layer. In practice, τ is linearly linked to the total vegetation water content W_{v} (kg/m^2) as [40]:

$$\tau = b \cdot W_{\mathrm{v}} \tag{1.16}$$

where b is a constant that can be calibrated for each crop type or for large categories of vegetation (leaf-dominated, stem-dominated and grass) [37].

According to the $\tau - \omega$ model, the total emission from soil and vegetation is the sum of three terms: (1) the direct vegetation emission; (2) the vegetation emission reflected by the soil and attenuated by the canopy layer; and (3) the soil emission attenuated by the canopy [37]. Assuming that the soil temperature T_{s} and the vegetation temperature T_{v} are approximately equal (i.e. $T_{\mathrm{s}} \approx T_{\mathrm{v}}$), the total emissivity from soil and vegetation can be expressed as:

$$E^T = (1-\omega)\,(1-\mu)\left(1+\mu\Gamma^{\mathrm{R}}\right) + \left(1-\Gamma^{\mathrm{R}}\right)\mu \tag{1.17}$$

where μ is an attenuation factor that can be derived from the optical depth τ and the incidence angle γ as:

$$\mu = e^{\frac{-\tau}{\cos(\gamma)}} \tag{1.18}$$

Another surface variable that should be accounted for when studying soil emissivity is the thermal radiation or brightness temperature T_b of the soil which is determined by the effective (physical) soil temperature T_s and emissivity E [25, 41]. The brightness temperature T_b can be expressed as :

$$T_b = E \cdot T_s \tag{1.19}$$

For bare soil surfaces, T_s is a weighted sum of soil temperatures at subsurface levels accounting for the penetration depth [42]. However, if soil temperature varies with depth and differs from the temperature of the vegetation, the effective temperature T_{eff} of all emitting elements is required [35]. In most studies, T_s or T_{eff} is derived from auxiliary remote sensing observations in the thermal infrared or microwave domain, from existing climate data or from atmospheric models [43, 44]. Several simple formulations have been developed to estimate the effective soil temperature from soil properties, and soil moisture and temperature profiles [45–47]. [47] introduced a simple parametrization model of the effective soil temperature based on an initial study presented in [45]. It is shown that the effective soil temperature can be derived from the soil temperature at deep soil T_∞ corresponding to a depth between 50 cm and 1 m and on a surface temperature T_{surf} corresponding to a depth interval of 0-5 cm which can be expressed as:

$$T_s = T_\infty + (T_{surf} - T_\infty) \cdot C_T \tag{1.20}$$

where C_T is a parameter depending mainly on the frequency band and soil moisture. In the initial study of [45], C_T was computed as a function of the frequency band only ($C_T = 0.246$ at L-band). The literature in [47] later refined equation (1.20) to account for the dependence of the parameter C_T on the soil moisture. This formulation is known as the Wigneron scheme and is expressed as:

$$C_T = \left(\frac{W_s}{W_0}\right)^{b_0} \tag{1.21}$$

where W_s is the 0-3 cm surface soil moisture, and W_0 and b_0 are semi-empirical parameters depending on specific soil characteristics. In a second step, [48] further improved the Wigneron scheme (equation (1.21)) by accounting for

the dependence of the W_0 and b_0 parameters on soil texture.

Reflectivity measurements can be derived from the soil emissivity as in equations (1.8) and (1.13) for smooth and rough surfaces, respectively. These measurements are linked to the dielectric constant of the soil using the reflection coefficients. Finally, the soil moisture content is derived from the dielectric constant according to the model presented in section 1.2.1.

1.3 Soil moisture remote sensing techniques

Several approaches have been employed to retrieve SMC from passive microwave satellites observations and from active radar techniques. Passive sensors have been shown to be more resilient than active sensors in microwave remote sensing of Earth surface, particularly in retrieving surface soil moisture content. In comparison to passive sensing, active sensing is heavily influenced by scattering and attenuation caused by plant cover and surface roughness effects. The lower spatial resolutions of spaceborne passive sensors, on the other hand, limit their applicability to a wide range of applications. Active sensors, such as spaceborne radars, provide better spatial resolution observations. However, estimating soil moisture using active measurements is challenging due to difficulties in characterizing the scattering effects.

1.3.1 Passive microwave remote sensing of soil moisture

Passive microwave remote sensing at L-band (1–2 GHz) with frequent revisit times is one of the most used approaches to monitor soil moisture at a global scale [49]. It is based on the measurement of the brightness temperature T_b of a target [50]. Brightness temperature measurements result in coarse resolution because the radiometer has to cover a sufficient surface to sense an acceptable quantity of emissions. While L-band microwave sensors provide maximum sensitivity to soil moisture, their long wavelength implies the need for large antennas to achieve a useful spatial resolution in the *km* range using the passive microwave brightness temperature measurements. For example, to obtain a ground resolution of 50 *km* or less using classical solutions on low-orbit satellites implies an antenna size of up to 20 *m*.

1.3.1.1 Soil moisture retrieval algorithms

Overall, retrieving soil moisture from passive microwave brightness temperature mainly consists of two stages. The first stage is to use a radiative transfer model in order to link the brightness temperature T_b and the soil dielectric constant ε. The second stage relates ε to SMC through dielectric mixing models as presented previously. Since 1970s, RTMs have been refined for both smooth and rough soils [51], and a general form of a Radiative Transfer Equation (RTE) was introduced by [42, 46]. Several research efforts and campaigns contributed to this development [52], which culminated in the ability to model the parameters that affect T_b measurements [53].

Currently, the soil moisture inversion algorithms can be divided into four categories [37]. The first is the 2-parameter (2-P) iterative approach which can estimate several parameters simultaneously (specifically the soil moisture and vegetation optical depth) based on the inversion of the L-band Microwave Emission of the Biosphere (L-MEB) model [39, 42]. The second is the Single-Channel Algorithm (SCA), which retrieves soil moisture using a single polarized brightness temperature sensor and a large amount of auxiliary data [54]. The third algorithm is the polarization-index algorithm, which estimates soil moisture using the polarization index [55], and the fourth is the intelligent inversion algorithm which is based on neural networks [56].

Despite the fact that these algorithms have indeed achieved good soil moisture estimation results, the whole estimation process remains complicated and involves a large number of input parameters, which are difficult to measure and obtain (such as effective scattering albedo, soil texture, etc...) [57].

1.3.1.2 Satellite missions for soil moisture estimation using passive microwave sensors

Currently, there are two L-band passive microwave spaceborne missions specifically devoted to measure soil moisture: Soil Moisture and Ocean Salinity mission (SMOS) launched by the European Space Agency (ESA) in November 2009 with contributions from the Centre National d'Etudes Spatiales (CNES), France and the Centro para el Desarrollo Teccnologico Industrial (CDTI), Spain [39, 42, 58], and Soil Moisture Active and Passive mission

(SMAP) launched by the National Aeronautics and Space Administration (NASA) in January 2015 [59–61].

The Soil Moisture and Ocean Salinity mission

The SMOS satellite, shown in Figure 1.1, is the first Earth Explorer Opportunity Mission dedicated to Surface Soil Moisture (SSM) retrievals over continental surfaces and Sea Surface Salinity (SSS) over the oceans with a nominal (extended) lifetime of 3 (5) years at 763 km altitude [58, 62]. The SMOS instrument, the Microwave Imaging Radiometer with Aperture Synthesis (MIRAS), is the first L-band (1.4 GHz) 2-D interferometric radiometer in space [63, 64]. It provides brightness temperature measurements using microwave emissions from the Earth surface to map levels of soil moisture, sea surface salinity, sea ice thickness and others geophysical variables such as wind speed over ocean and freeze/ thaw soil state [65, 66].

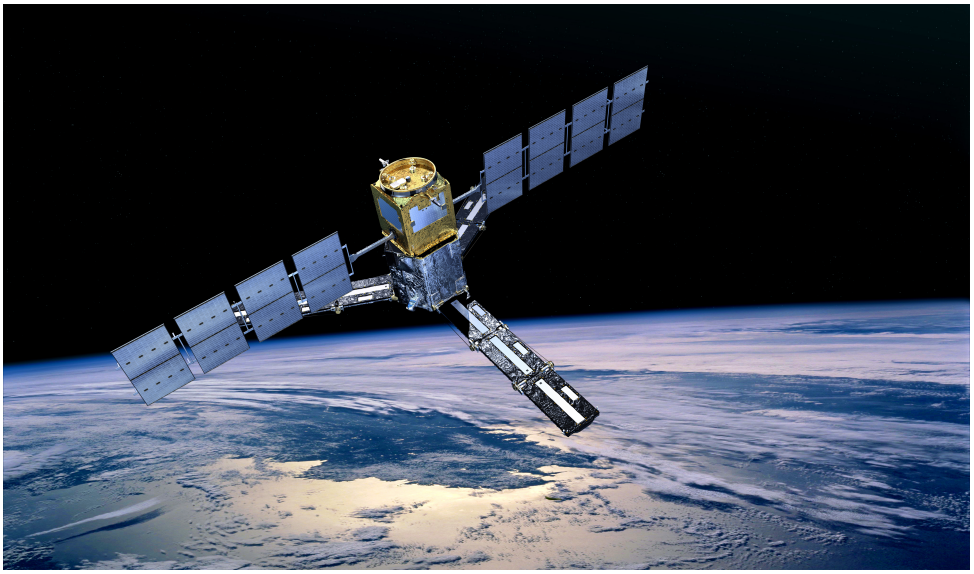

Source: ESA | (http://www.esa.int/)

FIGURE 1.1: SMOS in Orbit.

The spatial resolution of SMOS varies from 35 km at the Field of View (FoV) centre to 50 km at the border [67]. SMOS derives global maps of soil moisture and sea surface salinity every 3 days (temporal resolution), achieving a volumetric soil moisture accuracy of 4% (i.e. 0.04 m^3/m^3 volumetric humidity or better for vegetation water content $< 5\ kg/m^2$) over non forested areas of medium to low topography without snow of frozen soils [62, 68]. For bare soils, for which the influence of near-surface soil moisture on surface water fluxes is strong, it has been shown that a random error of 0.04 m^3/m^3

allows a good estimation of the evaporation and soil transfer parameters [69]. Moreover, this value corresponds to the typical root mean square (rms) dispersion of in situ soil moisture observations [68]. Over oceans, SMOS maps salinity down to 0.1 practical salinity units (psu, averaged over 10–30 days in areas measuring 200 × 200 km) [58]. Figure 1.2 provides a global view of the Earth soil moisture retrieved from SMOS Level 2 soil moisture product (MIR_SMUDP2) for the week of October 18, 2020 to October 26, 2020.

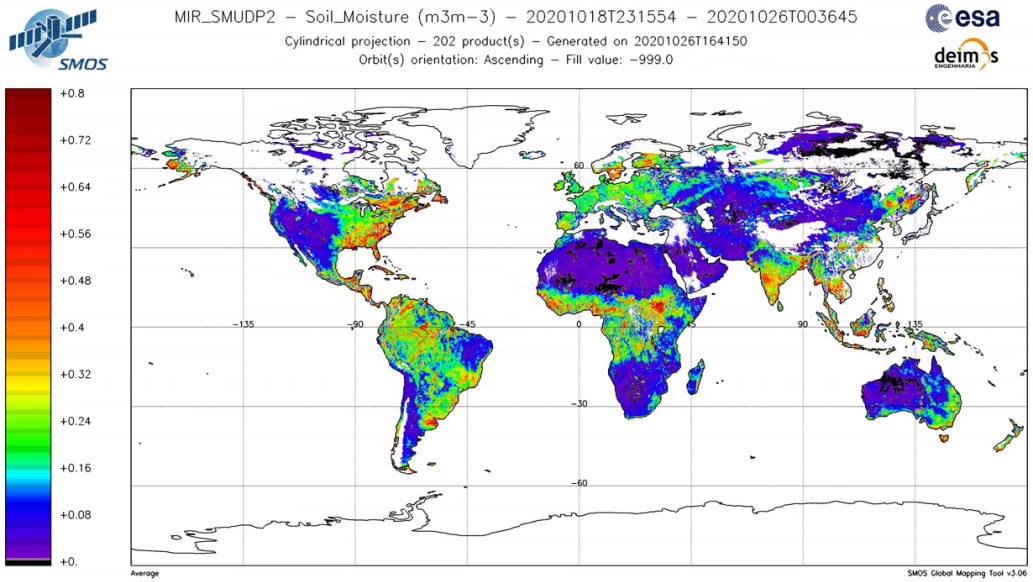

Source: ESA | (https://earth.esa.int/)

FIGURE 1.2: A global view of the average values of soil moisture data as derived from SMOS L2 product for the week of October 18, 2020 to October 26, 2020.

The black and violet coloring depict little to no moisture, while blue to yellow depict low to moderate levels of soil moisture. The red and orange coloring depict high levels of soil moisture. The white color depicts a lack of data in the map which is mainly due to contamination from radio frequency interference coming from land sites or ships and presence of sea-ice.

The Soil Moisture Active and Passive mission

NASA's SMAP mission (Figure 1.3) is an orbiting observatory with the main goal of providing a global mapping of high-resolution surface soil moisture, sea surface salinity, and landscape freeze/thaw state [49, 59]. SMAP has a circular, polar, sun-synchronous, 6:00 AM/PM equator crossing orbit located at 685 *km* altitude with a nominal lifetime of 3 years [70, 71]. SMAP's payload originally consisted of two instruments: An active Synthetic Aperture Radar (SAR) and a passive radiometer operating at L-band. The Synthetic

Aperture Radar instrument actively emits signals at 1.26 GHz and measures the backscatter from Earth surface, while the radiometer passively records the microwave signals that Earth emits naturally [72]. The strength of the emission is an indicator of the brightness temperature of the ground in that location. Both the radar and the radiometer share a 6 m diameter reflector antenna which rotates about its nadir axis.

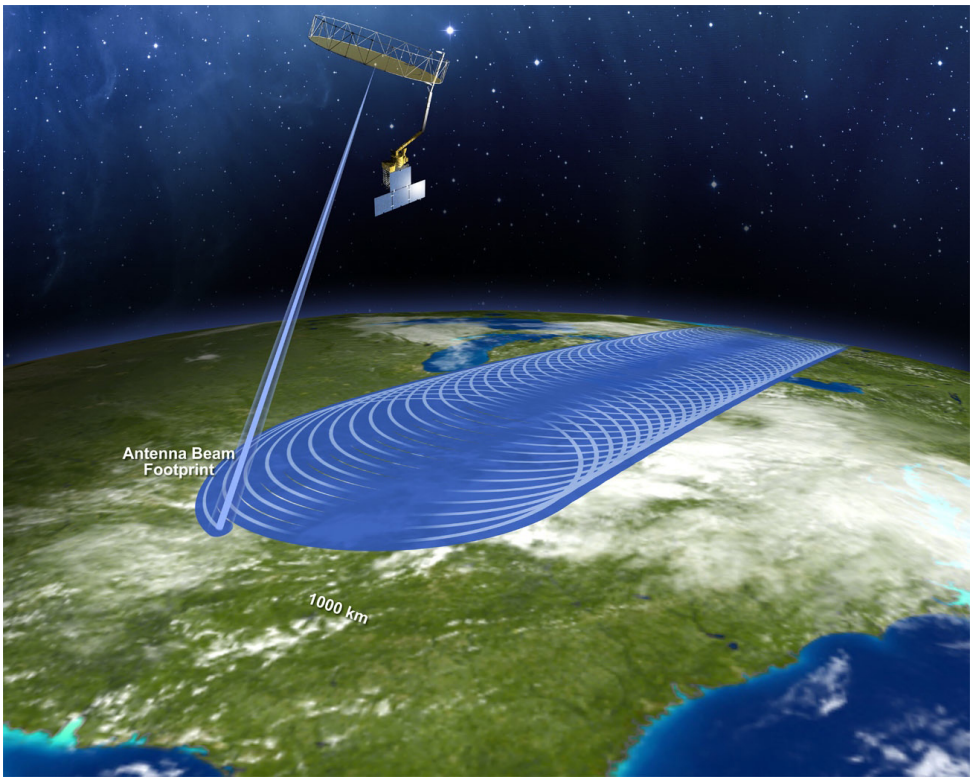

Source: NASA | (https://smap.jpl.nasa.gov/)

FIGURE 1.3: Artist's conception of SMAP. The SMAP spacecraft has a 1000 km swath width providing a radiometer footprint of about $\sim$ 36 km with 3-day revisit time.

SMAP was supposed to provide global coverage of SSM, SSS, and landscape freeze/thaw state at 3 different spatial resolutions: (i) high resolution ($\sim$ 3 km) provided by the active SAR on the expense of soil moisture accuracy, (ii) intermediate resolution ($\sim$ 9 km) provided by both the radar and radiometer, and (iii) low resolution ($\sim$ 36 km) provided by the radiometer with high soil moisture accuracy [71, 72]. In fact, the basic premise of the SMAP mission was that merging of the high-resolution active (radar) and coarse-resolution but high-sensitivity passive (radiometer) L-band observations would enable an unprecedented combination of accuracy, resolution, coverage, and revisit-time for soil moisture and freeze/thaw state retrievals

[60]. However, the radar instrument onboard SMAP satellite ceased operations on July 7, 2015 due to a problem in the radar's high-power amplifier while the L-band radiometer is still operational as designed [73].

Currently, SMAP derives global maps of soil moisture and freeze/thaw state from brightness temperature measurements at a spatial resolution of $\sim 36\ km$ with a 3-day revisit time [74]. Similar to SMOS, the measurements of global soil moisture are realized at the top 0-5 cm of the surface layer with an error no greater than 0.04 m^3/m^3 over global land areas excluding regions of snow and ice, open water, urban areas, and with a vegetation water content no greater than 5 kg/m^2 [71]. Figure 1.4, provides a global coverage of the Earth SSM (in m^3/m^3) and SSS (in psu) from SMAP Level 3 product (L3_SM_P) for the day of October 19, 2020. Areas with the lowest moisture are yellow-orange, and areas with the highest soil moisture are blue-purple.

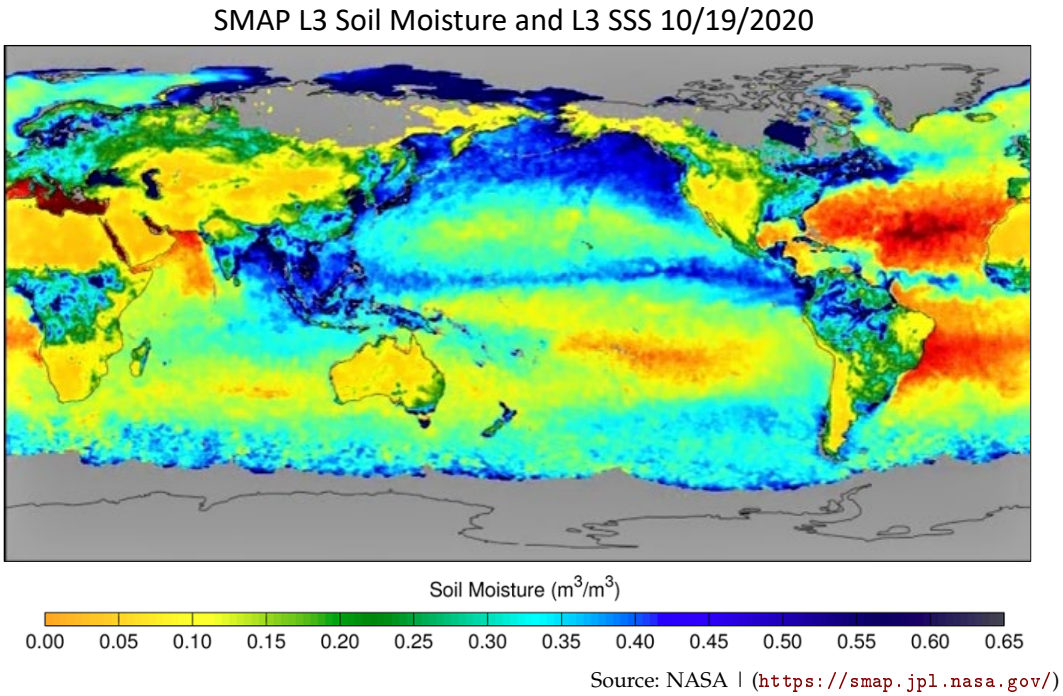

FIGURE 1.4: A global view of the average values of soil moisture and sea surface salinity as derived from SMAP L3 product for the day of October, 19 2020.

Other satellite missions

Another recent spaceborne mission that used the L-band passive remote sensing technology is the Aquarius mission launched by NASA in June 2011 [75].

Aquarius employed a set of three L-band radiometers and scatterometers, operating in a push-broom mode and covering a swath of about 300 *km* [76]. Even though the primary mission objective of Aquarius was to provide global observations of sea surface salinity, it was also used for global soil moisture before it was lost in June 2015. The C/X-band (~6/10 GHz) Advanced Microwave Scanning Radiometer (AMSR-E) launched by NASA in May 2002 also had the objective of sensing the soil moisture content, however, it ceased operations in December 2011 but was replaced by AMSR2 in May 2012 [44].

1.3.2 Active microwave remote sensing of soil moisture

Active microwave sensors (e.g. radars) receive backscattering coefficients from bare soil that have a strong correlation with soil moisture [77]. The challenging issue for soil moisture retrieval is that the relationship between soil moisture and the backward scattering coefficient is not linear. The strength of the echo is affected by roughness, vegetation cover, soil physical properties (structure, composition, etc.) and radar parameters [78].

1.3.2.1 Backscattering models

In active remote sensing, the received signal power is compared to that sent, thus allowing the backscattering coefficient σ^0 to be determined. The coefficient σ^0 depends on the radar characteristics and the soil electrical properties. Vegetation layers have a thickness sufficient to shield the scattering information from the soil surface, thus, vegetation is often regarded as the most important factor affecting soil moisture retrieval accuracy along with the surface roughness [79]. Active soil moisture remote sensing techniques can offer a high spatial resolution, however they suffer from a relatively poor accuracy. The key to improving the retrieval accuracy of soil moisture is to remove effectively the effects of surface roughness and vegetation cover [80]. Frequency, polarization and incidence angle (γ) of the sensor have effects on soil moisture retrieval that should also be taken into consideration. In active techniques, the dielectric constant of the soil is computed from σ^0, which is, in turn, converted into soil moisture through dielectric models [46].

Over the past decades, researchers have achieved great success in terms of soil moisture inversion for areas of bare soil or sparse vegetation cover. For modeling the radar backscattered signal, three kinds of models have been

used for soil-moisture estimation: the physical (theoretical) models, empirical models, and the semi-empirical models [81]. Physical models for active soil moisture retrieval are based on simulations of σ^0. In theory, there is a similarity between these physical models and the RTM of passive microwave systems. The Geometric Optic Model (GOM) [82], the Physical Optic Model (POM) [46], , the Small Perturbation Model (SPM) [83], the Small Slope Approximation (SSA) [84], the Integral Equation Model (IEM) [85], and the Advanced Integral Equation Model (AIEM) [86] are the most important physical models. The empirical or semi-empirical models mainly include the Oh model [87, 88], the Dubois model [89], and the Shi model [90].

In general, GOM is suitable under large surface roughness conditions, POM under moderate roughness conditions and the SPM model is suitable for relatively smooth, and a smaller correlation length surfaces. For SSA, only the roughness slope is required to be small enough and its main advantage is that it does not assume the correlation function to be slowly varying with the wavelength scale [91]. The IEM, and later its extension the AIEM, are the most referenced physical models. It is an RTE with physical basis, including GOM, POM, and SPM, which makes it applicable over a large range of roughness conditions. IEM shows both a high simulation accuracy and easier operation in practical applications. The IEM basically computes σ^0 considering the soil moisture content and surface roughness as unknown variables with a prior knowledge of the radar configuration [85]. The AIEM prediction accuracy is much improved compared to the original IEM [90]. Due to a difficult description of surface roughness, retrieving soil moisture using physical models is complicated and the empirical models are often preferred.

Empirical backscatter models result from several site experiment measurements of the backscattering coefficient σ^0 that are reflected from a particular soil surface to the radar sensor, and thus only valid under specific conditions. This means that empirical models may not be applicable when the set of conditions such as frequency, incidence angle, surface roughness, and vegetation density is changed [92]. Semi-empirical models can be seen as conciliation between empirical and physical models and could be used without any required condition on surface roughness. Such models are derived from experimental data to develop empirical fitting of backscatter measurements for the soil surface and could be used without any required condition on surface roughness [93]. The semi-empirical Oh model [88] employs the

backscattering coefficients ratio with separate polarization to relate them to volumetric soil moisture m_v and surface roughness as [94]:

$$p = \frac{\sigma^0_{hh}}{\sigma^0_{vv}} = \left[1 - e^{-kh_{\text{rms}}}\left(\frac{2m_v}{\pi}\right)^{\frac{1}{3\Gamma}}\right]^2 \tag{1.22}$$

$$q = \frac{\sigma^0_{hv}}{\sigma^0_{vv}} = 0.23\sqrt{\Gamma}\left(1 - e^{-kh_{\text{rms}}}\right) \tag{1.23}$$

where p is the σ^0 co-polarized ratio, q is the σ^0 cross-polarized ratio, kh_{rms} is the normalized root mean square height with k=$\frac{2\pi}{\lambda}$, and Γ is the Fresnel surface reflectivity computed using the Fresnel reflection coefficients derived in equations (1.9) and (1.10). Γ can be simply expressed as a function of the dielectric soil constant using the following expression:

$$\Gamma = \left|\frac{1 - \sqrt{\varepsilon}}{1 + \sqrt{\varepsilon}}\right|^2 \tag{1.24}$$

This model is valid for 9% < m_v < 31% and 0.1 < kh_{rms} < 6. The main advantage of the Oh model is that only the root mean square height is required as surface parameter. The semi-empirical Dubois model [89] considers the backscatter at co-polarization only and defines the coefficients as:

$$\sigma^0_{hh} = 10^{-2.75}\left(\frac{\cos^{1.5}\gamma}{\sin^5\gamma}\right)10^{0.028\varepsilon\tan\gamma}(kh_{\text{rms}}\cdot\sin\gamma)^{1.4}\lambda^{0.7} \tag{1.25}$$

$$\sigma^0_{vv} = 10^{-2.35}\left(\frac{\cos^3\gamma}{\sin^3\gamma}\right)10^{0.046\varepsilon\tan\gamma}(kh_{\text{rms}}\cdot\sin\gamma)^{1.1}\lambda^{0.7} \tag{1.26}$$

The soil dielectric constant can then be formalized by inverting equations (1.25) and (1.26). This model is valid for $m_v \leq 35\%$, $kh_{\text{rms}} \leq 2.5$, and $30° < \gamma < 65°$. The Dubois model is suited well under bare to sparsely vegetated regions [95]. The Shi model [90] computes σ^0 through the IEM single scattering process. This model works as a simple IEM for more practical completion and easy inversion. Similar to the Dubois model, the Shi model considers the backscatter at co-polarization only.

1.3.2.2 Active microwave sensors

Active microwave sensors, in contrast to passive sensors, use their own source of energy to illuminate the target. The most typical example of such devices is radars (operating with microwaves). There are imaging (two-dimensional) and non-imaging (linear) active radar altimeters and scatterometers employed

nowadays for ocean surface [96] and soil moisture studies [97]. Active satellite missions that provided soil moisture data sets that are available widely for research and applications use include: the C-band Advanced Synthetic Aperture Radar (ASAR) launched by ESA and was operational from March 2002 until the unexpected loss of contact in April 2012 [98], and the operational Advanced SCATterometer (ASCAT) launched by ESA in October 2006 [99].

Radars can be modeled as remote sensing transmitters that generate high-speed electromagnetic waves and emit it by the transmitting antenna. The receiving antenna captures the reflected electromagnetic waves by desired objects, and these waves are processed by the receiver to detect and measure the parameters of remote targets. One of the most commonly used type of radars in active remote sensing is monostatic radars.

Monostatic radars

Monostatic radars are radars where the transmitter and receiver are co-located, i.e. it uses the same antenna to transmit and receive signals. As there is one antenna used for transmission and reception, a duplexer is needed to separate the transmit chain from receive chain and vice versa. The monostatic radar equation which relates the power of the reflected signal to that of the transmitted signal is defined as:

$$P_r = \frac{P_t G^2 \lambda^2 \sigma}{(4\pi)^3 d_m^4} \tag{1.27}$$

where P_r is the received power, P_t is the transmitted power, G is the antenna gain, λ is the wavelength, σ is the scattering cross section, and d_m is the distance from the radar to the target.

Monostatic radar systems applies the backscattering phenomena to derive soil moisture from the backscattering cross section. The scattering cross section is defined as the amount of energy En scattered in a particular direction compared to a surface that radiates isotropically and it is given by:

$$\sigma_{pq} = \sigma^0 A = \frac{4\pi d_m^2 \left|En_q\right|^2}{\left|En_p\right|^2} \tag{1.28}$$

where σ^0 denotes the backscattering coefficient per unit area of the surface A, p denotes the transmitted polarization, q denotes the received polarization.

However, a perfectly smoothed surface will reflect no power back to the radar. In contrast, it would reflect all the energy in a path with an angle equal to the incident angle with respect to the surface normal. That is why monostatic radars are very sensitive to the roughness of the reflecting surface and don't operate well in smooth surface conditions. Thus, monostatic radar systems are limited to the measurements of rough surface backscattered signals, unlike the case of the bistatic radars which can cope well in smooth surface conditions. This is an important distinction to be made between monostatic and bistatic radars for surface remote sensing. An example of monstatic radar configuration is the classical Synthetic Aperture Radar.

Synthetic Aperture Radar

Synthetic Aperture Radar (SAR) is a microwave imaging system with a high spatial resolution ($\sim 10\ m - 1\ km$) [100]. Like all active systems, it has day and night operational capabilities. One way of collecting imagery from space on cloudy areas or at darkness conditions is to fly a SAR working at microwave frequencies [101]. SAR has been widely used in Earth-observing radar satellites and space missions including: SMAP (before it ceased operations), European Remote-Sensing Satellite (ERS-1 and ERS-2), Sentinel-1 and ASAR. The on-board SAR system receives the backscattering echoes from the ground, and then these echoes are transformed to baseband and digitized. As the satellite moves along its orbit, SAR looks out sideways from the direction of travel, acquiring the radar echoes (See Figure 1.5) which return from the radar swath of the Earth surface under observation.

SAR can, in principle, operate at any altitude with no variations in resolution. The detected SAR image contains a measurement of the amplitude of the radiation backscattered toward the radar by the objects (scatterers) contained in each SAR resolution cell. This amplitude is mostly influenced by surface roughness. Typically, exposed rocks and urban areas show strong amplitudes, whereas smooth flat surfaces (like quiet water basins) show low amplitudes, since the radiation is mainly mirrored away from the radar.

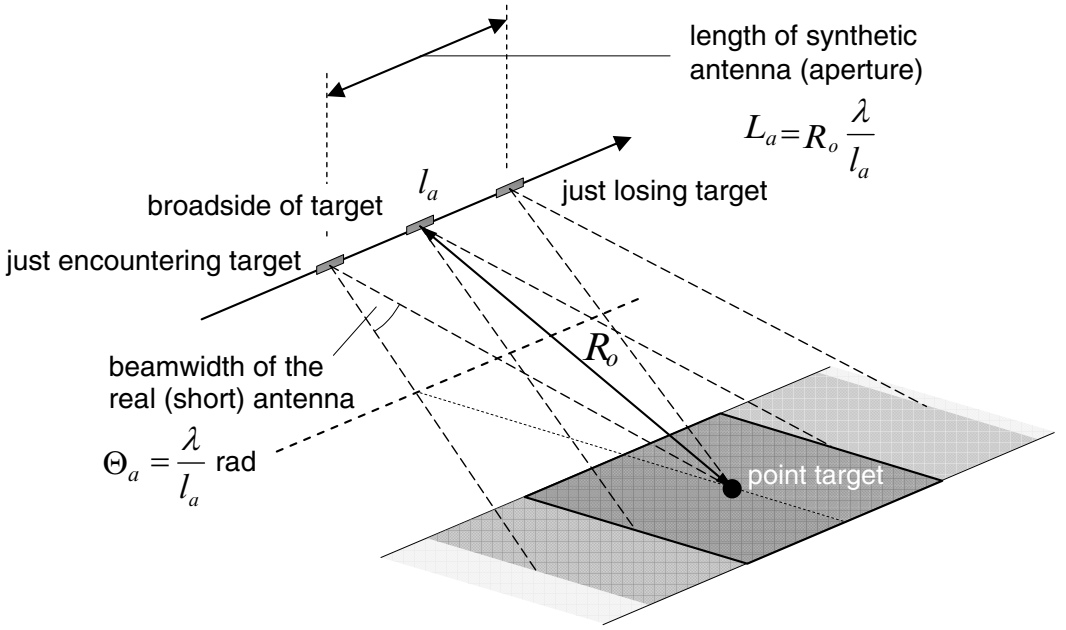

Source: Springer | (http://dx.doi.org/10.1007/978-3-642-02020-9)

FIGURE 1.5: SAR Geometry

1.4 Remote sensing using GNSS-R

1.4.1 GNSS-R as a bistatic remote sensing radar technique

GNSS-R is a bistatic radar technique where the transmitter and the receiver are not co-located. The transmitters are the GNSS satellites, the receiver is a GNSS sensor that can be fixed on ground, or mounted on an aircraft or spacecraft, and the target is an area of Earth surface. Therefore, it is always expected that GNSS sensors receive at least two signals from two different routes. One is the direct signal which propagates uninterrupted from the transmitter to the receiver and the other is the reflected signal from an area of Earth. Although a very rough surface can decrease the reflected signal power in the bistatic case, this effect can be mitigated through proper signal processing and continuous signal observations.

For land surfaces, the typical bistatic GNSS-R geometry consists of a transmitter and receiver above the surface, with scattering taking place mainly from a reflecting surface area surrounding a specular reflection point [36]. It is well known that once a signal hits a reflection point on earth, scattering will take place mainly from the region of the surface surrounding the specular reflection point. The geometry of the airborne bi-static GNSS-R setup implemented in this dissertation is depicted in Figure 1.6. An overview of other

GNSS-R geometries with single and dual antenna configurations is provided in the next section.

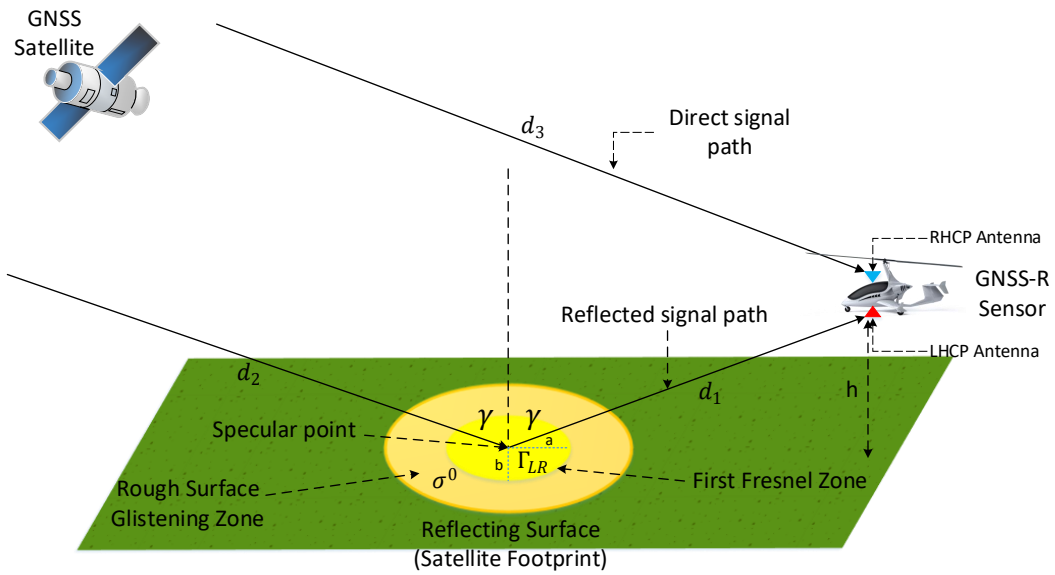

FIGURE 1.6: GNSS-R dual antenna geometry. An RHCP antenna receives the direct signals and an LHCP antenna receives the reflected signals from Earth surface.

In this dual antenna configuration, a GNSS-R receiver uses a Right-Hand Circular Polarized (RHCP) antenna pointing toward the zenith for the reception of the direct signals from satellites and a Left-Hand Circular Polarized (LHCP) antenna pointing towards the nadir for the reception of reflected signals after specular scattering. The specular point is defined as a reflection point at which the incident and reflected angles are equal. It also provides the shortest path in the GNSS-R geometry (i.e. transmitter-surface-receiver). For a perfectly flat, dielectric surface, the specularly reflected power is strongly coherent and governed solely by the Fresnel reflection coefficient of the active narrow region from which the power is reflected [102]. In this case, the size of the active region is usually considered to be the first Fresnel zone for which the differential phase change across the surface is constrained to $\frac{\lambda}{2}$, where λ is the GPS signal wavelength (for GPS L1 signals: $\lambda = 19.042\ cm$) [36]. Consequently, the spatial resolution of GNSS-R receivers is mostly linked to the size of the first Fresnel zone, which is a reason why GNSS-R provides a better spatial resolution when compared to microwave radiometry sensors.

The GPS satellites are located at approximately $20,180\ km$ above Earth surface. This means that no matter the height of a ground-based or airborne

GNSS receiver on Earth surface, the distance from the transmitter to the receiver is much larger than the distance from the reflecting surface to the receiver. In this case, the semi-major axis a and semi-minor axis b of the first Fresnel ellipse are dependent on the incidence angle γ, and the height of the receiver above ground surface h by:

$$a = \frac{\sqrt{2\delta h \cos(\gamma)}}{cos^2(\gamma)}, \; b = \frac{\sqrt{2\delta h \cos(\gamma)}}{cos(\gamma)} \tag{1.29}$$

where δ is the the differential phase change across the surface ($\delta = \frac{\lambda}{2}$). The incident angle γ can be derived from the elevation angle of the satellite (θ) where $\gamma = \frac{\pi}{2} - \theta$.

If GNSS signals are scattered by rough surfaces, the coherent component of the reflected signal decreases and the power is scattered randomly in all directions, with its magnitude smaller than the coherent component [36]. This implicates that the coherency parameter of the reflected signal is high for relatively smooth surfaces and low for very rough surfaces [103]. This parameter is essential for detecting the nature of the reflecting surface and more importantly for the modeling of the GNSS signals when geophysical properties of Earth surface need to be estimated [104, 105].

For rough surfaces, the active scattering region expands beyond the first Fresnel zone to a glistening zone [106]. The size of the glistening zone depends on surface roughness. In general, the glistening zone size widens with the increase in the surface roughness. In this case, the scattered power consists of two parts: a specular coherent component, and an incoherent component caused by the roughness [5]. The total power measured at the GNSS-R receiver can be derived from the general bistatic radar total scatter power defined in [36] as:

$$P^r_{pq} = P^c_{pq} + P^i_{pq} \tag{1.30}$$

where p and q are polarizations for the incident and scattered signals, and P^c_{pq} and P^i_{pq} are the coherent and incoherent power, respectively. On flat areas (no topography) and smooth surfaces where the specularly reflected power is strongly coherent, the bistatic radar equation for the coherent component in the case of like polarized GPS bistatic radar can be written as [107]:

$$P_{LR}^{c} = \frac{P_r^t G^t}{4\pi \left(d_1 + d_2\right)^2} \frac{G^r \lambda^2}{4\pi} \Gamma_{LR} \tag{1.31}$$

where LR stands for the left polarized scattering, P_r^t is the transmitted signal power, G^t is the transmitter antenna gain, G^r is the receiver antenna gain, and λ is the wavelength. The variables d_1 and d_2 are the distances between the specular point and the receiver, and the specular point and the satellite respectively. The cross-polarization smooth surface reflectivity Γ_{LR} can be derived from the Fresnel reflection coefficients defined in equations (1.9) and (1.10) as:

$$\Gamma_{LR} = |R_{\mathrm{LR}}(\varepsilon, \gamma)|^2 = \left| \frac{R_{\mathrm{V}}(\varepsilon, \gamma) - R_{\mathrm{H}}(\varepsilon, \gamma)}{2} \right|^2 \tag{1.32}$$

Similarly, the co-polarization Fresnel reflectivity Γ_{RR} can be expressed as:

$$\Gamma_{RR} = |R_{\mathrm{RR}}(\varepsilon, \gamma)|^2 = \left| \frac{R_{\mathrm{V}}(\varepsilon, \gamma) + R_{\mathrm{H}}(\varepsilon, \gamma)}{2} \right|^2 \tag{1.33}$$

The changes in SMC, expressed by the dielectric soil constant ε, can then be solved by inverting the Fresnel reflection coefficient. The incoherent component can be expressed as follows [108]:

$$P_{LR}^{i} = \frac{(\lambda)^2}{(4\pi)^3} \frac{P_r^t G^t G^r}{d_1^2 d_2^2} \sigma_{LR} \tag{1.34}$$

where σ_{LR} represents the bistatic radar cross section which is equivalent to the scattering cross section in the monostatic case defined in equation (1.28) and can be derived using the normalized backscattering radar coefficient σ^0. The reflectivity Γ^R of rough surfaces can be derived from the Fresnel reflectivity Γ and the roughness parameter h_{s} as defined in equation (1.13).

In addition to these components, when retrieving the soil moisture content from vegetated lands, additional parameters should be considered in order to remove the effect of vegetation on soil moisture estimation [109]. Currently, most GNSS-R techniques don't provide direct information on the coherency parameter nor on the vegetation cover. Regardless, measuring the soil moisture content of flat (smooth) surface areas is the main concern of this dissertation, and thus the effects of surface roughness on the reflected signals are not studied.

1.4.2 GNSS-R methodologies

GNSS-R techniques can be applied to retrieve some geophysical characteristics of Earth surface (e.g. SMC). These methodologies can be broadly divided into 2 groups. The first group uses a classical GNSS receiver with only one antenna and it is only applicable in situ and for low-altitude flights. This group relies on Interference Pattern Techniques (IPT) and multi-path effects. The second group uses bistatic (dual-antenna) methods to analyze the GNSS signals by utilizing specific receivers with at least two antennas. This group is applicable for in situ, aircraft, and satellite measurements.

1.4.2.1 GNSS signal processing techniques

Concerning the GNSS signal processing techniques, there exist the conventional GNSS-R (cGNSS-R) and the interferometric GNSS-R (iGNSS-R) in addition to IPT. In this dissertation, cGNSS-R is used which consists in correlating the direct signal $s^d(t)$ or reflected signal $s^r(t)$ with a clean replica $c(t)$ generated by the receiver. The amplitude of correlation Y_c^r corresponding to cross-correlating the reflected GNSS signal with $c(t)$ can be written as:

$$Y_c^r\left(t_0,\tau,f\right)=\frac{1}{T_c}\int_{t_0}^{t_0+T_c}s^r(t)\,c(t)dt \tag{1.35}$$

where T_c is the coherent integration time and t_0 is the time marking the beginning of the coherent integration. τ is the code delay and f is the carrier frequency of the local replica. In our research work, we apply cGNSS-R signal processing techniques on GPS L1 C/A signals. In this case, the GPS L1 signals are correlated with the Coarse/Acquisition (C/A) code generated by the receiver. Then expression (1.35) is written as [110]:

$$Y_c^r\left(t_0,\tau,f\right)=\frac{1}{T_c}\int_{t_0}^{t_0+T_c}s^r(t)CA(t-\tau)e^{-j2\pi ft}dt \tag{1.36}$$

In the case where a number of non-coherent integrations K^r is employed in order to improve the SNR, Y_c^r becomes:

$$\left\langle\left|Y_c^r\left(\tau,f\right)\right|^2\right\rangle\approx\frac{1}{K^r}\sum_{k=1}^{K^r}\left|Y_c^r\left(t_k,\tau,f\right)\right|^2 \tag{1.37}$$

where $\langle.\rangle$ denotes the averaging operator along time. Several advantages of this technique include separating the signals through their exact Pseudo-Random Noise (PRN) code and the ability to use smaller antennas for the

tracking of the reflected signals as compared to iGNSS-R.

The locally generated codes usually have a narrower bandwidth than encrypted codes contained in some GNSS signals. For scatterometry applications, the width of the auto-correlation function is not critical, unlike the case in altimetry applications where the width of the auto-correlation function determines the range resolution of the application [111]. One way to overcome the bandwidth limitation is the use of the iGNSS-R concept introduced in 1993 by Martin-Neira [112]. iGNSS-R consists of the cross-correlation of the reflected and direct signals which allows to use the entire signal bandwidth, including the encrypted codes that present a wider spectrum. In this case, the amplitude of correlation Y_i^r can be written as [110]:

$$Y_i^r(t_0,\tau,f) = \frac{1}{T_c}\int_{t_0}^{t_0+T_c} s^r(t)s^d(t-\tau)e^{-j2\pi ft}dt \tag{1.38}$$

$$\left\langle \left|Y_i^r(\tau,f)\right|^2 \right\rangle \approx \frac{1}{K^r}\sum_{k=1}^{K^r}\left|Y_r^i(t_k,\tau,f)\right|^2 \tag{1.39}$$

iGNSS-R allows not only the use of GNSS signals, but any other sources of opportunity with possibly larger transmitted power and larger bandwidth. The performance of the iGNSS-R is proportional to the SNR. As the direct signal is correlated with the reflected signal, the wider signal bandwidth will result in a higher thermal noise. Therefore, it is necessary to use a higher gain direct and reflected signal receiving antennas to improve the SNR. In this regard, the main drawbacks of iGNSS-R are the large antenna size (directivity) required for the up-looking antenna, the higher sensitivity to radio frequency interference (compared to cGNSS-R), and the need to separate the different satellites from their location when studying the power of the signals with respect to different ranges of delay and Doppler values [111].

1.4.2.2 Single Antenna Interference

Single antenna interference methods are based on measuring the power or phase fluctuations of the interference of the direct and reflected electric fields as the GNSS satellite moves. There are 2 main categories of single antenna interference: the interference pattern technique and the multipath method.

Interference Pattern Technique

The Interference Pattern Technique (Figure 1.7a), consists of the coherent addition of the direct and reflected signals in the receiving antenna [113]. This

results in interference patterns (fading) with high and low frequency components. As a result of fading the detected power oscillates, and its amplitude varies with the soil reflection coefficient which is related to the dielectric soil constant from which the soil moisture content can be retrieved [113].

Several works have been published regarding the use of IPT as a GNSS-R method for soil moisture estimation in [19, 113–115].The literature in [113] extends the use of the IPT from vertical polarization (V-Pol) only [19, 114] to the use of both the vertical (V-Pol) and horizontal (H-Pol) polarizations. The method uses the H-Pol to retrieve the amplitude of the interference pattern which eliminates the amplitude ambiguities of V-Pol. The larger the value of the reflection coefficient, the larger the amplitude of the interference pattern [113]. This change is more noticeable using H-Pol than V-Pol making it more accurate for soil moisture retrieval.

In order to estimate the interference patterns of both polarizations, the Fresnel reflection coefficients R_H and R_V for H-Pol and V-Pol are first derived using equations (1.9) and (1.10) respectively. Then the IPT equation in [19] is reformulated to include the reflection coefficients of both polarizations as in [113]. Using the IPT equation, the maxima $P_{q_{max}}$ and minima $P_{q_{min}}$ power values can then be obtained as [113]:

$$P_{q_{\max}}(\theta,\varepsilon) = F_n(\theta)\cdot\left|E_{0_i}\right|^2\cdot\left|1+\left|R_P(\theta,\varepsilon)\right|\right|^2 \tag{1.40}$$

$$P_{q_{\min}}(\theta,\varepsilon) = F_n(\theta)\cdot\left|E_{0_i}\right|^2\cdot\left|1-\left|R_P(\theta,\varepsilon)\right|\right|^2 \tag{1.41}$$

where θ is the elevation angle, $F_n(\theta)$ is the antenna radiation pattern, E_{0_i} is the incident electric field amplitude, and $R_P(\theta,\varepsilon)$ is the Fresnel reflection coefficient at P polarization. Then, the overall reflection coefficient at polarization P for a whole interference pattern can be expressed as [113]:

$$\left|\hat{R}_P(\theta,\epsilon)\right| \approx \frac{\sqrt{\frac{P_{q_{max}}(\theta,\varepsilon)}{P_{q_{min}}(\theta,\varepsilon)}}-1}{\sqrt{\frac{P_{q_{max}}(\theta,\varepsilon)}{P_{q_{min}}(\theta,\varepsilon)}}+1} \tag{1.42}$$

In this equation, the reflection coefficient is a function of the elevation angle θ and the dielectric soil constant ε. $\left|\hat{R}_q(\theta,\epsilon)\right|$ is an amplitude estimator of the Fresnel Reflection coefficient using different elevation angles at polarization P [113]. Thus, ε estimates are linked to the soil moisture content at

different θ values.

Multi-path method

The multi-path method (Figure 1.7b) employs a standard ground-based nearly hemispherical antenna to estimate the changes in the soil moisture content by analyzing the temporal fluctuations in the phase of the Signal-to-Noise Ratio (SNR) data for the direct and reflected signal [20, 116, 117]. It's possible to equip the antenna with an absorbing plane on the lower hemisphere to filter the signals picked up. The GPS-Interferometric Reflectometry (GPS-IR) technique introduced in [20] employs an algorithm for detecting and possibly correcting the changes in the SNR phase due to the effects of vegetation. For low satellite elevations, the interference between the direct and reflected signals induces an oscillatory pattern on the direct signals. The change in the interference pattern of the direct and reflected signals are recorded in SNR data as interferograms. In this technique, the SNR^i interferogram is expressed as [116]:

$$SNR^i = A\cos\left(\frac{4\pi H_0}{\lambda}\sin(\theta) + \phi\right) \tag{1.43}$$

where A is the amplitude of the signal, θ is the elevation angle of the satellite, λ is the GPS wavelength, and ϕ is the SNR phase shift. H_0 is within a few centimeters of the height of the antenna phase center above the top of the soil for bare flat surfaces.

Specific SNR metrics are derived to calculate the changes in the phase ϕ due to vegetation in [20]. The changes in ϕ due to vegetation are removed from the ϕ time series to maintain only the effect of the change in the soil moisture content on ϕ, which are linked to the soil moisture estimates. Then the soil moisture content (SMC) can be expressed as [20]:

$$SMC_t = S_t \Delta\phi_{SMC,t} + SMC_{resid} \tag{1.44}$$

where $\Delta\phi_{SMC,t}$ is the expected phase change due to soil moisture at time t after subtracting the effect of phase change due to vegetation, S_t is the expected slope between phase and soil moisture, and SMC_{resid} is the residual moisture content of the soil at the site which would be measured through the use of gravimetry.

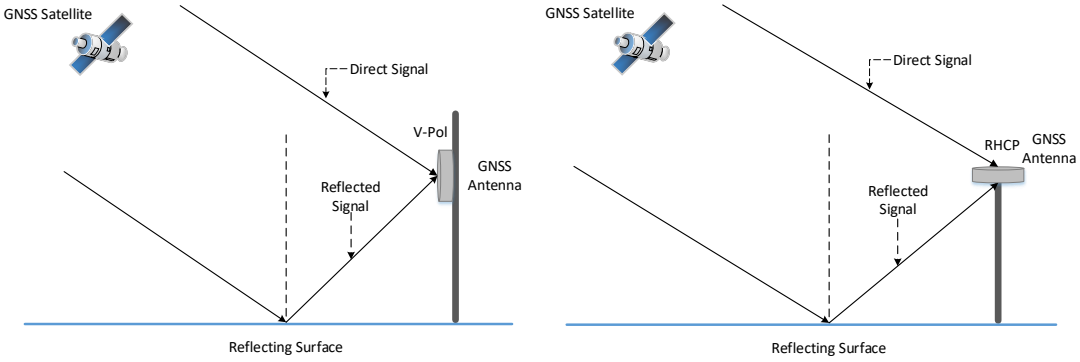

FIGURE 1.7: Single antenna interference schemes. (a) represents the geometry of single antenna (usually Vertical Polarized) GNSS-R for the IPT method, and (b) represents the geometry of a GNSS-R receiver with an omni-directional single antenna (usually RHCP) for studying multipath effects.

1.4.2.3 Dual-Antenna GNSS-R methods

Dual-antenna methods are based on the separate reception of the direct and reflected signals using two different antennas and on the separate measurement of signal powers. Based on the antenna configuration, three possible observing systems are identified:

a. **An up-looking RHCP and a down-looking LHCP antenna:** This is the GNSS-R bistatic configuration described in section 1.4.1 and used in this dissertation. In this method, measurements of reflectivity are derived using the bistatic radar equations defined in the previous section [5] or using the ratio of the reflected signal over the direct signal [12, 118]. The reflectivity is a function of the dielectric constant of the soil, the elevation angle, and the surface roughness. Refer to section 1.4.1 for a detailed explanation on this configuration and to Figure 1.6 for the geometry.

b. **An up-looking antenna (RHCP) and two down-looking antennas (one RHCP and one LHCP):** With this configuration (Figure 1.8a), it is possible to measure both the co-polar component of the terrain reflectivity by using the LHCP signal and the cross-polar component by using the RHCP antenna [119, 120].

c. **An up-looking RHCP and a down-looking LHCP antenna, receiving the direct and the reflected signals respectively, but with horizontal (H) and vertical (V) polarization for both directions:** In this configuration (1.8b), the ratio between the reflected over the direct power on the horizontal and

vertical polarizations is written as function of the surface roughness and reflectivity. For orthogonal polarization power ratio, the surface roughness influence can be canceled. The final expression was verified to hold under various scattering models, implying that it could be applied to a wide range of surface roughness [121]. The dielectric constant ε is retrieved using the ratio of power densities scattered at HH and VV polarizations at various incidence angles γ [36]. This ratio is a function of both the elevation angle and the dielectric constant. Therefore, for a better computation of ε, measurements at minimum of two different elevation angles θ using the minimum least square technique must be employed [36].

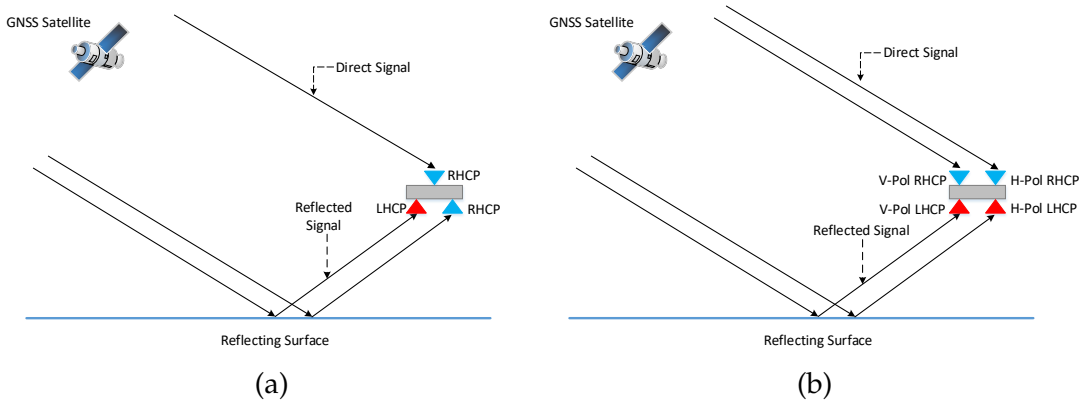

FIGURE 1.8: GNSS-R dual-antenna schemes of different observing strategies. In (a), the dual-antenna configuration consists of one up-looking RHCP antenna and two down-looking RHCP and LHCP antennas, while the geometry in (b) consists of an up-looking RHCP and a down-looking LHCP antenna, with horizontal and vertical polarizations for both directions.

The primary observable in GNSS-R dual-antenna configurations is the Delay-Doppler Map (DDM) which is obtained by cross-correlating the direct or reflected signals with the PRN code replica respectively (in this case, cGNSS-R is considered), shifted to have a range of different delays and Doppler values, thereby building up a map of direct or reflected power centered around the delay and Doppler of the reflection point. This method is mainly employed for ocean applications and SMC measurements. The estimated co- and cross-polarization Fresnel reflectivity, Γ_{LR} and Γ_{RR}, can be defined as the ratio of the direct Y_c^d and reflected Y_c^r signal powers measured at different polarizations as:

$$\Gamma_{LR} = \left| \left\langle \frac{Y^r_{c,L}\left(\Delta\tau, f^D\right)}{Y^d_{c,R}\left(0, f^D\right)} \right\rangle \right|^2 \tag{1.45}$$

$$\Gamma_{RR} = \left| \left\langle \frac{Y^r_{c,R}\left(\Delta\tau, f^D\right)}{Y^d_{c,R}\left(0, f^D\right)} \right\rangle \right|^2 \tag{1.46}$$

where L and R stand for left and right hand circular polarizations, respectively. $\Delta\tau$ is the delay difference between the direct and reflected signal and f^D is the doppler frequency. For ground-based or low-altitude receivers, the doppler frequency shift of the direct and reflected signals can be assumed to be equal, and the dependency on f^D can thus be dropped. The choice of $\tau = \Delta\tau$ for the reflected signal and $\tau = 0$ for the direct signal ensures that the waveforms respective peaks are selected. The co- and cross-polarization Fresnel reflectivity, Γ_{RR} and Γ_{LR} and its polarimetric ratio $\frac{\Gamma_{LR}}{\Gamma_{RR}}$ are the three main observable parameters that can be obtained via DDM observations.

SMC retrieval using GNSS-R dual antenna configuration relies mostly on estimating the SNR ratio of the reflected signals over the direct signals to obtain measurements of reflectivity which can be related to the soil dielectric constant and consequently to SMC. The relation between SNR and reflectivity in such configuration will be investigated thoroughly in chapter 2 section 2.4.3.

1.4.3 GNSS-R applications

GNSS-R is based on the measurements reflected by GNSS signals which are employed to estimate Earth geophysical parameters. The reflecting surface can be an ocean, in which case, the ocean altimetry, wind speed and salinity can be estimated [112, 122–124], or land for estimating the snow depth [125, 126] and the soil moisture content [12, 26, 127].

1.4.3.1 Altimetry

The first historical application of GNSS-Reflectometry was the study of ocean altimetry, that is, determination of the sea surface height. In 1993, the Passive Reflectometry and Interferometry System (PARIS) concept was proposed by Martin-Neira [112], which consisted of using GNSS reflected signals for multipoint mesoscale ocean altimetry. The aim of GNSS-R altimetry is to detect

the height between the receiver and a reflecting surface and/or the vertical location of the specular point (with respect to a reference ellipsoid or geoid). The observables to deal with are the distances between transmitter, receiver, and/or surface [128]. Although GNSS-R altimetry mainly involves measuring the sea surface height, altimetry techniques can be applied to any surface, but its performance will depend on the detecting environment. In most cases, GNSS-R altimetry is applied on perfectly flat surfaces such as water [129] or ice [130].

Several works have been developed using GNSS-R altimetry including experimental ground-based and airborne campaigns for retrieving sea surface height estimates from GNSS-R instrumentation [15, 122, 128, 131]. In [17], a circular regression technique applied to GNSS-R altimetry was presented. This technique can be also referred to as carrier phase altimetry and it provides a much better precision than group delay altimetry which relies on the code delay of the direct and reflected signals.

1.4.3.2 Sea state and salinity

The study of sea state using GNSS-R mainly involves the characterization of ocean wind and roughness as well as the ocean permittivity. The use of GNSS reflected signals as wind scatterometers was first suggested in [132]. In fact, both GNSS reflectometry and wind scatterometers measure surface roughness, not wind speed directly, and it is widely assumed that surface roughness is closely linked to wind stress on sea surface rather than the wind speed [111]. As the GNSS signal reflects off sea surface, its roughness might scatter the signal in a wide range of output directions. In general, the reflected waveforms present lower amplitudes when roughness increases.

Many ocean applications require the wind stress, while meteorological applications often prefer the effective wind at a certain altitude. Using airborne data collected in 1997, the literature in [132] first demonstrated the potential for retrieving sea state from the dependence of the GNSS sea surface reflection waveform width on wind speed. Since then, a variety of techniques have been developed for retrieving surface mean square slope and wind speed, and many have been tested using ground [124, 133] and airborne [134–136] field campaigns. Recently, ocean wind speed and surface

roughness studies are carried out over relatively large areas using DDM observables from a receiver mounted on an aircraft or satellite.

For ocean surface, the permittivity at the L-band of the electromagnetic spectrum is essentially given by the salinity and the temperature. The inversion of the polarimetric measurements derived in the previous section is used because it is sensitive to the permittivity of the reflecting surface. Few studies have focused on ocean salinity using GNSS-R [137]. However, this application is more complex to implement than altimetry or other sea state applications because it requires terrain models for a usable estimate of ocean salinity [124].

1.4.3.3 Cryosphere

GNSS signals penetrate snow to a depth of few meters, and is partially reflected by each layer of snow encountered. This allows the estimation of snow and ice thickness from reflected GNSS signals. The delays of each resulting component in the reflected signal make it possible to model the depth of each layer as a function of the incidence angle or relative amplitudes between different polarizations [138].

Works on the characterization of ice thickness, surface roughness and permittivity with GNSS-R have been proposed in [125, 126, 139]. The literature in [139] derived the condition of sea and fresh-water ice as well as the freeze/thaw state of frozen ground from aircraft experiments with GNSS-R. Studies on sea ice cover and ice age have also been carried out in [140]. The distinction between frozen and non-frozen areas of the ocean is obtained by studying the temperature of the reflecting surface. Both permittivity and surface roughness retrievals were achieved by analyzing the polarimetric reflectivity ratio in order to study the condition of sea-ice[141].

1.4.3.4 Soil moisture and vegetation

Ground-based experiments

Several ground-based experiments have been proposed to prove the GNSS-R sensitivity to soil moisture [13, 19, 20, 41, 50, 106, 113–115, 117, 119]. Many studies have employed information on multipath effects from ground-based GNSS receivers to retrieve soil moisture content and biomass content sensing [13, 20, 117]. In [19, 114, 115], the Interference Pattern Technique (IPT) was

employed to estimate the soil moisture content. A Dual-Polarization GNSS-R IPT was presented in [113] which is assumed to increase the accuracy of the estimated soil moisture content. [119] conducted the LEiMON experiment, a ground-based experimental campaign, that is based on continuous polarimetric measurements of GNSS scattered signals in order to improve the accuracy of the reflectivity measurements.

Airborne campaigns

The use of an aircraft as a GNSS-R platform offers dedicated applications for regional scale Earth surface remote sensing. Typically, a GNSS-R dual antenna configuration is used for airborne GNSS-R missions (which is the case in this dissertation), although some low-altitude airborne missions have already used single antenna configurations.

Several airborne campaigns have shown the feasibility of retrieving soil moisture using reflected GNSS signals [5, 12, 16, 41, 104, 142–148]. In [5], an airborne soil moisture remote sensing experiment was conducted in order to extract the soil moisture content from the measurements of the surface reflectivity by deriving the relation between the power of the GNSS signals, the Fresnel coefficient and the soil moisture content. A continuation of this work was presented in [12] in which a calibration method was also applied to both the direct and reflected signal through several experimental procedures in order to reduce fluctuations in reflectivity that are not related to surface features. In this work, a GPS reflectometer was installed on an HC130 aircraft during the Soil Moisture Experiment 2002 (SMEX02). Soil reflectivity and dielectric constant were obtained by normalizing the power of the calibrated reflected signal using the calibrated direct signal.

In 2015, [16] developed a GNSS-based sensor for UAVs and small manned aircraft, used to classify lands according to their soil water content. The classification is based on the SNR ratio between the direct and reflected signals. This experiment used a dual antenna configuration with one (RHCP) up-looking antenna and two (RHCP and LHCP) down-looking antennas (see Figure 1.8a). The sensor was mounted on two different platforms, a manned ultra-light aircraft (Digisky's Tecnam P92) and a UAV (Nimbus' CFly). The sensitivity of the approach was tested on an in-land water body surface. Its main limitations arise from (1) the use of different components in the receiving channels, leading to power and phase variations between the LHCP and

RHCP channels, and (2) the instrument's antennas, which are affected by cross-polarization isolation issues, thus preventing reliable polarimetric measurements. Another study that used the same setup was developed in [146]. The expected coherence time of such setup was 0.1 - 0.5 seconds.

The literature in [144] performed several low-altitude airborne experiments to determine GNSS-R sensitivity to soil moisture content using polarimetric measurements. In 2016, [148] introduced the GLObal navigation satellite system Reflectometry Instrument (GLORI), dedicated to the study of land surfaces (soil moisture, vegetation water content, forest biomass) and in-land water bodies from airborne flights. This instrument used two hemispherical GPS dual-frequency (L1 and L2) dual-polarization active antennas and mainly relied on DDM with a total integration time of 1 second to obtain measurements of surface reflectivity. The DDMs were analyzed from an altitude of approximately $600m$.

At the beginning of 2021, a study [149] performed a comparison of two different data sets acquired with the Microwave Interferometer Reflectometer (MIR), an airborne-based dual-band (L1/E1 and L5/E5a), multiconstellation (GPS and Galileo) GNSS-R instrument. The plane flew at an altitude of $h \sim 500\ m$ at an average speed of $v \simeq 75\ m/s$. In this work, the impact of surface roughness and vegetation attenuation on the reflectivity of the GNSS-R signal is assessed at both L1 and L5 bands and the effective integration time had to be increased to 5 s to neglect surface roughness effects. This increase in the integration time leads to an expected decrease in the spatial resolution.

Few studies [8, 16, 36] have been conducted concerning detection of in-land water body surfaces using airborne GNSS-R techniques. These studies also lacked a parameter analysis concerning the localization accuracy of the detected water body surfaces and the detection capacity of the proposed techniques over a large flight trajectory and mostly recurred to very few number of test areas.

Spaceborne missions

The potential of using GNSS-R to perform land Earth observations on a global scale was first demonstrated from a spacecraft in 2003 with the UK Disaster Monitoring Constellation (UK-DMC) mission [118], followed by TechDemoSat-1 (TDS-1) launched in 2014 at $\sim$ 825 km orbit height [150]. In December

2016, NASA successfully launched the Cyclone GNSS (CyGNSS) mission at $\sim$ 500 *km* orbit height. Other spaceborne missions include the 3CAT-2 of Polytechnic University of Catalonia (UPC) and the GNSS REflectometry, Radio Occultation and Scatterometry (GREOS) developed by ESA. Currently, spaceborne GNSS-R technology is developing rapidly with ESA planning to launch 'HydroGNSS' as a Scout Earth Observation small satellite mission in 2024. HydroGNSS will consist of dual satellites that use GNSS-R to sense Essential Climate Variables (ECVs) such as soil moisture, inundation/wetlands, freeze/thaw state, and biomass.

GNSS-R spaceborne missions promises enhanced resolution compared to passive satellite missions for soil moisture remote sensing, though it still suffers from a relatively low spatial and temporal resolution compared to ground-based and airborne experiments. The primary GNSS-R spaceborne missions (UK-DMC, TDS-1, and CyGNSS) employ cGNSS-R signal proccessing techniques to obtain DDM observables which is the basic product containing physical information of a surface.

Although most of the current GNSS-R missions were initially designed and conceived to observe ocean altitudes, winds, and tropical cyclones, recent studies have exhibited capabilities for sensing land surface attributes. Currently, spaceborne GNSS-R studies for soil moisture detection mainly include data from UK-DMC, TDS-1, and CyGNSS, in which exhaustive demonstration of the sensitivity of spaceborne reflected GPS signals to changes in the soil moisture has been carried out very recently using data from TDS-1 [109, 151, 152] and data from the CyGNSS mission [103, 105, 153–155].

1.5 Conclusion

Soil moisture content can be estimated by measuring the dielectric constant to which the emissivity is related by passive sensors (radiometers), and to the radar backscattering intensity by measuring through active radar sensors. Microwave radiometers measure the thermal radiation of the soil surface as a function of the soil dielectric constant, the viewing angle, and the surface roughness. Radiometers suffer from poor spatial resolution because the measurements are influenced by diurnal temperature fluctuations of the soil surface and usually require very large antennas for soil moisture sensing.

However, passive radiometers have higher accuracy than active monostatic radars which rely on backscattering measurements because it is less sensitive to surface roughness effects. In fact, active backscattering radars have larger spatial resolution than passive techniques, however their accuracy is hugely influenced by the surface roughness. Active monostatic radars measure rough surface backscattered signals and retrieve the soil moisture content by estimating the backscattering cross section which is a function of the soil dielectric constant, the viewing angle, and the surface roughness. Monostatic radars do not operate well in perfectly smoothed surface because no power will reflect back to the radar making it irrelevant for soil moisture estimation in such cases. Bistatic radars, on the other hand, are less sensitive to surface roughness effects and have higher spatial resolution than other active and passive techniques.

GNSS-R implements a bistatic configuration that uses GNSS signals as sources of opportunity to characterize Earth surface. Numerous advantages are provided with this approach including the use of free-source transmitters (i.e. the GNSS satellites) with 24 hours global coverage, the use of the highly sensitive L-band signals for remote sensing, and the ability to utilize high-end receiver hardware and dedicated software receiver configurations. The possibility of estimating soil moisture content using GNSS-R methodologies has been extensively addressed using ground-based experiments and airborne campaigns, and recently extended to investigate the feasibility of measuring soil moisture using GNSS-R based spaceborne missions. This variety of applications has provided GNSS-R techniques with the potential to measure soil moisture on different land scales with high temporal and spatial resolution. Based on the type of application intended, the appropriate GNSS-R system configuration should be implemented.

In GNSS-R single antenna configuration, reflectivity measurements from which the soil dielectric constant can be derived, are obtained by measuring the power or phase fluctuations of the interference between the direct and reflected signals. In the dual-antenna configuration (which is the most suitable for airborne and spaceborne applications), measurements of reflectivity are obtained using the SNR of the reflected signal and the direct signal which is the subject of the next chapter. In this work, we adapt an airborne GNSS-R dual antenna configuration using cGNSS-R signal processing techniques.

Chapter 2

Carrier-to-Noise Estimation : Application to Soil Moisture Retrieval using GNSS-R

2.1 Introduction

Telecommunication systems use the power of the received signal, normalized by the noise power, as an indicator of the quality of reception. The Signal-to-Noise Ratio (SNR) is called Carrier-to-Noise ratio (C/N_0) when the noise power is defined for a unit of bandwidth. C/N_0 measurements are often used in GNSS applications to monitor the receiver processing and its response to noisy environments [156, 157], determine whether the code and carrier tracking loops are in lock, and to detect the signal-to-noise environment in order to predict the performance of the receiver [113]. High rate variations in the C/N_0 are associated with multi-path disturbances [158], and low rate variations with indoor or in forest positioning [159].

The carrier-to-noise ratio is used to observe the amplitude of a GNSS signal. However, this amplitude can't be directly estimated because the GNSS antenna perceives a combination of all the GNSS signals from the satellites in view, which results in mixing the received signals. In this context, the inversion of the antenna measurements to retrieve the C/N_0 of the signals from each satellite in view is an unmixing problem. However, each GNSS satellite signal can be differentiated with its Code Division Multiple Access (CDMA) code [160]. The C/N_0 of the received signals can, therefore, be derived from the demultiplexing and demodulation processes [161].

In fact, each received signal can be expressed as a complex sum of a sine function and a cosine function (i.e. 90 degrees out of phase). The sine part

is denoted as the in-phase component and the cosine part as the quadrature component of the signal. The stages of demodulation and demultiplexing are realized respectively with a Phase Lock Loop (PLL) and a Delay Lock Loop (DLL) providing the in-phase component I and quadrature component Q measurements for each satellite. It can be shown that I are noisy observations of the signal amplitude and Q are observations of the noise [162]. In the classical approach, the statistics of these two components are used to estimate the SNR, which is proportional to the signal amplitude. Finally C/N_0 is derived from the product of the SNR with the noise equivalent bandwidth of the receiver Radio Frequency (RF) front end.

Several C/N_0 estimators have been proposed for GNSS applications in order to maximize the accuracy with minimal implementation complexity. Some estimators rely on knowledge of the transmitted data and are designated as data-aided. Other C/N_0 estimators tend to estimate C/N_0 directly from the in-phase and quadrature components of the signal. However, most C/N_0 estimation algorithms extract the SNR and then convert it to C/N_0 measurements.

In GNSS-R, the SNR (or C/N_0) of the direct and reflected GNSS signals are used to provide reflectivity measurements of a surface from which the soil dielectric constant and soil moisture content can be derived. Different algorithms have been proposed for the retrieval of soil moisture using the SNR of GNSS signals depending on the geometry of the GNSS-R setup. Some algorithms use the LHCP antenna signals only while other approaches utilize both the LHCP and RHCP antenna signals in different configurations for the retrieval of the SNR ratio.

This chapter first introduces the GNSS signal model, in particular that of the GPS C/A, addressing the fundamentals of GNSS front end processing that leads to the derivation of the C/N_0 expression from the SNR and the noise equivalent bandwidth of the receiver RF front end using the statistical properties of the two signal components. Then, some of the most popular C/N_0 estimation algorithms are highlighted while assessing their performance in terms of accuracy and computational complexity. Finally, the mechanisms for soil moisture content retrieval using the SNR of GNSS signals in different GNSS-R dual antenna configurations are presented.

2.2 Signal and system model

2.2.1 GNSS front end processing

In a GNSS receiver, it is the statistics of the correlation provided by the code and phase tracking loops that is used to estimate the carrier-to-noise ratio. The accumulated correlator outputs on the prompt channel are usually the input observations to the C/N_0 estimators. This section is dedicated to GPS C/A front end processing. A GPS C/A signal broadcasted by NAVSTAR satellites consists of a CDMA code (C/A code) with a chipping rate of 1.023 MHz and a period of 1023 bits (1 ms). This PRN code spreads the 50 bits/s navigation message. The resultant C/A signal is then modulated via Binary Phase Shift Keying (BPSK) with a carrier frequency of $f_{L1} = 1575.42\ MHz$ (L1 frequency). The signal is then sent through the communication channel. The incoming signal $s^R(t)$ for a satellite l sensed by the GNSS antenna can be expressed as:

$$s^R(t) = \sum_{l \in V} A_l^R CA_l(t + \tau_l) n_l(t + \tau_l) \sin\left[2\pi(f_{L1} + f_l^D)\, t + \phi_l^R\right] + \eta^R(t) \quad (2.1)$$

where V is the set of visible satellites, $A_l^R(t)$ is the amplitude of the incoming signal, and $CA_l(t)$ is the CDMA code of satellite l. $n_l(t)$ is the navigation data signal, τ_l is the code delay, ϕ_l^R is the phase shift of the carrier, f_l^D is the Doppler frequency associated to satellite l and $\eta^R(t)$ is a noise term. In some GNSS signal propagation environments, especially in the ionosphere and urban areas with heavy multipath, GNSS signals encounter not only an additive noise but also a multiplicative noise [163]. In this dissertation, the noise is assumed to be an Additive White Gaussian Noise (AWGN) and the multiplicative noise is not taken into account.

This signal is processed in the receiver front end. The purpose of the RF front end is to provide digital signal samples to the signal processing block. The signal $s^R(t)$ sensed by the GNSS antenna is amplified using a Low Noise Amplifier (LNA) due to the fact that the signals are immersed in noise. The LNA is characterized by its gain and noise figure [164]. Then, the amplitude of the signal is regulated using an Automatic Gain Control (AGC). After that, the received signal is down converted with a local oscillator frequency f_{LO} to an intermediate frequency f_{IF} before Analog-to-Digital Conversion (ADC).

A scheme of the RF front end of a GNSS receiver is depicted in figure 2.1. Consider the following GPS C/A signal $s(t)$ after down conversion to an intermediate frequency f_{IF}:

$$s(t) = \sum_{l \in V} K\, A_l C A_l(t + \tau_l) n_l(t + \tau_l) \sin(2\pi f_l\, t + \phi_l) + K\, \eta(t) \tag{2.2}$$

where $A_l(t)$ is the amplitude of the signal, K is the gain of the AGC, and τ is the code delay. f_l and ϕ_l are respectively the frequency and the phase delay of the carrier with $f_l = f_{IF} + f_l^D$, $\eta(t)$ is a zero mean additive Gaussian model with a unit variance. In our model, we fix the noise power and therefore the SNR variations are included in the amplitude value A_l.

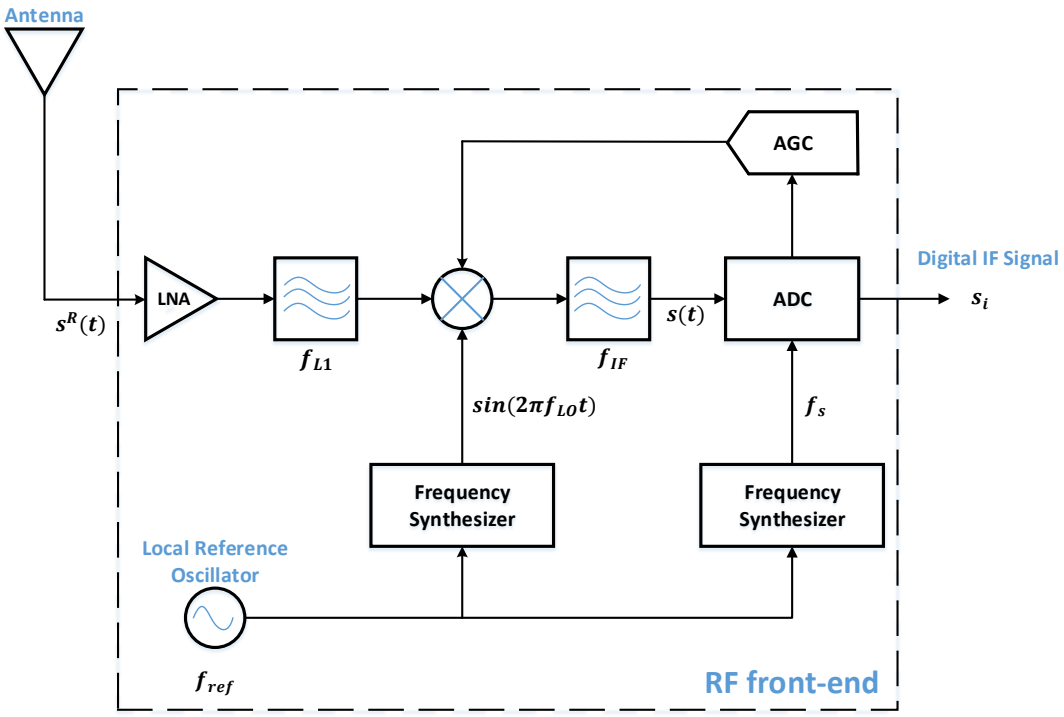

FIGURE 2.1: RF front end of a GNSS receiver. In the RF front end, the signal $s^R(t)$ sensed by the GNSS antenna is amplified using a Low Noise Amplifier before being regulated by the Automatic Gain Control. Then, using a Frequency Synthesizer, the received signal is down converted with a local oscillator frequency f_{LO} to an intermediate frequency f_{IF}. Finally Analog-to-Digital Conversion is applied to the down-converted signal $s\,(t)$ with a sampling frequency f_s to obtain the digital signal s_i.

The expression of the signal $s(t)$ after digitization can be written as:

$$s_i = \sum_{l \in V} K A_l CA_l(t_i + \tau_l) n_l(t_i + \tau_l) \sin(2\pi f_l \, t_i + \phi_l) + K\eta_i \tag{2.3}$$

A front end processes an in-phase component and a quadrature component of the received signal with local replicas. A GNSS receiver applies signal acquisition in a first stage. The purpose of the acquisition step is to estimate an initial approximation of the code delay and the carrier frequency of a signal. At the end of this first stage, the receiver tracks the variations of these parameters along with the phase delay as a function of time in a tracking module consisting of a DLL and a PLL. In the tracking process, the message of navigation is extracted and thus can be removed. The DLL process involves refining the coarse value of the code delay by correlating the in-phase I and quadrature-phase Q components of the signal with 3 locally generated replicas of the PRN code. The 3 generated replicas designates the early (suffix E), prompt (suffix P), and late (suffix L) versions of the PRN code. The PLL corrects the Doppler and phase delay initial estimates.

In practice, the GNSS receivers are numerical, therefore the local replicas generated at the receiver are digitized. The prompt local replicas are defined for a satellite v by the following expressions:

$$ci_{v,i} = CA_v(t_i + \tau_v) \sin(2\pi f_v \, t_i + \phi_v) \tag{2.4}$$

$$cq_{v,i} = CA_v(t_i + \tau_v) \cos(2\pi f_v \, t_i + \phi_v) \tag{2.5}$$

where t_i is the time instant associated to the sampling frequency f_s and τ_v is the code delay. f_v and ϕ_v are respectively the frequency and the phase delay estimates of the carrier.

The in-phase component of correlation I_v and the quadrature component Q_v for each satellite v are obtained by integrating the sampled signals over the coherent integration time T_c (therefore with $f_s \, T_c$ samples). For GPS C/A, the integration time typically varies from the 1 *ms* GPS C/A code repetition rate to the 20 *ms* navigation data message rate. In this regard, accumulating the received data over a small integration time provide SNR estimations at higher rate, however, a larger integration time increases the SNR of the signal. The accumulated in-phase, I, and quadrature, Q, samples from the

prompt correlator are expressed as:

$$I_v = \sum_{i=1}^{f_s\, T_c} s_i\, ci_{v,i} \tag{2.6}$$

$$Q_v = \sum_{i=1}^{f_s\, T_c} s_i\, cq_{v,i} \tag{2.7}$$

The correlation outputs of the I and Q prompt channels are then passed to the algorithms for C/N_0 estimation. Figure 2.2 shows a general block diagram of the software receiver implemented in this effort for GPS C/A data in the presence of AWGN interference from the receiver hardware.

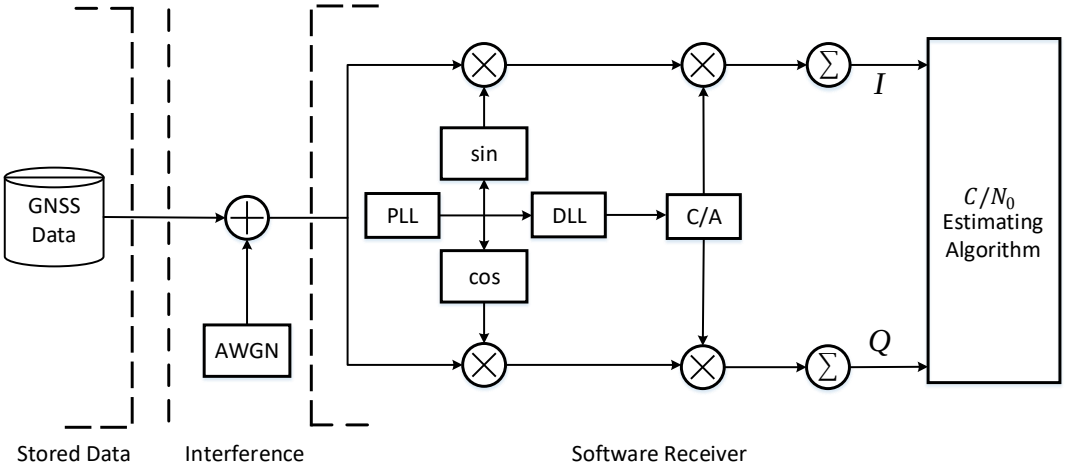

FIGURE 2.2: Block diagram of a software receiver implemented to get I and Q samples from raw GNSS data sets. The correlation outputs prompt channels are then passed to C/N_0 estimating algorithms.

2.2.2 Derivation of the carrier-to-noise ratio expression

The navigation signal at the output of the prompt correlator can be modeled as a sequence of BPSK symbols in additive noise, with a symbol rate equal to the inverse of the coherent integration time, $\frac{1}{T_c}$ [165]. In this case, the additive noise can be modeled as a discrete-time Gaussian process, white over the bandwidth $\frac{1}{2\,T_c}$. In practice, most GNSS receivers estimate the post-correlation SNR and later converts it into C/N_0 estimates. The SNR is defined as the ratio of the useful data signal power P_d over the noise power P_n. It can also be derived from the statistical properties of the 2 signal components of correlation. In this context, a classical definition of the SNR is given by [166, 167]:

$$SNR = \frac{P_d}{P_n} = \left(\frac{mean(I_v)}{std(Q_v)} \right)^2 \tag{2.8}$$

where *std* and *mean* are respectively the standard deviation and mean estimates. The carrier-to-noise ratio (C/N_0) can then be related to the SNR through the normalized equivalent noise bandwidth [168]. In ideal code delay and carrier tracking conditions, the normalized noise equivalent bandwidth of the receiver RF front end BW can be expressed as [165]:

$$BW = \frac{1}{T_c} \tag{2.9}$$

Consequently, the carrier-to-noise ratio in dB-Hz is expressed as:

$$C/N_0 = 10\, log(SNR) + 10\, log(BW) \tag{2.10}$$

Several methods are used to estimate the SNR and consequently C/N_0 from the prompt correlator components, taking into account both performance and implementation complexity. In the model that is derived in chapter 3, C/N_0 is estimated using the in-phase component of the signal as observation. The in-phase component of correlation is expressed as a function of the amplitude of the GNSS signal. Assuming that the local code and carrier are perfectly aligned with the received signals (i.e. $\tau_v = \tau_l$, $f_v = f_l$, $\phi_v = \phi_l$), equations (2.6) and (2.7) can be written as:

$$I_v = \frac{K\, A_v\, f_s\, T_c}{2} + K\, \eta_v^I \tag{2.11}$$

$$Q_v = K\, \eta_v^Q \tag{2.12}$$

where η_v^I and η_v^Q are random noises distributed according to a centered Gaussian distribution of variance $\frac{f_s\, T_c}{2}$. Then, the SNR of equation (2.8) is given by:

$$SNR = \left(\frac{mean(I_v)}{std(Q_v)} \right)^2 = \frac{A_v^2\, f_s\, T_c}{2} \tag{2.13}$$

In this equation, the SNR is proportional to the square of the amplitude of the signal and independent of K, the AGC Gain. This is the reason why the SNR is used as an observation of the signal amplitude. The carrier-to-noise ratio in dB-Hz can then be expressed as:

$$C/N_0 = 20\log\left(\frac{A_v\sqrt{f_s\,T_c}}{\sqrt{2}}\right) + 10\log(BW) \tag{2.14}$$

where $\frac{A_v}{\sqrt{2}}$ is the Root Mean Square voltage of the carrier and BW is the noise equivalent bandwidth of the receiver RF front end. This is the equation that is used in chapter 3 to derive C/N_0 using the amplitude estimates.

2.3 C/N_0 estimators

The C/N_0 estimators are divided into 2 groups: the first group estimates the C/N_0 directly from the accumulated outputs of the prompt correlator, whereas the second group estimates the SNR, which is then converted to C/N_0 using the noise equivalent bandwidth of the receiver RF front end. The estimators performance is assessed in the presence of additive noise in terms of estimation accuracy and computational complexity.

2.3.1 Direct Estimation of C/N_0

2.3.1.1 Narrowband-Wideband Power Ratio Method (NWPR)

Also called the Standard Estimate (SE), the Narrowband-Wideband Power Ratio (NWPR) is probably the most widely used C/N_0 estimator [162, 169]. It is an incoherent method that involves the comparison of powers in two different noise bandwidths in order to estimate C/N_0 directly without the need to estimate the SNR. The wideband power P_W is calculated over a noise bandwidth of $\frac{1}{T_c}$. The narrowband power P_N is taken over a noise bandwidth of $\frac{1}{M\,T_c}$ for the accumulation time T_c. M is the total number of T_c blocks used for coherent integration. Bit synchronization is neccessary to estimate the C/N_0 using this method [170]. The navigation bit transitions should be determined in order to prevent summing over a bit transition that would result in inaccurate estimates.

This method, described in [169, 171, 172], uses the accumulated in-phase I and quadrature Q samples from the prompt P correlator [172]. It starts by expressing the accumulated in-phase and quadrature samples from the prompt correlator as:

$$I_P = \sqrt{2(C/N_0)T_c}\,sinc(\pi f_e^D T_c)R(\tau_e)cos(\phi_e) + \eta_{IP} \tag{2.15}$$

$$Q_P = \sqrt{2(C/N_0)T_c}\, sinc(\pi f_e^D T_c) R(\tau_e) sin(\phi_e) + \eta_{QP} \tag{2.16}$$

where T_c is the coherent integration time over which the correlator outputs are accumulated for input to the discriminators, R is the correlation function, τ_e is the signal – reference code phase error in code chips, f_e^D is the frequency tracking error, ϕ_e is the signal – reference carrier phase error, $sinc(\alpha) = sin(\alpha)/\alpha$, and η are normalized random noise samples following a zero mean unit variance Gaussian distribution [172].

Then, an expectation operator $E()$ is used in [172] to check if the receiver is correctly tracking the signal, in which case $E()$ is written as:

$$E\left(sinc^2(\pi f_e^D T_c) R^2(\tau_e)\right) \approx 1 \tag{2.17}$$

where f_e^D ans τ_e are assumed to be close to zero when the local replicas are aligned with the incoming signal. The expectations and variances of the noise samples are given in [172] as:

$$\begin{aligned} E({\eta_{IP}}^2) &= E({\eta_{QP}}^2) &= 1 \\ E(\eta_{IP}) &= E(\eta_{QP}) &= 0 \end{aligned} \tag{2.18}$$

From equations (2.15), (2.16) and (2.17), I_P and Q_P can be rewritten as:

$$I_{Pi} = \sqrt{2(C/N_0)T_c}\, cos(\phi_e) + \eta_{I_P} \tag{2.19}$$

$$Q_{Pi} = \sqrt{2(C/N_0)T_c}\, sin(\phi_e) + \eta_{QP} \tag{2.20}$$

These samples are used to calculate the narrowband power P_N, and the wideband power P_W as [172]:

$$P_N = \left(\sum_{i=1}^{M} I_{Pi}\right)^2 + \left(\sum_{i=1}^{M} Q_{Pi}\right)^2 \tag{2.21}$$

$$P_W = \sum_{i=1}^{M} \left(I_{Pi}^2 + Q_{Pi}^2\right) \tag{2.22}$$

These power quantities are calculated using samples within the same navigation bit. For a coherent integration time that is equal to the code period in GPS C/A signals (i.e. $T_c = 1\ ms$), a maximum of $M = 20$ correlator values

within a single navigation bit that has a bit rate of 50 Hz can be chosen. Thus in order to avoid summation over transition bits, $M \in [1, 2, 4, 5, 10, 20]$.

Substituting the sampled I and Q components in equations (2.19) and (2.20) into P_N and P_W and applying equation (2.18), the expectation operators for P_N and P_W can be written as [172]:

$$E(P_N) = 2(C/N_0)T_cM^2 + 2M = 2M((C/N_0)MT_c + 1) \quad (2.23)$$

$$E(P_W) = 2(C/N_0)T_cM + \sum_{i=1}^{M} 2 = 2M((C/N_0)T_c + 1) \quad (2.24)$$

The narrow-to-wide power ratio $P_{N/W}$ is the ratio of the two power measurements averaged over $\frac{N}{M}$ iterations (N is the number of samples in the averaging time interval) to reduce the noise. It can be expressed as:

$$P_{N/W} = \frac{M}{N} \sum_{r=1}^{N/M-1} \frac{P_{N,r}}{P_{W,r}} \quad (2.25)$$

Then, applying the relevant mean properties for a measurement of the form $Z = X/Y$ [171], the expectation of the averaged narrow-to-wide power ratio is given by [172]:

$$E(P_{N/W}) \approx \frac{M((C/N_0)T_cM + 1)}{M + (C/N_0)T_cM} \quad (2.26)$$

Finally, the measured carrier-to-noise ratio in dB-Hz after rearrangement can be written as:

$$C/N_0^{NWPR} = 10\ log\left(\frac{P_{N/W} - 1}{M - P_{N/W}}\right) + 10\ log\left(\frac{1}{T_c}\right) \quad (2.27)$$

2.3.1.2 Correlator Comparison Method (CC)

An incoherent way to measure C/N_0 directly using the accumulated in-phase and quadrature components from the prompt correlator, is to compare the I_p and Q_p samples with an unsynchronized accumulated correlator output I_N that can be shared among all tracking channels. I_N is measured post-correlation to correctly reflect the receiver's response to noise in different parts of the signal spectrum [172]. This method [172, 173] uses a measurement Z that can be written as:

$$Z = \frac{\sum_{i=1}^{M} \left(I_{Pi}^2 + Q_{Pi}^2\right)}{2\sum_{i=1}^{M} I_{Ni}^2} \tag{2.28}$$

where M is the number of iterations averaged over to smooth noise [172]. If $Z = X/Y$ where X and Y are averaged separately as in equation (2.28) then:

$$X = \sum_{i=1}^{M} \left(I_{Pi}^2 + Q_{Pi}^2\right), \qquad Y = 2\sum_{i=1}^{M} I_{Ni}^2 \tag{2.29}$$

Using the I_{pi} and Q_{pi} equations defined in (2.19) and (2.20) respectively, and the statistical properties of the noise samples defined in equation (2.18), the expectations of X and Y can be written as:

$$E(X) = 2M((C/N_0)T_c + 1), \qquad E(Y) = 2M \tag{2.30}$$

Subsequently, the expectation of Z can be written as [173]:

$$E(Z) = \left((C/N_0)T_c + 1\right)\left(1 + \frac{2}{M}\right) \tag{2.31}$$

Rearranging this equation, the carrier-to-noise ratio in dB-Hz using the correlator comparison method can be written as [173]:

$$C/N_0{}^{CC} = 10\,log\left(\frac{M}{M+2}Z - 1\right) + 10\,log\left(\frac{1}{T_c}\right) \tag{2.32}$$

It is worth noting that the correlator comparison method consistently produces noisier carrier-to-noise ratio measurements than the NWPR method, but becomes less biased for very high C/N_0 environments [172].

2.3.2 Estimation of C/N_0 using SNR

2.3.2.1 Variance Summation Method (VS)

This incoherent method of C/N_0 estimation was described thoroughly in [174, 175]. It starts by defining the sample of measurement Z using the accumulated in-phase and quadrature components from the prompt correlator as:

$$Z_k = I_{v,k}^2 + Q_{v,k}^2 \tag{2.33}$$

Then, this method derives the mean $\bar{Z}$ and variance σ_Z^2 of the resulting time series Z as:

$$\bar{Z} = \frac{1}{k}\sum_{k=1}^{f_s\ T_c} Z_k \tag{2.34}$$

$$\sigma_Z^2 = \frac{1}{k-1}\sum_{k=1}^{f_s\ T_c} Z_k - \bar{Z} \tag{2.35}$$

from which the accumulation power (after removing the AGC gain) can be expressed as:

$$\left(\frac{fs\ T_c\ A}{2}\right)^2 = \sqrt{\bar{Z}^2 - \sigma_Z^2} \tag{2.36}$$

where $f_s\ T_c$ is the number of samples with f_s being the sampling frequency and T_c being the coherent integration time. For the I and Q noise components, the variance of the noise accumulation terms is [174]:

$$\sigma_{IQ}^2 = \frac{1}{2}\left(\bar{Z} - \sqrt{\bar{Z}^2 - \sigma_Z^2}\right) \tag{2.37}$$

from which the SNR can be obtained as:

$$SNR^{VS} = \frac{\left(\frac{fs\ T_c\ A}{2}\right)^2}{\sigma_{IQ}^2} \tag{2.38}$$

Finally, the carrier-to-noise ratio in dB-Hz can be expressed as a function of SNR and BW:

$$C/N_0^{VS} = 20\ \log\left(\frac{fs\ T_c\ A}{2\sigma_{IQ}}\right) + 10\ log(BW) \tag{2.39}$$

Notice that if the I and Q noise components are distributed according to a centered Gaussian distribution of variance $\sigma_{IQ}^2 = \frac{fsT_c}{2}$, then the carrier-to-noise ratio derived in expression (2.39) will be equal to that of expression (2.14) derived in the previous section. These 2 equations relate C/N_0 to the signal amplitude using the in-phase component of the signal as observation.

2.3.2.2 Beaulieu's Method (BL)

Norman C. Beaulieu introduced in [176] an intuitively motivated coherent algorithm to measure C/N_0 using the accumulated I and Q samples from the prompt P correlator. This method achieves high accuracy with minimum

complexity. The "observable" signal stream from the prompt correlator output is sampled in order to calculate C/N_0 and can be written as [176]:

$$r_C[n] = \sqrt{P_d}D[n] + \sqrt{P_n}\eta[n] \tag{2.40}$$

where n is the discrete time, $D[n] = \pm e^{j\theta_n}$ are the navigation bit samples (which can be determined and removed). θ_n is the residual carrier phase. P_d and P_n are the power associated to the data and the noise respectively, and $\eta[n] = \eta_{Re}[n] + j\eta_{Im}[n]$ expresses the complex noise samples. Then, the following equations are defined [170, 176]:

$$\hat{P}_{d,v} = r_{C,Re}[v]^2 + r_{C,Im}[v]^2 \tag{2.41}$$
$$\hat{P}_{n,v} = (|r_{C,Re}[v]| - |r_{C,Im}[v]|)^2 \tag{2.42}$$

where the random variable $\hat{P}_{d,v}$ is the instantaneous signal-plus-noise power of $r_C[v]$, which better approximates the signal power P_d as much as the noise contribution is small. In Quadrature Phase Shift Keying (QPSK), $|D_{Re}[v]| = |D_{Im}[v]|$. Thus, the random variable $\hat{P}_{n,v}$ is an approximation of the instantaneous power of $(\eta_{Re}[v] + \eta_{Im}[v])$, i.e., of the total noise $\eta[v]$. In case of BPSK modulated data, the navigation data bits appear at the in-phase correlator output, while only noise is present at the output of the quadrature branch. Thus, each sample $r_{C,Im}[v]$ can be replaced by the previous real sample $r_{C,Re}[v-1]$, without significantly affecting the estimator performance. In this case, P_d and P_n can be written as:

$$P_{d,v} = \frac{1}{2}(r_{C,Re}[v]^2 + r_{C,Re}[v-1]^2) \tag{2.43}$$
$$P_{n,v} = (|r_{C,Re}[v]| - |r_{C,Re}[v-1]|)^2 \tag{2.44}$$

Then, the SNR can be defined as:

$$SNR^{BL} = \left[\frac{1}{N}\sum_{v=1}^{N}\frac{P_{n,v}}{P_{d,v}}\right]^{-1} \tag{2.45}$$

where N is the number of samples used to produce one SNR estimate. Finally, C/N_0 is the product of the SNR and the noise equivalent bandwidth of the receiver's RF front end (BW) given in dB-Hz as:

$$C/N_0^{BL} = 10\,log(SNR^{BL}) + 10\,log(BW) \tag{2.46}$$

2.3.2.3 Moments Method (MM)

This incoherent method is based on the second- and fourth-order moments of the input process to obtain a separate estimation of the carrier and noise strengths in AWGN channels [165, 170, 177]. Take into consideration the sampled signal at the output of the prompt correlator $r_C[n]$ defined in expression (2.40). Using the theoretical formulation of the second- ($M_2 = E\{|r_C[n]|^2\}$) and fourth- ($M_4 = E\{|r_C[n]|^4\}$) order moments of the received constellation in noise, the following MM estimation algorithm can be derived [177]:

$$M_2 = \frac{1}{N}\sum_{v=1}^{N}|r_C[v]|^2 \tag{2.47}$$

$$M_4 = \frac{1}{N}\sum_{v=1}^{N}|r_C[v]|^4 \tag{2.48}$$

Assuming that the signal and noise are zero-mean, independent random processes, and the in-phase and quadrature components of the noise are independent, equations (2.47) and (2.48) are written as:

$$M_2 = P_d + P_n \tag{2.49}$$

$$M_4 = k_\alpha P_d^2 + 4P_dP_n + k_\omega P_n^2 \tag{2.50}$$

where k_α and k_ω are the kurtosis of the signal and the kurtosis of the noise, respectively. For any M-ary PSK signal over complex AWGN channels, $k_\alpha = 1$ and $k_\omega = 2$ so that the carrier power P_d and the noise power P_n can be expressed as [170]:

$$P_d = \sqrt{2M_2^2 - M_4} = \sqrt{2\left(\frac{1}{N}\sum_{v=1}^{N}|r_C[v]|^2\right)^2 - \frac{1}{N}\sum_{v=1}^{N}|r_C[v]|^4} \tag{2.51}$$

$$P_n = M_2 - P_d = M_2 - \sqrt{2M_2^2 - M_4} \tag{2.52}$$

then, the SNR is expressed as:

$$SNR^{MM} = \frac{P_d}{P_n} = \frac{\sqrt{2M_2^2 - M_4}}{M_2 - \sqrt{2M_2^2 - M_4}} \tag{2.53}$$

Finally, the carrier-to-noise ratio can be derived according to equation (2.10). This method provides a robust approach for estimating the C/N_0 at the expense of computational complexity.

2.3.2.4 Real Signal-Complex Noise Method (RSCN)

The Real Signal-Complex Noise (RSCN) method is a coherent approach described in [170, 178, 179]. As previously mentioned, the output of the I correlator is proportional to the noisy amplitude of the GNSS signal, while the output of the Q correlator is just noise. This allows to estimate the noise power at the output of the Q correlator. Consider the sampled signal stream from the prompt correlator of equation (2.40), then we have [170]:

$$P_n = \frac{2}{N}\sum_{v=1}^{N}|r_{C,Im}[v]|^2 \tag{2.54}$$

$$P_r = \frac{1}{N}\sum_{v=1}^{N}|r_C[v]|^2 \tag{2.55}$$

where P_n is the power associated to the noise at the output of the Q correlator and P_r is the total received signal power. The SNR can be written as:

$$SNR^{RSCN} = \frac{P_d}{P_n} = \frac{P_r - P_n}{P_n} \tag{2.56}$$

The carrier-to-noise ratio can then be estimated according to equation (2.10). This method requires perfect carrier synchronization because it is quite sensitive to any residual carrier phase offsets. A non-zero residual phase offset denotes an increase in the noise power measured on the output of the Q correlator.

2.3.2.5 Maximum Likelihood SNR Estimator (ML)

The Maximum Likelihood (ML) estimator described in [177, 180–183] is a coherent data aided algorithm that performs well under the assumption of known data bits. The ML method is an extension in QPSK modulation to the squared Signal-to-Noise Variance estimator (SNV) proposed for BPSK modulation in [177]. Several versions of this estimator have been proposed with [183] or without [180] perfect phase synchronization and for modern GNSS signals that have pilot and data channels [182]. The ML estimator is based

on recording the observations of N_p samples of the complex received signal given by [180]:

$$r_k = Ad_k + n_k, \quad k = 1, 2, ..., N_p \tag{2.57}$$

where A is the signal amplitude, d_k is a known preamble symbol belonging to a QPSK alphabet, and n_k is a zero-mean Gaussian complex circular random variable with variance σ_n^2 . The SNR can then be written as:

$$SNR = \frac{P_d}{P_r - P_d} = \frac{P_d}{P_n} = \frac{A^2}{\sigma_n^2} \tag{2.58}$$

where P_d is the useful signal power, P_r is the total received signal power, and P_n is the noise power. Expression (2.57) can be written in terms of real and imaginary parts as [180]:

$$r_k = u_k + jv_k = \sqrt{P_d}(d_k^I + jd_k^Q) + \sqrt{P_n}(z_k^I + jz_k^Q) \tag{2.59}$$

where I and Q denotes the in-phase and quadrature-phase components of the signal, and z_k represents the complex zero mean AWGN sample with unit variance [180].

The ML SNR estimate can be derived as the ratio of the two ML power estimates P_d and P_n over N_p observation samples. The two ML power estimates are given as [181]:

$$P_d = \left[\frac{1}{N_p}\sum_{k=1}^{N_p} Re\{r_k d_k^*\}\right]^2 \tag{2.60}$$

$$P_n = P_r - P_d = \frac{1}{N_p}\sum_{k=1}^{N_p} |r_k|^2 - P_d \tag{2.61}$$

Thus, the ML SNR estimate is expressed as:

$$SNR^{ML} = \frac{P_d}{P_n} = \frac{\left[\frac{1}{N_p}\sum_{k=1}^{N_p} Re\{r_k d_k^*\}\right]^2}{\frac{1}{N_p}\sum_{k=1}^{N_p} |r_k|^2 - \left[\frac{1}{N_p}\sum_{k=1}^{N_p} Re\{r_k d_k^*\}\right]^2} \tag{2.62}$$

The carrier-to-noise ratio C/N_0 in units of dB-Hz can then be derived from the SNR estimates by:

$$C/N_0^{ML} = 10\,log\left(SNR^{ML}\right) + 10\,log\,(BW) \tag{2.63}$$

A modified structure of the ML data aided estimator, referred to as the Modified Maximum Likelihood (MML) estimator, was proposed in [184] to improve its accuracy. In this approach, the noise variance is estimated using a non-existing PRN code that is not transmitted by any GNSS satellite. After correlating the incoming signal with the non-existing PRN code, the resulting complex correlator output is given as [184]:

$$\tilde{r}_{ext} = I_{ext} + jQ_{ext} \tag{2.64}$$

where I_{ext} and Q_{ext} are the accumulated in-phase and quadrature components after correlation with a non-existing code. The noise variance of the correlator output can be estimated using $\tilde{r}_{ext}$ as [184]:

$$\begin{aligned}\sigma^2_{MML} &= \frac{1}{2(N_p-1)}\sum_{i=1}^{N_p}\left|\tilde{r}_{ext,i} - \frac{1}{N_p}\sum_{m=1}^{N_p}\tilde{r}_{ext,m}\right|^2 \\ &= \frac{1}{2(N_p-1)}\sum_{i=1}^{N_p}\left[(I_{ext,i}-\bar{I}_{ext})^2 + (Q_{ext,i}-\bar{Q}_{ext})^2\right]\end{aligned} \tag{2.65}$$

where $\bar{I}_{ext}$ and $\bar{Q}_{ext}$ are the sample means of the in-phase and quadrature components. The mean component has been removed in order to account for any residual signal component. The noise variance values estimated in this approach are nearly unbiased. The MML SNR estimate is given by:

$$SNR^{MML} = \frac{A^2}{\sigma^2_{MML}} = \frac{\left[\frac{1}{N_p}\sum_{k=1}^{N_p} Re\{r_k d_k^*\}\right]^2}{\frac{1}{2(N_p-1)}\sum_{i=1}^{N_p}\left|\tilde{r}_{ext,i} - \frac{1}{N_p}\sum_{m=1}^{N_p}\tilde{r}_{ext,m}\right|^2} \tag{2.66}$$

2.3.3 Performance evaluation of the C/N_0 estimators

The above estimators performance is compared hereafter using simulated in-phase and quadrature correlator outputs in presence of AWGN with zero mean and unit variance. The coherent integration time is set to $T_c = 1\ ms$. The number of samples used to produce one C/N_0 estimate is set to $N =$

1000. For NWPR and CC methods, M is set to 20. An ideal front-end is assumed with perfect carrier synchronization (no frequency and phase tracking errors). This process is averaged over 50 iterations.

In this study, the performance of NWPR, CC, VS, BL, RSCN, MM and SNV is compared to true C/N_0 values ranging between 20 and 80 dB-Hz with a step of 5 db-Hz. This allows to compare the behavior of the estimators in different C/N_0 environments. SNV is referred in this section rather than ML because the signals at the output of the GNSS data channels are BPSK signals and all other estimators are adapted perfectly to this type of modulation. In SNV, the SNR is derived as in equation (2.62).

Figure 2.3 shows the estimators performance in terms of estimated C/N_0 values in dB-Hz as a function of the simulated (true) C/N_0 values (black dashed line). We also record the standard deviation of each method denoted by the error bars at each corresponding C/N_0 value.

From Figure 2.3a, we notice that the NWPR, SNV and RSCN estimators have similar overall performance except for the range [20-35] dB-Hz, where the SNV C/N_0 estimates experience a higher estimation error than the other two estimates, and the RSCN estimates are less accurate (higher std). These three estimators perform coherently and accurately with minimal estimation error under moderate C/N_0 environment in the range [35-48] dB-Hz. However, the NWPR, SNV and RSCN methods saturate and thus become unreliable for higher C/N_0 conditions (beyond 48 dB-Hz). The CC method produces noisy and inaccurate C/N_0 estimates as compared to other estimators and thus considered to be unreliable under different C/N_0 environments, though it becomes less biased in moderate C/N_0 environment. The VS method produces biased estimates in most C/N_0 conditions.

On the other hand, we notice from Figure 2.3b that the Beaulieu's method performs generally well under different C/N_0 environments, though the C/N_0 estimated using BL method experiences a considerably high estimation error in the range [20-35] dB-Hz. This error decreases significantly under moderate and high C/N_0 environments ([35-75] dB-Hz range) before it starts to increase again beyond this range. Finally, the MM method shows a good overall C/N_0 estimation performance where it operates accurately and coherently with minimal estimation error under various C/N_0 conditions except for low

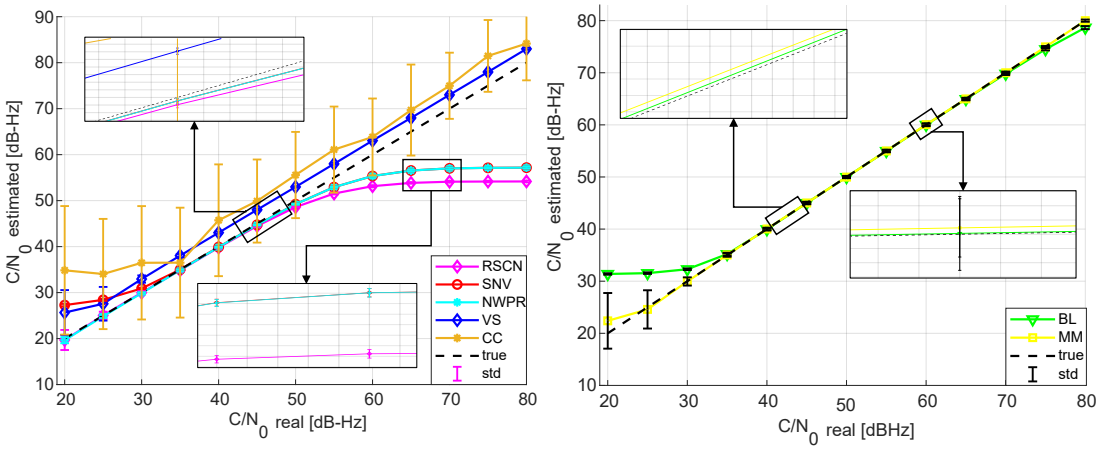

(a) (b)

FIGURE 2.3: Assessing the performance of different C/N_0 estimators. The black dashed line represents the true C/N_0 values ranging between 20 and 80 dB-Hz with a step of 5 db-Hz. C/N_0 is estimated for $T_c = 1\,ms$, $N = 1000$ and $M = 20$ averaged over 50 iterations (thus producing 13 C/N_0 mean values for each estimator). The error bars represent the std of the estimates.

C/N_0 values where the error is more significant and the estimates are less accurate. Since the C/N_0 of a good GNSS signal strength typically ranges between 35 to 55 dB-Hz, it can be concluded that Beaulieu's Method and the Moments Method are the two best approaches for GNSS C/N_0 estimation, though Beaulieu's Method yields the best performance in terms of C/N_0 estimation in this range (see zoomed part of Figure 2.3b). NWPR, SNV and RSCN methods also perform well in moderate GNSS C/N_0 environments.

In order to properly assess the performance of the different estimators, the computational complexity should be evaluated. The second study concerns the evaluation of complexity, in terms of number of real operations (additions, multiplications, and divisions) required to compute one C/N_0 estimate for the estimators that perform considerably well in GNSS C/N_0 conditions (i.e. MM, BL, NWPR, SNV and RSCN). The results of this study are reported in Table 2.1.

From Table 2.1, it can be observed that the Moments Method is the most computationally expensive method with the SNV method being the lowest demanding estimator in terms of number of real operations followed by RSCN. Beaulieu's Method also has a considerably low number of operations as compared to MM.

TABLE 2.1: Evaluation of the computational complexity required to compute one C/N_0 estimate for the different estimators.

Method	Additions	Multiplications	Divisions
MM	4N	5N + 5	1 + 1 square root
BL	3N + 1	3N + 3	N + 1
SNV	3N - 1	2N + 4	1
RSCN	3N + 1	3N + 3	1
NWPR	4N - $\frac{N}{M}$+1	2N + 2 $\left(\frac{N}{M}\right)$ + 2	$\frac{N}{M}$ + 1

From these two studies, it can be concluded that Beaulieu's Method yields the best overall performance in terms of C/N_0 estimation and computational complexity under good GNSS C/N_0 environments. Consequently, the performance of our proposed method for on-line estimation of the GNSS carrier-to-noise ratio is compared to Beaulieu's Method in chapter 4 using real data.

2.4 Soil moisture retrieval from GNSS-R

Soil moisture retrieval process using GNSS-R dual antenna configuration aims to link the received GNSS signals and the dielectric constant of the soil ε. This link is established by relating the SNR observations of the direct and reflected GNSS signals to the reflectivity measurements from which the dielectric soil constant and consequently SMC can be derived. The retrieval of the SNR data is usually done in the post-processing phase using SNR estimators such as those presented in the previous section. In this section, different GNSS-R methodologies for SMC retrieval using the SNR data as observations are introduced based on the different GNSS-R dual antenna configuration presented in section 1.4.2.3.

2.4.1 SMC retrieval using LHCP reflected signals only

If the reflecting surface can be well approximated as a perfectly smooth surface, then a specular reflection can be assumed. In such a case, the effect

of surface roughness and incoherent components in the reflection can be neglected and thus the surface reflectivity is limited to the first Fresnel reflection coefficients (i.e. $\Gamma_{LR} = |R_{\mathrm{LR}}(\varepsilon, \gamma)|^2$ for cross-polarization reflection) [16]. Then, the reflected GNSS signals results in being mainly LHCP, in particular considering the satellites with close to the zenith elevation. The dielectric constant is retrieved from the SNR of the LHCP reflected signals which can be processed by the open loop method [50]. The SNR can be expressed as the power ratio of the reflected signal over the noise related to the LHCP channel [36]:

$$SNR_{LR}^{refl} = \frac{P_r^t G^t}{4\pi \left(d_1 + d_2\right)^2} \frac{G_r^{refl} \lambda^2 G_D}{4\pi P_n^{refl}} \Gamma_{LR} \tag{2.67}$$

where LR stands for the left polarized scattering with L denoting the left hand polarization of the reflected signal and R indicating the right hand polarization of the incident wave. P_r^t is the transmitted signal power, G^t is the transmitter antenna gain, G_r^{refl} is the receiver antenna gain, and λ is the wavelength. The variables d_1 and d_2 are the distances between the specular point and the receiver, and the specular point and the satellite respectively. P_n^{refl} is the noise power and G_D is the processing gain due to the de-spread of the PRN code. The cross-polarization smooth surface reflectivity Γ_{LR} can be derived from the Fresnel reflection coefficients as defined in equation (1.32).

By signal post-processing, the SNR can be estimated from which the Fresnel reflectivity is retrieved. The dielectric constant ε is then derived by combining equations (1.9), (1.10), (1.32) and (2.67). Input parameters such as P_r^t, G^t, G_r^{refl}, and G_D are usually seen to be constants. P_n is related to the aforementioned system parameters and should be estimated or calculated properly. d_1, d_2, and the incidence angle γ are geographic information related to the satellite and receiver positions and can be calculated using GNSS-R geometry (such as that of Figure 1.6). SNR is the input parameter obtained from signal post-processing using the SNR estimators.

2.4.2 SMC retrieval using LHCP reflected signals and RHCP direct signals

In this approach, reflectivity measurements are obtained using the LHCP reflected signals and RHCP direct signals. The dielectric constant is obtained as the power ratio of the SNR of the LHCP reflected signal over the SNR of the

RHCP direct signal, provided that direct RHCP signals are processed with the same approach to get SNR. The SNR expression of the peak power for the direct RHCP signal is [50]:

$$SNR_{RR}^{dir} = \frac{P_r^t G^t}{4\pi \left(d_3\right)^2} \frac{G_r^{dir} \lambda^2 G_D}{4\pi P_n^{dir}} \tag{2.68}$$

where RR stands for the right hand polarization of both the incident wave and the received signal. d_3 is the distance between the GNSS satellite and receiver. The ratio of the LHCP reflected and RHCP direct signals SNRs is written as:

$$\frac{SNR_{LR}^{refl}}{SNR_{RR}^{dir}} = \frac{d_3^2}{\left(d_1 + d_2\right)^2} \Gamma_{LR} \cdot C_p \tag{2.69}$$

In this equation, d_1, d_2, d_3 and γ can be obtained from the GNSS-R geometry (Figure 1.6). $C_p = \frac{G_r^{refl}}{P_n^{refl}} \cdot \frac{P_n^{dir}}{G_r^{dir}}$ is a calibration parameter that depends on the hardware differences in the receiving chains, mainly due to antennas and RF filtering gains [16]. The actual value of C_p must either be ignored if there is no way to calibrate the system or calculated. One of the most used calibration mechanisms for soil moisture purposes is the on-water (usually using reflections from in-land water body surfaces) calibration, used in [12], through multiple over-water overflights. This is because the reflected signal power over calm water is well known given the incidence angle γ as compared to over the terrain reflections where the uncertainty is much higher.

For more accurate calibration, a measurement campaign should be done in situ for different soil types and moisture conditions using different sensors over very large intervals of time. Then, the obtained results would be compared with all the other sensors in the terrain. The dielectric soil constant ε can then be obtained from equation (2.69) given all the input parameters involved.

2.4.3 SMC retrieval using both LHCP and RHCP reflected signals

The above retrieval algorithms are based on the assumption of having a smooth reflecting surface with considerably high satellites elevation angles

where the reflected signals are mainly observed using the LHCP link. However, in order to take into account the effects of surface roughness and to observe reflections of satellites with low elevation angles, SMC should be measured using both LHCP and RHCP reflected GNSS signals. In this regard, the estimated reflected LHCP and RHCP SNRs are linked to the normalized bistatic radar cross section σ^0_{pq}. σ^0_{pq} is a function of the dielectric properties of the material and separates into a horizontal and a vertical polarization component [16]. This approach estimates the dielectric constant of the soil using the normalized backscattering cross section for the two circular polarizations of the reflected GNSS signals. The SNR can be expressed for both the LHCP and the RHCP reflections as [16]:

$$SNR^{refl}_{LR} = \frac{G^t\, G^{refl}_{r,LR}\, \lambda^2\, |\sigma_{LR}|\, P^t_r}{(4\pi)^3\, d_1^2\, d_2^2\, P^{refl}_{n,LR}} \tag{2.70}$$

$$SNR^{refl}_{RR} = \frac{G^t\, G^{refl}_{r,RR}\, \lambda^2\, |\sigma_{RR}|\, P^t_r}{(4\pi)^3\, d_1^2\, d_2^2\, P^{refl}_{n,RR}} \tag{2.71}$$

where the subscript LR indicates a left polarization of the reflected signal and a right polarization of the incident wave. The subscript RR indicates a right polarization for both the incident wave and reflected signal. σ_{LR} represents the cross-polarization radar cross section and σ_{RR} represents the co-polarization radar cross section. All remaining parameters are as defined in the previous sections. The co- and cross-polarization radar cross section can be written as [16, 185]:

$$\sqrt{\sigma_{LR}} = \frac{\sqrt{Ar}}{2}\left(\sqrt{\sigma^0_{HH}} + \sqrt{\sigma^0_{VV}}\right) \tag{2.72}$$

$$\sqrt{\sigma_{RR}} = \frac{\sqrt{Ar}}{2}\left(\sqrt{\sigma^0_{HH}} - \sqrt{\sigma^0_{VV}}\right) \tag{2.73}$$

where σ^0_{HH} and σ^0_{VV} are the horizontal and vertical polarization components of the normalized radar backscattering coefficient and Ar is the total illuminated area, or glistening zone, which depends on the GNSS-R geometry [186]. Combining equations (2.70) and (2.71) with equations (2.72) and (2.73), the ratio of the SNR of the LHCP reflected signal over the SNR of the RHCP reflected signal can be written as:

$$\frac{SNR_{LR}^{refl}}{SNR_{RR}^{refl}} = \frac{\left|\sqrt{\sigma_{HH}^{0}} + \sqrt{\sigma_{VV}^{0}}\right|}{\left|\sqrt{\sigma_{HH}^{0}} - \sqrt{\sigma_{VV}^{0}}\right|} \cdot C_p' \tag{2.74}$$

where $C_p' = \frac{G_{r,LR}^{refl}}{P_{n,LR}^{refl}} \cdot \frac{P_{n,RR}^{refl}}{G_{r,RR}^{refl}}$ is a calibration parameter similar to C_p.

In practice, σ_{HH}^{0} and σ_{VV}^{0} are functions of the soil dielectric constant and the incidence angle and can be described through proper scattering models that take into account various other physical parameters involved in the reflection phenomena [16]. σ_{HH}^{0} and σ_{VV}^{0} are polarization sensitive parameters that can be related to the Fresnel reflection coefficients and other polarization independent surface roughness parameters through physical scattering models such as GOM, POM and SPM described in the previous chapter. In such a case, expression (2.74) can be re-written (ignoring C_p') as [36]:

$$\frac{SNR_{LR}^{refl}}{SNR_{RR}^{refl}} = \frac{||R_{\mathrm{H}}(\varepsilon,\gamma)| + R_{\mathrm{V}}(\varepsilon,\gamma)||}{||R_{\mathrm{H}}(\varepsilon,\gamma)| - R_{\mathrm{V}}(\varepsilon,\gamma)||} \tag{2.75}$$

where $R_{\mathrm{H}}(\varepsilon,\gamma)$ and $R_{\mathrm{V}}(\varepsilon,\gamma)$ are the Fresnel reflection coefficients defined in equations (1.9) and (1.10) respectively. Note that this power ratio is independent of the surface roughness and is only a function of the dielectric constant and incident angle. If semi-empirical scattering models are used, such as Oh model or Dubois model described in the previous chapter, then σ_{HH}^{0} and σ_{VV}^{0} are written as a function of the Fresnel reflectivity and other surface roughness dependent parameters (refer to equations (1.22), (1.23), (1.24) for Oh model and equations (1.25) and (1.26) for Dubois model), and thus the dielectric constant can be derived by substituting the corresponding equivalent expressions of σ_{HH}^{0} and σ_{VV}^{0} in equation (2.74). After post processing with the proper SNR estimator, the SNR for both LR and RR polarizations are obtained as input parameters and ε can be derived. Finally, a dielectric constant model (such as that described in section 1.2.1) is used to relate the dielectric constant of the soil to the soil moisture content.

2.5 Conclusion

The carrier-to-noise ratio is the ratio of the received carrier power level to the noise power level in a unit bandwidth. It can be seen as a normalized measure of the SNR which can be derived from the accumulated in-phase and

quadrature components of the signal at the prompt channel. The in-phase and quadrature components of correlation are provided by code tracking loops and then passed to algorithms for C/N_0 estimation. The GNSS signal carrier-to-noise ratio can be written in terms of the signal amplitude using the in-phase component of the signal as observation. This formulation will be used in the next chapter in order to derive high rate GNSS C/N_0 estimates.

Several C/N_0 estimators have been introduced in this chapter and their performance was compared in terms of estimation accuracy and number of real operations required. The most widely used estimate is the Narrowband-to-Wideband Power Ratio. This estimate uses the accumulated I and Q samples from the prompt correlator to directly estimate the C/N_0. The NWPR performs well under weak and moderate signal environments, but saturates at higher C/N_0 conditions. Another way to measure C/N_0 directly using the accumulated in-phase and quadrature components from the prompt correlator is the Correlator Comparison method. The CC method perform poorly in GNSS C/N_0 environments and is highly sensitive to noise.

Beaulieu's method is introduced as an intuitively motivated algorithm that measures C/N_0 by estimating the SNR using the accumulated I and Q samples from the prompt channel. This method achieves high accuracy with low complexity. The Moments-based method is an accurate C/N_0 estimator but has a high complexity cost. The Real Signal - Complex Noise shows similar performances to NWPR. The Variance Summation method relates the C/N_0 to the signal amplitudes but produces biased observations of the C/N_0 as compared to other estimators. The Maximum Likelihood Estimate and its BPSK counterpart the Signal-to-Noise Variance estimator provides a good compromise in terms of complexity and accuracy. It performs well under low to moderate C/N_0 environments but saturates at high levels.

We show that Beaulieu's method provides the best trade-off performance between accuracy and complexity under the typical GNSS C/N_0 range and thus will be used for comparison with our proposed on-line estimator of the GNSS C/N_0. It is important to note that all studied C/N_0 estimators require a relatively high integration time to produce reliable C/N_0 estimates.

Finally, the soil moisture retrieval process using SNR data in GNSS-R dual antenna configuration is presented. This is done by linking the SNR to the

reflectivity measurements from which the soil dielectric constant and SMC can be derived. SNR can be retrieved by using LHCP reflected signal only, LHCP reflected and RHCP direct signals, or both LHCP reflected and RHCP reflected signals. In this dissertation, we derive reflectivity measurements from the ratio of the LHCP reflected signal over the RHCP direct signal.

Chapter 3

A Probabilistic Model for On-line Estimation of the GNSS Carrier-to-Noise Ratio

3.1 Introduction

A GNSS antenna receives signals from different GNSS satellites in view at a time. In a GNSS receiver, it is the statistic of the correlation provided by the code tracking loop that is used to estimate the carrier-to-noise ratio. In practice, the difficulty associated to the estimation of the C/N_0 is the derivation of the statistical parameters of the two components in quadrature. This estimation process assumes that the noise is stationary and the signal amplitude is constant. This assumption is less restrictive for high rate estimations. However, the accuracy of the estimation depends on the duration of the observation. In this context, accuracy and estimation rate are two ambivalent parameters.

In a classical GNSS receiver, 1-bit or 2-bit quantization is sufficient. However, in some military applications, 8 bits are necessary to accurately process the Power Spectral Density (PSD) of the signal in order to prevent GNSS spoofing. We developed for this work, a bit grabber to record the data with 1-bit quantization. The PLL and FLL (Frequency Lock Loop) estimate the parameters of the signal in our self-built 1-bit GNSS software receiver. The software receiver processes the data on-line. The on-line loops correct the phase delay error, the code delay error and the error in Doppler during the tracking process. We show in a preceding work [187], that we can indeed reach centimeter precise position estimates every 1 *ms*. In this case, observations of phase and Doppler were used to process the code delay of the GNSS signal obtained every 1 *ms*. Concerning GNSS applications, the minimum

length of integration $T_c = 1\ ms$ (code period for GPS C/A) is known and is an objective in our development. We aim at high rate carrier-to-noise estimation, namely the code repetition rate (e.g. 1 ms for GPS C/A), in order to maximize the time resolution of carrier-to-noise observations.

In this chapter, we use 1-bit quantization because the digitized signals are independent of the AGC. We show that the mean value of the in-phase component of correlation I, provides a direct observation of the signal amplitude and therefore of C/N_0. We estimate the GNSS signal amplitudes at high rate (1 ms rate for GPS C/A) using 1 ms rate observations of I. High rate C/N_0 estimation is essential in multipath, and dynamic GNSS-R applications, where the C/N_0 estimation rate determines the system's ability to cope with the rapid displacement of the GNSS receiver and defines the rate at which the environment can be analyzed. However, the model that links the signal amplitude to the 1 ms rate observations of I is non-linear and we derive its expression. In this context, we propose an on-line estimate of the amplitudes of the signals based on an Extended Kalman Filter (EKF) that uses measurements of I as observations. The linearization of the measurement equation that links I to the signal amplitude is then derived.

Based on the foregoing, this chapter is organized as follows: the next section highlights the principles of 1-bit coherent detection. The third section presents the GNSS one bit front end model while recalling some of the basic principles of the GNSS front end processing presented in the previous chapter. In the fourth section, an on-line estimate of the signal amplitude in the form of an EKF is introduced, while interpreting the non-linear expression that links the observations of I to the amplitudes of the signals. The proposed methodology is assessed using both synthetic and real data in the fifth section. We show using real data that, for a 1-bit quantization receiver, the proposed estimator can achieve the same accuracy as a widely known commercial GNSS receiver with a much higher data rate. Conclusions are provided in the final section.

3.2 1-bit coherent detection principle

In this work, a probabilistic model of the front end architecture of a coherent detector is proposed. Coherent detectors are used in several applications like GNSS, telecommunication systems and radar systems. For this work, 1-bit

GNSS software receiver is developed in order to estimate the signal parameters. In this software, the accumulated in-phase component at the output of the prompt correlator provides a direct observation of the signal amplitude and therefore of C/N_0. We assume that the DLL and PLL estimated parameters are perfectly aligned with the input signal, and thus the detections are coherent detections.

We show in Figure 3.1, a reference signal (blue dashed line) and a noisy signal (red line), i.e. after adding noise. In this study, the noise is a zero mean additive Gaussian noise with unit variance, the sampling frequency is 100 KHz and the amplitude is fixed to 2. The noisy signal is a real signal received by the receiver and the reference signal is a signal generated by the receiver.

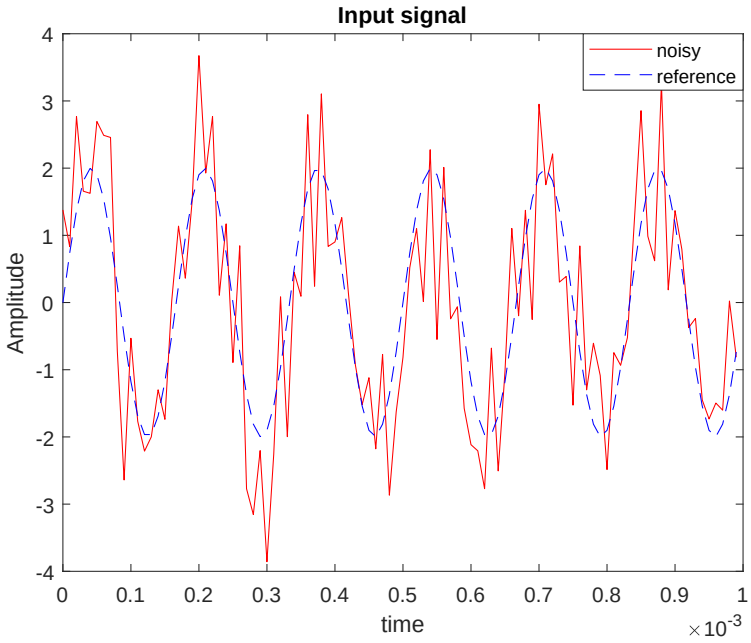

FIGURE 3.1: Reference and noisy observations of an input signal (SNR=53 dB-Hz).

We present in Figure 3.2a, the classical architecture of a coherent detector. From Figure 3.2a, the quantized digital signal samples are accumulated at the output of the product over a specified integration time T_c in order to obtain the in-phase component of correlation I. However, during the accumulation process, not only the amplitudes of the signal are accumulated, but also the additive noise. This is why the accumulated value is directly linked to the C/N_0. We assume that the amplitude of the signal remains constant over the integration time. We show in Figure 3.2b , the digitized reference and noisy

signals after applying 1-bit quantization. The 1-bit quantized coherent reference (i.e. signal without noise) and noisy signal are multiplied to obtain the quantized detection samples at the output of the product (Figure 3.3a). The detection samples at the output of the product take the value +1 when the quantified real and reference signals have the same value and -1 otherwise. The value -1 occurs due to the noise on the real signal. Finally, these samples are accumulated over the coherent integration time T_c to obtain the accumulated in-phase component of correlation I.

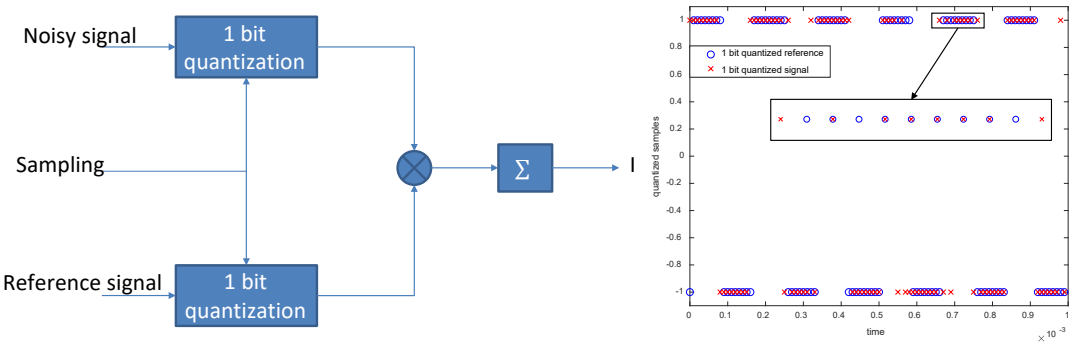

(a) (b)

FIGURE 3.2: 1-bit Coherent Detection principle. (a) the 1-bit coherent detector architecture , and (b) the 1-bit quantized reference and real signals

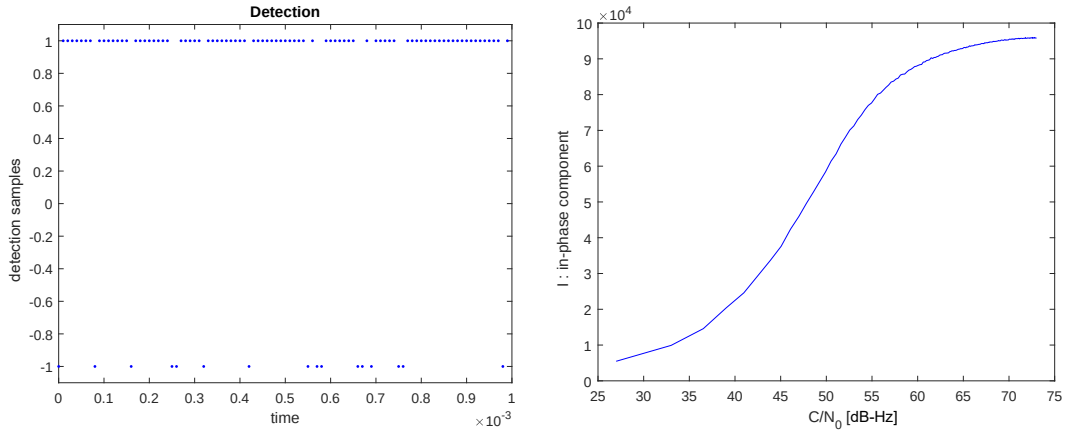

(a) (b)

FIGURE 3.3: Coherent Detection principle. (a) The quantized detection samples at the output of the correlator after multiplying the 1-bit quantized reference and noisy signals.
(b) The sensibility of C/N_0 to the accumulated in-phase component of correlation I.

To investigate the sensibility of C/N_0 to the prompt correlator output I, we present in Figure 3.3b, the accumulated in-phase component of correlation I as a function of C/N_0. For this Figure, the amplitude of the signal ranges from 0.1 to 20 with a step of 0.1 producing 200 different C/N_0 values. The C/N_0 is defined as:

$$C/N_0 = 20\log\left(\frac{A_v\sqrt{f_s\,T_c}}{\sqrt{2}}\right) + 10\log(BW) \tag{3.1}$$

where $\frac{A_v}{\sqrt{2}}$ is the Root Mean Square voltage of the carrier and BW is the noise equivalent bandwidth of the receiver RF front end. We observe an increase in the C/N_0 with the increase in the value of the accumulated in-phase component I until saturation at very high C/N_0 environments (beyond 65 dB-Hz). This increase is most sensible in the typical range of GNSS C/N_0 (approximately 40 to 58 dB-Hz). Therefore, we can conclude that the in-phase component of correlation is directly linked to the C/N_0 and to the amplitude of the signal.

3.3 GNSS front end

3.3.1 GNSS front end model

The RF front end, presented in section 2.2.1, provides digital signal samples of the GNSS signals sensed by a GNSS antenna. The AGC regulates the GNSS signals through a feedback loop to preserve the signals within the input range of the individual filters. After amplification and filtering, the RF signals are converted to IF signals in order to reduce the bandwidth of interest. Frequency synthesizers provide the frequency needed to shift the RF content to IF as well as the sampling frequency f_s. Then the Analog-to-Digital (ADC) module with 1-bit quantization (in this case) converts the analog IF signals to digital IF signals with a sampling period $T_s = \frac{1}{f_s}$. The RF front end of a GNSS receiver is depicted in Figure 2.1 of section 2.2.1.

Consider the GPS C/A signal s_i of equation (2.3) after down conversion and digitization in a numerical GNSS receiver. In our approach, the navigation data message is extracted and removed from the signal through the code tracking process. Then, s_i can be written as:

$$s_i = \sum_{l \in V} K\, A_l(t) CA_l(t + \tau_l) \sin(2\pi f_l\, t + \phi_l) + K\, \eta(t) \tag{3.2}$$

where V is the set of visible satellites. $A_l(t)$ is the amplitude of the signal, $CA_l(t)$ is the CDMA code of satellite l and τ_l is the code delay. f_l and ϕ_l are respectively the frequency and the phase delay of the carrier. f_l^D is the Doppler frequency associated to satellite l with $f_l = f_{IF} + f_l^D$. $\eta(t)$ is a zero mean additive Gaussian noise with a unit variance and K is the gain of the AGC. The digitized local replicas $ci_{v,i}$ and $cq_{v,i}$ are defined as:

$$ci_{v,i} = CA_v(t_i + \tau_v) \sin(2\pi f_v\, t_i + \phi_v) \tag{3.3}$$

$$cq_{v,i} = CA_v(t_i + \tau_v) \cos(2\pi f_v\, t_i + \phi_v) \tag{3.4}$$

where t_i is the time instant associated to the sampling frequency f_s and τ_v is the code delay. f_v and ϕ_v are respectively the frequency and the phase delay estimates of the carrier.

In this chapter, the accumulated in-phase component of correlation I_v and quadrature component Q_v at the output of the prompt correlator are obtained by integration of the sampled signals over one period of CDMA code (i.e $T_c = 1\ ms$) and are represented as:

$$I_v = \sum_{i=1}^{f_s\, T_c} s_i\, ci_{v,i} \tag{3.5}$$

$$Q_v = \sum_{i=1}^{f_s\, T_c} s_i\, cq_{v,i} \tag{3.6}$$

We assume that the local code and carrier are perfectly aligned with the received signals (i.e. $\tau_v = \tau_l$, $f_v = f_l$, $\phi_v = \phi_l$), thus I_v and Q_v can be derived as:

$$I_v = \frac{K\, A_v\, f_s\, T_c}{2} + K\, \eta_v^I \tag{3.7}$$

$$Q_v = K\, \eta_v^Q \tag{3.8}$$

where η_v^I and η_v^Q are random noises distributed according to a centered Gaussian distribution of variance $\frac{f_s\, T_c}{2}$.

3.3.2 GNSS one bit front end model

We show in Figure 3.4, the processing block diagram of the in-phase component in a GNSS receiver front end. In this Figure, $s^R(t)$ and $s(t)$ are defined as in equations (2.1) and (2.2) respectively. We show in Figure 3.5, the principle of the Analog to Digital Conversion (ADC) on 1 bit.

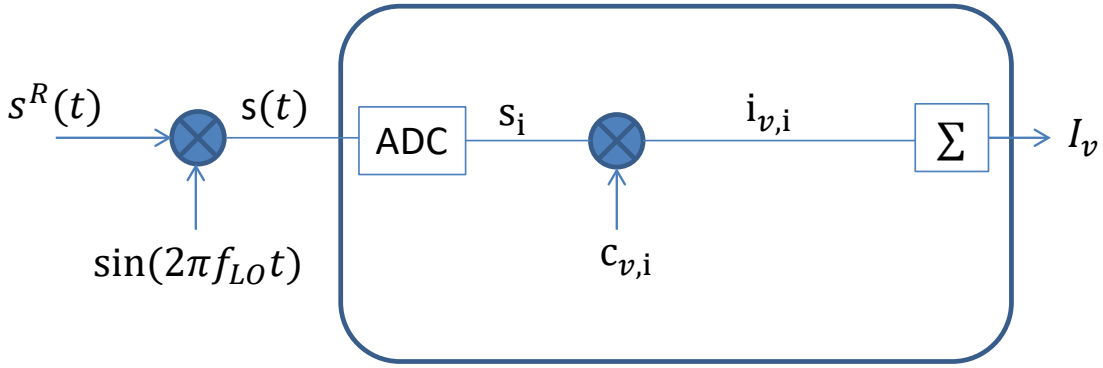

FIGURE 3.4: Radio frequency GNSS receiver block diagram.

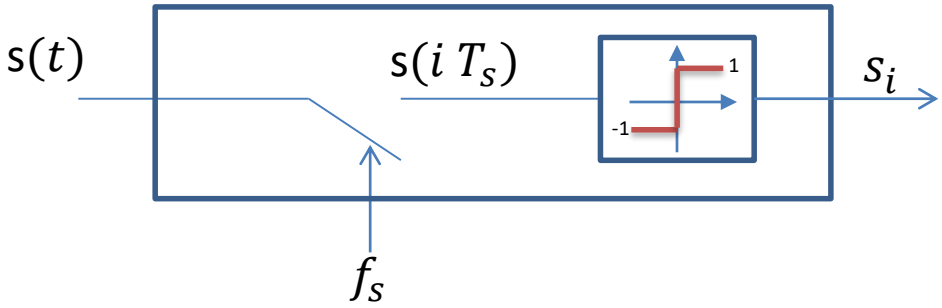

FIGURE 3.5: Analogic to Digital Conversion (ADC) with 1-bit of quantization.

The expressions of the signals in Figure 3.4 are defined after digitization by:

$$s_i = \left\lfloor \sum_{l \in V} K A_l C A_l(t_i + \tau_l) \sin(2\pi f_l\, t_i + \phi_l) + K\eta_i \right\rfloor_{>0} \tag{3.9}$$

$$c_{v,i} = \lfloor C A_v(t_i + \tau_v) \sin(2\pi f_v\, t_i + \phi_v) \rfloor_{>0} \tag{3.10}$$

where s_i and $c_{v,i}$ are respectively the digitized signal and local replica. $\lfloor \ldots \rfloor_{>0}$ is a sign function that associates -1 to the negative values of the signal and +1

to positive (or zero) values.

Our aim is to derive an expression that links the amplitude A_v of the received signal to the mean value of the in-phase component. In this context, we define $i_{v,i} = s_i\, c_{v,i}$ to take the value +1 when s_i is equal to $c_{v,i}$ and -1 when they are different. Let's define the mean value of $i_{v,i}$ as:

$$\begin{aligned} E(i_{v,i}) &= \sum_{x\in\{-1,1\}} x\, P(i_{v,i} = x) \\ &= 2\, P(i_{v,i} = 1) - 1 \end{aligned} \tag{3.11}$$

where $P(i_{v,i} = x)$ is the probability of $i_{v,i} = s_i\, c_{v,i}$ to take the value x. In our GNSS front end model, the noisy samples $i_{v,i}$ are integrated on one period of CDMA code ($T_c = 1\ ms$). Assuming that the random values of $i_{v,i}$ are identically distributed, we derive the mean value of I_v as follows:

$$E(I_v) = E(i_{v,i})\, T_c f_s \tag{3.12}$$

where $T_c f_s$ is the number of samples integrated over one period of code. $E(I_v)$ is defined by the probability $P(i_{v,i} = 1)$. We show in section 3.4.3 that this probability is a function of A_v.

3.4 Estimation of the GNSS signal amplitude

3.4.1 The Kalman filter

3.4.1.1 Principles of Kalman filter

The Kalman filter is an optimal recursive linear Minimum Mean-Squared Error (MMSE) estimator that estimates the state of a linear dynamic system perturbed by noise. Because the true state of the system cannot be observed, we must rely on measurements or observations that are immersed in noise. The purpose of filtering is to extract the required information from a signal, ignoring everything else effectively mitigating the noise in the process. Consider a discrete, linear, time varying system in the state space notation, given by equations (3.13) and (3.14).

$$x_k = F_k x_{k-1} + w_k \tag{3.13}$$
$$y_k = H_k x_k + v_k \tag{3.14}$$

Equation (3.13) is denoted as the state equation. It models the evolution of the true state of the system over time. Equation (3.14) is known as measurement or observation equation. It models the observations on the states. x_k and y_k are the the state vector and the measurement vector, respectively. k denotes the time instant and F_k denotes the state transition matrix of the process from the state at instant $k-1$ to the state at instant k. H_k is the measurement matrix that relates the states to the observations. w_k and v_k are the state and measurement noise vectors and are assumed to be zero mean white Gaussian noise processes with co-variance matrices Q_k and R_k, respectively.

The co-variance matrix R represents the confidence in the measurements and can be determined based on the statistics of the noise on the measurements. The co-variance matrix Q represents the uncertainty on the state model. The value of Q is dependent on the application, and is determined based on the constraints and aims of the application.

The Kalman filter, as well as the Extended Kalman filter, compute the optimal state recursively, using a predictor-corrector structure in which a prediction is computed prior to the availability of the observation at current time instant k, and the prediction is updated once the observation at time instant k is available. The innovation ϵ_k of the filter can be interpreted as the new information that is available in the observation y_k relative to all the past observations up to the instant $k-1$. Thus, it can be utilized for detecting changes in the measurements. The Kalman filter solution can be adopted for the non-linear dynamic systems through an approximate linearization procedure and the resulting filter is known as the Extended Kalman Filter (EKF). Consider a non-linear dynamic system described by the state (3.15) and measurement (3.16) equations.

$$x_k = f_k(x_{k-1}) + w_k \tag{3.15}$$
$$y_k = h_k(x_k) + v_k \tag{3.16}$$

In this case, $f_k(.)$ and $h_k(.)$ denote the non-linear state transition function and the measurement function, respectively. w_k and v_k are the zero mean white Gaussian state and measurement noise vectors with co-variance matrices Q_k and R_k, respectively. The non-linear system dynamics can be linearized through a first order Taylor approximation at each time instant, around the most recent state estimate.

3.4.2 Kalman estimate of the signal amplitude

In our approach, we construct a state estimate that uses the in-phase components of correlation as observations. The observations $I_{v,k}$, are processed by the receiver at instant k every period of code ($T_c = 1\ ms$). The state model is a classical second order state equation used for data smoothing where the second state is the rate of change of the first state.

For a satellite l in the set V of visible satellites, $A_{l,k}$ with $l \in V$ are the amplitudes of the received GNSS signals. We assume that the amplitudes are constant during one period of the CDMA code. Let $n = Card\{V\}$ be the number of visible satellites. We consider n observations $I_{V,k}$ of the in-phase component at each instant k. The aim is to estimate the n amplitudes $A_{V,k}$ from the n observations $I_{V,k}$. This problem is non-linear because the expectation $E(i_{v,i})$ in expression (3.12) is a non-linear function of the signal amplitude.

The rate of change of $A_{l,k}$ is denoted as $\dot{A}_{l,k}$. We consider the following equations for our system :

$$x_k = Fx_{k-1} + Bw_k \tag{3.17}$$

$$y_k = h_k(x_k) + v_k \tag{3.18}$$

where, for n satellites, $x_k = \left[A_{1,k}, \ldots, A_{n,k}, \dot{A}_{1,k}, \ldots, \dot{A}_{n,k}\right]^T$. With :

$$F = \begin{pmatrix} 1 & 0 & 0 & \dots & 0 & T_c & 0 & 0 & \dots & 0 \\ 0 & 1 & 0 & \dots & 0 & 0 & T_c & 0 & \dots & 0 \\ . & . & . & . & . & . & . & . & . & . \\ . & . & . & . & . & . & . & . & . & . \\ . & . & . & . & . & . & . & . & . & . \\ 0 & 0 & 0 & \dots & 1 & 0 & 0 & 0 & \dots & T_c \\ 0 & 0 & 0 & \dots & 0 & 1 & 0 & 0 & \dots & 0 \\ 0 & 0 & 0 & \dots & 0 & 0 & 1 & 0 & \dots & 0 \\ . & . & . & . & . & . & . & . & . & . \\ . & . & . & . & . & . & . & . & . & . \\ . & . & . & . & . & . & . & . & . & . \\ 0 & 0 & 0 & \dots & 0 & 0 & 0 & 0 & \dots & 1 \end{pmatrix} \tag{3.19}$$

$$B = \begin{pmatrix} T_c^2/2 & 0 & \dots & 0 \\ . & . & . & . \\ . & . & . & . \\ 0 & 0 & \dots & T_c^2/2 \\ T_c & 0 & \dots & 0 \\ . & . & . & . \\ . & . & . & . \\ 0 & 0 & \dots & T_c \end{pmatrix} \tag{3.20}$$

The observation is defined by $y_k = [I_{1,k}, \dots, I_{n,k}, 0, \dots, 0]^T$. Where $I_{v,k}$ is given by :

$$I_{v,k} = h_{v,k}(x_k; \theta_k) + \omega_k \tag{3.21}$$

where $h_{v,k}(x_k; \theta_k) = E(I_v)$ is defined by expression (3.12). We show in the next section that the expression of h(...) is a function of the parameters $\theta_k = \left[\hat{\tau}_{1,k}, \hat{f}_{1,k}, \hat{\phi}_{1,k}, \dots, \hat{\tau}_{n,k}, \hat{f}_{n,k}, \hat{\phi}_{n,k}\right]$. These GNSS signal parameters are provided by the PLL and DLL components of the receiver. The receiver architecture principle is presented in Figure 3.6.

As shown in Figure 3.6, the signal received from the satellites in view is tracked by a Delay Lock Loop and a Phase Lock Loop. This tracking module

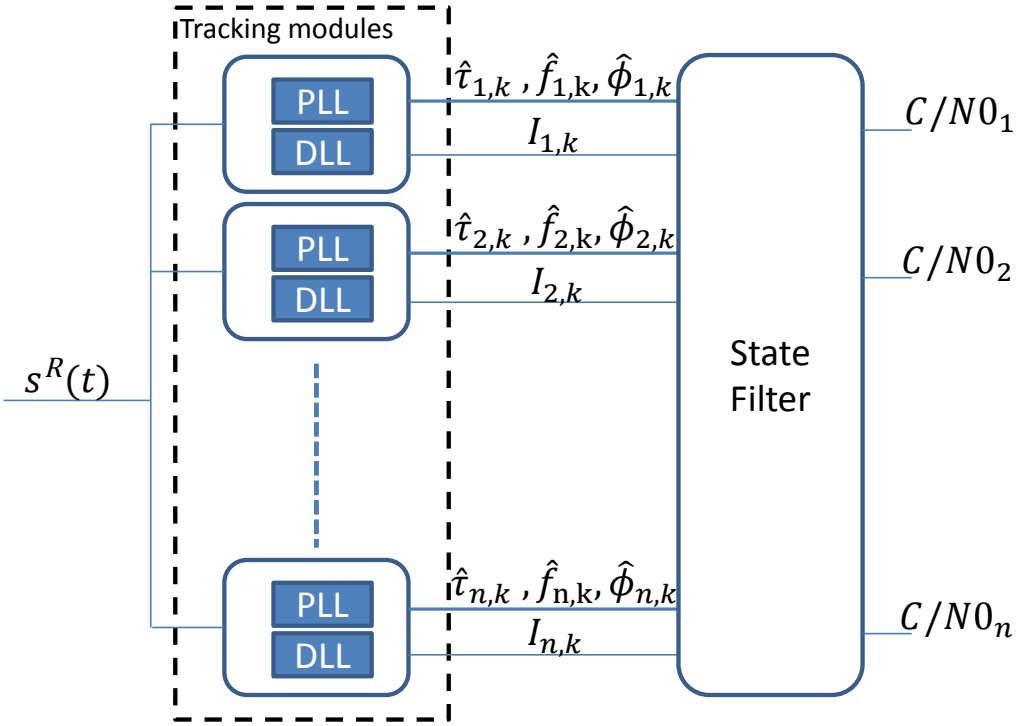

FIGURE 3.6: Implementation of the proposed estimate in a GNSS receiver.

provides, for each satellite, observations of the code delay, phase, Doppler frequency and the in-phase component I which are used as an input to the state filter. The EKF (state filter) processes these observations to estimate the GNSS signal amplitude and the carrier-to-noise ratio of each satellite. In our implementation of the EKF, we express $h(x_k)$ in the form of a linearized expression $H.x_k$ instead of deriving $h(x_k)$ as a function of x_k to find H.

3.4.3 Linearization of the measurement equation

3.4.3.1 Statistical front end model

The probability for the random variable $i_{v,k}$ to take the value +1 is a function of the values of the local code and the received signal. These two signals sampled and quantified on one bit take the values +1 or -1. This probability is expressed as:

$$\begin{aligned} P\left(i_{v,i}=1\right) &= P\left(c_{v,i}=1\right)P\left(s_i=1/c_{v,i}=1\right) \\ &+ P\left(c_{v,i}=-1\right)P\left(s_i=-1/c_{v,i}=-1\right) \end{aligned} \tag{3.22}$$

where $i_{v,k}$ the product of s_i with $c_{v,i}$ is equal to one in both cases. Let us construct the following model approximation of the sampled signal of satellite v after digitization:

$$\hat{s}_i = \sum_{v\in V} A_v C A_v(t_i+\hat{\tau}_v)\sin(2\pi\hat{f}_v\, t_i+\hat{\phi}_v) \tag{3.23}$$

$$s_i \approx \left\lfloor \hat{s}_i+\eta_i \right\rfloor_{>0} \tag{3.24}$$

and

$$c_{v,i} \approx \left\lfloor CA_v(t_i+\hat{\tau}_v)\sin(2\pi\hat{f}_v\, t_i+\hat{\phi}_v)\right\rfloor_{>0} \tag{3.25}$$

In practice, the estimates $\hat{\tau}_v$ and $\hat{f}_v, \hat{\phi}_v$ are respectively provided by the DLL and the PLL of the GNSS receiver presented in Figure 3.6. Therefore, A_v is the parameter to estimate. Expression (3.22) can be written as :

$$\begin{aligned} P\left(i_{v,i}=1\right) &= P\left(c_{v,i}=1\right)P\left(\eta_i\geq -\hat{s}_i/c_{v,i}=1\right) \\ &+ P\left(c_{v,i}=-1\right)P\left(\eta_i< -\hat{s}_i/c_{v,i}=-1\right) \end{aligned} \tag{3.26}$$

The probabilities in expression (3.22) can then be approximated as:

$$P\left(c_{v,i}=-1\right) = \frac{\sum_{i=1}^{f_sT_c}|c_{v,i}-1|}{2f_sT_c} \tag{3.27}$$

$$\begin{aligned} P\left(c_{v,i}=1\right) &= 1-P\left(c_{v,i}=-1\right) \\ &= \frac{\sum_{i=1}^{f_sT_c}(c_{v,i}+1)}{2f_sT_c} \end{aligned} \tag{3.28}$$

An estimate of the first probability of expression (3.26) associated to the additive random noise on the signal is defined as:

$$P\left(\eta \geq -\hat{s}_i / c_{v,i} = 1\right) = \frac{2}{\sum_{i=1}^{f_s T_c} \left(c_{v,i} + 1\right)} \sum_{\{\tilde{i}\}_v^1} P(\eta \geq -\hat{s}_i) \tag{3.29}$$

where the set $\{\tilde{i}\}_v^1$ defines the values of the index i as $i/c_{v,i} = 1$. The noise is assumed to be distributed according to a Gaussian density with a unit variance. The probability $P(\eta \geq -\hat{s}_i)$ is processed with the tabulated error function as follows:

$$\begin{aligned} \sum_{\{\tilde{i}\}_v^1} P(\eta \geq -\hat{s}_i) &= \sum_{\{\tilde{i}\}_v^1} \int_{-\hat{s}_i}^{+\infty} \frac{1}{\sqrt{2\pi}} exp(\frac{-x^2}{2})\, dx \\ &= \sum_{\{\tilde{i}\}_v^1} \frac{1}{2} erfc\left(\frac{-\hat{s}_i}{\sqrt{2}}\right) \end{aligned} \tag{3.30}$$

The second probability estimate of expression (3.26) associated to the additive random noise on the signal is defined as:

$$P\left(\eta < -\hat{s}_i / c_{v,i} = -1\right) = 1 - \frac{2}{\sum_{i=1}^{f_s T_c} \left|c_{v,i} - 1\right|} \sum_{\{\tilde{i}\}_v^2} P(\eta \geq -\hat{s}_i) \tag{3.31}$$

where the set $\{\tilde{i}\}_v^2$ defines the values of the index i as $i/c_{v,i} = -1$. For a set of estimates $\{\hat{\tau}_v, \hat{f}_v, \hat{\phi}_v\}_{v \in V}$, the probability of expression (3.26) is a function of $\{\hat{A}_v\}_{v \in V}$. In this context, the mean value of I_v is a function of A_v.

3.4.3.2 Derivation of the linearized measurement equation

According to equations (3.11), (3.12) , and (3.26) we derive the following expression :

$$\begin{aligned} h_{v,k}\left(\{A_{v,k}\}_{v \in V}; \{\theta_{v,k}\}_{v \in V}\right) &= 2T_c f_s\, P\left(c_{v,i} = 1\right) P\left(\eta \geq -\hat{s}_i / c_{v,i} = 1\right) \\ &+ 2T_c f_s\, P\left(c_{v,i} = -1\right) P\left(\eta < -\hat{s}_i / c_{v,i} = -1\right) - T_c f_s \end{aligned} \tag{3.32}$$

Considering that the values of I_v are obtained at instants k, the preceding expression can be written as below after simplification :

$$
\begin{aligned}
h_{v,k}\left(\{A_{v,k}\}_{v\in V};\{\theta_{v,k}\}_{v\in V}\right) &= \sum_{\{\tilde{i}\}_{v,k}^{1}} erfc\left(\frac{-\hat{s}_i}{\sqrt{2}}\right) \\
&- \sum_{\{\tilde{i}\}_{v,k}^{2}} erfc\left(\frac{-\hat{s}_i}{\sqrt{2}}\right) \\
&+ \sum_{i=1}^{f_s T_c} |c_{v,i}-1| - T_c f_s
\end{aligned} \tag{3.33}
$$

The GPS signal is very weak, so the values of $\hat{s}_i$ are small. Therefore, the following approximation (the first order of the Taylor Series expansion at zero) of the $erfc(...)$ function can be used:

$$
erfc(x) \approx 1 - \frac{2}{\sqrt{\pi}}x \tag{3.34}
$$

In this context, an approximation of the function $h_{v,k}(...)$ is given as :

$$
\begin{aligned}
h_{v,k}\left(\{A_{v,k}\}_{v\in V};\{\theta_{v,k}\}_{v\in V}\right) &\approx \frac{\sum_{i=1}^{f_s T_c}(c_{v,i}+1)}{2} + \frac{2}{\sqrt{2\pi}}\sum_{\{\tilde{i}\}_{v,k}^{1}}\hat{s}_i \\
&- \frac{\sum_{i=1}^{f_s T_c}|c_{v,i}-1|}{2} - \frac{2}{\sqrt{2\pi}}\sum_{\{\tilde{i}\}_{v,k}^{2}}\hat{s}_i \\
&+ \sum_{i=1}^{f_s T_c}|c_{v,i}-1| - T_c f_s
\end{aligned} \tag{3.35}
$$

and after simplification :

$$
h_{v,k}\left(\{A_{v,k}\}_{v\in V};\{\theta_{v,k}\}_{v\in V}\right) \approx \frac{2}{\sqrt{2\pi}}\left(\sum_{\{\tilde{i}\}_{v,k}^{1}}\hat{s}_i - \sum_{\{\tilde{i}\}_{v,k}^{2}}\hat{s}_i\right) \tag{3.36}
$$

In order to find a linear expression between $I_{v,k}$ and $A_{v,k}$, we develop the expression of $\hat{s}_i$:

$$h_{v,k}\left(\{A_{v,k}\}_{v\in V};\{\theta_{v,k}\}_{v\in V}\right) \approx \frac{2}{\sqrt{2\pi}}\left(\sum_{v\in V}A_{v,k}\left(\sum_{\{\tilde{i}\}_{v,k}^{1}}CA_v(t_i+\hat{\tau}_{v,k})\sin(2\pi\hat{f}_{v,k}\,t_i+\hat{\phi}_{v,k})\right.\right. \\ \left.\left. - \sum_{\{\tilde{i}\}_{v,k}^{2}}CA_v(t_i+\hat{\tau}_{v,k})\sin(2\pi\hat{f}_{v,k}\,t_i+\hat{\phi}_{v,k})\right)\right) \tag{3.37}$$

Finally, for a set V of n satellites in view we have the following linear expression :

$$I_{V,k} \approx HA_{V,k} + \omega_k \tag{3.38}$$

with $I_{V,k} = [I_{1,k},\ldots,I_{n,k}]^T$ and $A_{V,k} = [A_{1,k},\ldots,A_{n,k}]^T$. The expression of an element $h_{i,j}$ of H is given by :

$$h_{i,j} = \frac{2}{\sqrt{2\pi}}\left(\sum_{\{\tilde{i}\}_{v,k}^{1}}CA_v(t_i+\hat{\tau}_{v,k})\sin(2\pi\hat{f}_{v,k}\,t_i+\hat{\phi}_{v,k}) - \sum_{\{\tilde{i}\}_{v,k}^{2}}CA_v(t_i+\hat{\tau}_{v,k})\sin(2\pi\hat{f}_{v,k}\,t_i+\hat{\phi}_{v,k})\right) \tag{3.39}$$

We present in Figure 3.7 the different elements of H. In this matrix, we note the cross-correlation contributions and the correlation contributions in the observations $I_{v,k}$ for each satellite. The component $h_{i,j}$ represents the contribution of satellite j when a replica of the signal of satellite i is used to demodulate and demultiplex the signal. In this context, for a component $I_{i,k}$, $h_{i,i}$ is the correlation contribution of the signal from satellite i and $h_{i,j}$ is the inter correlation contribution of the signal from satellite j. We define the cross-correlation contribution $\mathbf{h}_{i,j\neq i} = \sum_{j\neq i} h_{i,j}$ and the global contribution $\mathbf{h}_{i,\forall j} = \sum_{j=1}^{n} h_{i,j}$. One of the interests of the proposed approach is to study the effect of the cross-correlation contribution on the estimation. We show by experimentation the impact of this contribution on the accuracy of the estimated amplitudes of GNSS signals.

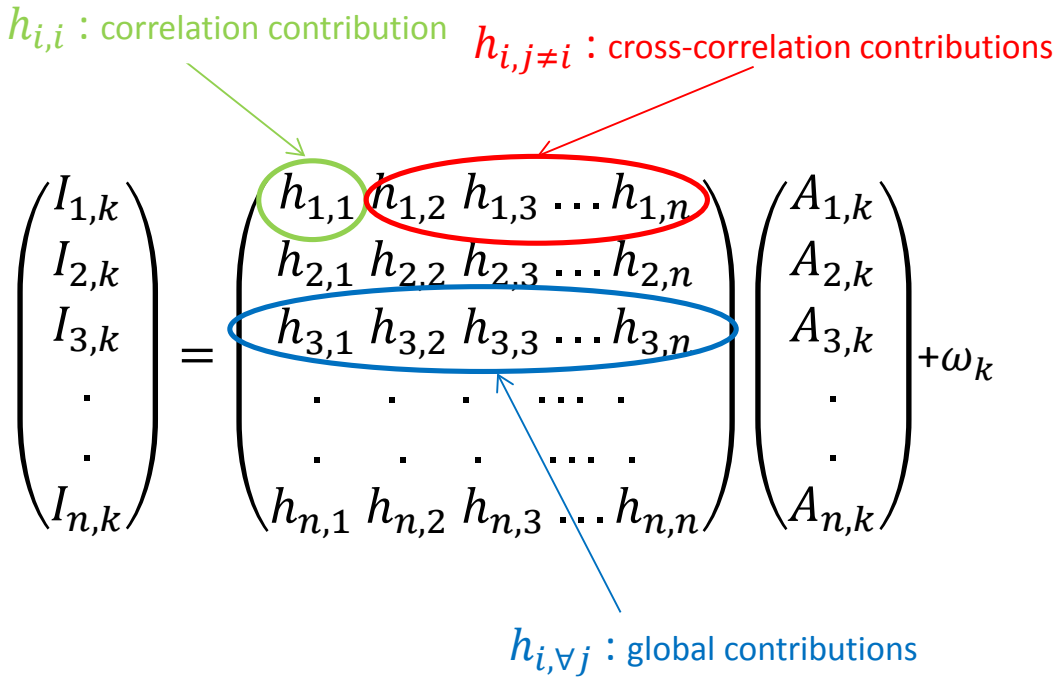

FIGURE 3.7: Contribution of each satellite in the observations $I_{v,k}$. Each element $h_{i,j}$ of H is processed using equation (3.39). For a component $I_{i,k}$, $h_{i,i}$ is the correlation contribution of the signal from satellite i and $h_{i,j}$ is the inter correlation contribution of the signal from satellite j.

3.5 Experimentation

3.5.1 Assessment on synthetic data

The aim of this experimentation is to assess the proposed amplitudes estimator on GPS C/A signals and study the effect of the correlation contribution on the carrier-to-noise estimation. In order to be independent of the AGC gain, we compare the carrier-to-noise ratio in dB-Hz using the expressions below, derived from the classical definition of the SNR in equation (2.13) :

$$C/N_0^k = 20\log\left(\frac{A_v\sqrt{f_s\,T_c}}{\sqrt{2}}\right) + 10\log(BW) \tag{3.40}$$

$$C/N_0^c = 20\log\left(\frac{mean(I_{v,k=1:1000})}{std(I_{v,k=1:1000})}\right) + 10\log(BW) \tag{3.41}$$

where C/N_0^k is the carrier-to-noise expression used in our approach based on equation (2.14), and C/N_0^c is a classical carrier-to-noise definition. $\frac{A_v}{\sqrt{2}}$ is the Root Mean Square voltage of the carrier and BW is the noise equivalent

bandwidth of the receiver RF front end.

We show in Figure 3.8, the observations $I_{1,k}$ and $E(I_{1,k})$ for satellite PRN 12 during 1 second (k=1:1000). This means that one value of $I_{1,k}$ and $E(I_{1,k})$ is obtained every millisecond. In this experimentation, $A_{V,k} = 0.05$ for all satellites in view and η_i, the Gaussian noise on the received signal, have a variance 1. The amplitudes of the signals are fixed to 0.05 and the noise power to 1 in order to provide a true value of 43.98 dB-Hz (i.e. $C/N_0^t = 43.98$ db-Hz) for the carrier-to-noise ratio of GPS C/A signals. In Figure 3.8, we observe the evolution of $E(I_{v,k})$ due to the global correlation contribution and the random like evolution of $I_{v,k}$ due to the global correlation contribution and the noise on the received signal. We show by experimentation, that the statistics of $I_{v,k}$ and the classical SNR estimates are functions of the cross-correlation contribution.

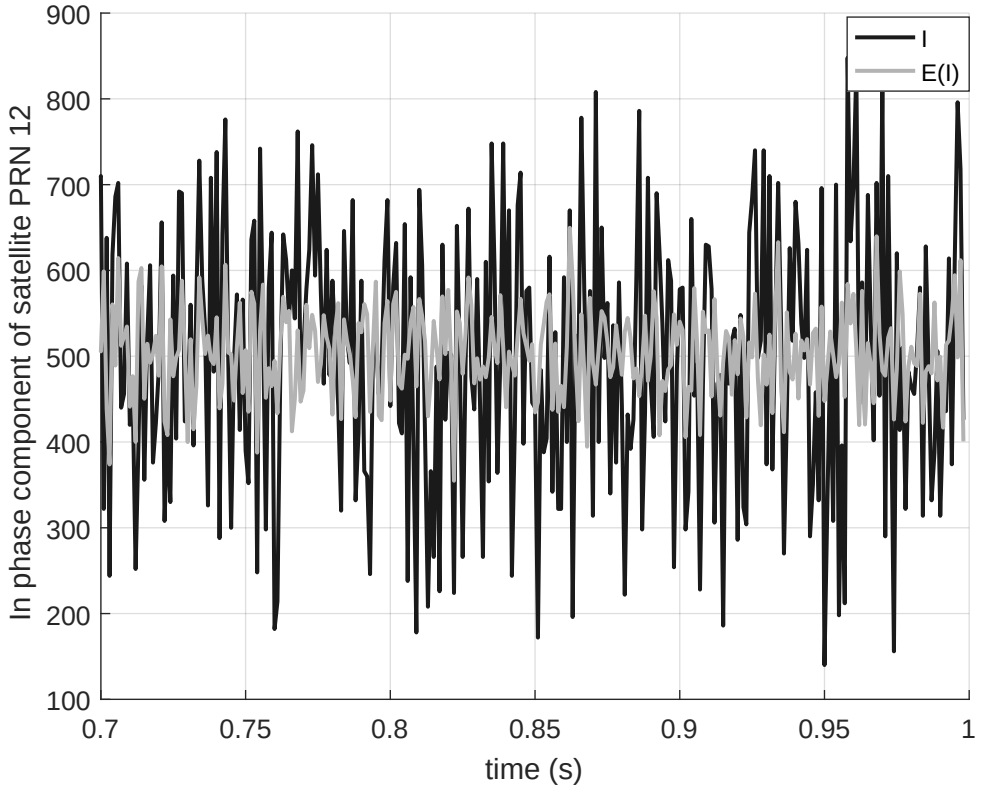

FIGURE 3.8: Noisy observations $I_{1,1:1000}$ and $E(I_{1,1:1000})$ for satellite PRN 12

We assess the statistic of $I_{v,k}$ from the analysis of matrix H. This study is independent of the amplitudes $\{A_{v,k}\}_{v\in V}$ and of η_i the noise on the received signal. C/N_0^c is used to assess the cross-correlation contribution on

the statistic of $I_{v,k}$. We report in Table 3.1, the Doppler frequency of the visible satellites during the simulation as well as the standard deviation of the cross-correlation contribution $\mathbf{h}_{i,j\neq i}$ processed over different satellites for one second of observations, and the standard deviation of the contribution $h_{i,i}$ calculated for every satellite along the observation time. We also report in Table 3.1, the mean value and the standard deviation of the total contribution $\mathbf{h}_{i,\forall j} = \sum_{j=1}^{n} h_{i,j}$ processed over different satellites for one second of observations. Finally, we calculate the classical carrier-to-noise ratio C/N_0^c and the true carrier-to-noise ratio C/N_0^t obtained using equation (3.40) with $A_{V,1:1000} = 0.05$ for all satellites in view.

TABLE 3.1: Cross-correlation impact

Sats	Doppler freq. f_l^D	$\sigma_{\mathbf{h}_{i,j\neq i}}$	$\sigma_{h_{i,i}}$	$\bar{\mathbf{h}}_{i,\forall j}$	$\sigma_{\mathbf{h}_{i,\forall j}}$	C/N_0^t (dB-Hz)	C/N_0^c (dB-Hz)
30	-3312	1054	386	10155	1125	43.98	42.75
28	-2422	1009	355	10109	1068	43.98	43.18
10	2224	1031	467	10145	1134	43.98	42.67
20	**123**	1077	**4386**	10179	**4463**	43.98	33.41
11	**634**	988	**960**	10155	**1387**	43.98	41.58
24	2268	918	463	10108	1036	43.98	43.1
19	3297	938	391	10149	1015	43.98	43.46
12	3987	1080	322	10144	1127	43.98	43.4
13	-2398	1049	374	10149	1114	43.98	42.9
15	-874	936	704	10109	1164	43.98	42.73
17	1873	1021	436	10126	1116	43.98	43.02

We notice in Table 3.1 that the mean contribution $\bar{\mathbf{h}}_{i,\forall j}$, proportional to the mean value of $I_{v,k}$, is independent of the satellites, because the values of $\bar{\mathbf{h}}_{i,\forall j}$ are indeed close. However, the standard deviations $\sigma_{\mathbf{h}_{i,\forall j}}$ of the global contribution are dependent of the satellites. The standard deviations $\sigma_{\mathbf{h}_{i,j\neq i}}$ associated to the cross-correlation contribution are close, so weakly dependent of the satellites. The dependence is due to the correlation contribution of each satellite defined as the standard deviation $\sigma_{h_{i,i}}$. This standard deviation is indeed a function of the Doppler frequency. For low Doppler, like satellites

PRN 11 and 20, the standard deviation $\sigma_{h_{i,i}}$ and the standard deviation $\sigma_{\mathbf{h}_{i,\forall j}}$ of the global contribution increase notably (in bold). Finally, we observe in Table 3.1 that the carrier-to-noise ratio C/N_0^c and the true carrier-to-noise ratio C/N_0^t are different. The difference is due to the cross-correlation contribution of the satellites. This difference increases with the low values of the Doppler frequency, which is noticed by the very low C/N_0^c values for satellites PRN 11 and 20.

In practice, the carrier frequency f_l of a down converted signal constitutes of the intermediate frequency f_l^{IF} and the Doppler frequency f_l^D where $f_l = f_l^{IF} + f_l^D$. This means that for high f_l^{IF}, the Doppler effect will be notably mitigated, and the standard deviation of the correlation contributions will be very close for every satellite. Thus, in order to study the Doppler effect on the correlation contributions, we consider that $f_l^{IF} = 0\ Hz$ and therefore, $f_l = f_l^D$. This is only applicable for assessment on synthetic data. In the real case, f_l^{IF} is always present for any GNSS receiver which hugely alters the Doppler effect.

We report, in Table 3.2, the mean and standard deviation of the total contribution $\mathbf{h}_{i,\forall j}$ of satellite PRN 12. In this table, we show the total contribution as a function of the number of visible satellites. We also report the classical carrier-to-noise ratio C/N_0^c and the true carrier-to-noise ratio C/N_0^t. With Table 3.2, we conclude that the statistic of $I_{v,k}$ is a function of the number of satellites. The standard deviation $\sigma_{h_{i,\forall j}}$ indeed increases with the number of satellites whereas the mean value of the global contribution is nearly constant. The standard deviation is inversely proportional to C/N_0^c. The increase in the standard deviation, leads to an expected decrease in C/N_0^c. Therefore, the difference between C/N_0^c and C/N_0^t increases with the increase in the standard deviation and thus with the number of satellites. This also proves the influence of the correlation contribution of the satellites on the carrier-to-noise estimation.

Finally, we present in Table 3.3, the estimate C/N_0^k obtained with the proposed approach. In this case, C/N_0^k is processed with expression (3.40) and the estimated amplitudes are provided by the Kalman filter every 1 ms. We compare C/N_0^k with the true carrier-to-noise ratio C/N_0^t to prove the accuracy of the proposed approach. In Table 3.3, R and Q are the co-variance matrices of the measurements and state noises respectively. Columns 3 and

TABLE 3.2: The impact of the number of satellites

Number of satellites	Visible satellites PRN	$\sigma_{h_{i,\forall j}}$	$\bar{\mathbf{h}}_{i,\forall j}$	C/N_0^t (dB-Hz)	C/N_0^c (dB-Hz)
1	12	322	10149	43.98	43.69
2	12,17	467	10148	43.98	43.64
3	12,17,19	545	10149	43.98	43.51
4	12,17,19,13	687	10149	43.98	43.46
5	12,17,19,13,24	756	10148	43.98	43.42
6	12,17,...,24,28	829	10149	43.98	43.35
7	12,17,...,28,10	941	10149	43.98	43.22
8	12,17,...,10,15	995	10149	43.98	43.16
9	12,17,...,15,11	1034	10148	43.98	43.12
10	12,17,...,11,20	1085	10144	43.98	42.98
11	12,17,...,20,30	1127	10144	43.98	42.84

4 show respectively, the mean estimate and the standard deviation of the carrier-to-noise ratio when the observations are not smoothed by the filter. In columns 5 and 6, we report the same parameters when the observations are smoothed by the filter.

Since I are noisy observations, the choice of the Kalman filter parameters is important for the accuracy of the estimate. In our approach, we determine the values of R and Q with the observations and the estimations. In this regard, we determine a fixed value of R with the measurements of the noise on the observations of the in-phase component of the signal. However, the tuning of Q is dependent on the application and must be done according to the constraints of this application. The value of Q is determined while taking into consideration that there is a trade-off between the accuracy of the estimation and the ability to follow the changes in the observations. In our approach, we fix R and tune the value of Q to obtain the same accuracy as the NovAtel GNSS receiver, which is a widely known commercial scientific GNSS receiver. In fact, the information provided by the NovAtel GNSS receiver is used as a reference in many GNSS-R applications. Based on the forgoing, we choose for our application a high co-variance matrix of the measurement

noise R and a small covariance of the process noise Q because the variations in the signal amplitude are low. For this experimentation, R=10,000,000,000 and Q=0.05.

TABLE 3.3: Estimated carrier-to-noise ratio

$C/N0$ (dBHz)	C/N_0^t	C/N_0^k $R = Q$		C/N_0^k $R >> Q$	
Sats		mean	std	mean	std
30	43.98	43.32	3.01	43.85	0.24
28	43.98	43.57	2.72	43.92	0.22
10	43.98	43.52	2.97	43.99	0.24
20	43.98	43.37	6.03	43.88	0.26
11	43.98	43.4	3.31	43.99	0.18
24	43.98	43.55	2.75	43.91	0.32
19	43.98	43.52	2.82	43.98	0.22
12	43.98	43.31	2.86	43.91	0.19
13	43.98	43.56	2.77	43.92	0.24
15	43.98	43.57	2.86	43.97	0.24
17	43.98	43.72	2.78	44.01	0.25

From Table 3.3, we notice that the carrier-to-noise estimate C/N_0^k does not depend on the satellite, so its computation removes the cross-correlation error. This can be clearly seen by comparing the mean of C/N_0^k in columns 3 and 6 with C/N_0^c in Table 3.1 for satellites PRN 11 and 20 obtained with 1000 samples of I. By comparing columns 3 and 4 with columns 5 and 6, we show that the proposed filter smooths the estimate and improves its accuracy. The values of the mean of C/N_0^k in column 6 are indeed closer to the true carrier-to-noise ratio C/N_0^t. From the preceding, we can conclude that the proposed approach can remove the error due to the cross-correlation contribution and improve the accuracy of the carrier-to-noise ratio estimate.

3.5.2 Assessment on real data

The experiment started at 15h20 UTC the 13^{th} of December 2019 and lasted for 1 minute. A NovAtel GNSS-850 antenna was mounted on the top of the

LISIC laboratory building at $(50.953228^{\circ}N; 1.880285^{\circ}E)$. In this experiment, a NovAtel OEM7 receiver was used to provide RINEX observation and navigation files. The observation file contains data such as the total number of satellites in view at each instant, the PRN codes of the satellites, and the carrier-to-noise ratio for each signal at different instants. A Syntony Echo-L bit-grabber was used to digitize the received signals. This experimentation is dedicated to the use of GPS C/A signals. We present in Figure 3.9, the experimental setup.

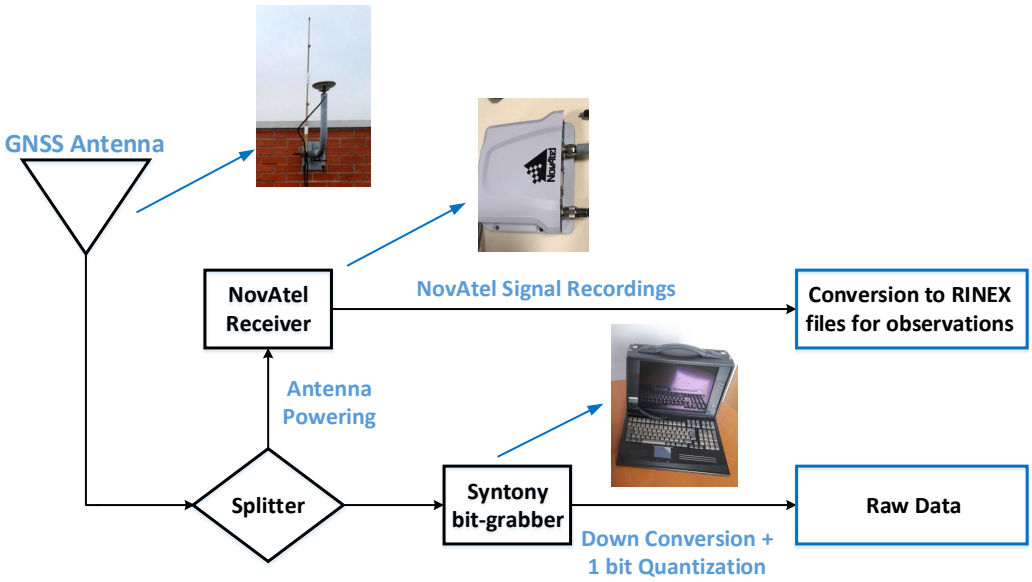

FIGURE 3.9: Experimental setup showing the connections between the various elements and its roles. The GNSS antenna, powered by the NovAtel receiver, captures signals from all the satellites in view. Then, the received signals enter a splitter and are passed to the NovAtel receiver and to the Syntony bit-grabber. Using the NovAtel signal recordings, RINEX files are generated from which the carrier-to-noise ratio provided by the NovAtel receiver are retrieved. The Syntony bit-grabber digitizes the received signals with down conversion and 1-bit quantization to provide raw data, which are processed to estimate the carrier-to-noise ratio.

The data collected by the NovAtel receiver and the raw data provided by the Sytnony bit-grabber are not synchronized. Therefore, data synchronization is applied. In this regard, the received signals have several essential components to be identified: the carrier frequency, the PRN code unique to each satellite, the code delay, the phase delay, and the navigation message from which the GPS time and pseudo-range can be retrieved. In order to

recover these components and date the signals for synchronization, signal acquisition and tracking are implemented. As a result, the message of navigation is extracted, which is then used for signal dating.

The message of navigation provides timing information that allows to calculate the seconds of the GPS week, which constitute the GPS time along with the GPS week number. Then using the estimated GPS time of the digitized signals and the GPS time of the signals provided by the RINEX observation file, data synchronization is applied for assessment of the proposed approach. We present in Figure 3.10, a sky plot of the satellites constellation which shows the positions of the satellites as recorded by the NovAtel receiver.

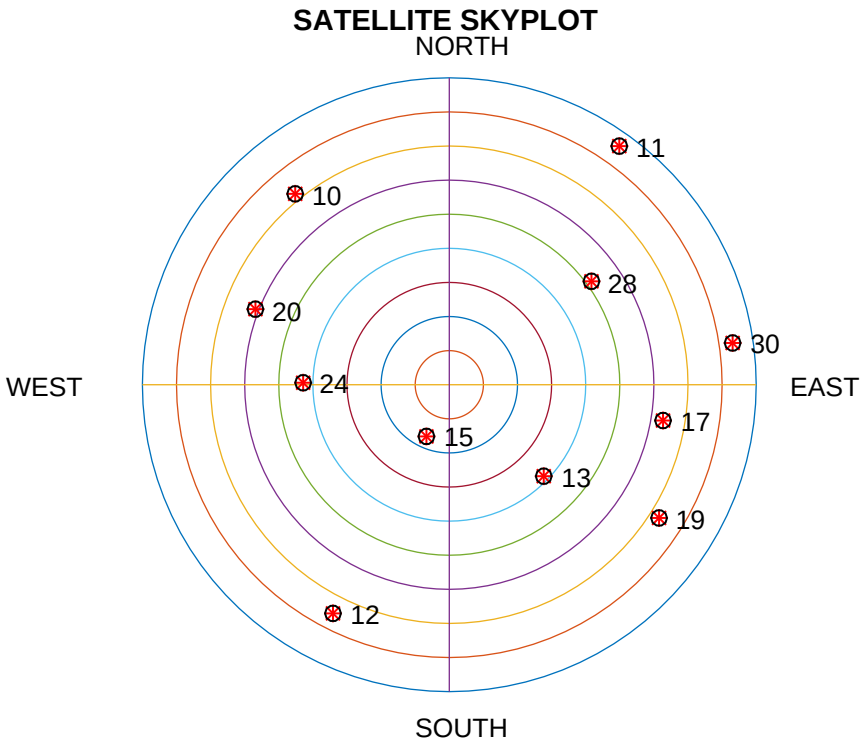

FIGURE 3.10: Constellation of the visible GPS satellites as recorded by the NovAtel receiver

The assessment of the proposed GNSS signal amplitude estimator which uses a 1-bit quantization GNSS receiver, is realized by comparing the carrier-to-noise ratio C/N_0^k obtained with the proposed approach and the carrier-to-noise ratio C/N_0^r provided by the RINEX observation file for each satellite v via the NovAtel GNSS receiver. As in the synthetic case, we calculate the estimated C/N_0^k using equation (3.40), where the amplitudes of the signals

are provided by the Kalman filter every 1 *ms*. In this experimentation, the observations are smoothed by the Kalman filter with R=10,000,000,000 and Q=0.0001.

We show in Figure 3.11, the C/N_0^r provided by the NovAtel receiver every 1 second and the C/N_0^k estimated by the proposed approach every 1 *ms* for different satellites (satellites PRN 19, 28, 12 and 15). We also report the 1 *ms* rate carrier-to-noise observations C/N_0^o obtained using the amplitudes derived from equation (3.38).

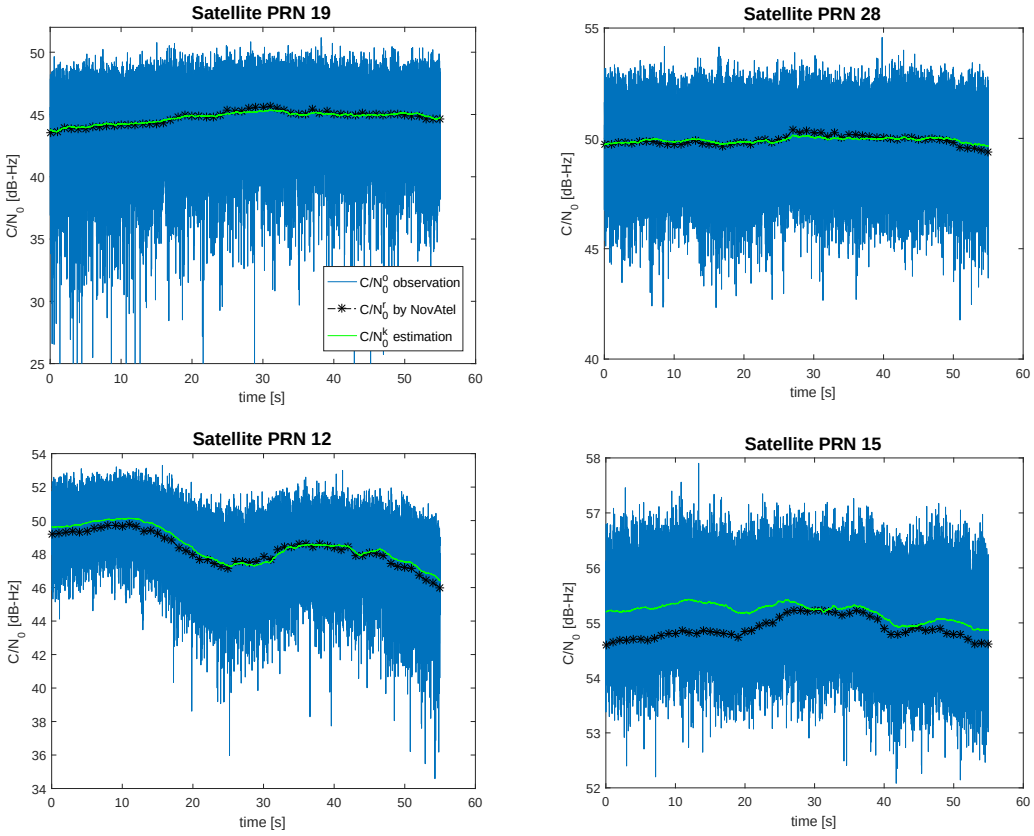

FIGURE 3.11: C/N_0 estimation assessment. In this figure, C/N_0^r is the carrier-to-noise ratio provided by the NovAtel receiver every 1 second, C/N_0^k is the carrier-to-noise ratio estimated by the proposed approach every 1 *ms* and C/N_0^o is the 1 *ms* rate carrier-to-noise observations obtained using the amplitudes derived from equation (3.38). Note that the intervals of the ordinate axes are not fixed in the figures presented.

The obtained results show good agreement between the carrier-to-noise ratio C/N_0^r provided by the NovAtel GNSS receiver and C/N_0^k estimated by our approach. For satellite PRN 19, where C/N_0 is relatively low and its rate of change is approximately steady, the evolution of C/N_0^k estimated

by our model every 1 *ms* fits accurately the evolution of C/N_0^r provided by the NovAtel receiver every 1 *s*. The same observation can be deduced from satellites PRN 28 and 12, where the evolution of our model estimate is coherent with the evolution of the C/N_0^r even in the case of fast changes in the carrier-to-noise observations as in satellite PRN 12. This also shows our model's ability to track the evolution of the carrier-to-noise observations precisely. However, it can be observed from satellite PRN 15, that for high C/N_0 environments ($\gtrapprox$ 54 dB-Hz), our model doesn't perfectly fit the evolution of C/N_0^r. This is due to the fact that in high C/N_0 environments, the proposed non-linear model doesn't fit the *erfc* function which performs generally on low and moderate values. This results in our model being less accurate for high C/N_0 environments.

Finally, we present in Table 3.4, C/N_0^r provided by the NovATel receiver and the mean ($\overline{C/N_0^k}$) of the carrier-to-noise estimates C/N_0^k for all satellites in view provided by the Kalman filter every 1 *ms*. In this experimentation, we assess the mean $\overline{C/N_0^k}$ over 1 second of C/N_0^k estimation to align with the rate of observation provided by the NovAtel GNSS receiver. The mean values $\overline{C/N_0^k}$ calculated over 1 second of estimation are indeed very close to C/N_0^r provided by the NovAtel receiver for different satellites and at different instants of time.

Therefore, we conclude that our approach, which uses a 1-bit quantization GNSS receiver can provide an accuracy similar to that of the NovAtel GNSS receiver. However, it is important to note that, for all satellites in view, the proposed model provides C/N_0 estimations at a much higher rate (1000 Hz) than the NovAtel GNSS receiver (1 Hz), which is proven to be crucial in multipath, and dynamic GNSS-Reflectometry applications, where the C/N_0 estimation rate defines the rate at which the environment can be analyzed.

TABLE 3.4: Carrier-to-noise ratio mean estimation assessment

	t= 5 sec		t=25 sec		t= 50 sec	
Sats	C/N_0^r	$\overline{C/N_0^k}$	C/N_0^r	$\overline{C/N_0^k}$	C/N_0^r	$\overline{C/N_0^k}$
10	44.93	44.90	47.05	47.13	47.94	48.14
11	41.65	41.48	40.71	39.80	41.72	41.31
12	49.23	49.63	47.66	47.87	48.02	48.26
13	51.99	52.28	52.11	52.20	51.85	51.64
15	54.64	55.21	54.85	55.23	54.86	55.02
17	49.30	49.76	48.86	49.18	50.02	50.13
19	43.58	43.79	44.90	44.88	45.02	44.96
20	45.83	46.13	45.94	46.07	45.36	45.24
24	52.33	52.75	52.18	52.54	52.04	52.18
28	49.74	49.78	49.74	49.83	49.95	50.03
30	46.29	45.95	44.34	43.70	38.60	36.91

3.6 Conclusion

In this chapter, we propose an on-line estimate of the amplitudes of GNSS signals in the form of an Extended Kalman Filter that uses the 1 ms rate of the in-phase components of the signals as observations. In order to be independent of the automatic gain control, 1-bit quantization digital receiver is used. The estimated amplitudes of the signals provide direct observations of C/N_0, therefore the carrier-to-noise ratio is estimated. This estimator can provide robust amplitude values and, consequently C/N_0 estimations at a high rate of 1000 Hz. In our model, we take into account the cross correlation between the different satellites. We also take into account the receiver-satellite velocity in the carrier frequency. The model in the context of this application shows different complexities that can be included in the probabilistic model of a coherent detector. We assess the performance of the estimator using synthetic and real data.

In modernized GNSS signals, there is a primary PRN code in addition to a secondary code or/and a sub-carrier. To use the proposed method in such cases, not only the message of navigation should be removed but also the secondary code. Otherwise, the pilot channel of the signal can be used (e.g. L5).

For low frequency sub-carrier such as the Binary Offset Carrier modulation, the proposed model can be modified to take into account other PRN codes and secondary codes in the definition of the local replica and the model of the received signal.

In the synthetic case, we show that the proposed approach can remove the error due to the cross-correlation contribution and improve the accuracy of the carrier-to-noise estimate when the data are smoothed by the filter. We also show, in real experimentation, that the proposed estimator, which uses a 1-bit quantization receiver, performs coherently with the widely known NovAtel receiver. It is also noted that the proposed approach performs at a much higher rate than the NovAtel GNSS receiver.

In the next chapter, we propose a change point detection algorithm in order to segment the GNSS signals into stationary parts based on the changes that occur on the signal amplitudes. We also assess the performance of our GNSS amplitude estimator in the presence of abrupt changes in the observations.

Chapter 4

Segmentation of the GNSS Signal Amplitudes

4.1 Introduction

The aim of this chapter is to develop an automatic segmentation model that divides the GNSS signals into stationary segments associated with different mean signal levels based on the changes in the amplitudes of the reflected GNSS signals. We propose in this chapter a mixture of an on-line/off-line change point detection and localization algorithm. We separate the problem of change point detection from that of change point localization.

In the presence of large amount of data that needs to be processed, an on-line change detection process needs to be implemented. In this regard, we use the CUSUM algorithm [188–190] to detect a change on-line. In the CUSUM approach, the dynamic of the change is assumed to be known. For this case, the CUSUM algorithm is considered to be the most efficient change point detector [188, 189]. Moreover, the CUSUM change detector is capable of detecting changes associated to the model of transition that we use in this chapter.

After the changes are detected on-line, an off-line localization approach is proposed to localize the change. We propose a Maximum Likelehood Estimate for change localization. This approach is close to the optimal estimation because we maximize in this case the size of the working window in which the detected change point is localized.

In the presence of noise, the CUSUM detector provides false alarm detections. We propose an off-line interval merging algorithm to remove the false

alarms and reduce the number of over detections. Finally, the signals are segmented into stationary parts based on the locations of the change points after integrating all the previous processes.

This chapter is organized as follows: the next section presents the change point detection principle used in this work. The third section presents the different processing steps of the proposed segmentation system. In the fourth section, the proposed model is assessed using synthetic data and evaluated on real data. Finally, conclusions are provided in the fifth section.

4.2 Change point detection principle

4.2.1 Generality

Change points are abrupt variations in time series data. Such abrupt changes may represent transitions that occur between states. Change point detection algorithms can be classified as "on-line" or "off-line" [188–191].

On-line or real-time change point detection algorithms [192–194] process each data point as it becomes available, with the intent of detecting state changes as soon as possible after it occurs, ideally before the availability of the next data point. Such algorithms assess only the most recent change in the time series, not previous changes.

In contrast, off-line change point detection algorithms [195–197] don't use live streaming data to process changes in a data sequence. Instead, they consider the entire data set at once, and look back in time to recognize where the change occurred. This means that in off-line processing all data are received and processed at the same time. Furthermore, all change points are of interest, not just the most recent change in the sequence.

In practice, no change point detection algorithm operates in perfect real-time, because it must examine the new data point before determining if a change point is detected between the old and the new data points. In this regard, on-line algorithms differ from one another by the amount of new data required to determine if a change point is detected. In general, off-line approaches are considered more accurate because they analyze the whole time series at once while on-line approaches are seen to be faster. In fact, change

point detection is linked to the problem of change point estimation. However, the aim of change point estimation is to localize and detect the changes in the time series rather than just identifying that a change has occurred. In this regard, change point estimations are used to characterize the type and extent of a change.

In this chapter, we propose the following modelization for our system:

- We assume that the GNSS measurements obtained during the airborne experiment are piecewise stationary.
- The noise on the observations is assumed to be additive, Gaussian and centered.
- A transition model is adapted to characterize the changes in the amplitudes of the reflected GNSS signals associated to the displacement of the satellites footprints from one area to another along the airborne experiment.
- The system is implemented to operate efficiently on huge amounts of data (GNSS measurements).

4.2.2 Transition model

In our radar application, the amplitude of the reflected GNSS signal changes as a function of time. This amplitude is indeed a function of the surface of reflection. The aim of this work is to present a change point detector that divides the GNSS signal amplitude in stationary segments associated with different areas of reflection.

We assume that the GNSS signal amplitude is proportional to the ground reflectivity contained in the surface of the first Fresnel zone of the satellite footprint. The first Fresnel zone is an ellipse centered on the specular reflection point. The displacement of this ellipse on the ground follows the satellite trace. We show in Figure 4.1, the satellite footprints displacement from one area to another. We show in Figure 4.2, the signal model in the working window. When the mean value of the GNSS signal amplitude is equal to m_1, the ellipse is on the first area, and when the mean value of the GNSS signal amplitude is equal to m_2, the ellipse is on the second area.

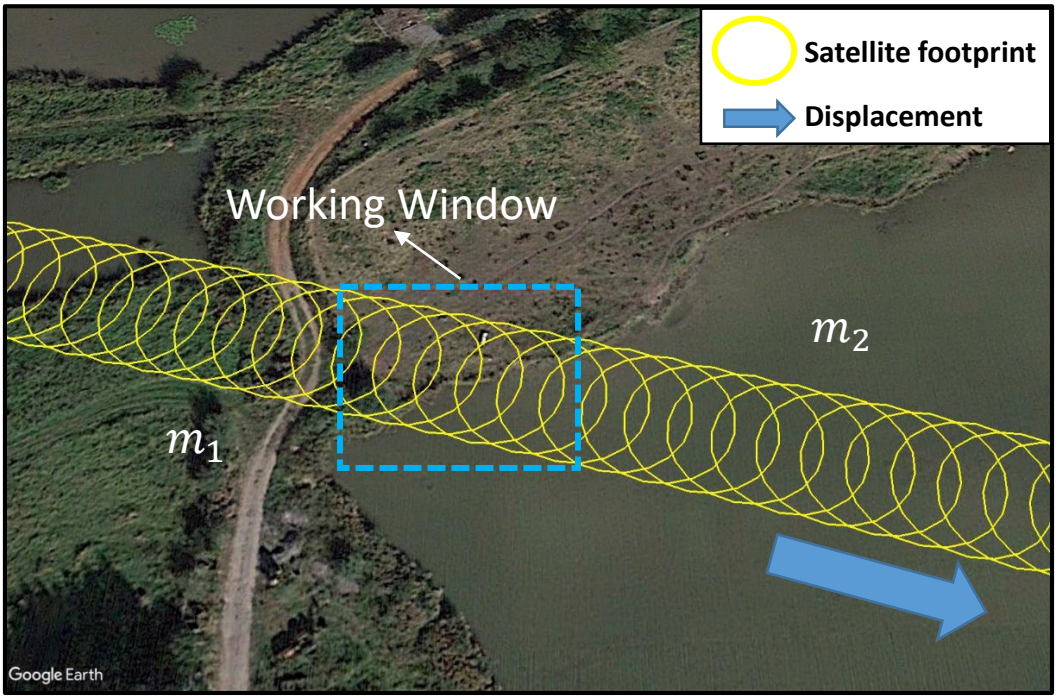

FIGURE 4.1: Satellite footprints displacement from one area to another.

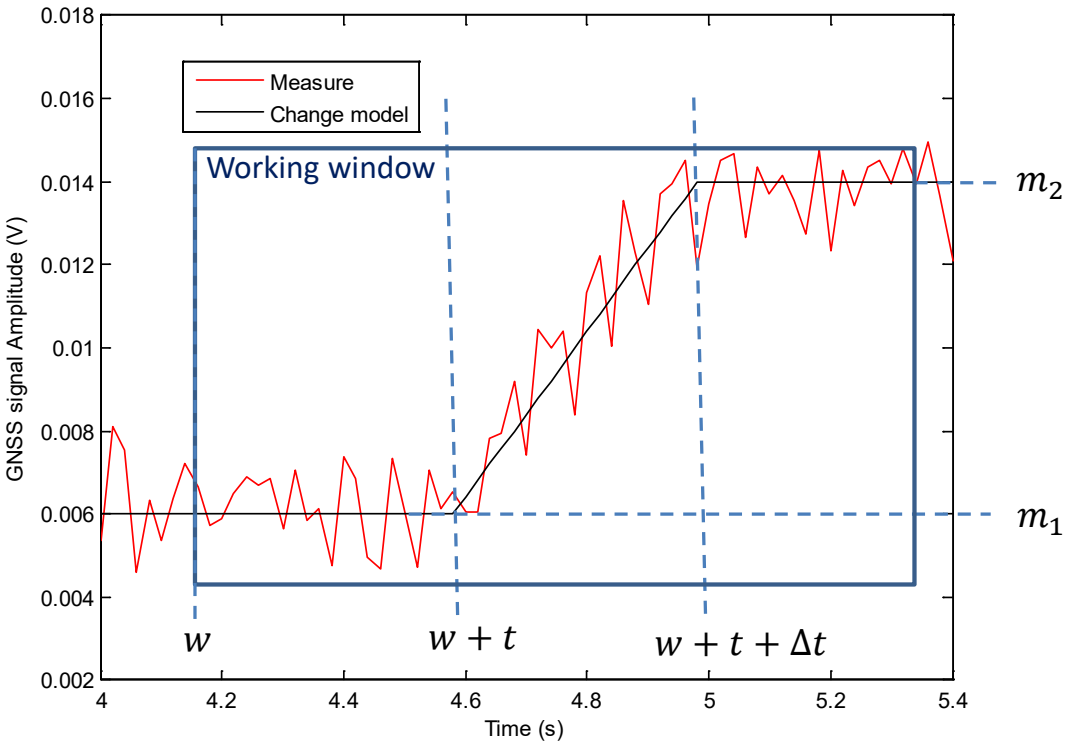

FIGURE 4.2: Signal model in a working window.

We can observe in Figure 4.2 the increasing evolution of the signal model

between the mean values m_1 and m_2 associated to the satellite footprint displacement from one area to another as shown in Figure 4.1. This increasing evolution models a linear transition from a surface of low reflectivity (land) to a surface of higher reflectivity (water body). We define in section 4.3.2 the start and end instants of the working window in order to optimize the estimation.

4.3 On-line/Off-line change detection system

4.3.1 Change detection

4.3.1.1 Architecture of the change point detector

We show in Figure 4.3 the architecture of the change point detector. A Kalman filter and a CUSUM algorithm are used to detect a change at instant $t^a_{l,i}$ and to localize the change at the position $n^c_{l,i}$. l is the satellite and i is an instant of time. x_k and y_k are respectively the state and measurement equations. ϵ_k is the innovation of the EKF and S_k is the covariance of the innovation. When a change is detected an alarm is generated to initialize the Kalman filter.

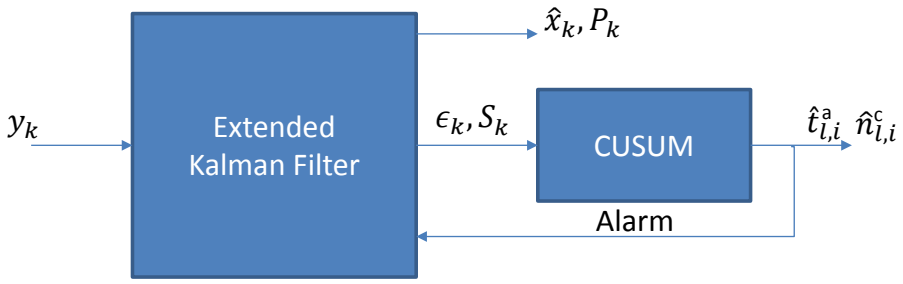

FIGURE 4.3: Architecture of the change point detector.

4.3.1.2 Implementation of the Kalman filter

We recall the state x_k and measurement y_k equations for our system:

$$x_k = Fx_{k-1} + Bw_k \quad (4.1)$$

$$y_k = h_k(x_k) + v_k \quad (4.2)$$

All the parameters of this system are defined in chapter 3 section 3.4.2. The predicted state covariance $P_{k/k-1}$ and state covariance P_k of the EKF are processed with the following equations:

$$\begin{aligned} P_{k/k-1} &= FP_{k-1}F^T + BQB^T && (4.3)\\ K_k &= P_{k/k-1}H_k(H_kP_{k/k-1}H_k^T + R)^{-1} && (4.4)\\ P_k &= P_{k/k-1} - K_kH_kP_{k/k-1} && (4.5) \end{aligned}$$

The predicted estimate state $\hat{x}_{k/k-1}$ and estimate state $\hat{x}_k$ are processed with the following expressions :

$$\begin{aligned} \hat{x}_{k/k-1} &= F\hat{x}_{k-1} && (4.6)\\ \hat{x}_k &= \hat{x}_{k/k-1} + K_k(y_k - h_k(\hat{x}_{k/k-1})) && (4.7) \end{aligned}$$

with $h_k(\hat{x}_{k/k-1}) = [h_{1,k}(\hat{x}_{k/k-1};\theta_k), \ldots, h_{n,k}(\hat{x}_{k/k-1};\theta_k), 0, \ldots, 0]^T$. Let us define the following auxiliary expressions for the innovation ϵ_k and the covariance of the innovation S_k:

$$\begin{aligned} \epsilon_k &= y_k - h_k(\hat{x}_{k/k-1}) && (4.8)\\ S_k &= H_kP_{k/k-1}H_k^T + R && (4.9) \end{aligned}$$

4.3.1.3 Implementation of the CUSUM detector

We assume a change has occurred in the mean of the innovation. The mean value after the change is either $\mu_1^+ = \mu_0 + \nu$ or $\mu_1^- = \mu_0 - \nu$ with ν, the dynamic of the change, assumed to be known. In this work we use a two side CUSUM algorithm [190]. The CUSUM detection process is defined by:

$$\begin{aligned} g_k^+ &= \left(g_{k-}^+ + \epsilon_k - \mu_0 - \nu/2\right)^+ && (4.10)\\ g_k^- &= \left(g_{k-}^- - \epsilon_k + \mu_0 - \nu/2\right)^+ && (4.11)\\ \hat{t}_{l,i}^a &= min\left\{k : (g_k^+ \geq \lambda) \cup (g_k^- \geq \lambda)\right\} && (4.12) \end{aligned}$$

where $(X)^+ = max(X, 0)$ and $t_{l,i}^a$ is the i^{th} instant of change detected for satellite l. In the case of an innovation process where $\mu_0 = 0$, g_k^+ and g_k^-, the integration of the innovation process, evolves as a Gaussian random walk before the change. After the change instant $w + t$ defined in Figure 4.2, g_k^+

and g_k^- are monotonic increasing functions.

According to the transition model defined in Figure 4.2, the theoretical value of the detection threshold λ can be defined as $\lambda = \frac{\Delta t\, \nu}{2} - \frac{\nu}{2}$ with $\nu = m_2 - m_1$. In practice, ν is a parameter defined by the user. It represents the minimum change dynamic that we want to detect. In our application, Δt, the length of the transition area in the change model, is defined with the satellite elevation angle, as well as the speed and height of the airborne carrier.

In the CUSUM detection process, it is also possible to define a likelihood estimate of the change instant. This estimator is based on a likelihood ratio test. We define the following expressions for the CUSUM change point localization process:

$$d_k = ln\left(\frac{p(\epsilon_k;\theta_1)}{p(\epsilon_k;\theta_0)}\right) \tag{4.13}$$

$$D_k = \sum_{n=1}^{k} d_n \tag{4.14}$$

$$\hat{n}_{l,i}^c = \underbrace{argmin}_{1\leq n_c\leq k} D_{n_c} \tag{4.15}$$

where the parameters of the distribution of ϵ_k are: θ_1 after the change and θ_0 before the change. k is the instant at which a change is detected. d_k is the log-likelihood ratio that defines the following test:

$$ln\left(\frac{p(\epsilon_k;\theta_1)}{p(\epsilon_k;\theta_0)}\right) \begin{array}{c}<^{H_0}\\ >_{H_1}\end{array} 0 \tag{4.16}$$

where H_0 is the hypothesis that ϵ_k is the innovation before the change and H_1 is that after the change. According to this property D_k, decreases with the increase of k before the change and increases with k after the change. In this case, the minimum value of D_k is the localized change instant.

Finally, the Kalman-CUSUM change point estimate of Figure 4.3 is described in Algorithm 1. In our implementation, we assume that the innovation before and after the change is distributed according to a Gaussian distribution notice $N(\mu,\sigma)$ where μ and σ are respectively the mean and the standard deviation of the distribution. The normalized innovation process

$\epsilon_k S_k^{-1/2}$ is distributed according to $N(0,1)$ before the change and $N(\nu,1)$ after the change.

Data: Noisy observations: innovation ϵ_k.
Algorithm parameters: change dynamic ν, transition duration Δt.
Result: change instant $t^a_{l,i}$, change localization $n^c_{l,i}$
Algorithm
———-*Initialization*———-
$\lambda = \frac{\Delta t\ \nu}{2}$
$k = 1$
$i = 1$
———-*Implementation*———-
while *the algorithm is not stopped* **do**
  $d_k = \ln\left(\frac{N(\epsilon_k S_k^{-1/2}-\nu;1)}{N(\epsilon_k S_k^{-1/2};1)}\right)$
  $D_k = \sum_{n=1}^{k} d_k$
  $g_k^p = max(g_{k-1}^p + \epsilon_k, 0)$
  $g_k^m = max(g_{k-1}^m - \epsilon_k, 0)$
  if $(g_k^p > \lambda) \cup (g_k^m > \lambda)$ **then**
    $\hat{t}^a_{l,i} = k$
    $\hat{n}^c_{l,i} = \underbrace{argmin}_{1\leq J\leq k} D_j$
    i=i+1
    ———-*Reset the Kalman filter*————
    $x_k = y_k$
    $P_k = P_1$
  end
  k=k+1
end

Algorithm 1: Kalman-CUSUM change point algorithm

We note the absence of the factor $\frac{\nu}{2}$ in the definition of the threshold in Algorithm 1. This factor was introduced as an additional drift parameter on the threshold that ensures that the change point is localized at the center of the transition. In practice, the subtraction of the factor $\frac{\nu}{2}$ from the threshold value decreases the detection threshold and increases the number of false detections (detection of noise) . Thus, it is removed in the detection process.

4.3.2 Change localization

In this work, the dynamic of the change is not known. We propose a Maximum Likelihood Localization Estimate (MLLE) for change point localization

that replaces the CUSUM likelihood change localization estimate. We show in Figure 4.4 the architecture of the proposed change point estimate.

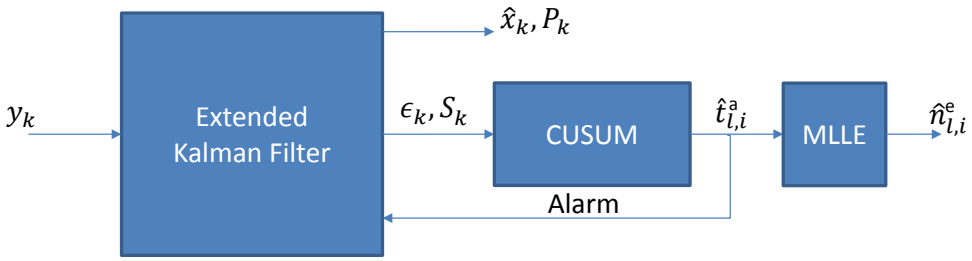

FIGURE 4.4: Architecture of the change point localization algorithm. MLLE stands for Maximum Likelihood Localization Estimate

According to the signal model of Figure 4.2 and assuming that the noise is additive, white centered and Gaussian, we derive a maximum likelihood estimate of t, the starting instant of the transition and Δt, the duration of the transition. The estimates are processed with the GNSS signal amplitudes observations in the working window $(\tilde{x}_{\hat{n}^e_{l,i-1}}, \ldots, \tilde{x}_{\hat{t}^a_{l,i+1}})$. The GNSS amplitude observations $\tilde{x}_k$ are obtained from the in-phase observations y_k using expression (3.38) of chapter 3. $\hat{n}^e_{l,i}$ is the localization of the i^{th} change for satellite l and $\hat{t}^a_{l,i}$ is the i^{th} detected change instant provided by the CUSUM detector for satellite l. In the rest of the section, we will note $\hat{n}^e_{l,i}$ as n^e_i and $\hat{t}^a_{l,i}$ as t^a_i to simplify notations. N is the number of samples in the working window defined between n^e_{i-1}, the previous localized change by MLLE and t^a_{i+1}, the next detected change by CUSUM.

In practice, the CUSUM detector detects a change after its actual position (before localization). In this case, the working window is not optimal, but nearly optimal with a difference of very small number of samples at the end of the window. This number of samples represents the difference between the detected t^a_{i+1} and localized n^e_{i+1} change point position at the instant $i+1$.

To estimate the localized change instant n^e_i, we define the likelihood function as:

$$
\begin{aligned}
f(\tilde{X}_{n_{i-1}^e}, \ldots, \tilde{X}_{t_{i+1}^a}) &= \frac{1}{(\sigma_1\sqrt{2\pi})^t} \exp\left(-\frac{\sum_{n=n_{i-1}^e}^{n_{i-1}^e+t-1}(\tilde{x}_n - m_1)^2}{2\sigma_1^2}\right) \\
&\quad \frac{1}{(\sigma_f\sqrt{2\pi})^{\Delta t}} \exp\left(-\frac{\sum_{n=n_{i-1}^e+t}^{n_{i-1}^e+t+\Delta t-1}(\tilde{x}_n - f_n)^2}{2\sigma_f^2}\right) \\
&\quad \frac{1}{(\sigma_2\sqrt{2\pi})^{N-t-\Delta t+1}} \exp\left(-\frac{\sum_{n=n_{i-1}^e+t+\Delta t}^{t_{i+1}^a}(\tilde{x}_n - m_2)^2}{2\sigma_2^2}\right)
\end{aligned} \tag{4.17}
$$

m_1 and m_2 are the mean values of the GNSS signal amplitude before and after the change, respectively. f_n is a sampling line that models the growth of the reflectivity from m_1 to m_2 defined between $(n_{i-1}^e + t, m_1)$ and $(n_{i-1}^e + t + \Delta t, m_2)$. We can express the negative log likelihood as follows:

$$
\begin{aligned}
-L(f\ldots)) &= t\ \log(\sigma_1\sqrt{2\pi}) + \frac{\sum_{n=n_{i-1}^e}^{n_{i-1}^e+t-1}(\tilde{x}_n - m_1)^2}{2\sigma_1^2} \\
&+ \Delta t\ \log(\sigma_f\sqrt{2\pi}) + \frac{\sum_{n=n_{i-1}^e+t}^{n_{i-1}^e+t+\Delta t-1}(\tilde{x}_n - f_n)^2}{2\sigma_f^2} \\
&+ (N - t - \Delta t + 1)\log(\sigma_2\sqrt{2\pi}) + \frac{\sum_{n=n_{i-1}^e+t+\Delta t}^{t_{i+1}^a}(\tilde{x}_n - m_2)^2}{2\sigma_2^2}
\end{aligned} \tag{4.18}
$$

In practice, the parameters of the log likelihood function are estimated using empirical maximum likelihood estimation. The empirical variances are defined by:

$$
\hat{\sigma}_1^2 = \frac{1}{t}\sum_{n=n_{i-1}^e}^{n_{i-1}^e+t-1}(\tilde{x}_n - m_1)^2 \tag{4.19}
$$

$$
\hat{\sigma}_f^2 = \frac{1}{\Delta t}\sum_{n=n_{i-1}^e+t}^{n_{i-1}^e+t+\Delta t-1}(\tilde{x}_n - f_n)^2 \tag{4.20}
$$

$$
\hat{\sigma}_2^2 = \frac{1}{N - t - \Delta t + 1}\sum_{n=n_{i-1}^e+t+\Delta t}^{t_{i+1}^a}(\tilde{x}_n - m_2)^2 \tag{4.21}
$$

We can derive the expression of the empirical maximum likelihood estimate of $\hat{t}$ and $\widehat{\Delta t}$ by:

$$\begin{aligned}(\hat{t},\widehat{\Delta t}) &= \underbrace{Argmin}_{t,\Delta t}\{t\ \log(\hat{\sigma}_1) + \frac{\sum_{n=n_{i-1}^e}^{n_{i-1}^e+t-1}(\tilde{x}_n - m_1)^2}{2\hat{\sigma}_1^2} \\ &+ \Delta t\ \log(\hat{\sigma}_f) + \frac{\sum_{n=n_{i-1}^e+t}^{n_{i-1}^e+t+\Delta t-1}(\tilde{x}_n - f_n)^2}{2\hat{\sigma}_f^2} \\ &+ (N-t-\Delta t+1)\log(\hat{\sigma}_2) + \frac{\sum_{n=n_{i-1}^e+t+\Delta t}^{t_{i+1}^a}(\tilde{x}_n - m_2)^2}{2\hat{\sigma}_2^2}\}\end{aligned} \tag{4.22}$$

Finally, the empirical maximum likelihood estimate is given by:

$$(\hat{t},\widehat{\Delta t}) = \underbrace{Argmin}_{t,\Delta t}\left\{t\ \log(\hat{\sigma}_1) + \Delta t\ \log(\hat{\sigma}_f) + (N-t-\Delta t+1)\log(\hat{\sigma}_2)\right\} \tag{4.23}$$

In practice, the estimate value $\hat{t}$ is searched in a working window of N samples defined between n_{i-1}^e and t_{i+1}^a. The estimate value $\widehat{\Delta t}$ is searched between $n_{i-1}^e + \hat{t}$ and $n_{i-1}^e + \hat{t} + \Delta t^M - 1$. The value of Δt^M is dependent on the application. For our application to airborne GNSS-R data, Δt^M is a function of the length of the major axis a of the first Fresnel zone ellipse associated with the satellite footprint. According to the signal model, the true position of the border between two different areas which corresponds to the true change point position is assumed to be at $n_i^e = n_{i-1}^e + \hat{t} + \frac{\widehat{\Delta t}}{2}$. This position can be in practice the beginning or the end of the edge of a water body along the satellite footprint trace.

4.3.3 Change merging

At the end of the segmentation process the signal is divided into different parts associated to different mean amplitude levels based on the estimated change positions. However, we observe that the segments can be merged based on a developed merging criteria to decrease the number of false detections and increase the length of the stationary parts in each area of reflection. We show in Figure 4.5 the architecture of the segmentation algorithm that integrates the merging processing step.

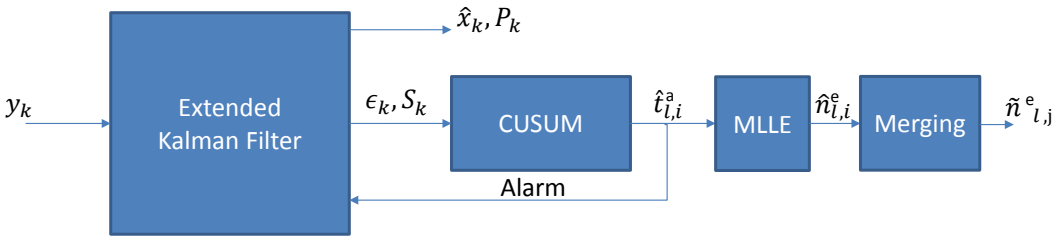

FIGURE 4.5: Architecture of the change point algorithm with merging.

The proposed merging process starts by defining the confidence interval (expression (4.24)) of the mean estimate m for each segment of the signal. This interval has a specific level of confidence that defines the percentage of time the true mean μ^m lies in the interval estimate given. In our case, the mean follows a Student's t-distribution since the population standard deviation σ is not known. Let us define the following expressions for the change point merging process:

$$m_i - E_i < \mu_i^m < m_i + E_i \tag{4.24}$$

$$E_i = t_{\alpha/2,i} \frac{s_i^f}{\sqrt{n_i^f}} \tag{4.25}$$

E_i is the maximum error of the estimate and is one-half of the width of the confidence interval. s_i^f is the unbiased sample standard deviation and n_i^f is the number of samples in the segment S_i defined between $\hat{n}^e_{l,i-1}$ and $\hat{n}^e_{l,i}$. The t-score is a factor of the level of confidence and the degree of freedom df which is related to the sample size ($df = n_i^f - 1$). α is the significance level and $\alpha/2$ represent the area in one tail for a confidence interval. The most commonly used significance level is $\alpha = 0.05$, implying a confidence level of 95%.

To determine whether the difference between two means is statistically significant, we compare the confidence intervals for consecutive segments. If the intervals overlap with high percentage, we note that the difference between the two means is not statistically significant and thus the 2 segments in study can be merged. If there is no overlap or the 2 segments overlap with

a percentage less than a predefined degree of overlap, the difference is significant and the segments are not merged. We note the predefined degree of overlap between the two intervals as the merging threshold λ^m.

Consider 2 successive segments S_i and S_{i+1} of mean values m_i and m_{i+1} and of maximum errors E_i and E_{i+1}, respectively. We define the associated confidence interval of each segment as in equation (4.24). The ranges of each confidence interval can be defined as:

$$\begin{aligned} d &= m_{i+1} + E_{i+1} \\ c &= m_{i+1} - E_{i+1} \\ b &= m_i + E_i \\ a &= m_i - E_i \end{aligned} \tag{4.26}$$

The merging process of Figure 4.5 is described in Algorithm 2. Figure 4.6 represents the 3 different cases of the confidence intervals that are considered in our merging algorithm.

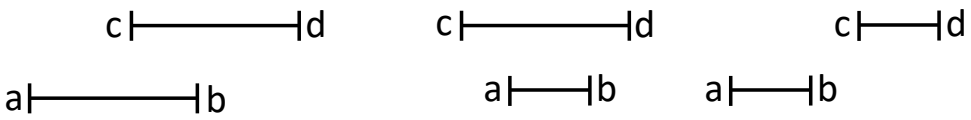

(a) Overlapping (b) Inclusion (c) Non-Overlapping

FIGURE 4.6: The different cases of the confidence intervals.

In the case of overlapping (Figure 4.6a), the percentage of overlapping p^f can be defined as:

$$\begin{aligned} p^f &= \frac{overlapping\ region}{overlapping\ region\ +\ nonoverlapping\ region} \times 100 \\ &= \frac{min(d,b) - max(c,a)}{min(d,b) - max(c,a) + ||d-b| + |c-a||} \times 100 \end{aligned} \tag{4.27}$$

The 2 overlapped segments are merged if the following condition is satisfied:

$$p^f \geq \lambda^m \tag{4.28}$$

Data: amplitude observations $\tilde{x}_k$, change points localized $\hat{n}^e$
Result: change points after merging $\tilde{n}^e$, segmentation m
Algorithm
———*Initialization*———
set values for : α, CL, λ^m *and* λ^s; $i = 1$; $j = 1$
———*Implementation*———
while *the algorithm is not stopped* **do**
  $m_i = mean(\tilde{x}_{\hat{n}^e_{i-1}} \dots \tilde{x}_{\hat{n}^e_i})$; $m_{i+1} = mean(\tilde{x}_{\hat{n}^e_i} \dots \tilde{x}_{\hat{n}^e_{i+1}})$;
  $s^f_i = std(\tilde{x}_{\hat{n}^e_{i-1}} \dots \tilde{x}_{\hat{n}^e_i})$; $s^f_{i+1} = std(\tilde{x}_{\hat{n}^e_i} \dots \tilde{x}_{\hat{n}^e_{i+1}})$;
  n^f_i=$length(\tilde{x}_{\hat{n}^e_{i-1}} \dots \tilde{x}_{\hat{n}^e_i})$; n^f_{+1}=$length(\tilde{x}_{\hat{n}^e_i} \dots \tilde{x}_{\hat{n}^e_{i+1}})$;
  $t_{\alpha/2,i} = tinv(CL, n^f_i - 1)$; `/* Student's T Critical Values */`
  $t_{\alpha/2,i+1} = tinv(CL, n^f_{i+1} - 1)$;
  $E_i = t_{\alpha/2}\frac{s^f_i}{\sqrt{n^f_i}}$; $E_{i+1} = t_{\alpha/2,i+1}\frac{s^f_{i+1}}{\sqrt{n^f_{i+1}}}$;
  $d = m_{i+1} + E_{i+1}$; $c = m_{i+1} - E_{i+1}$; $b = m_i + E_i$; $a = m_i - E_i$;
  if $(min(d,b) - max(c,a) > 0)$ **then**
    if $(min(d,b) = d$ ***and*** $max(c,a) = c)$ ***or*** $(min(d,b) = b$ ***and*** $max(c,a) = a)$ **then**
      ————————*Inclusion*————————
      $p^s = ||d - b| - |c - a||$
      if $p^f \leq \lambda^s$ **then**
        $m_i = m_{i+1} = mean(\tilde{x}_{\hat{n}^e_{i-1}} \dots \tilde{x}_{\hat{n}^e_{i+1}})$; `/* Merge */`
      else
        $\tilde{n}^e_j = \hat{n}^e_i$
        j=j+1;
      end
    else
      ————————*Overlapping*————————
      $p^f = \frac{min(d,b)-max(c,a)}{min(d,b)-max(c,a)+||d-b|+|c-a||}$
      if $p^f \geq \lambda^m$ **then**
        $m_i = m_{i+1} = mean(\tilde{x}_{\hat{n}^e_{i-1}} \dots \tilde{x}_{\hat{n}^e_{i+1}})$; `/* Merge */`
      else
        $\tilde{n}^e_j = \hat{n}^e_i$
        j=j+1;
      end
    end
  else
    ————————*No Overlapping*————————
    $\tilde{n}^e_j = \hat{n}^e_i$;
    j=j+1;
  end
  i=i+1;
end

Algorithm 2: Merging algorithm

In practice, λ^m is defined by the user and is dependent on the constraints of the application.

If one segment is subset of the other, we are in the case of inclusion (Figure 4.6b). In this case, the decision of merging depends on the degree of symmetry p^s defined as:

$$p^s = ||d-b| - |c-a|| \leq \lambda^s \tag{4.29}$$

where λ^s is a predefined threshold in the order of 10^{-2}.

In fact, the degree of symmetry defines how close is the estimated mean of the 2 segments. If the means are too close we merge, otherwise the segments are considered asymmetrical. When the segments are not overlapped (Figure 4.6c), i.e. $min(d,b) - max(c,a) < 0$, the segments are not merged. As a result, the number of change points after merging $\tilde{n}_j^e$ will be lower than the number of changes detected $\hat{n}_i^e$ since we eliminate the false alarm detections. Finally the signals are segmented based on the localized change points after merging.

4.4 Experimentation

4.4.1 Assessment on synthetic data

4.4.1.1 Empirical distribution of the change point estimation

The aim of this experimentation is to assess the accuracy of the proposed change point estimation algorithm on synthetic signal amplitude measurements. We present in Figure 4.7, the generated signal amplitudes along 2 seconds of observation. We also show the signal change model associated to it. The decreasing transition of the signal in this case between the mean values m_1 and m_2 as shown in Figure 4.7 models the satellite footprints displacement from an area with high reflectivity to an area with lower reflectivity. In this experiment, we choose $m_1 = 0.014$ and $m_2 = 0.006$ in order to emulate the GNSS reflected signal amplitude levels that we observe in the real airborne experiment. The Gaussian noise on the signal has a standard deviation of 0.001.

We apply the change point detection and localization algorithm to extract the estimated starting instant of the transition $\hat{t}$, the estimated duration of the transition $\widehat{\Delta\, t}$, and the estimated ending instant of the transition $\hat{t} + \widehat{\Delta\, t}$. Consequently, the estimated change point position which corresponds to the estimated location of the border between two areas would be at $\hat{t} + \frac{\widehat{\Delta\, t}}{2}$.

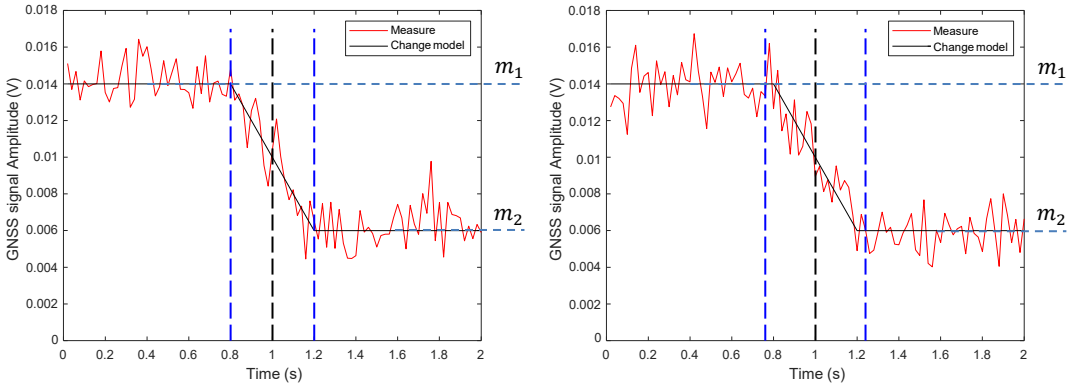

(a) (b)

FIGURE 4.7: Different estimates of the start and end instants of the transition (blue dashed lines) as well as the estimated change point position (black dashed line) using the proposed change point algorithm. We show in this figure the generated signal amplitude measurements along with the signal change model associated to it.

We show in Figure 4.7 different estimates of the start and end instants of the transition (blue dashed lines) as well as the estimated change point position (black dashed line) associated to different realizations of the signal using the proposed algorithm. Figure 4.7a shows accurate estimation of the start and end instants of the transition. Subsequently, the estimated position of the border is at the true change point position. Figure 4.7b shows the estimates when the detected starting instant is advanced and the detected ending instant of the transition is delayed. Although, the estimates of the transition start and end are indeed shifted, the estimated change point position is still at the true position. We show why this effect makes the estimate of the change position more accurate (lower standard deviation) than the estimates of the transition start and end.

To evaluate the proposed approach we apply a statistical analysis over 100 realizations of the simulated signal. We show in Figure 4.8 the empirical distribution of the detected transition start and end instants as well as the

estimated change point instant.

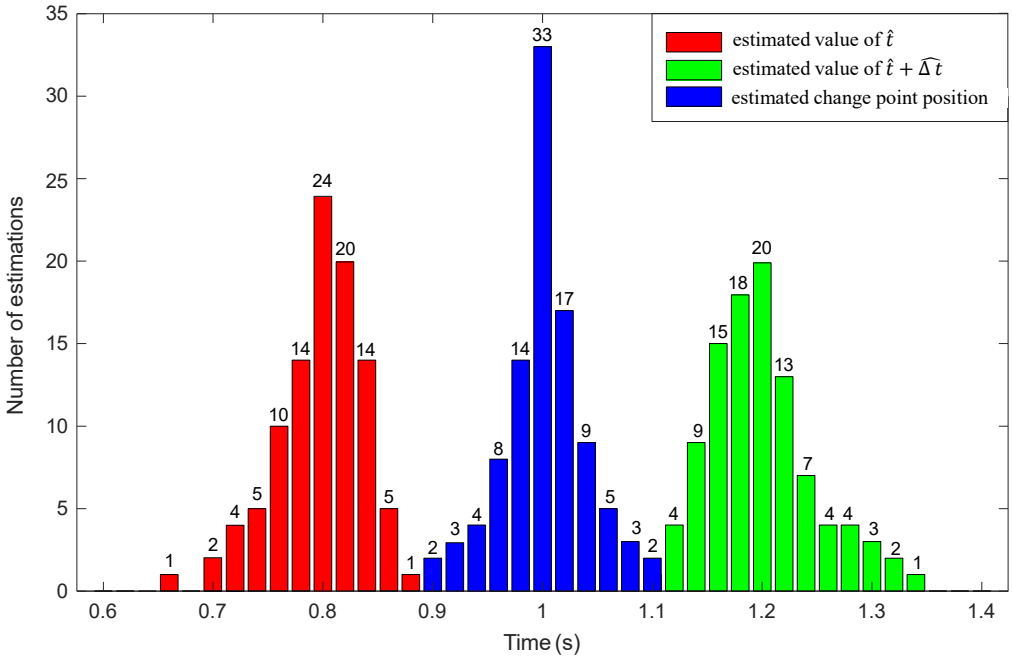

FIGURE 4.8: The estimated values (in seconds) of the transition start and end instants as well as the estimated change point position over 100 iterations using the proposed change point localization algorithm. The figure is zoomed on the area where the distribution is concentrated.

We notice in Figure 4.8 that the statistics of the estimated change point position follow an exponential distribution maximized at the true value of the change point position. We report in Table 4.1 the statistical parameters of the distributions. We observe that the standard deviation is indeed lower for the change position estimate which is in agreement with the conclusions derived from Figure 4.7.

TABLE 4.1: Statistical parameters of the empirical distributions.

	Transition start	Change position	Transition end
Mean(s)	0.08	1	1.2
Standard deviation(s)	0.04	0.038	0.047

4.4.1.2 Comparison with state-of-the-art methods

To assess the accuracy of the proposed approach in terms of change point localization, we compare the proposed change point localization approach described section 4.3.2 with the CUSUM change point localiztion method described in section 4.3.1. We show in Figure 4.9 the empirical distribution of the estimated change point location, processed with 100 realizations of the signal for the CUSUM and the proposed method (MLLE).

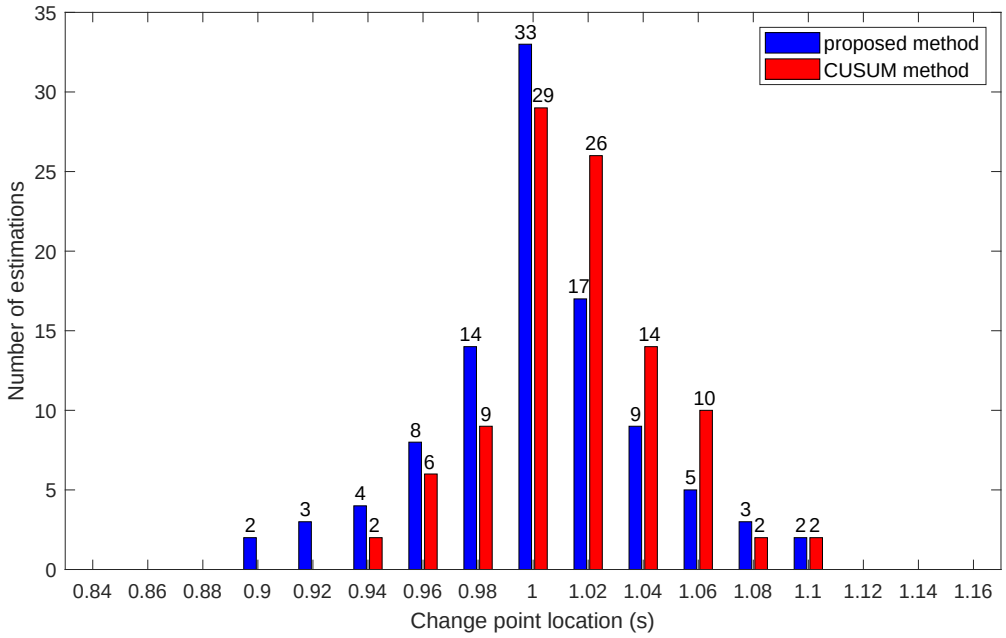

FIGURE 4.9: A comparison of the estimated change point location (in seconds) obtained by our proposed algorithm and by the CUSUM method over 100 iterations.

We report in Table 4.2 the mean and the standard deviation of the empirical distributions obtained with 1000 realizations of the signal. These parameters plus the number of detected changes are given as a function of the SNR. In this experimentation, the true change point position is at 40 *sec*, the change dynamic is $\nu = 1$ and the standard deviation of the noise vary from 0.01 to 1. The assessed methods are: the CUSUM, the Kalman Generalized Likelihood Ratio (GLR) [198] and the proposed MLLE approach. The CUSUM localization approach assumes that the dynamic of the transition is known, whereas the GLR estimates this change dynamic to localize the change points. The proposed MLLE apporoach for change localization do not take into account the dynamic of the transition while localizing the detected changes.

TABLE 4.2: Statistical parameters of the empirical distributions of the different change point detectors as a function of the SNR. The parameters are: the mean, the standard deviation and the number of detected changes (Nbr).

	CUSUM			GLR			MLLE		
SNR (dB)	Mean(s)	Std(s)	Nbr	Mean(s)	Std(s)	Nbr	Mean(s)	Std(s)	Nbr
58	39.73	1.09	1000	39.66	0.92	969	40.15	0.73	1000
40	39.61	1.92	1000	39.52	1.56	972	40.25	1.22	1000
30	39.67	2.68	1000	39.31	2.24	975	40.31	1.86	1000
20	38.64	6.41	1009	39.69	5.12	958	40.21	4.13	1009
12	17.18	15.88	1112	47.35	17.97	1172	43.27	11.73	1112
10	9.83	12.53	1192	50.63	20.37	1289	44.20	15.39	1192
8	5.53	7.92	1317	54.20	22.48	1484	46.57	18.71	1317
6	3.45	5.13	1465	55.84	22.53	1663	47.61	20.83	1465
0	1.66	1.38	2141	58.24	23.2	2158	49.94	25.68	2141

We observe in Table 4.2 that the standard deviation of the estimation increases when the SNR decreases. In other words, the change point localization accuracy decreases when the SNR decreases. The number of detected changes for the CUSUM and MLLE localization techniques is the same because both methods use the same Kalman-CUSUM change detector. We also observe that the number of detected changes becomes superior to 1000 and increases even further with the decrease of the SNR in these two approaches. The values superior to 1000 are associated to the over segmentation of the signal. We solve the problem of over segmentation by integrating the merging process to the proposed approach.

For GLR, we notice an under detection phenomena with high and moderate SNR. When the SNR becomes inferior to 20 dB, the GLR localization accuracy decreases significantly and the number of false alarm detections increases. This method estimates the change magnitude and detects a transition when the dynamic of the change is superior to a given threshold. When the SNR decreases, the GLR algorithm can not distinguish between the transitions due to the noise and the transitions due to the real signal. This leads to an increase in the number of false alarms associated to the detection of noise. In this context, the accuracy decreases because we process the mean localization with all the detected changes.

We can conclude from Table 4.2 that the proposed MLLE estimate is more accurate than other state-of-the-art approaches. The standard deviation of the empirical distribution of the change detection for our approach is indeed lower than that for the other methods. For very low SNR (inferior to 20 dB), the proposed approach proves to be more robust because the mean value of the localization stays coherent with the true value unlike the CUSUM and GLR localization approaches which become completely incoherent with the true value of the mean when the SNR is inferior to 20 dB. Furthermore, the proposed approach is the most accurate under various SNR environments including the typical range of SNR for reflected GNSS signals from Earth surface [20 dB - 45 dB]. Therefore, we can also conclude that our approach has the capacity to segment real GNSS signals in a dynamic environment.

Finally, we report in Table 4.3 the statistical parameters of the empirical distribution of the proposed MLLE approach before and after integrating the merging algorithm to the segmentation process. In this study, the confidence level is 95%, the merging threshold is $\lambda^m = 90\%$ and the symmetry threshold is $\lambda^s = 0.05$. We notice from Table 4.3 a decrease in the number of detections after integrating the merging algorithm to the proposed approach. This decrease is associated to the decrease in the number of false alarm detections after merging which significantly mitigates the over segmentation phenomena of the signal. As a result, the mean of the empirical distribution after integrating the merging algorithm becomes more coherent with the true value.

4.4.2 Assessment on real data

4.4.2.1 Evaluation by laboratory experiment

In this section, we assess the performance of the proposed change point estimator using GPS C/A signals. For this purpose, we record 6 seconds of raw GNSS data using the NovAtel GNSS-850 antenna introduced in section 3.5.2. We process 1 *ms* rate of GNSS signal amplitude measurements using 1 *ms* rate observations of the in-phase component of the signal based on the model proposed in chapter 3 section 3.4.

TABLE 4.3: Statistical parameters of the empirical distribution of the proposed MLLE approach before and after integrating the merging algorithm to the segmentation process.

	MLLE					
	without merging			with merging		
SNR (dB)	Mean	Std	Nbr	Mean	Std	Nbr
12	43.27	11.73	1112	41.44	9.48	1016
10	44.20	15.39	1192	41.67	10.18	1035
8	46.57	18.71	1317	42.31	13.26	1072
6	47.61	20.83	1465	43.29	14.92	1116
0	49.94	25.68	2141	45.13	18.51	1454

In order to prove our estimator's ability to detect abrupt changes in the GNSS signal amplitudes, we generate a change in the signal while recording the raw GNSS data. This abrupt change was implemented with the aid of an attenuator designed by HP (8494A Attenuator). The attenuator was set to 1 dB for approximately 0.5 seconds to generate the change. The abrupt change is detected by our approach through the innovation of the Kalman filter with the CUSUM algorithm. In this context, whenever an abrupt change is detected, the Kalman filter is re-initialized and the next measurement is used as the current state. We apply the change point localization algorithm described in section 4.3.2 to estimate the position of the change points after detection. We show in Figure 4.10 the 1 ms rate amplitude observations in the presence of abrupt change for PRN 2 satellite signal.

We report the change point locations estimated by our proposed change point detector (black dashed lines) as well as the change point locations estimated by the CUSUM method (red dashed lines). In this case, a change is detected using the CUSUM method when the cumulative sum drifts more than 15 standard deviations beyond the target mean. We notice from Figure 4.10a that both methods were able to localize the change in the signal amplitude level. Zooming in on the part where the change was simulated (Figure 4.10b), we notice that both methods localized the first change at the same instant at 1.946 s (the lines are coinciding in the Figure). However, our proposed algorithm localized the second change more accurately where we can notice a clear delay in the estimated change point location using the

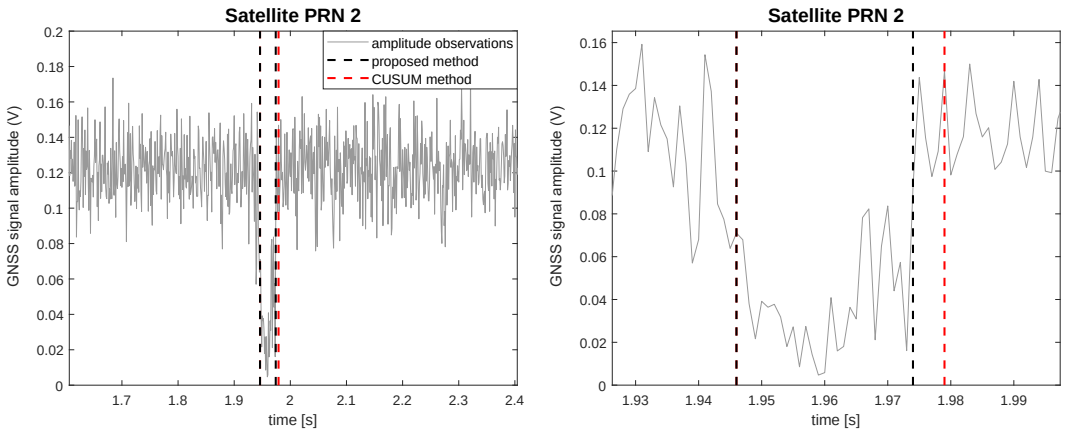

(a) (b)

FIGURE 4.10: Assessment of the proposed change point detection algorithm with abrupt changes. We report the change point locations estimated by our proposed algorithm (black dashed lines) as well as the change point locations estimated by the CUSUM method (red dashed lines) using 1 *ms* rate amplitude observations.

CUSUM method. This further proves the accuracy of our proposed change point estimation model.

In terms of execution time and computational load, both methods were implemented in MATLAB using the same workstation with core i5-6600 processor and 16 GB of RAM. The runtime to estimate the change point locations using our method was 27 *ms* compared to 18 *ms* for CUSUM method. This 9 *ms* difference is compensable given the improvement in accuracy.

4.4.2.2 Comparison of the proposed C/N_0 estimator with the state of the art

We introduced in chapter 3 a low complexity C/N_0 estimator with low computational load, as a trade off with the accuracy of our estimates. In order to prove our estimate's ability to cope with rapid and abrupt changes encountered in multipath and dynamic GNSS-R applications, we compare the proposed C/N_0 estimator with an accurate C/N_0 estimate provided by Beaulieu's method presented in section 2.3.2.2. In this experiment, we use the data recorded in section 4.4.2 in the presence of the abrupt change. The change point is detected based on the algorithm proposed in section 4.3.

We show in Figure 4.11, C/N_0^k estimated by the proposed approach every 1 *ms* according to equation (3.40) and C/N_0^{BL} estimated by Beaulieu's method according to equations (2.45) and (2.46) every 100 *ms*. We also report the 1 *ms* rate carrier-to-noise observations C/N_0^o with abrupt changes in the amplitude measurements for PRN 2 satellite signal. In this experiment, the parameters of the Kalman filter are set to R=10,000,000,000 and Q=0.0001 and the threshold of detection is set to 2 times the standard deviation of the noise.

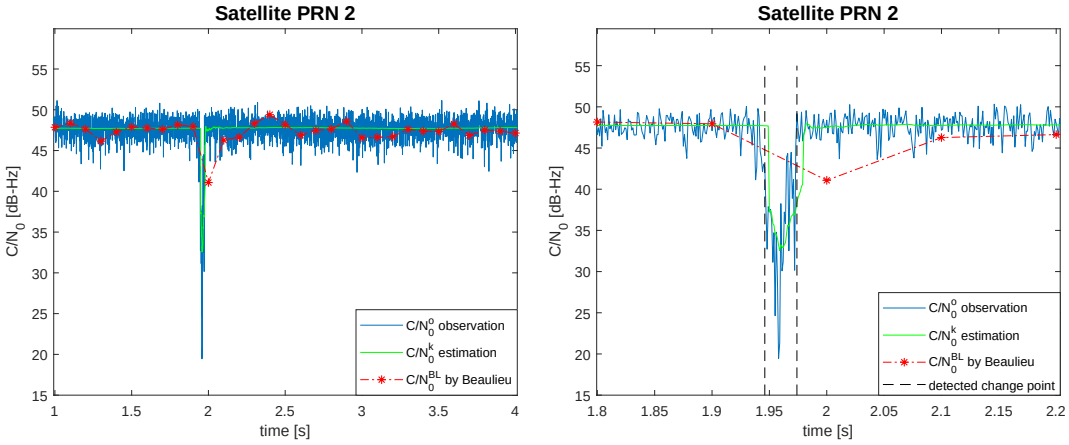

(a) (b)

FIGURE 4.11: C/N_0 estimation assessment with abrupt change. In this Figure, C/N_0^k is the carrier-to-noise ratio estimated by the proposed approach every 1 *ms*, C/N_0^{BL} is the carrier-to-noise ratio estimated by Beaulieu's method every 100ms, and C/N_0^o is the 1 *ms* rate carrier-to-noise observations.

From Figure 4.11a, we notice that the C/N_0^{BL} estimates provided by Beaulieu's method every 100ms, have a higher variance than C/N_0^k estimates provided by our approach every 1 *ms*. Furthermore, zooming in (Figure 4.11b) on the part where the abrupt change in the observations has took place, we notice that C/N_0^k follows this change more accurately and rapidly than Beaulieu's method. In practice, there is a trade-off between accuracy and capacity to follow a rapid change with respect to Beaulieu's method. With Beaulieu's method, the capacity to follow an abrupt change is improved when we decrease the processing step. However, the accuracy is decreased. The trade-off is less critical with respect to the proposed estimate that can be easily adapted to change point estimation. This further proves our estimate's ability to cope with rapid and abrupt changes in the observations and ensures the importance of high rate C/N_0 estimations in multipath and dynamic GNSS-R applications.

4.4.2.3 Evaluation using airborne GNSS measurements

The airborne experiment will be described in details in chapter 5. We show in Figure 4.12 the reflectivity measurements obtained with our GNSS-R receiver embedded in a gyrocopter. The signal of reflectivity is the ratio of the amplitude of the reflected GNSS signal by the soil and the amplitude of the direct GNSS signal. This reflectivity increases with the water content of the soil. Figure 4.12 shows abrupt changes in the signal associated to the reflection on water bodies. In order to detect and localize water bodies, we apply an automatic segmentation of the signal using the reflectivity measurements based on the segmentation model presented in this chapter. The signal segmentation shown in Figure 4.12 is obtained after integrating the merging process.

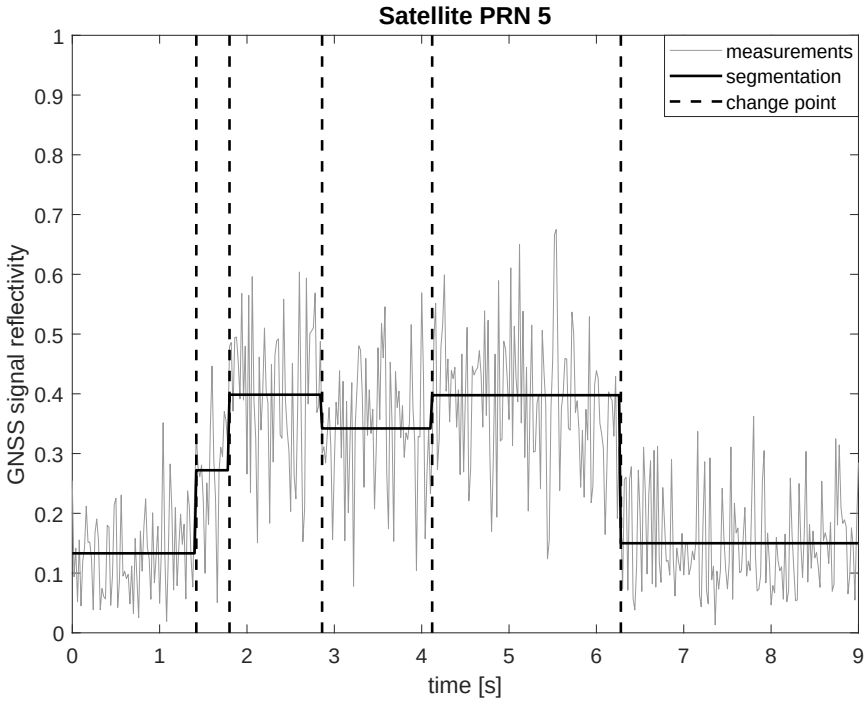

FIGURE 4.12: Reflectivity of a GNSS signal as a function of time with the associated segmentation model. The signal is obtained in an airborne experiment.

We show in Figure 4.13 the different steps of the signal segmentation. The first step is the change point detection process (Figure 4.13a) with the Kalman-CUSUM algorithm. The second step (Figure 4.13b) is the change localization process by the proposed maximum likelihood estimate (MLLE). In the third step 4.13c, we over segment the signal based on the localized change points. Each segment is defined by its mean and confidence interval. In the fourth step, the stationary zones obtained with the change estimator

are merged as shown in Figure 4.13d. Finally, signal segmentation after integrating the merging process is shown in Figures 4.13e and 4.13f with the mean and confidence intervals associated to each segment.

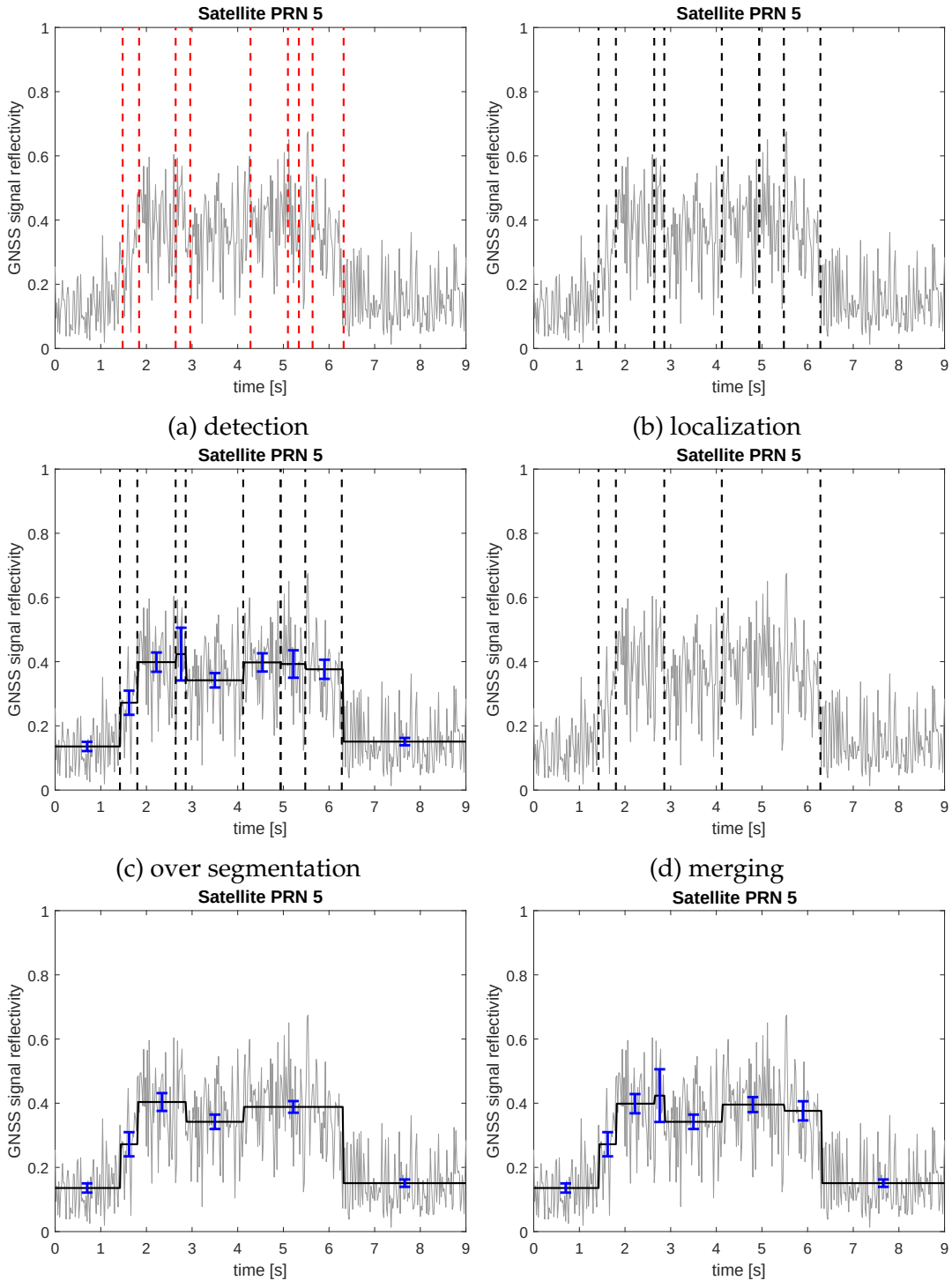

(a) detection

(b) localization

(c) over segmentation

(d) merging

(e) segmentation with $\lambda^m = 0.75$

(f) segmentation with $\lambda^m = 0.9$

FIGURE 4.13: The different steps of segmentation.

The merging threshold is set to 75% and the degree of symmetry is set to 0.05 in Figures 4.13d and 4.13e. Increasing the merging threshold to 90% and decreasing the degree of symmetry to 0.02 will further increase the number of false detections as shown in Figure 4.13f. On the other hand, we can observe from 4.13e that the confidence intervals of the remaining segments after merging are non-overlapped and thus no more merging can be applied. The choice of the merging threshold will affect the sensitivity of the proposed radar technique to detect changes within the same surface which can be of significant importance based on the application. In this regard, there is a trade-off between sensitivity to detect changes in the surface and the number of segments associated to the number of change point detections in the signal.

The results obtained in Figure 4.13 show the feasibility of our approach to segment a real reflectivity signal obtained in an airborne experiment. In this context, the proposed approach will be used in chapter 5 for the detection and localization of in-land water body surfaces. This evaluation is realized with signals of reflectivity obtained for different satellites along a trajectory of 45 *min* long.

4.5 Conclusion

In this chapter, we propose a mixture of an on-line/off-line change point detection and localization algorithm in order to segment the GNSS signals into stationary parts based on the changes that occur on the signal amplitudes. These changes are indeed associated with different areas of reflection. In our approach, a change in the mean of the signal amplitude separates two different reflecting areas. After detecting a change using the innovation of the Extended Kalman Filter by the CUSUM algorithm, we derive a maximum likelihood estimate of the start and end instants of a transition in a nearly optimized working window. As a result, the estimated change point position is derived from the estimated transition start and end instants. In the presence of noise, the CUSUM detector can generate false alarm detections. In order to mitigate the number of false detection, we propose an interval merging algorithm based on the Student's t-distribution.

We show that the proposed change point localization algorithm outperforms other state-of-the-art methods using synthetic data. The empirical distribution of the proposed MLLE approach stays coherent with the true

change position even in low SNR environments unlike other methods. We also use synthetic data to evaluate the merging algorithm. We notice that the number of detections indeed decreases as a result of merging which implies a decrease in the over segmentation phenomena of the signal as a result of false detections.

We also show, using real data, that the proposed MLLE approach performs more accurately than the CUSUM localization algorithm at high rates (1 *ms* rates) amplitude measurements. In a work that combines the two proposed models for C/N_0 estimation (chapter 3) and change point detection (chapter 4), we evaluate using real data, our methods abilities to cope with the abrupt changes in observations. This is done by comparing our C/N_0 estimator with an accurate C/N_0 estimate, namely Beaulieu's estimate, in the presence of abrupt changes in the 1 *ms* rate observations. The changes are detected using the proposed change point detection algorithm. The experimentation shows that there is a trade-off between accuracy and capacity to follow a rapid change with respect to Beaulieu's method, which is less critical with respect to the proposed estimator.

Finally, we show the different steps of the segmentation process on real data in order to divide the GNSS signal into stationary parts associated with different mean signal levels. We show on real data, that integrating the merging process into the segmentation algorithm decreases the number of false detections and shows more stationary parts of the signal associated to different areas of reflection. However, we also note that the choice of the merging and symmetry threshold is critical in defining the sensitivity of the application for detecting small changes in the signal.

The model studied in this chapter can be applied on dynamic GNSS-R applications in order to derive some characteristics of the reflecting surface (such as its size, height or moisture) and consequently, differentiate surfaces based on their reflectivity. In fact, the changes in the amplitudes of the reflected GNSS signals are directly linked to the changes in the reflectivity of different landforms. In case of airborne GNSS-R, it is crucial to obtain C/N_0 and amplitude estimates at high rates to cope with the rapid displacement of the airborne GNSS receiver. In such a dynamic environment, the reflectivity of different observed surfaces can change abruptly. Thus, the presented work in this chapter is used in the airborne GNSS-R experiment of chapter

5 for segmentation of the reflected GNSS signals with high rate reflectivity measurements.

Chapter 5

Airborne GNSS Reflectometry for Water Body Detection

5.1 Introduction

This chapter is dedicated to the study of airborne GNSS-R techniques for water body surface detection and edge localization using a lightweight low-altitude airborne carrier. In this work, we differentiate surfaces based on the reflectivity measurements. We derive high rate (20 *ms* rate) reflectivity measurements associated with different areas of reflection from the estimated GNSS signal amplitudes. We have shown in chapter 3, that for 1-bit quantization in a digital receiver, the digitized signals are independent of the automatic gain control, and that dedicated GNSS signal processing provides a direct observation of the GNSS signal amplitude. High rate GNSS measurements are processed in order to cope with the rapid displacement of the satellites footprints (i.e the reflecting surfaces) along the receiver trajectory.

We develop a GNSS-R setup onboard a gyrocopter. We estimate the 20 *ms* rate of the GNSS signals amplitudes using 20 *ms* rate observations. However, since the reflected GNSS signals are very low in power, the tracking loops (PLL and DLL) of the GNSS signal processing associated to the reflected signals are done in a master/slave configuration, while taking into consideration the path difference between the direct and reflected signals.

The GNSS signals are then segmented into stationary parts with different reflectivity measurements associated to different areas of reflection based on the change point detection and localization algorithm that is developed in chapter 4. In this work, we assume that a change in the mean of the reflectivity measurements separates 2 areas of reflection. Finally, the reflectivity

measurements defined in each segment of the signal are linked to the satellites footprints (reflecting surfaces) for surface detection and edge localization with a 50 Hz rate localization of the specular points of reflection. The GNSS measurements are imposed on maps for assessment.

We show, along a real flight experimentation, that our proposed radar technique is highly sensitive to changes in landforms. We show that we can detect the positions of different in-land water body surfaces along the traces of the satellites footprints. We also show that we can localize at meter accuracy, the edges of water body surfaces, i.e. the border between water and land. Finally, we verify that the proposed radar technique has the capacity to differentiate surfaces in landforms that are scanned by the traces of the satellites footprints such as: in-land water bodies, sandy beach, sea, land and vegetation (forests/groves).

Based on the foregoing, this chapter is organized as follows: Section 2 introduces the airborne GNSS system that we utilize in this work. Section 3 demonstrates the airborne experimental setup used for the flight experimentation along with the GNSS-R receiver hardware. Section 4 presents the GNSS-R software receiver. In section 5, we introduce the context of the real flight experimentation. Analysis of the data acquired during the flight for surface detection and water body edge localization are provided in section 6. Conclusions are provided in the final section.

5.2 Airborne GNSS system

5.2.1 Airborne bi-static GNSS-R configuration

GNSS-R consists in using GNSS signals received on Earth directly from the GNSS satellites as well as after a reflection on Earth surface. In our implementation, we use the GNSS-R dual antenna geometry depicted in Figure 1.6. In this context, the direct GNSS signals are received by an RHCP antenna, and the reflected GNSS signals are received by an LHCP antenna after specular scattering from different landforms along the flight trajectory as shown in Figure 5.1. When a signal hits a reflection point on Earth, scattering occurs primarily from the region of the surface surrounding the specular reflection point.

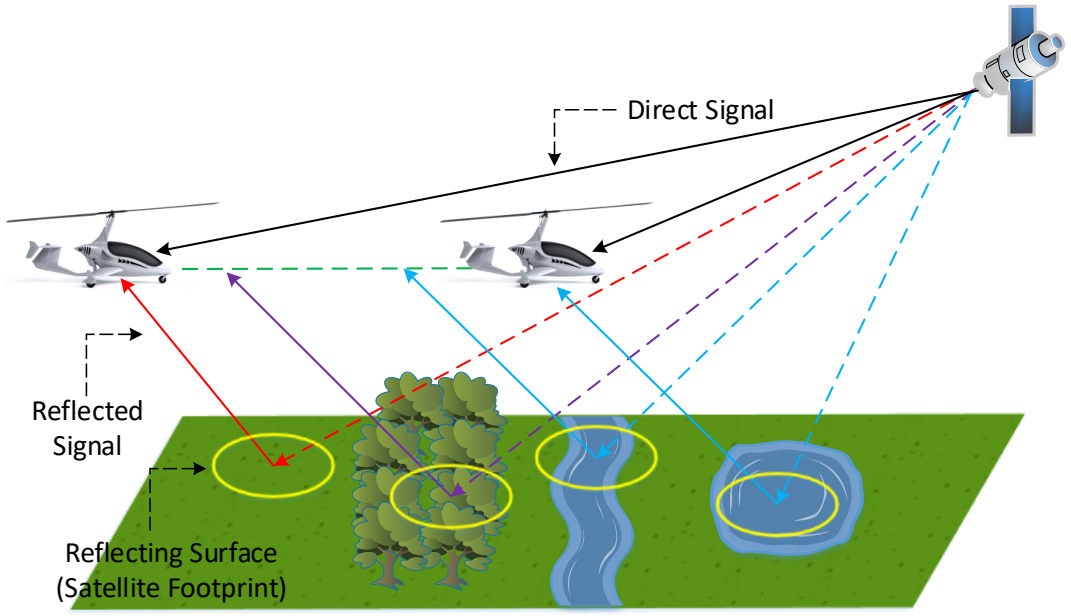

FIGURE 5.1: Airborne GNSS-R Geometry

On flat areas with no topography, the specularly reflected power can be derived solely from the Fresnel reflection coefficients. In this case, the spatial resolution of the GNSS measurements is mostly linked to the size of the first Fresnel zone. The co- and cross-polarization smooth surface reflectivity as well as its polarimetric ratio can be derived from the Fresnel reflection coefficients. In this work, we process 20 *ms* rate amplitudes of the RHCP and LHCP antenna signals in order to maximize the power of the GNSS signals compared to 1 *ms* rate measurements. The 20 *ms* rate reflectivity measurements are defined as the ratio of the amplitudes of the reflected LHCP antenna signals A^r_{LHCP} over the direct RHCP signals A^d_{RHCP} as shown below:

$$\Gamma(t) = \frac{A^r_{LHCP}(t)}{A^d_{RHCP}(t)} \tag{5.1}$$

We associate this measurement with 20 *ms* rate specular point localization.

5.2.2 Localization of the GNSS measurements

We present in Figure 5.2, a flow chart showing the implementation steps to link the GNSS observations with the reflecting surfaces. The data are first recorded during the flight and then processed off-line. The specular points are localized as a function of the GPS time with the use of RINEX files and

on-board drone card measurements as further described in appendix A.

The raw data recorded by the GNSS-R receiver corresponds to the samples of the direct and reflected GNSS signals at the output of the antennas (after frequency down conversion). After data collection, proper GNSS signal processing techniques are applied for the extraction of the required GNSS signal parameters. The digitized signals are processed by a PLL and a DLL to obtain the GNSS data. The message of navigation is extracted in the process and the GPS time of each data is derived after signal dating. We have shown in chapter 3 that the GNSS data obtained at the output of the PLL and DLL (i.e. in-phase component of the signal I, code delay, frequency delay and phase delay) can be processed to obtain observations of the GNSS signal amplitude as a function of the GPS Time. In this context, high rate (20 ms) amplitude estimations are obtained using 20 ms rate observations of I.

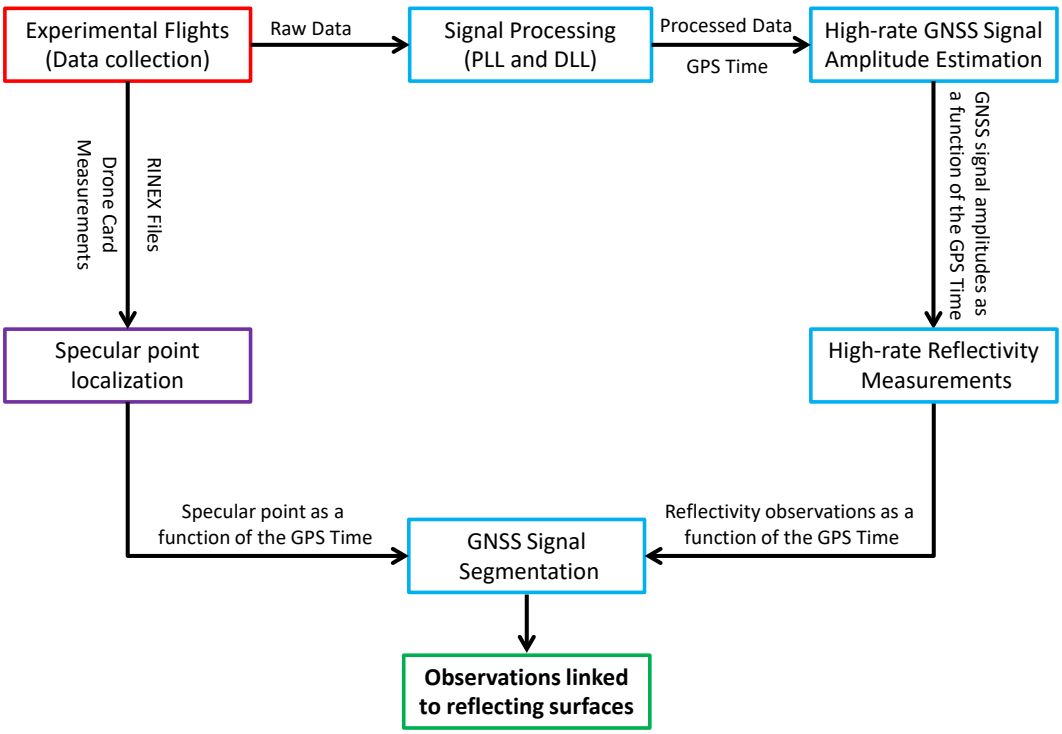

FIGURE 5.2: Linking the GNSS observations to reflecting surfaces

As a result, 20 ms rate reflectivity measurements are derived as a function of the GPS Time. Then, the GNSS signals are segmented into stationary parts based on the changes in reflectivity using the segmentation model developed in chapter 4. These segments are associated with different areas of

reflections represented by the specular point localization. For this purpose, the specular point coordinates and the reflectivity observations are linked using the GPS Time provided by on-board sensors and the GPS time extracted from the digitized GNSS signals. We present in the next section, the airborne experimental setup used for data collection.

5.3 Airborne experimental setup

5.3.1 Airborne GNSS-R system: on-board sensors

A GNSS-R setup on-board a gyrocopter with reduced size and weight has been developed specifically for this work. This setup consists of a typical GNSS-R sensor that uses an RHCP antenna and an LHCP antenna to capture GNSS signals. The RHCP antenna is fixed on the nose of the gyrocopter in order to receive direct GNSS signals and the LHCP antenna is mounted on the bottom of the gyrocopter for proper reception of the GNSS signals after reflection. A drone board sensor is also used in order to record the gyrocopter attitude, altitude and position with respect to the GPS Time along the duration of the flight. Figure 5.3 illustrates a scheme of the GNSS-R setup on-board a gyrocopter.

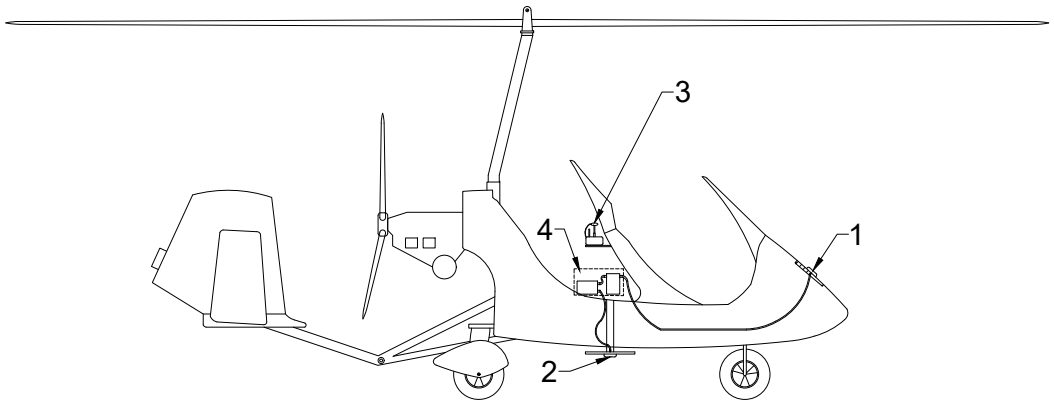

FIGURE 5.3: GNSS-R setup on-board a gyrocopter. (1) RHCP antenna, (2) LHCP antenna, (3) Drone Board Sensor and (4) Extra GNSS-R receiver hardware for data collection

Although the gyrocopter is a manned aircraft, it can fly at extremely low altitudes with relatively low speeds while being very agile. This is vital in our application which aims to maximize the spatial resolution of the airborne GNSS measurements. The size of the satellites footprints is indeed dependent on the height of the receiver. The gyrocopter can cover a distance

up to 500 *km* with 4 *hours* loft within a single flight. Flying at higher altitudes would increase the coverage area and the amount of data collected by the airborne GNSS-R system within the same flight duration, but that would come at the expense of the spatial resolution of the application. Nevertheless, there is always a trade-off between spatial resolution and global coverage. We show in Figure 5.4 the gyrocopter that was used for the flight experimentation with the different sensors embedded on it.

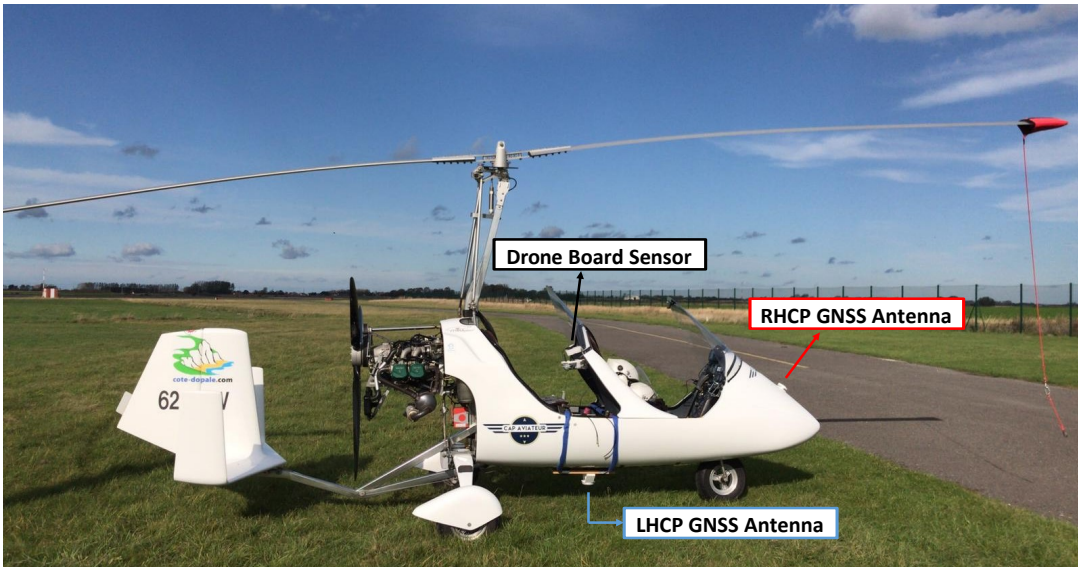

FIGURE 5.4: The gyrocopter that was used during the flight with the sensors embedded on it.

In addition to the on-board sensors, the gyrocopter is loaded with the necessary setup that constitute the GNSS-R receiver hardware for data collection (labeled (4) in Figure 5.3) along with the GNSS antennas. This hardware is introduced in the next section.

5.3.2 GNSS-R receiver hardware

5.3.2.1 Hardware architecture

Figure 5.5 presents a scheme of the GNSS-R receiver hardware. The GNSS antenna signals are amplified using a Low Noise Amplifier (LNA) because the signals are immersed in noise. A delay line is used to separate the RHCP antenna signals and the LHCP antenna signals in time so that both signals can be tracked independently using a single mono-channel bit grabber which is an important distinction of this work.

From Figure 5.5, the delay line constituting of a fiber optic coil delays the LHCP antenna signal before it is combined with the RHCP antenna signal. The composite signal (sum of direct and reflected GNSS signals) is then digitized using a mono-channel bit grabber. The digitized direct and reflected signal samples are stored in a storage device/card for signal processing using our self-built GNSS software receiver.

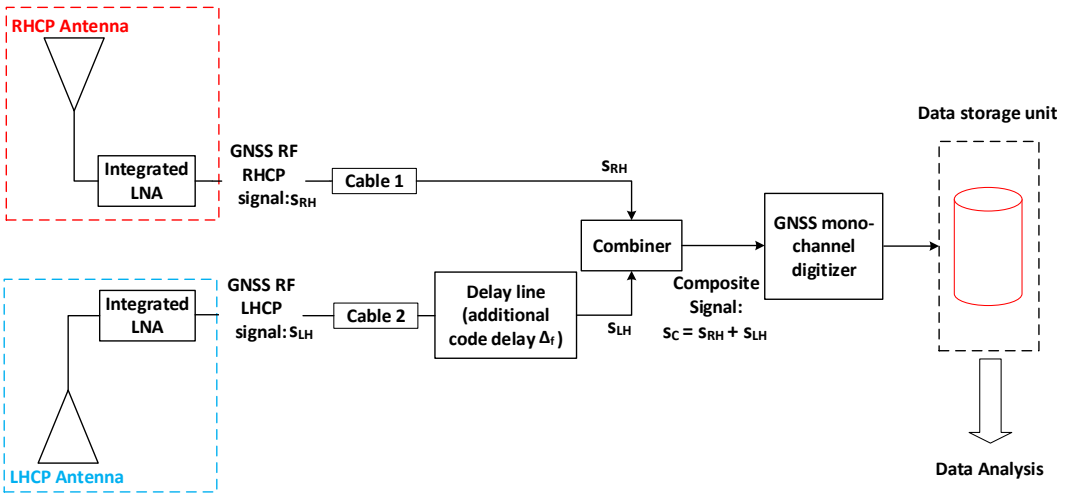

FIGURE 5.5: GNSS-R receiver architecture

The usage of the delay line along with the mono-channel bit grabber allows synchronous digitization of the GNSS signals from the two sensors. This front-end receiver configuration provides a more robust approach than classical GNSS-R multi-channel receiver setup which poses clock synchronization problems between the different bit grabbers used for the recording of the RHCP and LHCP antenna signals.

In addition, this front-end receiver has a sampling frequency up to 25 MHz and a bit quantization up to 2 bits. In our approach, a sampling frequency of 25 MHz and 1 bit quantization are used. The bit grabber records the digitized data in bytes format and thus its size will be considerably large depending on the duration of the flight.

The GNSS-R setup on-board the gyrocopter during the flight is composed of an L1-L5 bit grabber designed specifically for this work by a GNSS specialized firm called Syntony, a delay line, splitters/combiners, and power banks. The GNSS-R setup that is situated on-board the gyrocopter is presented in Figure 5.6.

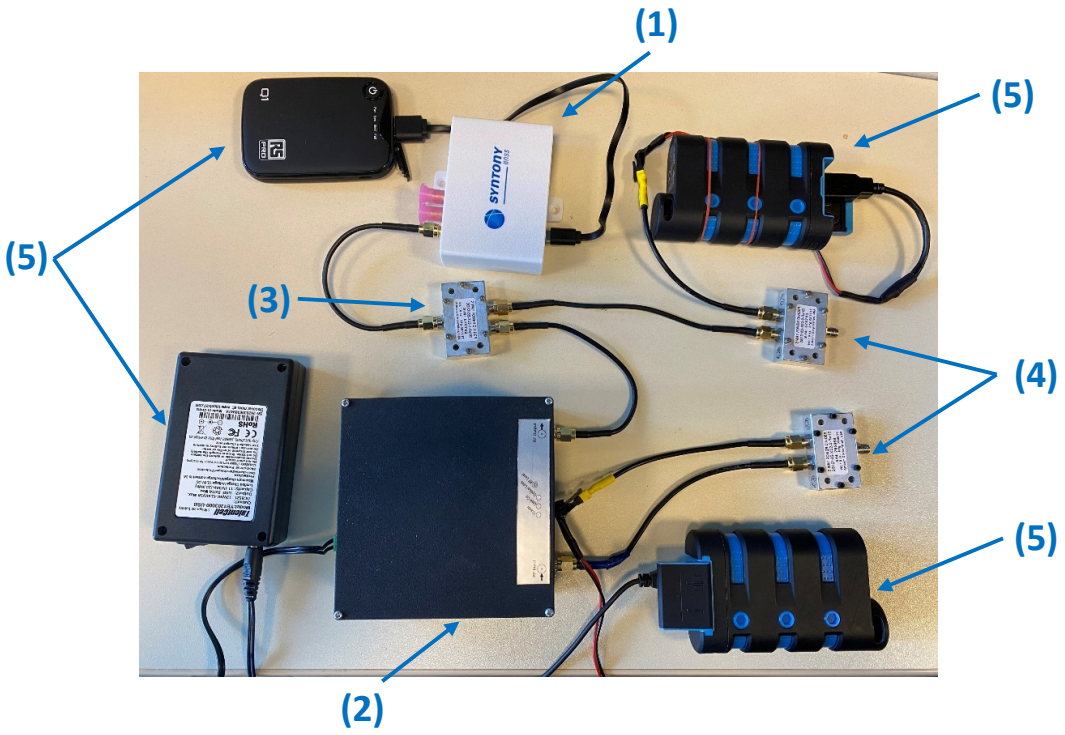

FIGURE 5.6: The GNSS-R setup on-board the gyrocopter during the flight experimentation. The setup consists of: (1) Syntony L1-L5 bit grabber, (2) delay line, (3) combiner, (4) splitters and (5) power banks.

5.3.2.2 Effect of the delay line

The delay line introduces an additional delay on the LHCP antenna signal denoted as Δ_f. This delay is known by the user and depends on the length of the coil. In this work, the length of the fiber optic coil used is $l_f = 1504\ m$ providing an additional delay of $\Delta_f = 5.01\ \mu s$ (taking into consideration that the signal travels through the fiber optic coil at the speed of light).

Figure 5.7 shows a Delay Doppler Map (DDM) of an RHCP antenna signal split into two: an undelayed reference and a delayed signal that was previously fed to the delay line. From this Figure, we notice that both signals are separated by $l_f = 1504\ m$. The introduced delay is sufficient enough for effectively separating the signals correlation peaks. However, we also notice from Figure 5.7 that the delay line amplifies the power of the delayed signal since higher power is associated to the delayed version. This effect can be calibrated and effectively removed since it does not change with time.

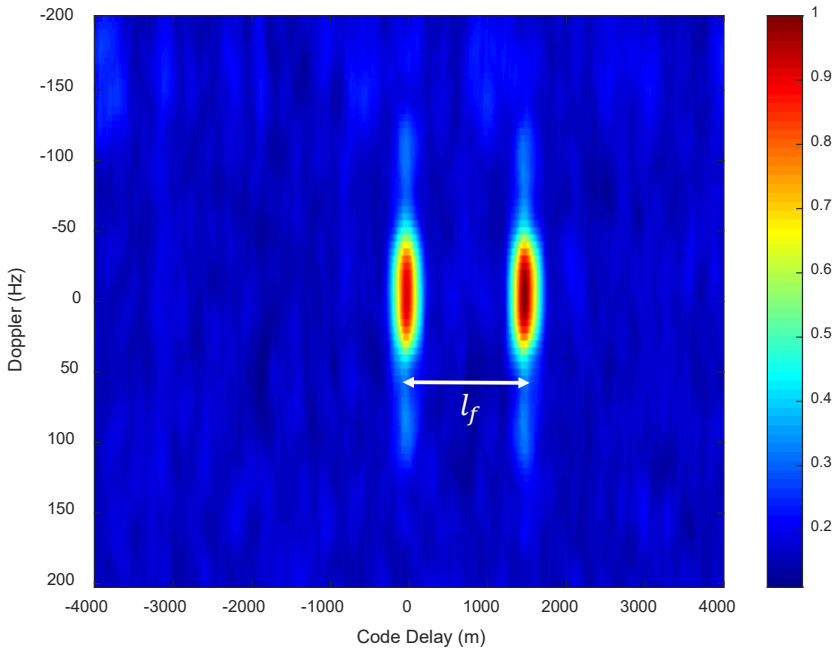

FIGURE 5.7: Effect of the delay line on an RHCP antenna signal split into an undelayed and a delayed version. In this DDM representation, both versions are separated in time associated to the additional delay of $\Delta_f = 5.01\ \mu s$

Tracking the LHCP antenna signals independently is generally impractical because such noisy signals are known for being very low in power, and thus the track of the signals can easily be lost. In our approach, both the RHCP and LHCP antenna signals of a satellite are realized at different code delays using a single-channel bit grabber. This provides a more practical signal processing approach for tracking the LHCP antenna signals which will be further described in the next section.

5.4 GNSS-R software receiver

5.4.1 Receiver architecture

Figure 5.8 depicts the master/slave signal processing front end architecture implemented in our own GNSS software receiver. The direct signal processing can be derived from the classical GNSS demultiplexing and demodulation processes. The stages of demodulation and demultiplexing are realized respectively with a Phase Lock Loop (PLL), a Delay Lock Loop (DLL) and a Frequency Lock Loop (FLL) providing the in-phase component I_v^d and quadrature component Q_v^d measurements for each satellite signal, the message of navigation, as well as the code delay $\hat{\tau}_v^d$, Doppler $\hat{f}_v^d$, and phase $\hat{\phi}_v^d$

estimates. The tracking process is realized with $T_c = 20\ ms$ of coherent integrations.

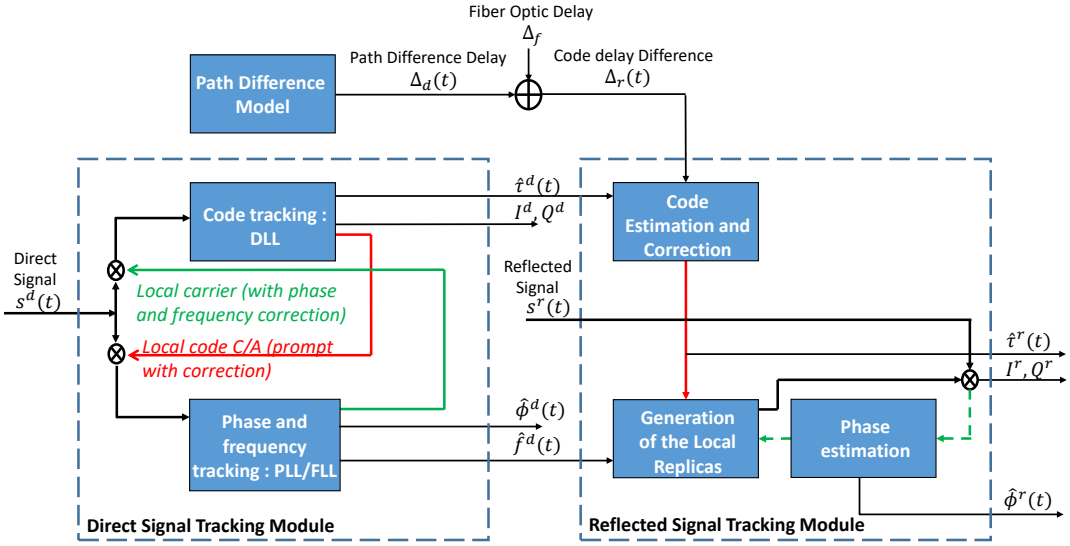

FIGURE 5.8: GNSS signal processing front end architecture.

In our application, it is indeed crucial to correct the Doppler frequency due to the dynamic displacement of the airborne GNSS receiver along the flight. Data message bit detection and synchronization are then applied using the corrected Doppler frequency and code delay estimates, in order to track the signals with 20 ms of coherent integrations without any loss in power due to the sign changes in the navigation message.

In the model aided tracking of the reflected signal, the DLL, PLL and FLL are not implemented to correct the code, phase and frequency delay estimates. The information regarding the code delay, and doppler frequency of the direct signal are used in the 20 ms coherent integrations tracking of the reflected signal. The estimated code delay of the reflected signal $\hat{\tau}^r(t)$ is derived from the code delay of the direct signal $\hat{\tau}^d(t)$ and the additional delay $\Delta_r(t)$ due to the path difference model ($\Delta_d(t) = (2\ h(t)\ sin\theta(t))/c$) and the effect of the delay line ($\Delta_f = 5.01\ \mu s$).

Data synchronization is applied in order to synchronize the path difference variations due to the displacement of the airborne GNSS-R receiver with the estimated code delay of the direct signal $\hat{\tau}^d(t)$. In our implementation, both the direct and reflected signals are realized with the same Doppler shift using a single mono-channel bit grabber, and therefore, $\hat{f}_v^d(t) = \hat{f}_v^r(t)$. The

phase of the reflected signal $\hat{\phi}^r(t)$ is only estimated in an open loop and is not corrected.

Finally, 20 *ms* observations of the direct and reflected in-phase and quadrature components of the signals are obtained. We show in the chapter 3 (expression (3.38)), that I_d^r and I_v^r are indeed observations of the amplitudes $A_l^d(t)$ and $A_l^r(t)$ of the direct and reflected GNSS signals, respectively. Thus 20 *ms* rate measurements of $A_l^d(t)$ and $A_l^r(t)$ are obtained for the derivation of the surface reflectivity.

5.4.2 GNSS data

A large amount of raw GNSS data was collected during the flight ($\sim$ 45 *min*). The bit grabber and antennas used in the experimentation are able to acquire and record L1 and L5 signals. The data constitutes the sampled direct and reflected GNSS signals that were digitized and stored by the Syntony L1-L5 bit grabber. Table 5.1 shows a summary of the type of data collected and its size after decompressing.

TABLE 5.1: Data collected during the flight.

Description	Size
L1-sig.bin	133.78 GB
L5-sig.bin	133.78 GB
Total	**267.56 GB**

We use the binary information provided by "L1-sig.bin" to process the GPS C/A signals. We process the direct and reflected GNSS signals of the GPS satellites in study for the whole flight excluding take-off and landing. The tracking of both the direct and reflected GNSS signals is realized with 20 *ms* of coherent integrations. We apply the master/slave configuration described in the previous section for the processing of the reflected GNSS signals. The data processing was implemented using MATLAB on a workstation with core i5-6600 processor and 16 GB of RAM. The execution time was estimated at approximately 2 days.

5.5 Flight Experimentation

5.5.1 Flight information

The flight took place in the North of France and started at 14h45 UTC, the 19th of October 2020 and ended at 15h30 of the same day lasting for 45 min. The gyrocopter took-off from Calais–Dunkerque Airport located in Marck, 7 km east-northeast of Calais, in the Hauts-de-France region. We scanned a large zone that borders the English Channel over a trajectory of $\sim$ 71 *km* between Calais, Escalles and Ardres. This trajectory is shown in Figure 5.9.

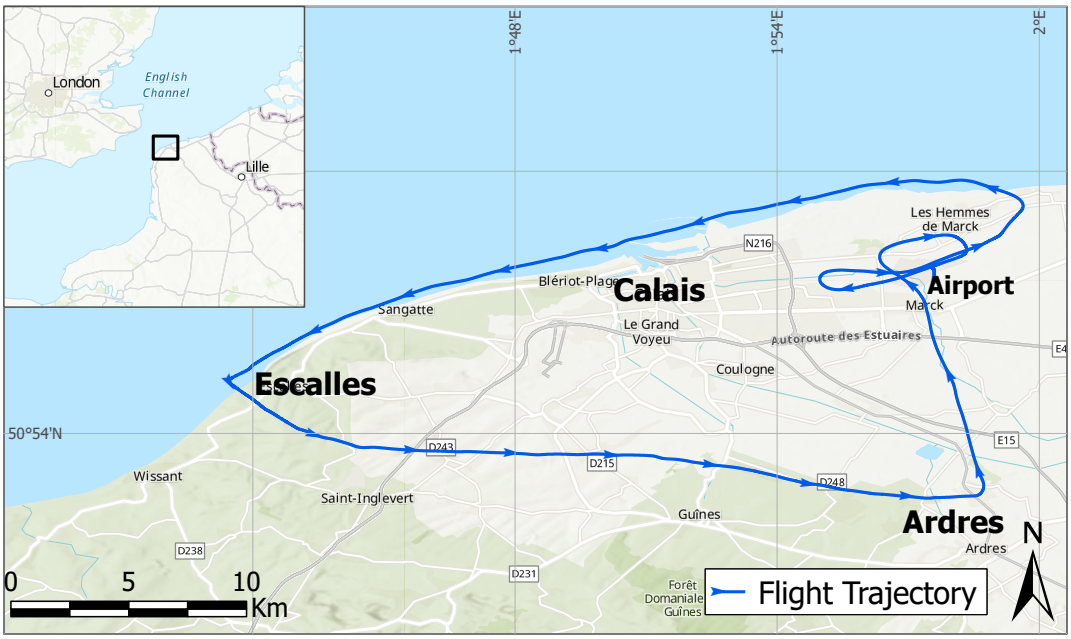

FIGURE 5.9: Flight trajectory.

The airborne GNSS-R platform flew along the coastline scanning areas from the sea and sandy beach before crossing south-west in order to scan water bodies contained in landforms. This study area was selected for experimentation because it contains a number of different landforms over a relatively small surface area especially that between Guînes and Ardres. This specific region holds over 50 different water body surfaces (such as lakes, ponds, rivers, swamps, etc...) with different nature and sizes. In addition, there are some other interesting landforms such as plain land, groves and forests that the flight will pass over. Such dynamic environment poses a major challenge to the accuracy and capacity of our approach to detect and localize surfaces with high spatial and temporal resolution.

During the flight, the gyrocopter maintained a low-altitude of approximately 315 m above the ground with an average speed of 95 km/h. The wind speed was approximately at 25 km/h. Table 5.2 presents an overview of the flight information.

TABLE 5.2: Flight Information

	Description
Date	19/10/2020
Location	North of France
Fight Duration	45 min
Distance Covered	71 km
Average Speed	95 km/h
Average Height	315 m
Wind Speed	25 km/h
Wind Direction	North

5.5.2 Flight trajectory

Figure 5.10 depicts the traces of the satellites footprints along the flight trajectory imposed on Google Earth software. The major axis size of the first Fresnel zone that constitute the detected footprints ranges between 1306 m for a minimum elevation angle of 3° and 16 m for a maximum elevation angle of 75°. The traces of very low elevation satellites are not shown in Figure 5.10.

In our application, we aim to study reflections from satellites with high elevation angles in order to maximize the spatial resolution of our application. In addition, higher elevation satellite signals are associated with better gain with respect to the LHCP antenna. In this regard, we fix the maximum size of the major axis to 23 m, so the minimum satellite elevation to 50 ^{o}. An average of 9 GPS satellites have been detected along the trajectory. 3 GPS satellite signals of elevation angles superior to 50 ^{o} were extensively analyzed to observe the reflectivity of the different areas of reflections. These signals corresponds to satellite PRNs 5, 7 and 30.

FIGURE 5.10: The satellite footprint traces along the flight trajectory imposed on Google Earth software. The traces of very low elevation satellites are not shown in the figure.

We show in Figure 5.11a the value of the Fresnel ellipse major axis, $(2\ a)$, as a function of the satellite elevation. In this figure, the height is fixed to $h = 315\ m$ and the wavelength is $\lambda = 19.042\ cm$ for GPS C/A signals. We show in Figure 5.11b the major axis of the footprints corresponding to satellites PRNs 5, 7 and 30 as a function of the satellite elevation along the receiver trajectory. From Figure 5.11b, we notice that the footprints of the 3 GPS satellites in study satisfy the condition set for the maximum size of the major axis and for the minimum satellite elevation along the whole flight trajectory.

Concerning the temporal resolution of the application, the raw data was sampled at a frequency of 25 MHz and the GNSS measurements are realized at a rate of 50 Hz. Taking into consideration the average speed of the gyrocopter (95 km/h), the distance between two consecutive specular points is approximately 0.5 m. This means that every 20 ms the footprints are displaced by 0.5 m.

We apply the GNSS signal segmentation in the next section for water body surface detection and edge localization.

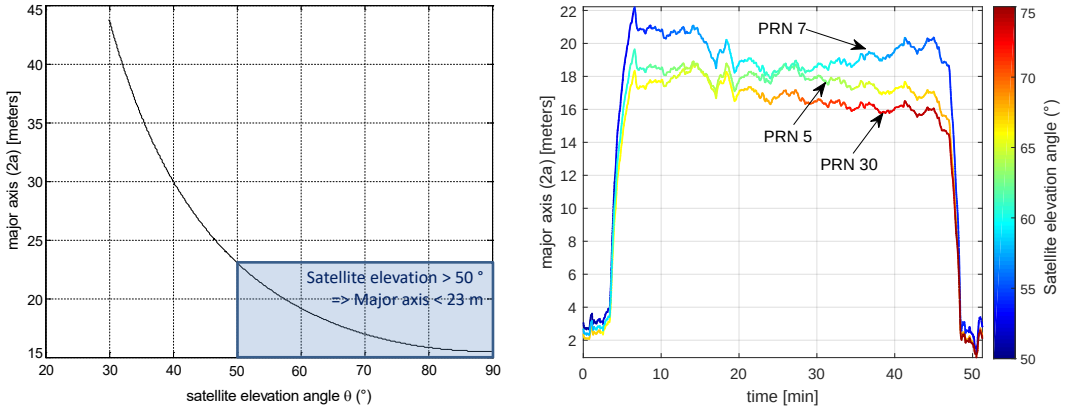

(a) (b)

FIGURE 5.11: Effect of the satellite elevation angle and the dynamic displacement of the receiver on the size of the footprint. In (a) we show the footprint major axis size as a function of the satellite elevation angle. In (b) we show the major axis of the footprints corresponding to satellites PRNs 5, 7 and 30 as a function of the satellite elevation along the flight duration.

5.6 Data analysis

5.6.1 Radar signal segmentation

Figure 5.12 presents the GNSS measurements for an area located at (50.888515° N, 1.871803° E) along the trajectory. On the upper figure, the traces of the satellites footprints are represented by 20 *ms* rate localization of the specular points of reflection. The colors of the points represent different reflectivity measurements associated with different kinds of reflecting surfaces. We observe that satellite PRN 7 detects a swamp, whereas satellite PRN 5 detects a wetland and a lake that is also detected by satellite PRN 30. The number in brackets notes the satellite elevation angle. On the lower figures, we show the GNSS reflectivity measurements and the automatic signal segmentation associated to it using our proposed radar technique over 12 *seconds* of data from this area. The graphs shown in Figure 5.12 are obtained after applying the merging algorithm on the segmented signal.

We can notice from the graphs that a difference in the mean of the measurements separates different areas of reflection. We remark a significant increase in reflectivity corresponding to water body surfaces. We note an increase of at least 0.13 in the reflectivity measurements for the satellites between land and water. This increase is not constant though and is dependent

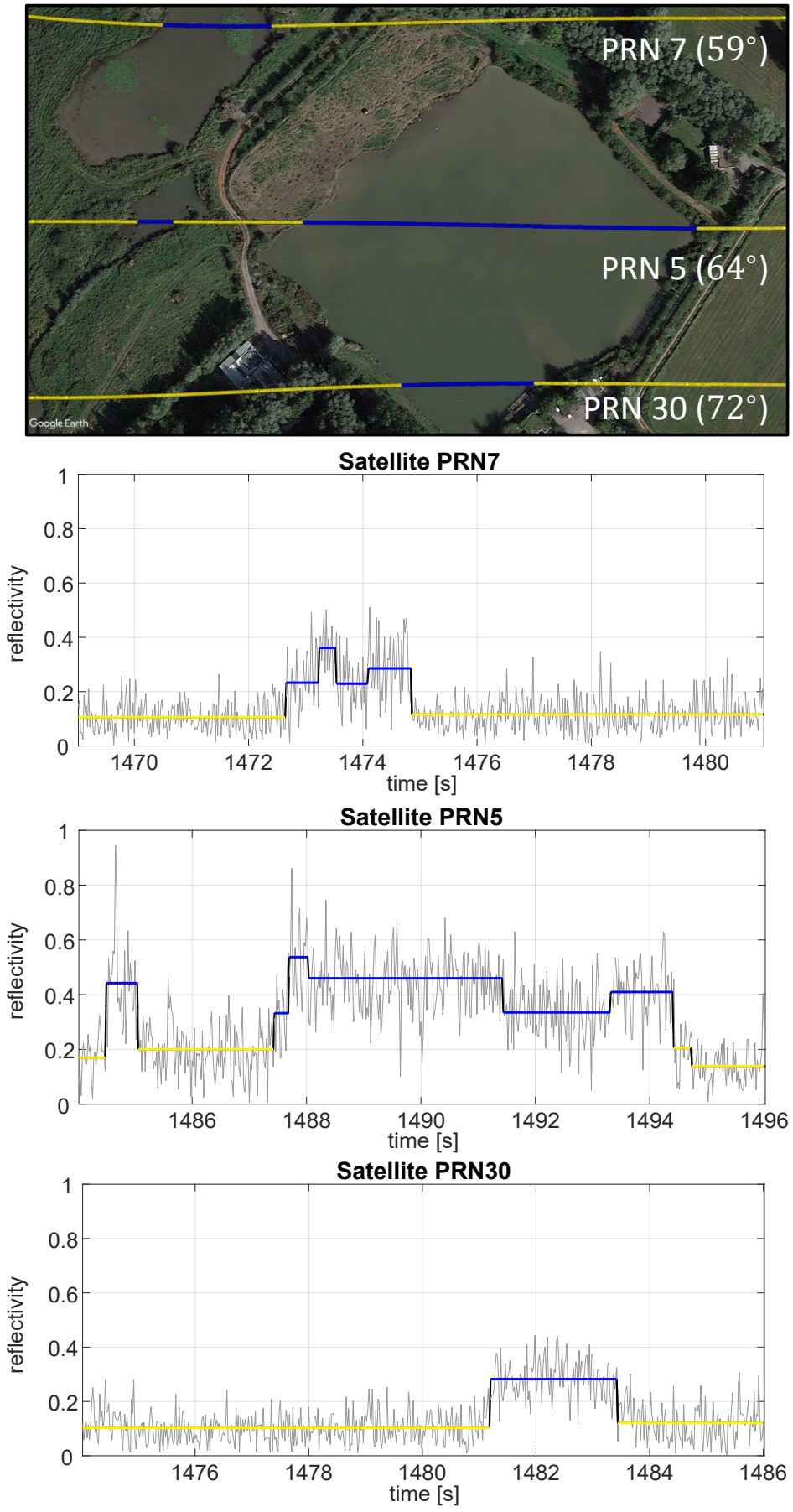

FIGURE 5.12: Automatic segmentation of the GNSS measurements by the proposed radar technique for an area located at (50.888515°, 1.871803°) along the trajectory.

on the type of land and water that the signals are reflecting from. For example, lower variations between land and water are observed in satellite PRN 5 as compared to satellite PRN 30 since the land reflections in satellite PRN 30 are partly affected by vegetation. The proposed radar technique detects different water bodies corresponding to different mean reflectivity levels shown in blue segments on the graphs whenever the reflectivity measurements are beyond a specified threshold (0.21 in this case). These segments are associated with a blue coloring of the specular points on the Google Earth image. The yellow coloring of the specular points is associated to land reflections. This demonstrates the automatic segmentation process by the proposed radar technique for the detection of water body surfaces using high rate reflectivity measurements.

We show in Figure 5.13 different types of water bodies detected along the traces of the satellites footprints. We observe that the radar technique detects in-land water bodies with various sizes and shapes and under different environments. It is worth noting that the approximate size is not the same for all the surfaces of the same water body type. We notice that we detect large-size contained water body surfaces such as lakes (Figure 5.13a), oxbow-lake (Figure 5.13b) and big swamps (Figure 5.13c). The oxbow-lake detected has a total approximate size of $480m \times 135m$ (including the land in the middle of the lake) along the trajectory. We also differentiate smaller contained water body surfaces such as ponds (Figure 5.13d) and wetlands (Figure 5.13g).

In our study, we differentiate lakes from ponds based on the size of the water body surface. We differentiate swamps from lakes and ponds based on the characteristics of the water body and the surrounding environment. Swamps are characterized by plant life dominated by trees and might be a mix of very wet land and water. However, this is not always explicit by manual inspection using Google Earth map imagery data.

Rivers of different widths along the trajectory are detected by the traces of all 3 satellites due to its length. The river shown in Figure 5.13e has a width of 21 m. We notice in Figure 5.13f, 2 small streams of 3.6 m and 5.76 m m width, while we notice in Figure 5.13h that the proposed radar technique was able to detect a small pool of $4.5m \times 9m$ size along the trace of satellite PRN 5 footprints. This shows the sensitivity of the proposed radar technique to changes in landforms and shows the importance of high spatio-temporal

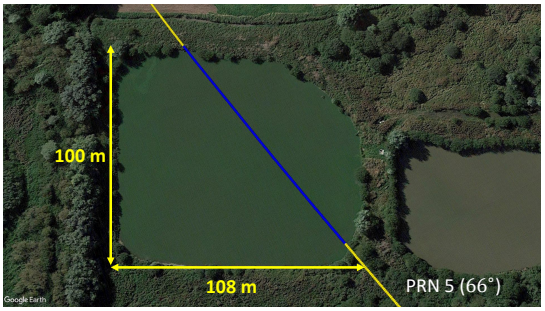

(a) Lake
(50.882083°N, 1.976546°E)

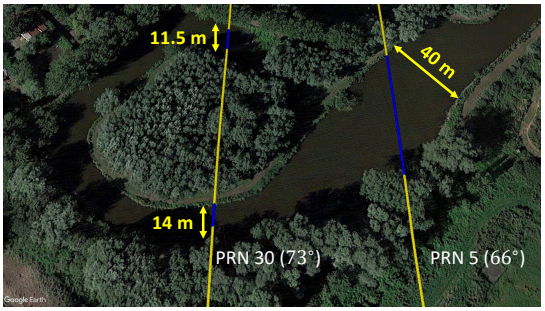

(b) Oxbow Lake
(50.875641°N, 1.946331°E)

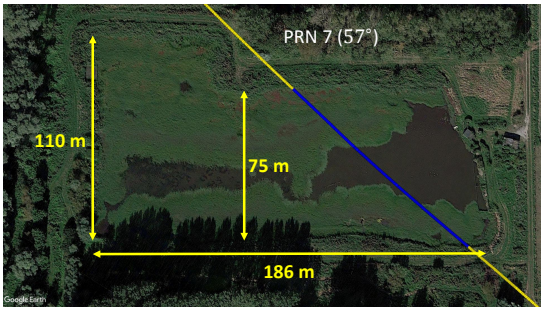

(c) Swamp
(50.876854°N, 1.948390°E)

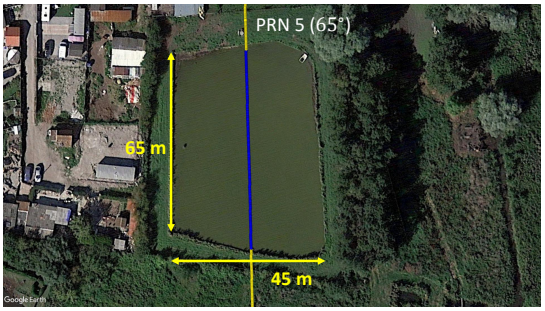

(d) Pond
(50.879548°N, 1.919523°E)

(e) River
(50.887720°N, 1.878526°E)

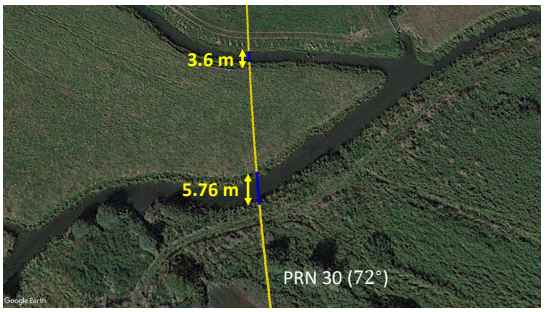

(f) Streams
(50.888385°N, 1.868127°E)

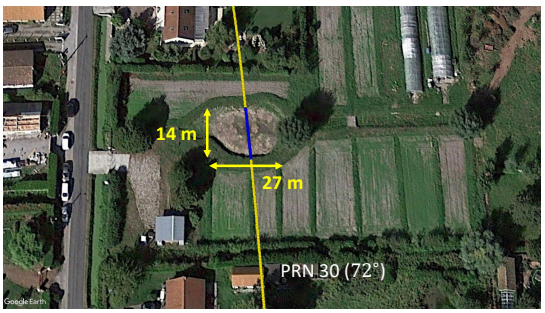

(g) Wetland
(50.883070°N, 1.900203°E)

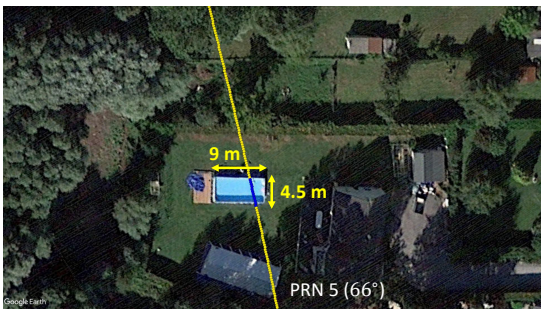

(h) Pool
(50.886888°N, 1.884547°E)

FIGURE 5.13: Detection of water body surfaces in landforms using the proposed automatic radar technique.

resolution in the detection of in-land water body surfaces using low-altitude airborne carrier.

5.6.2 Water body surface detection

The proposed radar technique is first applied for detecting water body surfaces in landforms. We represent the specular points of reflection corresponding to the detected water body surfaces by our radar technique for the 3 satellites in study on IGN maps using QGIS software. IGN maps provide up-to-date map schemes that clearly show the actual locations of the water body surfaces at the day of the experimentation. The aim is to assess the performance of the proposed method for water body surface detection. Figure 5.14 shows the detected water body surfaces using our proposed method for the area between Guînes and Ardres represented by a blue coloring of the specular points of reflection.

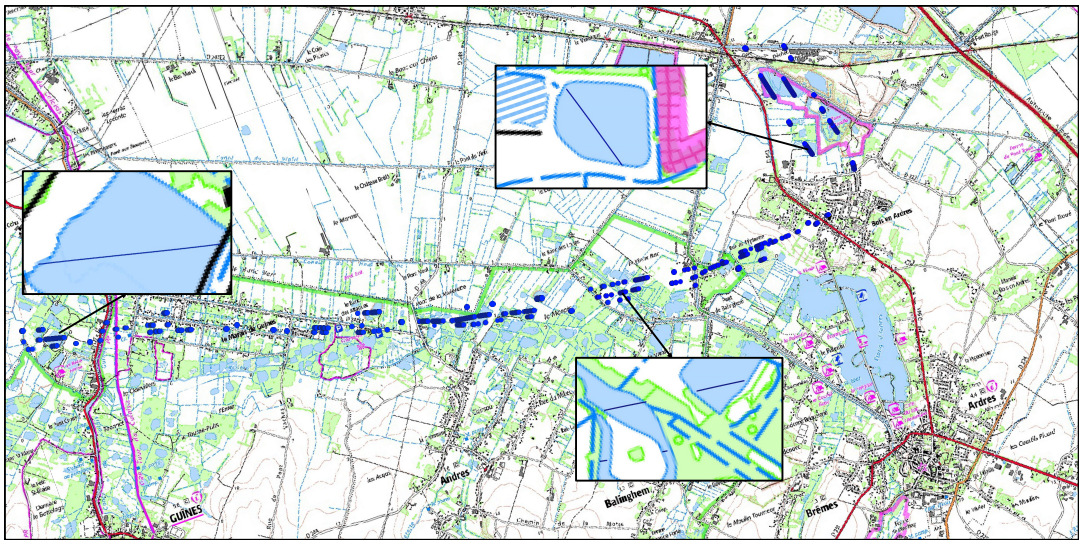

FIGURE 5.14: The detected water body surfaces using our proposed radar technique for the area between Guînes and Ardres. The specular points of reflection, represented by a blue coloring, are superimposed on IGN maps.

The proposed method detects water body surfaces whenever the reflectivity measurements are beyond a specified threshold. From the analysis of the GNSS measurements obtained, the reflectivity threshold used in this study is 0.21 for the 3 satellites. We compare the number of water body surfaces provided by IGN maps along the satellite footprints traces with the percentage of detections of these water bodies using our proposed approach. Table 5.3 details the results of the manual inspection applied between the IGN images

and our radar technique for water body surface detection.

TABLE 5.3: Performance assessment of the proposed radar technique for water body surface detection. Results of the manual inspection applied between the IGN images and our radar technique.

Water body	Number of surfaces using IGN maps	Percentage of detection using our radar technique
Lakes/ Large Swamps	20	100 %
Ponds/Swamps/Wetlands	17	94 %
Rivers/Canals	4	100 %
Streams/Brooks	6	83 %
Total	**47**	**96 %**

We show in Table 5.3 that our radar technique detects 96% of in-land water body surfaces (i.e. 45 out of 47 surfaces) along the satellites footprint traces as compared to the details provided by IGN maps. We detect 100% of large-size contained water body surfaces (i.e. Lakes/Large swamps) and of large waterways (such as rivers and canals). However, we miss 1 small-size contained water body surface and 1 stream along the trajectory. We can not clearly observe the reason using maps such as IGN or Google Earth as it is not evident whether the miss is due to a detection inaccuracy or due to the water bodies being masked by vegetation (such as trees or groves).

Although IGN provides updated map imageries, we can observe from Figure 5.14 that these maps don't provide sufficient information about the water body characteristics (e.g. type, shape and approximate size) nor the vegetation possibly covering it. Thus we propose to use satellite images provided by Google Earth software for water body edge localization.

5.6.3 Water body edge localization

The proposed radar technique is applied for localizing the edges of the detected water body surfaces along the satellites footprints traces. In our study, we represent the satellites traces by a localization of the specular points of reflection. In practice, Google Earth doesn't provide up-to-date map images. In this regard, the Google Earth images and the experimentation were obtained

with one year of difference (Google Earth dates its imagery data to September 2019). That is why we first analyze the locations of the water body surfaces that are used in this study using IGN, and then use Google Earth software for the detailed experimentation. We select in our study the water body surfaces that can be clearly observed using both IGN maps and Google Earth. Fortunately, the characteristics of the study area didn't change much over the coarse of 1 year, especially that the Google Earth images are obtained within the same period of the year as that of the experimentation. Therefore, we can assume that the water level was the same between the 2 dates.

We assess the accuracy of the proposed automatic edge localization technique using manual edge localization on Google Earth. This means that the accuracy of our approach for edge localization will be affected by any inaccuracies that Google Earth encounters while processing its map imagery. We report in Figure 5.15, the detected edges of different water bodies by the proposed radar technique and the edges obtained manually using Google Earth images.

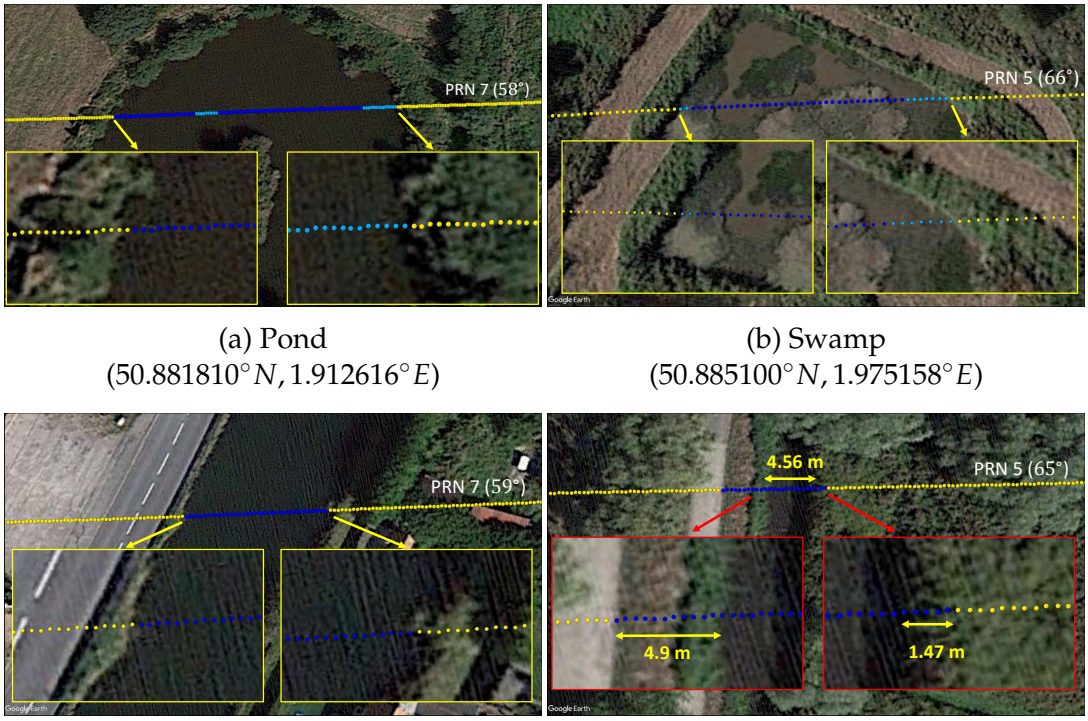

(a) Pond
(50.881810°N, 1.912616°E)

(b) Swamp
(50.885100°N, 1.975158°E)

(c) River
(50.887720°N, 1.878526°E)

(d) Stream
(50.887528°N, 1.880161°E)

FIGURE 5.15: Examples of manual and automatic edge localization of different water body surfaces along the traces of the satellites footprints.

At the edges of the water body surfaces, the satellite footprint covers the border between land and water. We note in Figure 5.15, the introduction of a light blue color for the specular points of reflection. This color is mostly associated to the decreased reflectivity at the border between land and water, and is defined using a decreased threshold that is set for each satellite based on the analysis of the reflectivity measurements associated to the edges of the water body surfaces in particular.

We show an agreement between the manual and automatic edge localization for the pond, swamp, and river shown in Figures 5.15a, 5.15b, and 5.15c, respectively. However, we report in Figure 5.15d a difference in edge localization between the automatic and manual techniques for a stream. In this example, the proposed radar technique detects the stream before its actual location in Google Earth by $+4.9m$ and localize the end of the water body surface after its manual border end by $+1.47m$ resulting in a total offset of $+6.37m$ between the two detections.

We report in Table 5.4 the parameters of the detected water body surfaces by satellite PRN 5 for 100 *sec* of an area along the trajectory. The detected water body surfaces by satellite PRN 5 trace in this area include the wetland, lake, river and stream shown in Figures 5.12, 5.13e, and 5.15d, respectively.

TABLE 5.4: Parameters of the detected water body surfaces by satellite PRN 5 trace between t=15h19m01s and t=15h20m41s.

Water body	Wetland	Lake	River	Stream
Approximate size (m)	40×48	125×141	$W = 22$	$W = 4.56$
Localization diff - Start (m)	$+3.45$	0	$+0.82$	$+4.9$
Localization diff - End (m)	0	0	0	$+1.47$
Distance error- Total (m)	3.45	0	0.82	6.37
Automatic detection length (m)	52.21	171.3	24.57	10.93
Manual detection length (m)	48.76	171.3	23.75	4.56

We report the approximate size (in meters) for each of the mentioned surfaces. We also report the difference in localization between the automatic and manual approach (in meters) for the starting and ending edges of the detected water body surfaces. These values can be positive or negative. In

addition, we record the total localization distance error (in meters), i.e. the total absolute offset for the start and end edges of each water body as well as the automatic and manual detection length (in meters), i.e. the length covered by the satellite footprints trace along the water body surface using the proposed radar technique and Google Earth, respectively.

We observe in Table 5.4, accurate edge localization (i.e. perfect agreement) for the lake by the proposed radar technique as compared to Google Earth. The localization of the river edges are less accurate especially for the start of the river but clearly better than that of wetland and stream. In this regard, edge localization requires precise measurements. The localization accuracy is affected by the characteristics of the water body surface (type, shape, size, etc...) as well as the nature of the landforms surrounding the water body at its edges. We can clearly observe that the stream reported in Table 5.4 and depicted in Figure 5.15d is small in size (4.56 m width), muddy, and surrounded by vegetation. It is worth noting that this stream reported the lowest localization accuracy among all the water body surfaces localized along the traces of the 3 satellites footprints during the whole trajectory. Other streams such as those shown in Figure 5.13f are accurately localized.

We apply the aforementioned parameter analysis for the detected water body surfaces by the traces of the 3 satellites footprints along the whole trajectory. We report in Table 5.5 the number of detections of each water body type as well as the percentage of accurate edge localizations. We also record the mean distance localization error (in meters) which is the absolute value of the offset in meters between the manual and the automatic edge localization. Finally, we record the localization difference standard deviation (in meters) which represents the standard deviation of the difference in the starting and ending edges.

In this study an accurate edge localization is recorded whenever a perfect agreement between the manual and automatic approaches is achieved (i.e. whenever the total localization distance error is 0). We can observe in the second column of Table 5.5, the percentage of accurate edge localizations. We can also observe on the histogram of Figure 5.16, a comparison of the number of accurate and inaccurate localization with respect to the total number of water body edge localizations per type. We notice that swamps had the highest localization accuracy with 86.70% (26 perfect localizations out of

TABLE 5.5: Assessment of the accuracy of proposed radar technique for water body edge localization. Statistical analysis of the difference between the automatic and manual edge localization for the detected water body surfaces by the traces of the 3 satellites footprints along the whole trajectory.

Water body	Number of detections	Percentage of accurate edge localizations	Mean distance localization error (in meters)	Localization difference - std (in meters)
Lakes	12	79.20%	0.59	0.69
Oxbow Lakes	4	62.50%	1.86	1.47
Ponds	11	72.70%	0.68	0.73
Pools	1	50.00%	0.82	0.41
Rivers/Canals	12	79.20%	0.63	0.93
Streams/Brooks	6	58.30%	1.75	1.38
Swamps	15	86.70%	0.36	0.50
Wetlands	4	75.00%	0.99	1.12
Total	**65**	**76.2%**	**0.96**	**0.9**

30) followed by lakes and rivers with an accuracy of 79.2% for each with the same number of detections. The pool had the lowest edge localization accuracy with 50% but from just 2 measurements. Apart from the only pool detected by the trace of satellite PRN 5, streams/brooks noted the second lowest edge localization accuracy with 58.3% from 12 localizations, followed by oxbow lake.

We can also note from Table 5.5, that swamps had the least mean localization error of 0.36 m and the lowest localization difference standard deviation of 0.5 m (after the pool). Although lakes and rivers have the same percentage of accurate edge localizations, we notice that the lakes had lower mean distance localization error and localization difference standard deviation, implying better overall localization accuracy for lakes. Wetlands achieved slightly better percentage of accurate localizations than ponds, but ponds recorded better mean distance localization error and localization difference standard deviation and with a higher number of detections. The oxbow lake and streams reported the highest statistical errors in terms of the recorded mean and std. We notice that the only oxbow lake detected along the trajectory in Figure 5.13b was surrounded by vegetation on its borders. In addition,

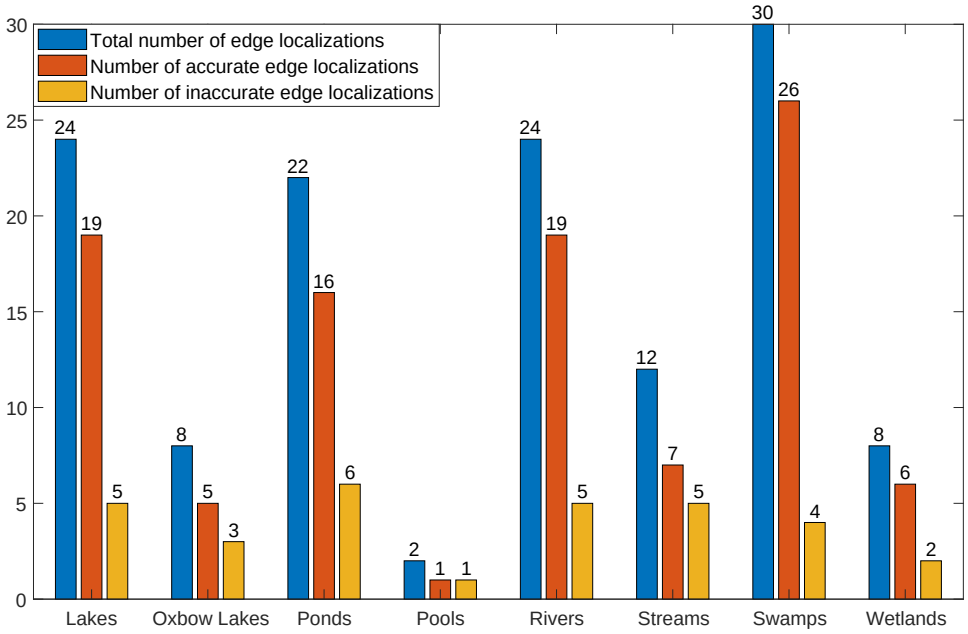

FIGURE 5.16: Statistics of water body edge localization by the proposed radar technique per water body type.

as previously discussed, the streams along the trajectory are mostly muddy and covered by trees. The results are in agreement with those derived in Table 5.4, but applied for the whole study area and for the 3 satellites. We can observe that the edge localization is affected by the type of the water body surface as well as the characteristics of the landforms surrounding the water body at its edges (vegetation biomass, roughness, etc...).

In total, the proposed radar technique achieved an overall water body edge localization accuracy of 76.2% with a mean distance localization error of 0.96 m and localization difference standard deviation of 0.9 m. From this study, we conclude that we can achieve the metric accuracy with our automatic approach as compared to manual localization using Google Earth taking into consideration the spatial resolution of our GNSS-R application and the approximate distance between 2 consecutive specular points ($\sim$ 0.5 m) for a gyrocopter average speed of $\sim$ 95 km/h.

5.6.4 Detection of landforms

5.6.4.1 Differentiation of water body surfaces

We record in Table 5.6 the mean and the mean standard deviation of the reflectivity levels defined in the segments of the signals associated with the different waterbody types for the three satellites in study. We can observe

that these satellites have different average elevation (θ) and azimuth (α) angles along the flight duration.

For each satellite in Table 5.6, we observe that streams/brooks reported the lowest mean reflectivity which is expected due to its size and texture. Wetlands, which are small wet areas on landforms, also recorded low mean reflectivity measurements. Rivers, on the other hand, show higher mean reflectivity levels than streams and wetlands for the three satellites, but still lower than lakes, ponds and swamps. We notice that the only detected pool by satellite PRN 5 reports a high mean reflectivity level although it is small in size. This is due to the fact that the bottom of the pool is mostly flat and might contain highly reflective materials such as steel and glass.

The parts of the oxbow lake detected by satellites PRN 7 and 30 also recorded very low mean reflectivity that is similar to streams or small rivers in each case as compared to that of satellite PRN 5. This difference is due to the trace followed by each of the satellites on the oxbow lake. We notice that the detection length of satellite PRN 5 was $\sim$ 53.5 m which is much larger than that covered by satellite PRN 7 ($\sim$ 17 m) and satellite PRN 30 which detects the oxbow lake 2 times with lengths of $\sim$ 11.57 m and $\sim$ 14.2 m. We notice that the covered length by satellite PRN 5 is nearly the size of a pond or small lake which explains the similarity in the mean reflectivity of oxbow lake 0.37 as compared to lakes (0.35) and ponds (0.30).

Apart from the detected pool by satellite PRN 5, the reflectivity increases with the increase in the size of the detected area in a water body as can be seen from the reflectivity corresponding to lakes, ponds and swamps which recorded the highest mean reflectivity levels as compared to smaller water body surfaces. The increase in reflectivity is associated to the increase in the detection length of a water body surface. As the size of the detected area increases, more measurements are obtained solely from the water body surface which are not affected by the roughness of the surfaces surrounding the water body. As the detection length decreases, the reflections are obtained more from the borders of the water body which decreases the reflectivity especially if the water body is surrounded by vegetation.

The reflectivity is also affected by the characteristics of the water body surface which explains the difference in the reflectivity between lakes, ponds

TABLE 5.6: Statistics of reflectivity in the different segments of the signal associated with the different waterbody types for the three satellites in study.

Satellite PRN 5 ($\theta = 65°$, $\alpha = 280°$)			
Water body	Number of detections	Mean reflectivity	Mean reflectivity std
Lakes	6	0.35	0.10
Oxbow Lakes	1	0.37	0.12
Ponds	6	0.32	0.10
Pools	1	0.30	0.11
Rivers/Canals	4	0.28	0.08
Streams/Brooks	2	0.24	0.09
Swamps	6	0.29	0.08
Wetlands	1	0.27	0.11
Total	**27**	**0.30**	**0.10**

Satellite PRN 7 ($\theta = 57°$, $\alpha = 70°$)			
Water body	Number of detections	Mean reflectivity	Mean reflectivity std
Lakes	2	0.28	0.10
Oxbow Lakes	1	0.20	0.10
Ponds	3	0.27	0.10
Pool	0	NA	NA
Rivers/Canals	4	0.23	0.09
Streams/Brooks	2	0.19	0.06
Swamps	5	0.26	0.09
Wetlands	0	NA	NA
Total	**17**	**0.24**	**0.09**

Satellite PRN 30 ($\theta = 73°$, $\alpha = 145°$)			
Water body	Number of detections	Mean reflectivity	Mean reflectivity std
Lakes	4	0.27	0.08
Oxbow Lakes	2	0.24	0.09
Ponds	2	0.30	0.10
Pool	0	NA	NA
Rivers/Canals	4	0.27	0.09
Streams/Brooks	2	0.21	0.06
Swamps	4	0.29	0.09
Wetlands	3	0.25	0.10
Total	**21**	**0.26**	**0.09**

and swamps for the three satellites in study. In this regard, we observe that lakes had the highest overall mean reflectivity measurements for the three satellites followed by ponds then swamps.

On the other hand, we observe that each of the satellites record different mean reflectivity for the same surface with satellite PRN 5 recording the highest overall reflectivity followed by satellite PRN 30 then satellite PRN 7. Several factors can contribute to this difference. As previously discussed, the traces followed by the 3 satellites are not the same, and thus the reflectivity measurements vary depending on the reflecting surface characteristics and the detection length by the satellites. The differences in azimuth angles can also contribute to this. The azimuth angle of PRN 5 satellite with respect to the tilt in the RHCP antenna implies that the trace of satellite PRN 5 footprints was generally on the back of the RHCP antenna during the measurements which decreases the amplitude of the direct signal and increases its reflectivity observations, in contrast to that of satellite PRN 7.

5.6.4.2 Differentiation of other surfaces

In this section, we show that the proposed radar technique has the capacity to detect other surfaces in landforms such as: sea, sandy beach, groves and land. Satellite PRN 30 has the highest elevation angle, and thus the lowest footprint size. We can assume that satellite PRN 30 is the most sensitive to changes in landforms and thus the traces of this satellite will be used in this section for surface differentiation. We show in Figure 5.17 the detected surfaces corresponding to groves, sandy beach and sea by the proposed radar technique along the trace of satellite PRN 30 footprints.

The color of the specular points is proportional to the reflectivity measurements associated to different surfaces of reflection. From the analysis of Table 5.6, the mean reflectivity (Γ) of in-land water body surfaces detected by satellite PRN 30 ranged between 0.21 and 0.3. This reflectivity level is denoted by a blue coloring of the specular point of reflection. The light blue color that was introduced in the previous section with an intermediate threshold for water body edge localization represents areas with mean reflectivity between 0.18 and 0.21 for satellite PRN 30. We note in Figure 5.17, the introduction of 2 new colors associated to different reflectivity levels of the surfaces. The dark blue color represents areas with reflectivity that is beyond 0.3 ($\Gamma > 0.3$). The red coloring of the specular point of reflection is associated to areas with

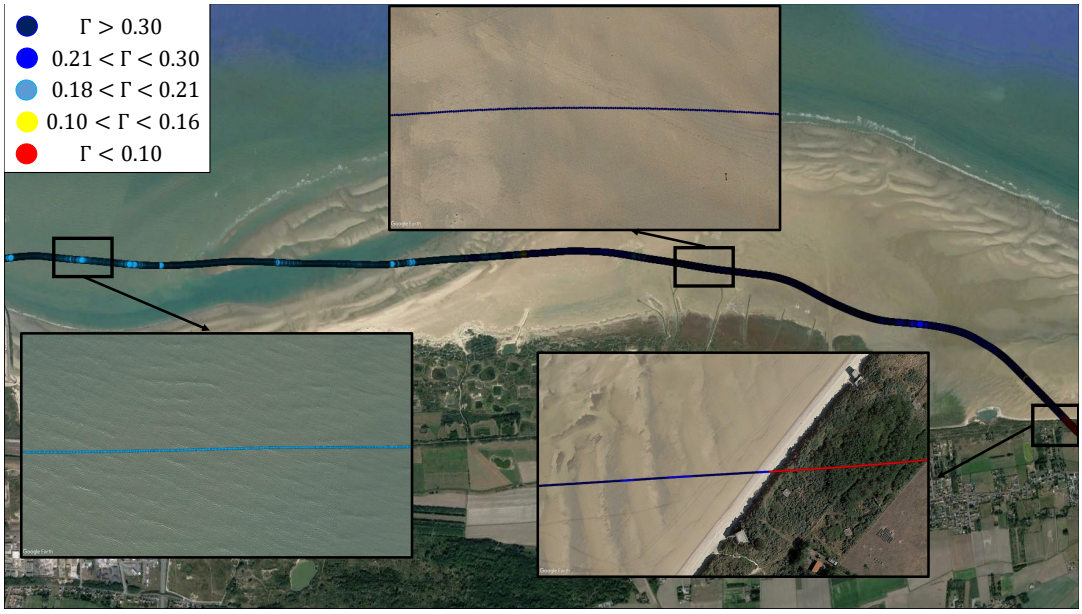

FIGURE 5.17: The detected surfaces corresponding to groves, sandy beach and sea by the proposed radar technique along the trace of satellite PRN 30 footprints.

very low mean reflectivity ($\Gamma < 0.1$). The yellow color is associated to other land surfaces with $0.1 < \Gamma < 0.18$.

We notice very high reflectivity measurements associated to sandy beach where the specular points of reflection are mostly colored in dark blue in this region. The reflections from sea are lower than those observed from sandy beach and in-land water bodies and are represented mostly by a light blue color. We also note very low reflectivity observations associated to groves which are represented in red coloring of the specular point of reflection. It is important to note that the mean reflectivity measurements associated to large surface areas such as sandy beach and sea are not always stationary. This is why we sometimes observe a decrease in the mean reflectivity associated to small areas of the beach.

We show in Figure 5.18 another example of surface differentiation using the GNSS measurements obtained from PRN 30 satellite signals. We observe very low reflectivity measurements associated to the 2 forests detected in this area. This is denoted by a red coloring of the specular point of reflection along most of the detected area of the forest. The yellow color is associated mainly to land reflections, whereas the in-land water bodies are detected in blue. This further proves the detection capacity of the proposed radar technique.

FIGURE 5.18: Surface differentiation using the GNSS measurements obtained from PRN 30 satellite signals.

Finally, we report in Table 5.7 the statistics of reflectivity associated to different kinds of reflecting surfaces over the whole trajectory for satellite PRN 30. It is important to note that the measurements associated to plain land surfaces are not included in this study because its statistics are very complex to derive in terms of the number of detected surfaces and its characteristics in such a large study area.

TABLE 5.7: Statistics of reflectivity associated to different kinds of reflecting surfaces.

Land form	Mean reflectivity	Mean reflectivity std
Sandy beach	0.34	0.07
Sea	0.21	0.04
In-land water body	0.26	0.09
Forests/Groves	0.09	0.005

We notice from Table 5.7 that the sandy beach recorded the highest mean reflectivity followed by in-land water body surfaces then sea. This is because the beach contains very wet sand which increases the moisture of the surface. Calm water from the sea can also cover part of the sandy beach area due to sea waves. In addition, the surface of the beach is mostly flat unlike

the sea where we can easily obtain a non-coherent reflection resulting from the signal reflecting from several points due to the sea roughness especially in such wind speed (25 km/h). Reflections from in-land water body surfaces are affected by the type and size of the water body surface, the detection length and the characteristics of the surfaces surrounding the water body at its edges. It is also worth noting that the detection length of sandy beach and sea are much larger than other surfaces which affects the measurements. Finally, we observe that the surfaces covered by vegetation such as forests or groves recorded the lowest mean reflectivity levels. This is because vegetation increases the surface roughness and decreases the reflectivity. We conclude from this study that our proposed radar technique is able to differentiate different kinds of surfaces based on the mean reflectivity measurements associated to each surface.

5.7 Conclusion

This airborne experiment studies the techniques for water body localization using GNSS-R. A GNSS-R setup of reduced size and weight has been developed specifically to meet the requirements of this application. The utilization of the delay line in the GNSS-R setup is a significance of this work. The delay line produces a delay that is sufficient enough to track the direct and reflected GNSS signals independently using a mono channel receiver which allows perfect synchronization of the RHCP and LHCP links. The observations are realized with high temporal and spatial resolution. We estimate 20 ms rate of reflectivity measurements as the ratio of the amplitudes of the reflected LHCP antenna signals over the direct RHCP antenna signals. The signals are segmented into stationary parts associated with different areas of reflection. We relate the 20 ms rate reflectivity measurements to the corresponding reflecting surfaces via a 20 ms localization of the specular point of reflection.

We apply a real flight experimentation using a low-altitude airborne carrier with high rate observations of the surface reflectivity. We show that our method is able to differentiate surfaces, and thus detect water bodies on landforms, based on the difference in reflectivity measurements associated to each surface. We show that our radar technique is able to detect 96% of the total number of water body surfaces on the traces of the satellites footprints in study as compared to the up-to-date data provided by IGN maps.

In a second analysis, we apply a manual inspection between the automatic edge localization provided by the radar technique and manual localization using Google Earth in order to assess the edge localization accuracy of the proposed approach. We show in this study that our proposed radar technique is highly sensitive to the changes in landforms with metric edge localization accuracy. The presence of vegetation on the border between land and water body surfaces affects the localization accuracy and we show that even in such cases the proposed radar is able to record a reasonable accuracy.

Finally, we show the capacity of the approach to differentiate surfaces in landforms such as in-land water body surfaces, sea, sandy beach, vegetation and land. We show in this study that sandy beach recorded the highest mean reflectivity followed by in-land water bodies then sea. We note that the forests/groves recorded the lowest reflectivity measurements. This shows the feasibility of the proposed automatic detection algorithm to investigate the sea state or the vegetation biomass.

General Conclusion

The work presented in this thesis focuses on GNSS signal processing techniques applied to water body detection and edge localization using a low altitude airborne carrier. We utilize a GNSS-R setup designed specifically for this work on-board a lightweight carrier. The aim of the thesis is to develop a radar technique for automatic GNSS signal segmentation in order to differentiate surfaces, and in particular water bodies, in landforms based on the reflectivity measurements associated to different areas of reflection. We estimate 20 *ms* rate reflectivity measurements in order to cope with the rapid displacement of the satellites footprints along the airborne experiment. These measurements are associated to the reflecting surfaces by 20 *ms* rate localization of the specular points of reflection. Several models and estimators are proposed in the frame work of the research work.

The dissertation consists of five chapters, the first of which is dedicated to remote sensing techniques for soil moisture detection. In this chapter, we addressed the fundamentals of soil moisture remote sensing from L-band emissions. We highlighted the different active and passive remote sensing techniques that are implemented in the literature review. We have shown that passive radiometers suffer from poor spatial resolution, and active radars suffer from low accuracy. The principle of GNSS-R as well as the different signal processing methodologies performed by traditional GNSS-R receivers were presented in this chapter. The different GNSS-R antenna configurations and the information carried by the reflected signal in each scenario were thoroughly discussed along with the various GNSS-R ground-based, airborne and space-borne applications. In this chapter, we demonstrated our decision to use conventional GNSS-R (cGNSS-R) signal processing techniques in a dual-antenna configuration for the airborne experiment.

The second chapter is devoted to the modeling of the GNSS signal for the derivation of the GNSS carrier-to-noise ratio. We also presented different C/N_0 estimators that are used by the GNSS-R community. The performance of the presented estimators were compared in terms of estimation accuracy

and computational complexity. We have shown that the C/N_0 estimated by Beaulieu's method provided the best trade-off results. For soil moisture retrieval using GNSS-R, the SNR of the LHCP and RHCP GNSS antenna signals can be linked to the reflectivity measurements from which the soil dielectric constant and consequently the soil moisture content can be derived. This is due to the fact that the SNR provides direct observation of the GNSS signal amplitudes. However, the processing of the GNSS signals for amplitude estimation is non-linear since the expression that links the in-phase component of the signal to the signal amplitude is non-linear.

For this purpose, we propose in the third chapter, an on-line probabilistic model for the estimation of the GNSS signal amplitudes and subsequently the carrier-to-noise ratio at high rates taking into consideration the non-linearity of the problem. We have shown in this chapter that in a 1-bit quantization receiver, the observations are independent of the automatic gain control, and thus, the in-phase component of the signal provides direct observation of the signal amplitude, and therefore of C/N_0. We proposed a state filter in the form of an Extended Kalman filter that estimates 1 *ms* rate GNSS signal amplitudes using 1 *ms* rate observations of the in-phase component of the signals. We have shown using real data that, for a 1-bit quantization receiver, the proposed estimator achieved the same accuracy as a widely known commercial GNSS receiver with a much higher data rate of 1000 *Hz*. We also showed using synthetic data that the proposed C/N_0 estimator can remove the error due to the cross-correlation contribution of the GNSS satellites and thus improve the accuracy of the C/N_0 estimations.

In the fourth chapter, we propose a mixture of an on-line/off-line change point detection and localization algorithm for the segmentation of the GNSS signals into stationary parts associated to different mean signal levels. In this work, we assume that the GNSS measurements are piecewise stationary, and the noise on the observations are additive, Gaussian and centered. The amplitudes of the reflected GNSS signals are proportional to the ground reflectivity. We use a transitional model to characterize the changes in the amplitudes of the reflected GNSS signals from one area to another. Since we process large amounts of data, we have proposed to detect the changes on-line using a Kalman-CUSUM algorithm. After change detection, we proposed an off-line maximum likelihood localization estimate (MLLE) to localize the detected changes in a working window that is close to optimality. In

the presence of noise, the CUSUM change detector generates false alarm detections and the signals would be over segmented. To solve the problem of over segmentation, we proposed a merging algorithm that investigates the difference between the statistical properties of the obtained stationary parts in order to decrease the number of false change detections. As a result, the segmentation showed more stationary parts associated to significantly different mean reflectivity signal levels.

We have assessed the performance of the automatic radar signal segmentation model in comparison with other state-of-the-art methods. We have shown that the proposed MLLE localization approach is more accurate than the CUSUM and GLR localization approaches under various SNR environments using synthetic data. We also showed on synthetic data that the merging algorithm indeed decreased the number of false detections. Using real data, we have shown that the proposed MLLE approach performed more accurately than the CUSUM localization algorithm. We also showed on real data that the proposed model for C/N_0 estimation in chapter 3 performs more accurately than Beaulieu's method in the presence of abrupt changes detected by the proposed change detection algorithm. The capacity of the proposed system to segment real airborne GNSS signals of reflectivity was also investigated by demonstrating the different processing steps of the radar signal segmentation on GNSS data collected during the airborne experiment.

The fifth chapter is dedicated to the airborne experiment for water body detection and edge localization using GNSS-R. We have presented in this chapter the bi-static airborne GNSS-R system that is used in the flight experimentation along with the on-board sensors and the GNSS-R receiver hardware. The use of the delay line in the GNSS-R receiver hardware is a distinction of the work because it delays the reflected GNSS signals allowing synchronous digitization of the direct and reflected GNSS signals on a mono channel bit grabber. Since the reflected GNSS signals are very low in power, they are processed in a master/slave configuration in our self built software receiver, while taking into consideration the path difference between the direct and reflected signals. The GNSS measurements are realized with high temporal and spatial resolution.

We implemented the radar signal segmentation model on the GNSS measurements obtained during the whole flight duration (45 *min*). We have

shown that the proposed radar technique is able to detect 96% of in-land water body surfaces provided by the up-to-date IGN maps along the footprint traces of the satellites in study. We have also applied a manual inspection between the automatic water body edge localization provided by the radar technique and the manual localization using Google Earth for all the water body surfaces detected. We show in this novel quantitative analysis that we can detect and localize at meter accuracy the positions of different in-land water body surfaces and their edges. The proposed radar technique has also displayed high sensitivity to changes in landforms which is invested to differentiate surfaces including: in-land water bodies, sea, sandy beach, vegetation and land.

Perspectives

One of the main perspectives of this work is to compare the results obtained for water body detection and edge localization using the proposed radar technique with the ground-truth data. This requires extensive in-situ measurement campaigns with the use of precise GNSS-R positioning techniques to accurately localize the starting and ending edges of the in-land water body surfaces. In order to better analyze the variations in the reflectivity of a water body surface, we can make use of real time images captured by action cameras embedded on the bottom of the gyrocopter as part of the new GNSS-R receiver setup.

We have seen from the analysis of the GNSS reflectivity measurements that it is exceptionally complicated to characterize plain land surfaces and thus derive the soil moisture content using 1-bit quantized realizations. The next step would be the development and utilization of a larger bit quantization digital receiver (e.g 4-bit quantization) that is able to provide information about the AGC gain in order to relate the in-phase component of the signal to the signal amplitude as in 1-bit quantized realizations. This is expected to increase the SNR of the reflected GNSS signals and thus provide more information regarding the signal amplitudes. As a result, the sensitivity of the proposed radar technique for the detection of the soil moisture content as well as detection of other surfaces will be increased. In addition, for more accurate reflectivity measurements the gain patterns of the antennas should be taken into account.

Another direction to advance in this topic is to further increase the temporal resolution of the application. We have indeed shown that the proposed radar technique achieves high temporal and spatial resolution compared to similar approaches. However, the proposed amplitude estimator and segmentation models proved to work accurately on even higher rates (1000 Hz) which opens up the possibility of adapting the radar technique to 1 ms rate observations instead of 20 ms rate.

One of the interesting aspects of the mono channel bit grabber used in this work is the digitization of L1 and L5 signals. The next step in this direction would be the processing of L5 signals and the fusion of L1 and L5 data to further increase the observables of the reflected GNSS signals. An information fusion algorithm based on statistical approaches would be developed for the integration of the GPS L1 and L5 signals. The GPS L5 signals have higher transmitted power than L1 signals and is expected to have deeper penetration capacity in land for more accurate reflectivity measurements allowing more precise detection of other surfaces in landforms (other than in-land water bodies).

The developed model for the estimation of the GNSS signal amplitudes at high rates shows different complexities that can be included in a probabilistic model of a coherent detector. A potential implementation of this model would be the use of the phase information in the complex GNSS samples to separate coherent and non-coherent reflections. Another possible application that uses the phase information of the reflected signal is the carrier-phase altimetry which can be implemented to observe the sea state.

An interesting approach would be to combine machine learning algorithms with the developed signal processing techniques for the classification of detected surfaces in landforms, and in particular its soil moisture content, based on the obtained reflectivity measurements as the models linking reflectivity to soil moisture are highly non-linear and depend on many parameters. This would open up the possibility for the classification of different vegetation covers using the proposed radar technique.

Appendix A

Specular Point Localization

It is important to localize the reflecting surfaces from which each processed signal has reflected, and thus detect which areas were scanned during the airborne experiment. Therefore, we process besides the raw GNSS data, the satellites and receiver's positions to map the measurements obtained from the airborne GNSS-R setup along the real flight experimentation.

In order to calculate the satellites positions along the receiver trajectory, a NovAtel receiver records the ephemeris and almanacs of the satellites in view (RINEX files). The actual geodetic coordinates and attitude of the receiver are recorded by the drone board sensor. The drone card (Pixhawk card) processes and synchronizes, with respect to the GPS Time, sensors data (GPS, IMU, electronic compass,...) and provides measurements of position and attitude at a rate of 5 Hz. The GPS data recorded by the drone board sensor references the altitude of the receiver to the WGS84 ellipsoid which is the same reference used by Google Earth for positioning.

In fact, georeferencing the specular points on maps are done based on the ENU local coordinate system by assuming that the surface is locally flat and that the surface height remains the same with that of the receiver projection position. A scheme representing the calculation process is depicted in Figure A.1.

A.1 Effect of Earth rotation on the satellites positions

In our work, we indeed take into account the effect of Earth rotation on the satellites positions (Figure A.2). Let $R_1(x^e_R, y^e_R, z^e_R)$ be the receiver's ECEF coordinates after Earth rotation. Let $S_0(x^e_{S_0}, y^e_{S_0}, z^e_{S_0})$ and $S_1(x^e_{S_1}, y^e_{S_1}, z^e_{S_1})$ be the

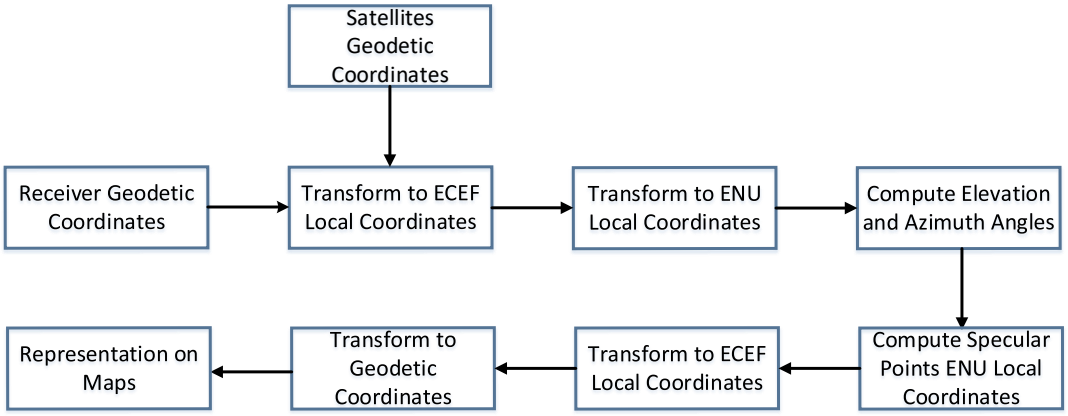

FIGURE A.1: Specular point localization process

ECEF coordinates of the satellite position with respect to the receiver before and after Earth rotation, respectively. Then, the time Δt^e associated to the change in the ECEF frame (from red to light blue in Figure A.2) due to Earth rotation can be expressed as:

$$\Delta t^e = \frac{\sqrt{X^e + Y^e + Z^e}}{c} \tag{A.1}$$

where c is the speed of light and:

$$X^e = (x^e_{S_0} - x^e_R)^2$$
$$Y^e = (y^e_{S_0} - y^e_R)^2$$
$$Z^e = (z^e_{S_0} - z^e_R)^2$$

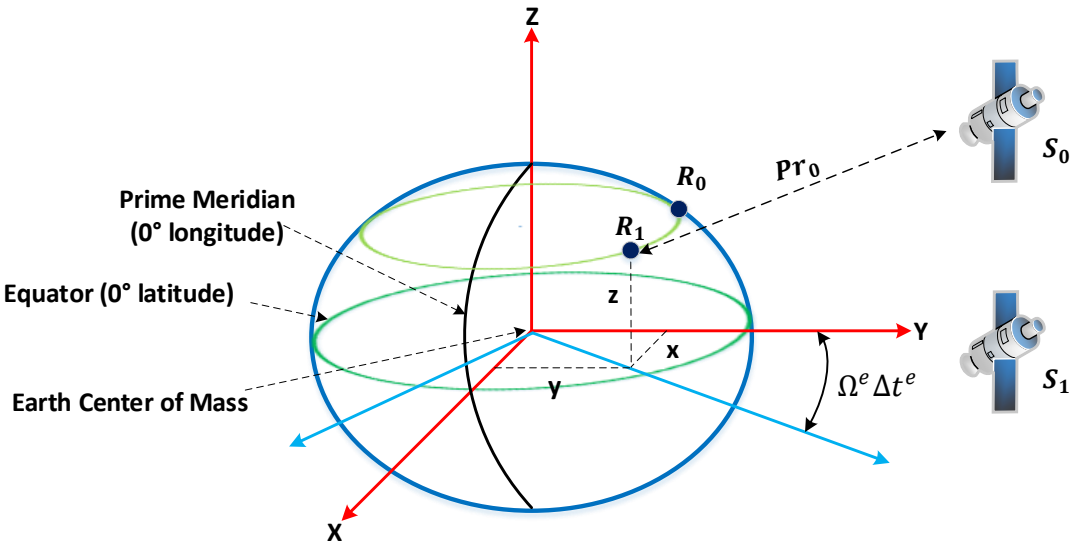

FIGURE A.2: Effect of earth rotation.

The receiver at position R_1 knows the signal emission time t_0 and the pseudo-range Pr_0 for the satellite at position S_0 (i.e. before Earth rotation). The position R_1 of the receiver is therefore processed with Pr_0 and S_0. The position S_1 of the satellite with respect to the receiver after Earth rotation can be derived from S_0 after a rotation around the z-axis of $-\Omega^e \Delta t^e$, where Ω^e is the pulsation of Earth rotation and is approximately equal to 7.292×10^{-5}.

A.2 Computation of the azimuth and elevation Angles

The localization of the satellites footprints along a specific receiver trajectory requires an accurate knowledge of the azimuth and elevation angles of the satellites in view. For this purpose, a series of transformations between the reference coordinate systems is first implemented. These transformations are depicted in Figure A.3. The transformation from Earth-centered, Earth-fixed (ECEF) to East, North, Up (ENU) frame requires setting a reference origin point. In this regard, the dynamic GNSS receiver position at height h is chosen to be the reference origin point at each instant along the flight trajectory. Further information about the reference coordinate systems used for localization of GNSS measurements can be found in appendix (refer to appendix of reference coordinate systems). After transformation to the ENU frame the next step is to calculate the azimuth and elevation angles.

Receiver $(\boldsymbol{R_1})$:

$$(L_R, L_R, H_R) \xrightarrow{\text{LLH To XYZ ECEF}} (x_R^e, y_R^e, z_R^e)_{ECEF} \xrightarrow[\text{orgxyz } (x_R^e, y_R^e, z_R^e)_{ECEF}]{\text{XYZ ECEF to XYZ ENU}} (0,0,0)_{ENU}$$

Receiver Projection $(\boldsymbol{R_2})$:

$$(L_{R_2}, L_{R_2}, H_{R_2}) \xrightarrow{\text{LLH To XYZ ECEF}} (x_{R_2}^e, y_{R_2}^e, z_{R_2}^e)_{ECEF} \xrightarrow[\text{orgxyz } (x_R^e, y_R^e, z_R^e)_{ECEF}]{\text{XYZ ECEF to XYZ ENU}} (0,0,-h)_{ENU}$$

Satellite $(\boldsymbol{S_1})$:

$$(L_{S_1}, L_{S_1}, H_{S_1}) \xrightarrow{\text{LLH To XYZ ECEF}} (x_{S_1}^e, y_{S_1}^e, z_{S_1}^e)_{ECEF} \xrightarrow[\text{orgxyz } (x_R^e, y_R^e, z_R^e)_{ECEF}]{\text{XYZ ECEF to XYZ ENU}} (x_{S_1}, y_{S_1}, z_{S_1})_{ENU}$$

Specular Reflection Point $(\boldsymbol{S})$:

$$(L_S, L_S, H_S) \xrightarrow{\text{LLH To XYZ ECEF}} (x_S^e, y_S^e, z_S^e)_{ECEF} \xrightarrow[\text{orgxyz } (x_R^e, y_R^e, z_R^e)_{ECEF}]{\text{XYZ ECEF to XYZ ENU}} (x_S, y_S, -h)_{ENU}$$

FIGURE A.3: A series of transformations between the reference coordinate systems

The azimuth angle α (Figure A.4a) is a horizontal angle measured clockwise from a north base line to a line that crosses a spot connecting the vertical

projection from a satellite with the horizon and passing through the origin. If $(x_{S_1}, y_{S_1}, z_{S_1})$ and (x_R, y_R, z_R) are the ENU coordinates of the satellite and the receiver respectively, the azimuth angle can be calculated as:

$$\begin{aligned} \alpha &= \tan^{-1}\left(\frac{X}{Y}\right) \\ &= \tan^{-1}\left(\frac{x_{S_1} - x_R}{y_{S_1} - y_R}\right) \end{aligned} \tag{A.2}$$

The elevation angle θ (Figure A.4b) is the angle between the local horizontal plane and the line pointing directly towards the satellite and is given by:

$$\theta = \tan^{-1}\left(\frac{Z}{\sqrt{X^2 + Y^2}}\right) \tag{A.3}$$

where

$$\begin{aligned} X &= x_{S_1} - x_R \\ Y &= y_{S_1} - y_R \\ Z &= z_{S_1} - z_R \end{aligned}$$

Consequently, the semi-major axis a and semi-minor axis b of the first Fresnel ellipse associated with the satellite footprint can be written as follows in terms of the satellite elevation angle:

$$a = \frac{\sqrt{\lambda h \cos(\pi/2 - \theta)}}{\cos^2(\pi/2 - \theta)} \tag{A.4}$$

$$b = \frac{\sqrt{\lambda h \cos(\pi/2 - \theta)}}{\cos(\pi/2 - \theta)} \tag{A.5}$$

where λ is the GPS signal wavelength ($\approx$ 19.042 cm for GPS C/A signals) and h is the height of the gyrocopter.

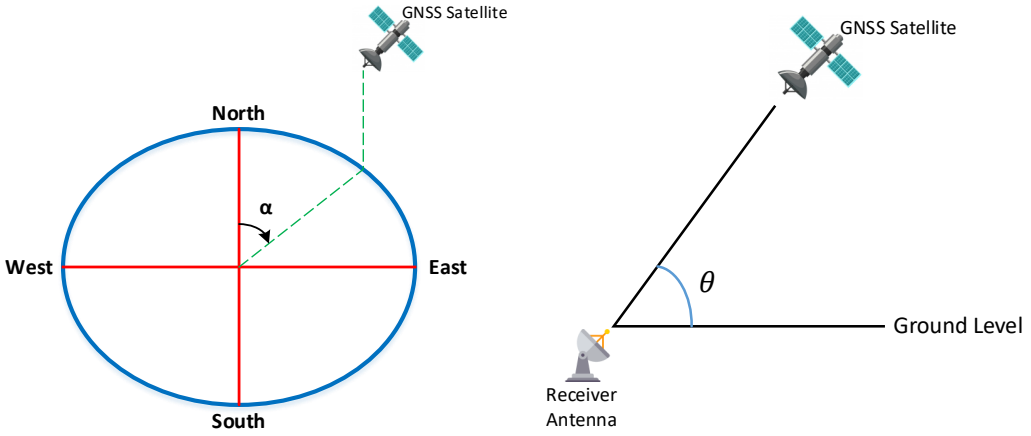

(a) Azimuth angle (b) Elevation angle

FIGURE A.4: Representation of the azimuth and elevation angles of a satellite in view with respect to a receiver's position.

A.3 Computation of the specular point coordinates

The specular point of reflection S is positioned at the center of the first Fresnel ellipse that constitute the satellite footprint. The ENU representation of the airborne GNSS-R system geometry is depicted in Figure A.5.

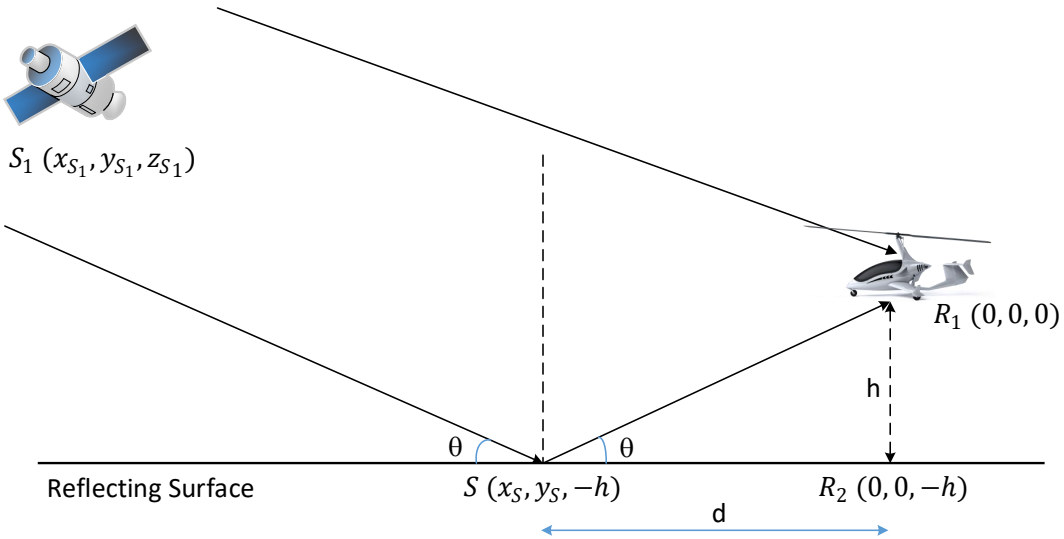

FIGURE A.5: ENU representation of the airborne GNSS-R geometry

To calculate the coordinates of the point S, the distance d between the receiver's projection on earth R_2 and S should be determined. Applying the

basics of such geometry, d can be deduced from the elevation angle and the receiver height h as:

$$d = \frac{h}{\tan(\theta)} \tag{A.6}$$

Having d, it is easy now to calculate the coordinates of the point S with the use of the azimuth angle. This relation is depicted in Figure A.6. Therefore, the coordinates of point S, the specular reflection point, are written as:

$$\begin{aligned} x_S &= \sin(\alpha) \times d \\ y_S &= \cos(\alpha) \times d \\ z_S &= -h \end{aligned} \tag{A.7}$$

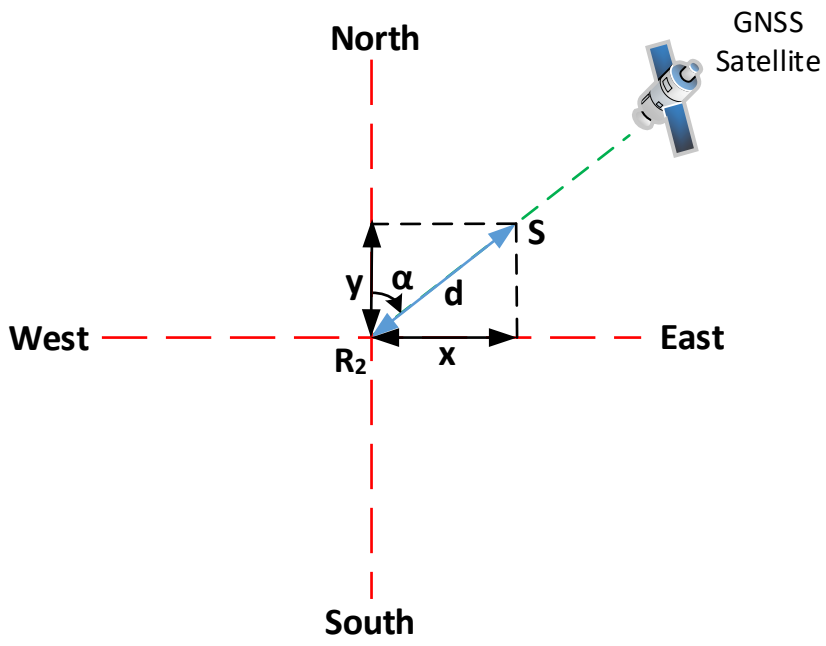

FIGURE A.6: Relation between the distance d and the azimuth angle

The coordinates of the points that constitute the first Fresnel ellipse of the satellite footprint can be derived from the specular points coordinates, the azimuth angles of the satellites and the major-axis size of the ellipse. Finally, the ENU coordinates of the ellipse points and the set of specular reflection points S are transformed back into ECEF coordinates and then into geodetic coordinates for representation on maps (Google Earth, IGN,...). This process is done every specified interval of time along the whole receiver trajectory. In this work, we superimpose the 20 ms rate GNSS measurements on Google

Earth software. These measurements are associated with a 20 *ms* rate localization of the specular reflection point only, since at such high rate, the satellites footprints will be immensely overlapped.

Bibliography

[1] A Egido. "GNSS reflectometry for land remote sensing applications". In: *Ph. D. dissertation* (2013).

[2] Luca Brocca et al. "Soil as a natural rain gauge: Estimating global rainfall from satellite soil moisture data". In: *Journal of Geophysical Research: Atmospheres* 119.9 (2014), pp. 5128–5141.

[3] Brigitte Mueller and Sonia I Seneviratne. "Hot days induced by precipitation deficits at the global scale". In: *Proceedings of the national academy of sciences* 109.31 (2012), pp. 12398–12403.

[4] Diego G Miralles et al. "El Niño–La Niña cycle and recent trends in continental evaporation". In: *Nature Climate Change* 4.2 (2014), pp. 122–126.

[5] Dallas Masters, Penina Axelrad, and Stephen Katzberg. "Initial results of land-reflected GPS bistatic radar measurements in SMEX02". In: *Remote sensing of environment* 92.4 (2004), pp. 507–520.

[6] Emanuele Santi et al. "Comparison between SAR soil moisture estimates and hydrological model simulations over the Scrivia test site". In: *Remote Sensing* 5.10 (2013), pp. 4961–4976.

[7] Maria Jose Escorihuela et al. "SMOS based high resolution soil moisture estimates for desert locust preventive management". In: *Remote Sensing Applications: Society and Environment* 11 (2018), pp. 140–150.

[8] Frédéric Frappart et al. "Automatic detection of inland water bodies along altimetry tracks for estimating surface water storage variations in the Congo Basin". In: *Remote Sensing* 13.19 (2021), p. 3804.

[9] NC Davidson, Etienne Fluet-Chouinard, and CM Finlayson. "Global extent and distribution of wetlands: trends and issues". In: *Marine and Freshwater Research* 69.4 (2018), pp. 620–627.

[10] M Acreman and J Holden. "How wetlands affect floods". In: *Wetlands* 33.5 (2013), pp. 773–786.

[11] PE O'neill and TJ Jackson. "Observed effects of soil organic matter content on the microwave emissivity of soils". In: *Remote sensing of environment* 31.3 (1990), pp. 175–182.

[12] Stephen J Katzberg et al. "Utilizing calibrated GPS reflected signals to estimate soil reflectivity and dielectric constant: Results from SMEX02". In: *Remote sensing of environment* 100.1 (2006), pp. 17–28.

[13] Kristine M. Larson et al. "Using GPS multipath to measure soil moisture fluctuations: initial results". In: *GPS Solutions* 12.3 (2008), pp. 173–177. ISSN: 1521-1886. DOI: 10.1007/s10291-007-0076-6. URL: https://doi.org/10.1007/s10291-007-0076-6.

[14] A. Azmani et al. "Soil Moisture Estimation using Land-Reflected GPS L2C Bi-Static Radar Measurements". In: *Proceedings of the 23rd International Technical Meeting of The Satellite Division of the Institute of Navigation (ION GNSS 2010)*. 2010, pp. 1031–1038.

[15] Miguel Angel Ribot et al. "Normalized GNSS Interference Pattern Technique for Altimetry". In: *Sensors* 14.6 (2014), pp. 10234–10257. ISSN: 1424-8220. DOI: 10.3390/s140610234. URL: http://www.mdpi.com/1424-8220/14/6/10234.

[16] Micaela Troglia Gamba et al. "Prototyping a GNSS-based passive radar for UAVs: An instrument to classify the water content feature of lands". In: *Sensors* 15.11 (2015), pp. 28287–28313.

[17] Jean-Christophe Kucwaj et al. "Circular regression applied to GNSS-R phase altimetry". In: *Remote Sensing* 9.7 (2017), p. 651.

[18] Eni G Njoku and Peggy E O'Neill. "Multifrequency microwave radiometer measurements of soil moisture". In: *IEEE Transactions on Geoscience and Remote Sensing* 4 (1982), pp. 468–475.

[19] Nereida Rodriguez-Alvarez et al. "Soil moisture retrieval using GNSS-R techniques: Experimental results over a bare soil field". In: *IEEE transactions on geoscience and remote sensing* 47.11 (2009), pp. 3616–3624.

[20] Clara Chew, Eric E Small, and Kristine M Larson. "An algorithm for soil moisture estimation using GPS-interferometric reflectometry for bare and vegetated soil". In: *GPS solutions* 20.3 (2016), pp. 525–537.

[21] TJ Jackson and TJ Schmugge. "Surface soil moisture measurement with microwave radiometry". In: *Acta Astronautica* 35.7 (1995), pp. 477–482.

[22] Joseph Knuble et al. "Airborne P-band Signal of Opportunity (SoOP) demonstrator instrument; status update". In: *2016 IEEE International Geoscience and Remote Sensing Symposium (IGARSS)*. IEEE. 2016, pp. 5638–5641.

[23] Nan Ye et al. "Toward P-band passive microwave sensing of soil moisture". In: *IEEE Geoscience and Remote Sensing Letters* 18.3 (2020), pp. 504–508.

[24] Ludovic Villard et al. "Forest biomass from radar remote sensing". In: *Land surface remote sensing in agriculture and forest*. Elsevier, 2016, pp. 363–425.

[25] Alessandra Monerris, Thomas Schmugge, and G Jedlovec. "Soil moisture estimation using L-band radiometry". In: *Advances in Geoscience and Remote Sensing* (2009).

[26] Brian W Barrett, Edward Dwyer, and Pádraig Whelan. "Soil moisture retrieval from active spaceborne microwave observations: An evaluation of current techniques". In: *Remote Sensing* 1.3 (2009), pp. 210–242.

[27] Myron C Dobson et al. "Microwave dielectric behavior of wet soil-Part II: Dielectric mixing models". In: *IEEE Transactions on geoscience and remote sensing* 1 (1985), pp. 35–46.

[28] James R Wang and Thomas J Schmugge. "An empirical model for the complex dielectric permittivity of soils as a function of water content". In: *IEEE Transactions on Geoscience and Remote Sensing* 4 (1980), pp. 288–295.

[29] Valery L Mironov et al. "Generalized refractive mixing dielectric model for moist soils". In: *IEEE transactions on Geoscience and Remote sensing* 42.4 (2004), pp. 773–785.

[30] S Saatchi, E Njoku, and U Wegmüller. "Synergism of active and passive microwave data for estimating bare soil surface moisture". In: *Passive Microwave Remote Sensing of Land-Atmosphere Interactions:[ESA/NASA International Workshop, Held at Saint Lary (France) from January 11–15, 1993]*. Walter de Gruyter GmbH & Co KG. 2020, p. 205.

[31] Lun Gao, Morteza Sadeghi, and Ardeshir Ebtehaj. "Microwave retrievals of soil moisture and vegetation optical depth with improved resolution using a combined constrained inversion algorithm: Application for SMAP satellite". In: *Remote Sensing of Environment* 239 (2020), p. 111662.

[32] Paolo Ferrazzoli, Leila Guerriero, and J-P Wigneron. "Simulating L-band emission of forests in view of future satellite applications". In: *IEEE Transactions on Geoscience and Remote Sensing* 40.12 (2002), pp. 2700–2708.

[33] Noemi Vergopolan et al. "Combining hyper-resolution land surface modeling with SMAP brightness temperatures to obtain 30-m soil moisture estimates". In: *Remote Sensing of Environment* 242 (2020), p. 111740.

[34] Monika A Tomaszewska, Lan H Nguyen, and Geoffrey M Henebry. "Land surface phenology in the highland pastures of montane Central Asia: Interactions with snow cover seasonality and terrain characteristics". In: *Remote Sensing of Environment* 240 (2020), p. 111675.

[35] J-P Wigneron et al. "Retrieving near-surface soil moisture from microwave radiometric observations: current status and future plans". In: *Remote Sensing of Environment* 85.4 (2003), pp. 489–506.

[36] Yan Jia and Yuekun Pei. "Remote Sensing in Land Applications by Using GNSS-Reflectometry". In: *Recent Advances and Applications in Remote Sensing*. IntechOpen, 2018.

[37] J-P Wigneron et al. "Modelling the passive microwave signature from land surfaces: A review of recent results and application to the L-band SMOS & SMAP soil moisture retrieval algorithms". In: *Remote Sensing of Environment* 192 (2017), pp. 238–262.

[38] JR Wang and BJ Choudhury. "Remote sensing of soil moisture content, over bare field at 1.4 GHz frequency". In: *Journal of Geophysical Research: Oceans* 86.C6 (1981), pp. 5277–5282.

[39] J-P Wigneron et al. "L-band Microwave Emission of the Biosphere (L-MEB) Model: Description and calibration against experimental data sets over crop fields". In: *Remote Sensing of Environment* 107.4 (2007), pp. 639–655.

[40] TJ Jackson and TJ Schmugge. "Vegetation effects on the microwave emission of soils". In: *Remote Sensing of Environment* 36.3 (1991), pp. 203–212.

[41] Victor Klemas, Charles W Finkl, and Nijad Kabbara. "Remote sensing of soil moisture: An overview in relation to coastal soils". In: *Journal of Coastal Research* 30.4 (2014), pp. 685–696.

[42] Yann H Kerr et al. "The SMOS soil moisture retrieval algorithm". In: *IEEE transactions on geoscience and remote sensing* 50.5 (2012), pp. 1384–1403.

[43] M Owe, AA Van de Griend, and ATC Chang. "Surface moisture and satellite microwave observations in semiarid southern Africa". In: *Water Resources Research* 28.3 (1992), pp. 829–839.

[44] IE Mladenova et al. "Remote monitoring of soil moisture using passive microwave-based techniques—Theoretical basis and overview of selected algorithms for AMSR-E". In: *Remote sensing of environment* 144 (2014), pp. 197–213.

[45] BJ Choudhury, TJ Schmugge, and T Mo. "A parameterization of effective soil temperature for microwave emission". In: *Journal of Geophysical Research: Oceans* 87.C2 (1982), pp. 1301–1304.

[46] Fawwaz Tayssir Ulaby. "Microwave remote sensing active and passive". In: *Rader remote sensing and surface scattering and emission theory* (1982), pp. 848–902.

[47] J-P Wigneron, Laurent Laguerre, and Yann H Kerr. "A simple parameterization of the L-band microwave emission from rough agricultural soils". In: *IEEE Transactions on Geoscience and Remote Sensing* 39.8 (2001), pp. 1697–1707.

[48] Jean-Pierre Wigneron et al. "Estimating the effective soil temperature at L-band as a function of soil properties". In: *IEEE Transactions on Geoscience and Remote Sensing* 46.3 (2008), pp. 797–807.

[49] Dara Entekhabi et al. "The soil moisture active passive (SMAP) mission". In: *Proceedings of the IEEE* 98.5 (2010), pp. 704–716.

[50] Komi Edokossi et al. "GNSS-Reflectometry and Remote Sensing of Soil Moisture: A Review of Measurement Techniques, Methods, and Applications". In: *Remote Sensing* 12.4 (2020), p. 614.

[51] Eni G Njoku and Jin-Au Kong. "Theory for passive microwave remote sensing of near-surface soil moisture". In: *Journal of Geophysical Research* 82.20 (1977), pp. 3108–3118.

[52] BJ Choudhury et al. "Effect of surface roughness on the microwave emission from soils". In: *Journal of Geophysical Research: Oceans* 84.C9 (1979), pp. 5699–5706.

[53] Fawwaz T Ulaby, Mohammad Razani, and Myron C Dobson. "Effects of vegetation cover on the microwave radiometric sensitivity to soil moisture". In: *IEEE Transactions on Geoscience and Remote Sensing* 1 (1983), pp. 51–61.

[54] Jiangyuan Zeng et al. "A preliminary evaluation of the SMAP radiometer soil moisture product over United States and Europe using ground-based measurements". In: *IEEE Transactions on Geoscience and Remote Sensing* 54.8 (2016), pp. 4929–4940.

[55] Eni G Njoku and Steven K Chan. "Vegetation and surface roughness effects on AMSR-E land observations". In: *Remote Sensing of environment* 100.2 (2006), pp. 190–199.

[56] Emanuele Santi et al. "Application of artificial neural networks for the soil moisture retrieval from active and passive microwave spaceborne sensors". In: *International Journal of Applied Earth Observation and Geoinformation* 48 (2016), pp. 61–73.

[57] Xingming Zheng et al. "A New Soil Moisture Retrieval Algorithm from the L-Band Passive Microwave Brightness Temperature Based on the Change Detection Principle". In: *Remote Sensing* 12.8 (2020), p. 1303.

[58] Yann H Kerr et al. "Overview of SMOS performance in terms of global soil moisture monitoring after six years in operation". In: *Remote Sensing of Environment* 180 (2016), pp. 40–63.

[59] Dara Entekhabi et al. "SMAP handbook–soil moisture active passive: Mapping soil moisture and freeze/thaw from space". In: (2014).

[60] Narendra N Das et al. "The SMAP mission combined active-passive soil moisture product at 9 km and 3 km spatial resolutions". In: *Remote sensing of environment* 211 (2018), pp. 204–217.

[61] Rocco Panciera et al. "The soil moisture active passive experiments (SMAPEx): Toward soil moisture retrieval from the SMAP mission". In: *IEEE transactions on geoscience and remote sensing* 52.1 (2013), pp. 490–507.

[62] Yann H Kerr et al. "The SMOS mission: New tool for monitoring key elements ofthe global water cycle". In: *Proceedings of the IEEE* 98.5 (2010), pp. 666–687.

[63] KD McMullan et al. "SMOS: The payload". In: *IEEE Transactions on Geoscience and Remote Sensing* 46.3 (2008), pp. 594–605.

[64] J-P Wigneron et al. "Two-dimensional microwave interferometer retrieval capabilities over land surfaces (SMOS mission)". In: *Remote Sensing of Environment* 73.3 (2000), pp. 270–282.

[65] Roger Oliva et al. "SMOS Third Mission Reprocessing after 10 Years in Orbit". In: *Remote Sensing* 12.10 (2020), p. 1645.

[66] Tianjie Zhao et al. "Retrievals of soil moisture and vegetation optical depth using a multi-channel collaborative algorithm". In: *Remote Sensing of Environment* 257 (2021), p. 112321.

[67] Jean-Pierre Wigneron et al. "SMOS-IC data record of soil moisture and L-VOD: Historical development, applications and perspectives". In: *Remote Sensing of Environment* 254 (2021), p. 112238.

[68] Long Zhao et al. "The scale-dependence of SMOS soil moisture accuracy and its improvement through land data assimilation in the central Tibetan Plateau". In: *Remote sensing of environment* 152 (2014), pp. 345–355.

[69] Michael Berger et al. "Measuring the Moisture in the Earth's Soil-Advancing the Science with ESA's SMOS Mission". In: *ESA bulletin* 115 (2003), pp. 40–45.

[70] Dara Entekhabi et al. "The nasa soil moisture active passive (smap) mission formulation". In: *2011 IEEE International Geoscience and Remote Sensing Symposium*. IEEE. 2011, pp. 2302–2305.

[71] Konstantina Fotiadou et al. "Recovery of Soil Moisture Active Passive (SMAP) Instrument's Active Measurements via Coupled Dictionary Learning". In: *Electronic Imaging* 2018.15 (2018), pp. 229–1.

[72] Amen Al-Yaari et al. "Evaluating soil moisture retrievals from ESA's SMOS and NASA's SMAP brightness temperature datasets". In: *Remote sensing of environment* 193 (2017), pp. 257–273.

[73] Steven K Chan et al. "Assessment of the SMAP passive soil moisture product". In: *IEEE Transactions on Geoscience and Remote Sensing* 54.8 (2016), pp. 4994–5007.

[74] Pang-Wei Liu et al. "Assessing Disaggregated SMAP Soil Moisture Products in the United States". In: *IEEE Journal of Selected Topics in Applied Earth Observations and Remote Sensing* 14 (2021), pp. 2577–2592.

[75] Lanjie Zhang, Ruanyu Zhang, and Qiurui He. "Sea Surface Salinity Retrieval from Aquarius in the South China Sea Using Machine Learning Algorithm". In: *IGARSS 2020-2020 IEEE International Geoscience and Remote Sensing Symposium*. IEEE, pp. 5643–5646.

[76] DM Le Vine et al. "Aquarius: Status and recent results". In: *Radio Science* 49.9 (2014), pp. 709–720.

[77] Mehrez Zribi, Azza Gorrab, and Nicolas Baghdadi. "A new soil roughness parameter for the modelling of radar backscattering over bare soil". In: *Remote Sensing of Environment* 152 (2014), pp. 62–73.

[78] Yuan Liu. "On sensitivity analysis and estimation of soil moisture from radar responses". PhD thesis. Université de Strasbourg, 2016.

[79] Hari Shanker Srivastava et al. "Large-area soil moisture estimation using multi-incidence-angle RADARSAT-1 SAR data". In: *IEEE Transactions on Geoscience and Remote Sensing* 47.8 (2009), pp. 2528–2535.

[80] Ross Bryant et al. "Measuring surface roughness height to parameterize radar backscatter models for retrieval of surface soil moisture". In: *IEEE Geoscience and Remote Sensing Letters* 4.1 (2007), pp. 137–141.

[81] Amer Ahmed, Yun Zhang, and Sue Nichols. "Review and evaluation of remote sensing methods for soil-moisture estimation". In: *SPIE reviews* 2.1 (2011), p. 028001.

[82] Alex Stogryn. "Electromagnetic scattering from rough, finitely conducting surfaces". In: *Radio Science* 2.4 (1967), pp. 415–428.

[83] Stephen O Rice. "Reflection of electromagnetic waves from slightly rough surfaces". In: *Communications on pure and applied mathematics* 4.2-3 (1951), pp. 351–378.

[84] AG Voronovich. "Small-slope approximation in wave scattering by rough surfaces, Engl. Transl". In: *Sov. Phys. JETP* 62.1 (1985), pp. 65–70.

[85] Adrian K Fung, Zongqian Li, and Kun-Shan Chen. "Backscattering from a randomly rough dielectric surface". In: *IEEE Transactions on Geoscience and remote sensing* 30.2 (1992), pp. 356–369.

[86] Kun-Shan Chen et al. "Emission of rough surfaces calculated by the integral equation method with comparison to three-dimensional moment method simulations". In: *IEEE Transactions on Geoscience and Remote Sensing* 41.1 (2003), pp. 90–101.

[87] Yisok Oh, Kamal Sarabandi, Fawwaz T Ulaby, et al. "An empirical model and an inversion technique for radar scattering from bare soil surfaces". In: *IEEE transactions on Geoscience and Remote Sensing* 30.2 (1992), pp. 370–381.

[88] Yisok Oh, Kamal Sarabandi, and Fawwaz T Ulaby. "Semi-empirical model of the ensemble-averaged differential Mueller matrix for microwave backscattering from bare soil surfaces". In: *IEEE Transactions on Geoscience and Remote Sensing* 40.6 (2002), pp. 1348–1355.

[89] Pascale C Dubois, Jakob Van Zyl, and Ted Engman. "Measuring soil moisture with imaging radars". In: *IEEE transactions on geoscience and remote sensing* 33.4 (1995), pp. 915–926.

[90] Jiancheng Shi et al. "Estimation of bare surface soil moisture and surface roughness parameter using L-band SAR image data". In: *IEEE Transactions on Geoscience and Remote Sensing* 35.5 (1997), pp. 1254–1266.

[91] Davide Comite and Nazzareno Pierdicca. "Monostatic and bistatic scattering modeling of the anisotropic rough soil". In: *IEEE Transactions on Geoscience and Remote Sensing* 57.5 (2018), pp. 2543–2556.

[92] KS Chen, SK Yen, and WP Huang. "A simple model for retrieving bare soil moisture from radar-scattering coefficients". In: *Remote sensing of environment* 54.2 (1995), pp. 121–126.

[93] G D'urso and M Minacapilli. "A semi-empirical approach for surface soil water content estimation from radar data without a-priori information on surface roughness". In: *Journal of Hydrology* 321.1-4 (2006), pp. 297–310.

[94] Jamal Ezzahar et al. "Evaluation of backscattering models and support vector machine for the retrieval of bare soil moisture from Sentinel-1 data". In: *Remote Sensing* 12.1 (2020), p. 72.

[95] Millie Sikdar and Ian Cumming. "A modified empirical model for soil moisture estimation in vegetated areas using SAR data". In: *IGARSS 2004. 2004 IEEE International Geoscience and Remote Sensing Symposium*. Vol. 2. IEEE. 2004, pp. 803–806.

[96] Charles Elachi and Jakob J Van Zyl. *Introduction to the physics and techniques of remote sensing*. John Wiley & Sons, 2021.

[97] Marco Trommler et al. *Scientific information portal in the world wide web: the global soil moisture archive 1992-2000 from ERS scatterometer data*. na, 2002.

[98] He Wang et al. "Indian Ocean Crossing Swells: New Insights from "Fireworks" Perspective Using Envisat Advanced Synthetic Aperture Radar". In: *Remote Sensing* 13.4 (2021), p. 670.

[99] Filipe Aires et al. "Statistical approaches to assimilate ASCAT soil moisture information—I. Methodologies and first assessment". In: *Quarterly Journal of the Royal Meteorological Society* (2021).

[100] Alberto Moreira. *Synthetic aperture radar (SAR): Principles and applications*. 2013.

[101] Richard Bamler. "Principles of synthetic aperture radar". In: *Surveys in Geophysics* 21.2 (2000), pp. 147–157.

[102] Hugo Carreno-Luengo, Guido Luzi, and Michele Crosetto. "First evaluation of topography on GNSS-R: An empirical study based on a digital elevation model". In: *Remote Sensing* 11.21 (2019), p. 2556.

[103] Andres Calabia, Iñigo Molina, and Shuanggen Jin. "Soil Moisture Content from GNSS Reflectometry Using Dielectric Permittivity from Fresnel Reflection Coefficients". In: *Remote Sensing* 12.1 (2020), p. 122.

[104] Yan Jia et al. "Estimation of surface characteristics using GNSS LH-reflected signals: Land versus water". In: *IEEE Journal of Selected Topics in Applied Earth Observations and Remote Sensing* 9.10 (2016), pp. 4752–4758.

[105] Maria Paola Clarizia et al. "Analysis of CYGNSS data for soil moisture retrieval". In: *IEEE Journal of Selected Topics in Applied Earth Observations and Remote Sensing* 12.7 (2019), pp. 2227–2235.

[106] Jabir Shabbir Malik, Zhang Jingrui, and Najam Abbas Naqvi. "Soil moisture content estimation using GNSS reflectometry (GNSS-R)". In: *2017 Fifth International Conference on Aerospace Science & Engineering (ICASE)*. IEEE. 2017, pp. 1–9.

[107] Roger D De Roo and Fawwaz T Ulaby. "Bistatic specular scattering from rough dielectric surfaces". In: *IEEE Transactions on Antennas and Propagation* 42.2 (1994), pp. 220–231.

[108] DS Masters. "Surface remote sensing applications of GNSS bistatic radar: Soil moisture and aircraft altimetry". PhD thesis. Citeseer, 2004.

[109] Adriano Camps et al. "Sensitivity of TDS-1 GNSS-R reflectivity to soil moisture: Global and regional differences and impact of different spatial scales". In: *Remote Sensing* 10.11 (2018), p. 1856.

[110] Hyuk Park et al. "Analysis of spaceborne GNSS-R delay-Doppler tracking". In: *IEEE Journal of Selected Topics in Applied Earth Observations and Remote Sensing* 7.5 (2014), pp. 1481–1492.

[111] Valery U Zavorotny et al. "Tutorial on remote sensing using GNSS bistatic radar of opportunity". In: *IEEE Geoscience and Remote Sensing Magazine* 2.4 (2014), pp. 8–45.

[112] Manuel Martin-Neira et al. "A passive reflectometry and interferometry system (PARIS): Application to ocean altimetry". In: *ESA journal* 17.4 (1993), pp. 331–355.

[113] Alberto Alonso Arroyo et al. "Dual-polarization GNSS-R interference pattern technique for soil moisture mapping". In: *IEEE Journal of Selected Topics in Applied Earth Observations and Remote Sensing* 7.5 (2014), pp. 1533–1544.

[114] Nereida Rodriguez-Alvarez et al. "Land geophysical parameters retrieval using the interference pattern GNSS-R technique". In: *IEEE Transactions on Geoscience and Remote Sensing* 49.1 (2010), pp. 71–84.

[115] Valery L Mironov et al. "The use of navigation satellites signals for determination the characteristics of the soil and forest canopy". In: *2012 IEEE International Geoscience and Remote Sensing Symposium*. IEEE. 2012, pp. 7527–7529.

[116] Kristine M Larson et al. "Use of GPS receivers as a soil moisture network for water cycle studies". In: *Geophysical Research Letters* 35.24 (2008).

[117] Valery U Zavorotny et al. "A physical model for GPS multipath caused by land reflections: Toward bare soil moisture retrievals". In: *IEEE Journal of Selected Topics in Applied Earth Observations and Remote Sensing* 3.1 (2009), pp. 100–110.

[118] Scott Gleason et al. "Detection and processing of bistatically reflected GPS signals from low earth orbit for the purpose of ocean remote sensing". In: *IEEE Transactions on Geoscience and Remote Sensing* 43.6 (2005), pp. 1229–1241.

[119] Alejandro Egido et al. "Global navigation satellite systems reflectometry as a remote sensing tool for agriculture". In: *Remote Sensing* 4.8 (2012), pp. 2356–2372.

[120] Nazzareno Pierdicca et al. "GNSS reflections from bare and vegetated soils: Experimental validation of an end-to-end simulator". In: *2011 IEEE International Geoscience and Remote Sensing Symposium*. IEEE. 2011, pp. 4371–4374.

[121] Emiliano Ceraldi et al. "On the use of the specular direction copolarised ratio for the retrieval of soil dielectric constant". In: *IGARSS 2003. 2003 IEEE International Geoscience and Remote Sensing Symposium. Proceedings (IEEE Cat. No. 03CH37477)*. Vol. 7. IEEE. 2003, pp. 4144–4146.

[122] Shuanggen Jin, Xiaodong Qian, and X Wu. "Sea level change from BeiDou Navigation Satellite System-Reflectometry (BDS-R): first results and evaluation". In: *Global and Planetary Change* 149 (2017), pp. 20–25.

[123] Shuanggen Jin, GP Feng, and S Gleason. "Remote sensing using GNSS signals: Current status and future directions". In: *Advances in space research* 47.10 (2011), pp. 1645–1653.

[124] F Soulat et al. "Sea state monitoring using coastal GNSS-R". In: *Geophysical research letters* 31.21 (2004).

[125] Estel Cardellach et al. "Characterization of dry-snow sub-structure using GNSS reflected signals". In: *Remote Sensing of Environment* 124 (2012), pp. 122–134.

[126] Nereida Rodriguez-Alvarez et al. "Snow monitoring using GNSS-R techniques". In: *2011 IEEE International Geoscience and Remote Sensing Symposium*. IEEE. 2011, pp. 4375–4378.

[127] Dallas Masters et al. "GPS signal scattering from land for moisture content determination". In: *IGARSS 2000. IEEE 2000 International Geoscience and Remote Sensing Symposium. Taking the Pulse of the Planet: The Role of Remote Sensing in Managing the Environment. Proceedings (Cat. No. 00CH37120)*. Vol. 7. IEEE. 2000, pp. 3090–3092.

[128] E Cardellach et al. "GNSS-R ground-based and airborne campaigns for ocean, land, ice, and snow techniques: Application to the GOLD-RTR data sets". In: *Radio Science* 46.6 (2011).

[129] George A Hajj and Cinzia Zuffada. "Theoretical description of a bistatic system for ocean altimetry using the GPS signal". In: *Radio Science* 38.5 (2003).

[130] Fran Fabra et al. "Phase altimetry with dual polarization GNSS-R over sea ice". In: *IEEE Transactions on Geoscience and Remote Sensing* 50.6 (2011), pp. 2112–2121.

[131] n G Ruffini et al. "The Eddy Experiment: Accurate GNSS-R ocean altimetry from low altitude aircraft". In: *Geophysical research letters* 31.12 (2004).

[132] James L Garrison, Stephen J Katzberg, and Michael I Hill. "Effect of sea roughness on bistatically scattered range coded signals from the Global Positioning System". In: *Geophysical research letters* 25.13 (1998), pp. 2257–2260.

[133] Shuanggen Jin, Estel Cardellach, and Feiqin Xie. *GNSS remote sensing*. Vol. 16. Springer, 2014.

[134] Estel Cardellach et al. "Mediterranean balloon experiment: Ocean wind speed sensing from the stratosphere, using GPS reflections". In: *Remote Sensing of Environment* 88.3 (2003), pp. 351–362.

[135] Estel Cardellach and Antonio Rius. "A new technique to sense non-Gaussian features of the sea surface from L-band bi-static GNSS reflections". In: *Remote Sensing of Environment* 112.6 (2008), pp. 2927–2937.

[136] James L Garrison et al. "Wind speed measurement using forward scattered GPS signals". In: *IEEE Transactions on Geoscience and Remote Sensing* 40.1 (2002), pp. 50–65.

[137] Roberto Sabia et al. "Potential synergetic use of GNSS-R signals to improve the sea-state correction in the sea surface salinity estimation: Application to the SMOS mission". In: *IEEE Transactions on Geoscience and Remote Sensing* 45.7 (2007), pp. 2088–2097.

[138] Fran Fabra et al. "An empirical approach towards characterization of dry snowlayers using GNSS-R". In: *2011 IEEE International Geoscience and Remote Sensing Symposium*. IEEE. 2011, pp. 4379–4382.

[139] Attila Komjathy et al. "Sea ice remote sensing using surface reflected GPS signals". In: *IGARSS 2000. IEEE 2000 International Geoscience and Remote Sensing Symposium. Taking the Pulse of the Planet: The Role of Remote Sensing in Managing the Environment. Proceedings (Cat. No. 00CH37120)*. Vol. 7. IEEE. 2000, pp. 2855–2857.

[140] Maria Belmonte Rivas. "Bistatic scattering of global positioning system signals from Arctic sea ice". PhD thesis. Citeseer, 2007.

[141] Maria Belmonte Rivas, James A Maslanik, and Penina Axelrad. "Bistatic scattering of GPS signals off Arctic sea ice". In: *IEEE Transactions on Geoscience and Remote Sensing* 48.3 (2009), pp. 1548–1553.

[142] Francisco Martín et al. "Airborne soil moisture determination using a data fusion approach at regional level". In: *2011 IEEE International Geoscience and Remote Sensing Symposium*. IEEE. 2011, pp. 3109–3112.

[143] Nereida Rodriguez-Alvarez et al. "Airborne GNSS-R wind retrievals using delay–Doppler maps". In: *IEEE transactions on geoscience and remote sensing* 51.1 (2012), pp. 626–641.

[144] Alejandro Egido et al. "Airborne GNSS-R polarimetric measurements for soil moisture and above-ground biomass estimation". In: *IEEE Journal of Selected Topics in Applied Earth Observations and Remote Sensing* 7.5 (2014), pp. 1522–1532.

[145] Nilda Sánchez et al. "On the synergy of airborne GNSS-R and Landsat 8 for soil moisture estimation". In: *Remote Sensing* 7.8 (2015), pp. 9954–9974.

[146] Y Jia et al. "GNSS reflectometry for remote sensing of soil moisture". In: *2015 IEEE 1st International Forum on Research and Technologies for Society and Industry Leveraging a better tomorrow (RTSI)*. IEEE. 2015, pp. 498–501.

[147] Wei Wan et al. "Initial results of China's GNSS-R airborne campaign: soil moisture retrievals". In: *Science Bulletin* 60.10 (2015), pp. 964–971.

[148] Erwan Motte et al. "GLORI: A GNSS-R dual polarization airborne instrument for land surface monitoring". In: *sensors* 16.5 (2016), p. 732.

[149] Joan Francesc Munoz-Martin et al. "Single-Pass Soil Moisture Retrieval Using GNSS-R at L1 and L5 Bands: Results from Airborne Experiment". In: *Remote Sensing* 13.4 (2021), p. 797.

[150] Martin Unwin et al. "Spaceborne GNSS-reflectometry on TechDemoSat-1: Early mission operations and exploitation". In: *IEEE Journal of Selected Topics in Applied Earth Observations and Remote Sensing* 9.10 (2016), pp. 4525–4539.

[151] C Chew et al. "The sensitivity of ground-reflected GNSS signals to near-surface soil moisture, as recorded by spaceborne receivers". In: *2017 IEEE International Geoscience and Remote Sensing Symposium (IGARSS)*. IEEE. 2017, pp. 2661–2663.

[152] Adriano Camps et al. "Sensitivity of GNSS-R spaceborne observations to soil moisture and vegetation". In: *IEEE Journal of Selected Topics in Applied Earth Observations and Remote Sensing* 9.10 (2016), pp. 4730–4742.

[153] CC Chew and EE Small. "Soil moisture sensing using spaceborne GNSS reflections: Comparison of CYGNSS reflectivity to SMAP soil moisture". In: *Geophysical Research Letters* 45.9 (2018), pp. 4049–4057.

[154] Christopher S Ruf et al. "A new paradigm in earth environmental monitoring with the cygnss small satellite constellation". In: *Scientific reports* 8.1 (2018), pp. 1–13.

[155] Hugo Carreno-Luengo, Guido Luzi, and Michele Crosetto. "Impact of the elevation angle on CYGNSS GNSS-R bistatic reflectivity as a function of effective surface roughness over land surfaces". In: *Remote Sensing* 10.11 (2018), p. 1749.

[156] J. W. Betz and K. R. Kolodziejski. "Generalized Theory of Code Tracking with an Early-Late Discriminator Part I: Lower Bound and Coherent Processing". In: *IEEE Transactions on Aerospace and Electronic Systems* 45.4 (2009), pp. 1538–1556. ISSN: 0018-9251. DOI: 10.1109/TAES.2009.5310316.

[157] J. W. Betz and K. R. Kolodziejski. "Generalized Theory of Code Tracking with an Early-Late Discriminator Part II: Noncoherent Processing and Numerical Results". In: *IEEE Transactions on Aerospace and Electronic Systems* 45.4 (2009), pp. 1557–1564. ISSN: 0018-9251. DOI: 10.1109/TAES.2009.5310317.

[158] C. J. Comp and P. Axelrad. "Adaptive SNR-based carrier phase multipath mitigation technique". In: *IEEE Transactions on Aerospace and Electronic Systems* 34.1 (1998), pp. 264–276. ISSN: 0018-9251. DOI: 10.1109/7.640284.

[159] SA Weaver et al. *Data from: How a GNSS receiver is held may affect static horizontal position accuracy*. 2015. DOI: doi:10.5061/dryad.8j616. URL: https://doi.org/10.5061/dryad.8j616.

[160] Mohinder S Grewal, Lawrence R Weill, and Angus P Andrews. *Global positioning systems, inertial navigation, and integration*. John Wiley & Sons, 2007.

[161] B. W. Parkinson and J. Spilker. *Global Positioning System: Theory and Applications Volume 1*. American Institute of Aeronautics and Astronautics, Washington, 1996.

[162] E. Kaplan and C. Hegarty. *Understanding GPS: Principles and Applications*. Artech House, 2005. ISBN: 9781580538954. URL: https://books.google.fr/books?id=-sPXPuOW7ggC.

[163] P Huang, Y Pi, and I Progri. "GPS signal detection under multiplicative and additive noise". In: *The Journal of Navigation* 66.4 (2013), pp. 479–500.

[164] Maherizo Andrianarison. "New methods and architectures for high sensitivity hybrid GNSS receivers in challenging environments". PhD thesis. École de technologie supérieure, 2018.

[165] Marco Pini, Emanuela Falletti, and Maurizio Fantino. "Performance evaluation of C/N0 estimators using a real time GNSS software receiver". In: *2008 IEEE 10th International Symposium on Spread Spectrum Techniques and Applications*. IEEE. 2008, pp. 32–36.

[166] John W Betz. "Effect of narrowband interference on GPS code tracking accuracy". In: *Proceedings of the 2000 National Technical Meeting of The Institute of Navigation*. 2000, pp. 16–27.

[167] Mohammad Zahidul H Bhuiyan et al. "Performance evaluation of carrier-to-noise density ratio estimation techniques for BeiDou Bl signal". In: *2014 Ubiquitous Positioning Indoor Navigation and Location Based Service (UPINLBS)*. IEEE. 2014, pp. 19–25.

[168] Sergio Benedetto and Ezio Biglieri. *Principles of digital transmission: with wireless applications*. Springer Science & Business Media, 1999.

[169] James J Spilker Jr et al. *Global positioning system: theory and applications, volume I*. American Institute of Aeronautics and Astronautics, 1996.

[170] Emanuela Falletti, Marco Pini, and Letizia Lo Presti. "Low complexity carrier-to-noise ratio estimators for GNSS digital receivers". In: *IEEE transactions on aerospace and electronic systems* 47.1 (2011), pp. 420–437.

[171] Michelle Marie Sayre. "Development of a block processing carrier to noise ratio estimator for the global positioning system". PhD thesis. Ohio University, 2003.

[172] Paul D Groves. "GPS Signal-to-Noise Measurement in Weak Signal and High-Interference Environments". In: *Navigation* 52.2 (2005), pp. 83–94.

[173] Xia Xue, Honglei Qin, and Hui Lu. "Signal power calibration of complex urban kinematic navigation system simulator based on C/N0 estimation". In: *Measurement* 136 (2019), pp. 415–428.

[174] Mohammad S Sharawi, Dennis M Akos, and Daniel N Aloi. "GPS C/N_0 estimation in the presence of interference and limited quantization levels". In: *IEEE transactions on aerospace and electronic systems* 43.1 (2007), pp. 227–238.

[175] Mark L Psiaki, Dennis M Akos, and Jonas Thor. "A comparison of" direct RF sampling" and" downconvert & sampling" GNSS receiver architectures". In: *Proceedings of the 16th International Technical Meeting of the Satellite Division of The Institute of Navigation (ION GPS/GNSS 2003)*. 2003, pp. 1941–1952.

[176] Norman C Beaulieu, Andrew S Toms, and David R Pauluzzi. "Comparison of four SNR estimators for QPSK modulations". In: *IEEE communications letters* 4.2 (2000), pp. 43–45.

[177] David R Pauluzzi and Norman C Beaulieu. "A comparison of SNR estimation techniques for the AWGN channel". In: *IEEE Transactions on communications* 48.10 (2000), pp. 1681–1691.

[178] Marc-Antoine Fortin. "Robustness Techniques for Global Navigation Satellite Systems (GNSS) Receivers". PhD thesis. École de technologie supérieure, 2015.

[179] M Petovello. "Carrier-to-noise density and AI for INS/GPS integration". In: *Inside GNSS* 4.5 (2009), pp. 20–29.

[180] Stefano Cioni, Giovanni E Corazza, and Michel Bousquet. "An analytical characterization of maximum likelihood signal-to-noise ratio estimation". In: *2005 2nd International Symposium on Wireless Communication Systems*. IEEE. 2005, pp. 827–830.

[181] R Gagliardi and C Thomas. "PCM data reliability monitoring through estimation of signal-to-noise ratio". In: *IEEE Transactions on Communication Technology* 16.3 (1968), pp. 479–486.

[182] Kannan Muthuraman and Daniele Borio. "C/N0 Estimation for Modernized GNSS Signals: Theoretical Bounds and Novel Iterative Estimator". In: *NAVIGATION, Journal of the Institute of Navigation* 57.4 (2010), pp. 309–323.

[183] S. Satyanarayana, D. Borio, and G. Lachapelle. "C/N0 estimation: design criteria and reliability analysis under global navigation satellite system (GNSS) weak signal scenarios". In: *IET Radar, Sonar Navigation* 6.2 (2012), pp. 81–89. ISSN: 1751-8784. DOI: 10.1049/iet-rsn.2011.0164.

[184] Shashank Satyanarayana, Daniele Borio, and Gérard Lachapelle. "C/N0 estimation: design criteria and reliability analysis under global navigation satellite system (GNSS) weak signal scenarios". In: *IET Radar, Sonar & Navigation* 6.2 (2012), pp. 81–89.

[185] Eugene F Knott. *Radar cross section measurements*. Springer Science & Business Media, 2012.

[186] Valery U Zavorotny and Alexander G Voronovich. "Bistatic GPS signal reflections at various polarizations from rough land surface with moisture content". In: *IGARSS 2000. IEEE 2000 International Geoscience and Remote Sensing Symposium. Taking the Pulse of the Planet: The Role of Remote Sensing in Managing the Environment. Proceedings (Cat. No. 00CH37120)*. Vol. 7. IEEE. 2000, pp. 2852–2854.

[187] Georges Stienne et al. "Cycle slip detection and repair with a circular on-line change-point detector". In: *Signal processing* 100 (2014), pp. 51–63.

[188] Michèle Basseville and Igor V. Nikiforov. *Detection of Abrupt Changes - Theory and Application*. Prentice Hall, Inc., 1993, p. 550.

[189] Fredrik. Gustafsson. *Adaptive filtering and change detection*. John Wiley & Sons Ltd, 2000, p. 500.

[190] E. S. PAGE. "CONTINUOUS INSPECTION SCHEMES". In: *Biometrika* 41.1-2 (June 1954), pp. 100–115.

[191] Samaneh Aminikhanghahi and Diane J Cook. "A survey of methods for time series change point detection". In: *Knowledge and information systems* 51.2 (2017), pp. 339–367.

[192] Ryan Prescott Adams and David JC MacKay. "Bayesian online changepoint detection". In: *arXiv preprint arXiv:0710.3742* (2007).

[193] F. Desobry, M. Davy, and C. Doncarli. "An online kernel change detection algorithm". In: *IEEE Transactions on Signal Processing* 53.8 (2005), pp. 2961–2974. DOI: 10.1109/TSP.2005.851098.

[194] Gerrit JJ van den Burg and Christopher KI Williams. "An evaluation of change point detection algorithms". In: *arXiv preprint arXiv:2003.06222* (2020).

[195] Charles Truong, Laurent Oudre, and Nicolas Vayatis. "Selective review of offline change point detection methods". In: *Signal Processing* 167 (2020), p. 107299.

[196] Venkata Jandhyala et al. "Inference for single and multiple change-points in time series". In: *Journal of Time Series Analysis* 34.4 (2013), pp. 423–446.

[197] Siddhartha Chib. "Estimation and comparison of multiple change-point models". In: *Journal of econometrics* 86.2 (1998), pp. 221–241.

[198] Alan S. Willsky and Harold L. Jones. "A generalized likelihood ratio approach to the detection and estimation of jumps in linear systems". In: *IEEE Transactions on Automatic Control* 21 (1976), pp. 108–112.

Résumé Étendu de la Thèse

L'eau contenue dans les sols et plans d'eau est un paramètre clé du cycle hydrologique [1, 2]. Les zones inondables et les plans d'eau couvrent au moins 8% des paysages sur Terre [8, 9]. Malgré son rôle important, peu de connaissances ont été acquises concernant l'eau stockée dans les zones humides jusqu'à ce que les techniques de télédétection apparaissent comme des instruments potentiels.

La Réflectométrie GNSS (GNSS-R) est une technique de télédétection bistatique émergente qui utilise les signaux des Systèmes Globaux de Navigation par Satellites (principalement les signaux GPS, en bande L) comme sources d'opportunité pour caractériser la surface terrestre. Un capteur GNSS-R reçoit les signaux GNSS directs des satellites ainsi que les signaux réfléchis par la surface de la Terre. Les signaux réfléchis transportent des informations sur la surface réfléchissante.

En GNSS-R, l'humidité du sol peut être obtenue à partir des mesures de réflectivité. Ces mesures sont directement liées aux amplitudes des signaux GNSS. Le rapport entre le niveau de puissance de la porteuse reçue et le niveau de puissance du bruit peut être utilisé pour observer l'amplitude du signal GNSS. Ce rapport est appelé rapport porteuse sur densité de bruit (C/N_0) lorsque la puissance du bruit est définie pour une unité de largeur de bande. Il s'agit d'une mesure normalisée du rapport signal à bruit (SNR).

Cette thèse est consacrée à l'étude de techniques GNSS-R pour la détection de plans d'eau à l'aide d'un capteur aéroporté à basse altitude. Nous estimons à un rythme élevé les amplitudes des signaux GNSS directs et réfléchis, à partir desquels la réflectivité de la surface est dérivée. Nous développons un capteur GNSS-R aéroporté léger permettant de répondre aux exigences de haute résolution temporelle et spatiale de notre application. Les signaux GNSS sont segmentés en parties stationnaires sur la base des ruptures dans les mesures de réflectivité associées aux différentes zones de réflexion. Les objectifs généraux et les contributions de ce travail peuvent être résumés

comme suit :

- Développement de techniques de traitement des signaux GNSS pour la réflectométrie aéroportée. Ces techniques impliquent l'acquisition, la poursuite et la datation des données GNSS brutes dans des configurations classiques et maître-esclave.
- Développement d'un nouveau modèle probabiliste utilisant des techniques de traitement du signal GNSS dédiées pour l'estimation en ligne des amplitudes du signal GNSS et, par conséquent, du rapport C/N_0 à un rythme élevé.
- Développement d'un nouveau système de segmentation des signaux GNSS qui associe des outils préexistants avec les techniques proposées pour différencier les surfaces des plans d'eau dans les reliefs.
- Évaluation des systèmes et méthodologies proposés sur données réelles. Les données sont enregistrées à l'aide d'un capteur GNSS conçu pour ce travail.
- Mise en œuvre d'une nouvelle analyse quantitative pour la détection des plans d'eau et la localisation de leurs bords à l'aide de la technique radar proposée, appliquée des données recueillies durant le vol.

Les techniques développées sont présentées dans ce manuscrit à travers cinq chapitres. Dans le premier chapitre, nous présentons brièvement la constante diélectrique du sol et les modèles d'émissions permettant de calculer la teneur en humidité du sol. Un intérêt particulier est porté au principe de GNSS-R dans ce chapitre. Les différentes configurations géométriques des systèmes GNSS-R sont discutées en détail. Nous présentons également les différentes applications du GNSS-R et les principales méthodes de traitement du signal utilisées dans son cadre.

Le deuxième chapitre présente une revue de la littérature sur les différentes techniques d'estimation du rapport porteuse sur densité de bruit et leur application à la détermination de l'humidité du sol par GNSS-R. Ce chapitre présente le modèle des signaux GNSS, ainsi que le traitement GNSS front-end pour aboutir à l'expression du rapport porteuse sur densité de bruit. Ce chapitre étudie également les différents algorithmes d'estimation de C/N_0 qui ont été publiés dans la littérature au cours des dernières décennies.

Dans le troisième chapitre, nous proposons un modèle qui estime le rapport C/N_0 à un rythme élevé afin de maximiser la résolution temporelle des observations. Nous montrons dans ce chapitre que, dans un récepteur à quantification 1 bit, la composante en phase du signal peut fournir une observation directe de l'amplitude. Nous proposons un filtre de Kalman étendu pour inverser l'expression non linéaire qui lie les amplitudes des signaux, variables dans le temps, avec les observations bruitées de la corrélation fournies par la boucle de poursuite. Nous montrons que l'estimateur d'amplitude GNSS proposé fournit des résultats similaires à un récepteur GNSS scientifique du commerce, mais avec un débit de données beaucoup plus élevé.

Dans le quatrième chapitre, nous proposons un modèle de segmentation qui divise les signaux GNSS en parties stationnaires associées à différentes zones de réflexion. Des ruptures d'amplitude des signaux GNSS réfléchis se produisent lorsque les empreintes des satellites évoluent d'un type de surface de réflexion à un autre. Nous proposons un algorithme qui localise les ruptures détectés dans le signal dans une fenêtre de travail optimale. Nous proposons également un algorithme de fusion afin de diminuer le nombre de fausses détections de rupture. Ce chapitre se termine par l'évaluation des performances du système proposé sur données synthétiques et par l'évaluation de ses performances sur des données GNSS aéroportées réelles.

Le cinquième chapitre est consacré à l'expérimentation GNSS-R aéroportée réalisée dans le cadre de ce travail ainsi qu'à ses résultats. Dans ce chapitre, nous présentons la configuration GNSS-R aéroportée, les techniques de traitement ainsi que le matériel GNSS-R utilisés pour localiser les observations GNSS-R. Nous évaluons l'architecture récepteur logiciel développée dans ce travail de thèse pour le traitement des données GNSS aéroportées. Nous exposons la capacité de l'approche proposée à détecter les plans d'eau à l'intérieur des terres. Il est démontré que la technique proposée permet de localiser au mètre près les bords des surfaces des plans d'eau détectés.

Dans ce qui suit, nous présentons les principales contributions de cette thèse à travers une série de brèves sections.

1 Modèle GNSS front-end

1.1 Traitement front-end des signaux GNSS

Cette section est consacrée au traitement front-end du signal GPS L1 C/A. Considérons le signal GPS C/A $s(t)$ après descente à une fréquence intermédiaire f_{IF} :

$$s(t) = \sum_{l \in V} K\, A_l CA_l(t + \tau_l) \sin(2\pi f_l\, t + \phi_l) + K\, \eta(t) \tag{1}$$

où V est l'ensemble des satellites visibles, $A_l(t)$ est l'amplitude du signal, K est le gain du contrôle automatique (AGC), et τ est le retard de code. f_l et ϕ_l sont respectivement la fréquence et le retard de phase de la porteuse avec $f_l = f_{IF} + f_l^D$, $\eta(t)$ est un bruit additif Gaussien de moyenne nulle de variance unitaire. Le signal $s(t)$ après numérisation peut s'exprimer comme suit :

$$s_i \;= \sum_{l \in V} K A_l CA_l(t_i + \tau_l) \sin(2\pi f_l\, t_i + \phi_l) + K\eta_i \tag{2}$$

Un front-end fournit une composante en phase et une composante en quadrature du signal reçu à l'aide de répliques locales. Les répliques locales synchronisées (Prompt) avec le signal reçu sont définies pour un satellite v par :

$$ci_{v,i} \;= CA_v(t_i + \tau_v) \sin(2\pi f_v\, t_i + \phi_v) \tag{3}$$

$$cq_{v,i} \;= CA_v(t_i + \tau_v) \cos(2\pi f_v\, t_i + \phi_v) \tag{4}$$

où t_i est l'instant associé à la fréquence d'échantillonnage f_s et τ_v est le retard du code. f_v et ϕ_v sont respectivement les estimées de la fréquence et du retard de phase de la porteuse.

La composante en phase de la corrélation I_v et la composante en quadrature Q_v pour chaque satellite v sont obtenues en intégrant les signaux échantillonnés sur le temps d'intégration cohérent T_c. Les échantillons accumulés en phase, I, et en quadrature, Q, du corrélateur prompt sont exprimés comme suit :

$$I_v = \sum_{i=1}^{f_s\ T_c} s_i\ ci_{v,i} \tag{5}$$
$$Q_v = \sum_{i=1}^{f_s\ T_c} s_i\ cq_{v,i} \tag{6}$$

Les résultats de corrélation des canaux prompt I et Q sont ensuite transmis aux algorithmes d'estimation de rapport C/N_0.

1.2 Dérivation de l'expression du rapport porteuse sur densité de bruit

Le rapport signal sur bruit SNR est dérivé des propriétés statistiques des deux composantes du signal de corrélation. En supposant que le code local et la porteuse sont parfaitement alignés avec les signaux reçus, les équations (5) et (6) peuvent être écrites comme suit :

$$I_v = \frac{K\ A_v\ f_s\ T_c}{2} + K\ \eta_v^I \tag{7}$$
$$Q_v = K\ \eta_v^Q \tag{8}$$

où η_v^I et η_v^Q sont des bruits aléatoires distribués selon une distribution gaussienne centrée de variance $\frac{f_s\ T_c}{2}$. Alors, une définition classique du SNR est donnée par :

$$SNR = \left(\frac{mean(I_v)}{std(Q_v)}\right)^2 = \frac{A_v^2\ f_s\ T_c}{2} \tag{9}$$

Dans cette équation, le SNR est proportionnel au carré de l'amplitude du signal et indépendant de K, le gain de l'AGC. Le rapport porteuse sur densité de bruit peut alors être exprimé en dB-Hz comme suit:

$$C/N_0^k = 20\log\left(\frac{A_v\ \sqrt{f_s\ T_c}}{\sqrt{2}}\right) + 10\log\left(BW\right) \tag{10}$$

où $\frac{A_v}{\sqrt{2}}$ est la valeur efficace de tension du signal et BW est la largeur de bande équivalente au bruit de l'étage d'entrée RF du récepteur. C'est cette équation qui est utilisée dans notre travail pour dériver le rapport C/N_0 à partir des estimations d'amplitude.

1.3 Modèle front-end GNSS à un bit

La Figure 1 montre le schéma fonctionnel de traitement de la composante en phase dans un récepteur front-end GNSS. Dans notre approche, une quantification de 1 bit est appliquée.

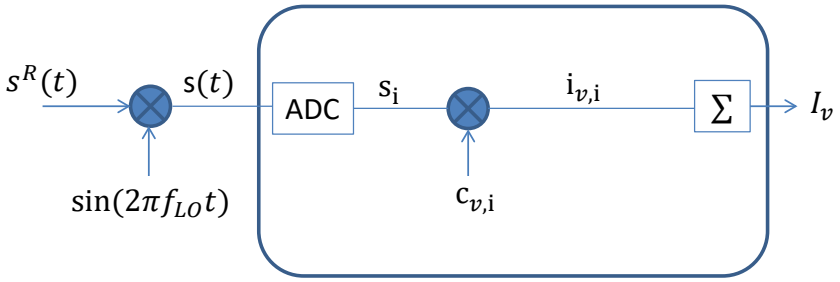

FIGURE 1: Schéma fonctionnel du récepteur radiofréquence GNSS.

Les expressions des signaux de la Figure 1 sont définies après numérisation par :

$$s_i = \left\lfloor \sum_{l \in V} KA_l CA_l(t_i + \tau_l) \sin(2\pi f_l \, t_i + \phi_l) + K\eta_i \right\rfloor_{>0} \tag{11}$$

$$c_{v,i} = \lfloor CA_v(t_i + \tau_v) \sin(2\pi f_v \, t_i + \phi_v) \rfloor_{>0} \tag{12}$$

où s_i et $c_{v,i}$ sont respectivement le signal numérisé et la réplique locale. $\lfloor \ldots \rfloor_{>0}$ est une fonction de signe qui associe -1 aux valeurs négatives du signal et +1 aux valeurs positives ou nulles.

Nous définissons $i_{v,i} = s_i \, c_{v,i}$ comme prenant la valeur +1 lorsque s_i est égal à $c_{v,i}$ et -1 lorsqu'ils sont différents. Définissons la valeur moyenne de $i_{v,i}$ comme :

$$\begin{aligned} E(i_{v,i}) &= \sum_{x \in \{-1,1\}} x \, P(i_{v,i} = x) \\ &= 2 \, P(i_{v,i} = 1) - 1 \end{aligned} \tag{13}$$

où $P(i_{v,i} = x)$ est la probabilité que $i_{v,i} = s_i \, c_{v,i}$ prenne la valeur x. Dans notre modèle GNSS front-end, les échantillons de bruit $i_{v,i}$ sont intégrés sur une période de code CDMA ($T_c = 1 \; ms$). En supposant que les valeurs aléatoires de $i_{v,i}$ sont identiquement distribuées, nous dérivons la valeur moyenne de I_v comme suit :

$$E(I_v) = E(i_{v,i})\ T_c f_s \tag{14}$$

où $T_c f_s$ est le nombre d'échantillons intégrés sur une période de code. $E(I_v)$ est défini par la probabilité $P(i_{v,i} = 1)$. Nous montrons dans la section 2.1 que cette probabilité est une fonction de A_v.

2 Estimation de l'amplitude du signal GNSS

2.1 Linéarisation de l'équation de mesure

Construisons le modèle d'approximation suivant du signal échantillonné du satellite v après numérisation :

$$\hat{s}_i = \sum_{v \in V} A_v CA_v(t_i + \hat{\tau}_v) \sin(2\pi \hat{f}_v\ t_i + \hat{\phi}_v) \tag{15}$$

$$s_i \approx \lfloor \hat{s}_i + \eta_i \rfloor_{>0} \tag{16}$$

and

$$c_{v,i} \approx \left\lfloor CA_v(t_i + \hat{\tau}_v) \sin(2\pi \hat{f}_v\ t_i + \hat{\phi}_v) \right\rfloor_{>0} \tag{17}$$

La probabilité que la variable aléatoire $i_{v,k}$ prenne la valeur +1 s'écrit comme suit :

$$\begin{aligned} P\left(i_{v,i} = 1\right) &= P\left(c_{v,i} = 1\right) P\left(\eta_i \geq -\hat{s}_i / c_{v,i} = 1\right) \\ &+ P\left(c_{v,i} = -1\right) P\left(\eta_i < -\hat{s}_i / c_{v,i} = -1\right) \end{aligned} \tag{18}$$

Une estimation de la probabilité que la réplique locale soit positive peut alors être écrite comme suit :

$$P\left(c_{v,i} = 1\right) = \frac{\sum_{i=1}^{f_s T_c} (c_{v,i} + 1)}{2 f_s T_c} \tag{19}$$

$P(c_{v,i} = -1)$ peut se calculer de manière similaire. Une estimée de la première probabilité de l'expression (18) associée au bruit aléatoire additif sur le signal est définie par :

$$P\left(\eta \geq -\hat{s}_i / c_{v,i} = 1\right) = \frac{2}{\sum_{i=1}^{f_s T_c} (c_{v,i} + 1)} \sum_{\{\tilde{i}\}_v^1} P(\eta \geq -\hat{s}_i) \tag{20}$$

où l'ensemble $\{\tilde{i}\}_v^1$ est constitué des valeurs de i telles que $c_{v,i} = 1$. La probabilité $P(\eta \geq -\hat{s}_i)$ est traitée avec la fonction d'erreur tabulée $erfc$ comme suit :

$$\begin{aligned} \sum_{\{\tilde{i}\}_v^1} P(\eta \geq -\hat{s}_i) &= \sum_{\{\tilde{i}\}_v^1} \int_{-\hat{s}_i}^{+\infty} \frac{1}{\sqrt{2\pi}} exp(\frac{-x^2}{2})\, dx \\ &= \sum_{\{\tilde{i}\}_v^1} \frac{1}{2} erfc\left(\frac{-\hat{s}_i}{\sqrt{2}}\right) \end{aligned} \tag{21}$$

L'estimée de la deuxième probabilité de l'expression (18) associée au bruit aléatoire additif sur le signal peut être dérivée comme l'expression (20) sur l'ensemble $\{\tilde{i}\}_v^2$ qui définit les valeurs de l'indice i telles que $c_{v,i} = -1$. Selon les équations (14), (14) et (18), nous dérivons l'expression suivante pour la fonction de mesure non linéaire $h(...)$:

$$\begin{aligned} h_{v,k}\left(\{A_{v,k}\}_{v\in V}; \{\theta_{v,k}\}_{v\in V}\right) &= \sum_{\{\tilde{i}\}_{v,k}^1} erfc\left(\frac{-\hat{s}_i}{\sqrt{2}}\right) \\ &- \sum_{\{\tilde{i}\}_{v,k}^2} erfc\left(\frac{-\hat{s}_i}{\sqrt{2}}\right) + \sum_{i=1}^{f_s T_c} |c_{v,i} - 1| - T_c f_s \end{aligned}$$

où $\theta_{v,k} = \{\hat{\tau}_{v,k}, \hat{f}_{v,k}, \hat{\phi}_{v,k}\}$ désigne les paramètres du signal GNSS fournis par la boucle à verrouillage de phase (PLL) et la boucle à verrouillage de délai de code (DLL) du récepteur. Le signal GPS étant de très faible rapport SNR, les valeurs de $\hat{s}_i$ sont faibles. L'approximation de Taylor suivante de la fonction tabulée peut dans ce cas être utilisée afin de linéariser l'expression :

$$erfc(x) \approx 1 - \frac{2}{\sqrt{\pi}} x \tag{22}$$

Après simplification, nous développons l'expression de $\hat{s}_i$ pour trouver une expression linéaire entre $I_{v,k}$ et $A_{v,k}$. Ainsi, pour un ensemble V de n satellites en vue, nous avons l'équation linéaire suivante :

$$I_{V,k} \approx HA_{V,k} + \omega_k \tag{23}$$

avec $I_{V,k} = [I_{1,k}, \ldots, I_{n,k}]^T$ et $A_{V,k} = [A_{1,k}, \ldots, A_{n,k}]^T$. H est une matrice qui représente la contribution des satellites dans $I_{v,k}$ et ω_k est un bruit gaussien. Nous présentons sur la Figure 2 les différents éléments de H. Pour une composante $I_{i,k}$, $h_{i,i}$ est la contribution de corrélation du signal du satellite i et $h_{i,j}$ est la contribution d'inter-corrélation avec le signal du satellite j. $h_{i,\forall j}$ est la contribution globale de tous les satellites dans $I_{i,k}$.

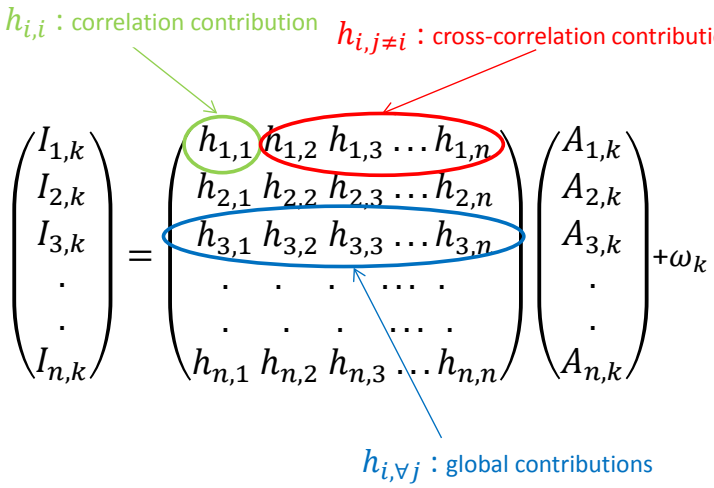

FIGURE 2: Contribution de chaque satellite dans les $I_{v,k}$.

2.2 Estimation Kalman étendue de l'amplitude du signal

Nous proposons un filtre d'état sous la forme d'un filtre de Kalman étendu qui utilise les composantes de corrélation du signal GNSS comme observations pour fournir des estimations de l'amplitude du signal GNSS à un taux de 1 *ms*, période du code CDMA. Nous supposons que les amplitudes sont constantes pendant cette durée. Le taux de variation de $A_{v,k}$ est noté $\dot{A}_{v,k}$. Nous considérons les équations d'état linéaires suivantes pour satellite v :

$$A_{v,k} = A_{v,k-1} + T_c \dot{A}_{v,k-1} + \nu_{1,k} \tag{24}$$

$$\dot{A}_{v,k} = \dot{A}_{v,k-1} + \nu_{2,k} \tag{25}$$

$\nu_{1,k}$, $\nu_{2,k}$ représentent les erreurs sur le modèle. Ils sont respectivement le bruit d'état sur l'amplitude et le bruit d'état sur les variations d'amplitude. L'équation de mesure non linéaire est définie par :

$$I_{v,k} = h\left(\{A_{v,k}\}_{v\in V}; \{\theta_{v,k}\}_{v\in V}\right) + \omega_k \tag{26}$$

où $h(...)$ est une fonction non linéaire et ω_k est un bruit gaussien de variance R. $\theta_{v,k} = \{\hat{\tau}_{v,k}, \hat{f}_{v,k}, \hat{\phi}_{v,k}\}$ désigne les paramètres du signal GNSS fournis par la boucle à verrouillage de phase (PLL) et la boucle à verrouillage de délai (DLL) du récepteur. Le principe de l'architecture du récepteur est présenté dans la Figure 3.

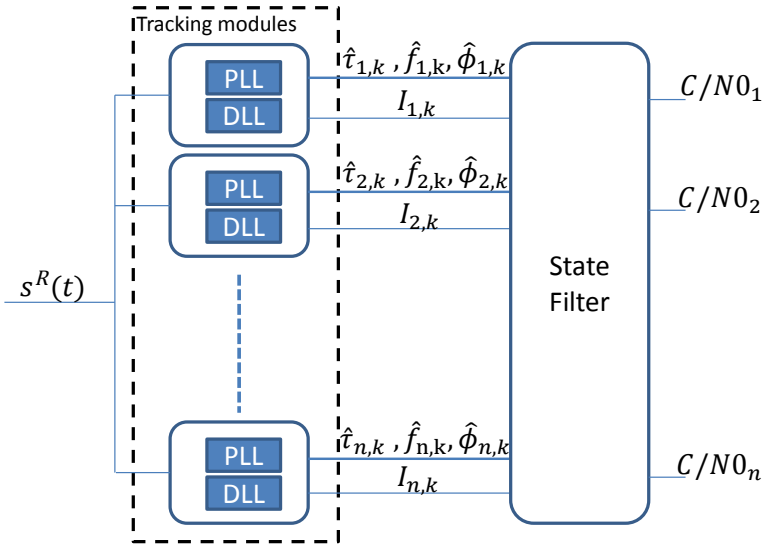

FIGURE 3: Implémentation de l'estimation proposée dans un récepteur GNSS.

2.3 Evaluation sur données réelles

L'objectif de cette expérimentation est d'évaluer l'estimateur d'amplitude proposé, qui utilise un récepteur GNSS à quantification 1 bit, sur des signaux GPS L1 C/A. L'évaluation est réalisée en comparant le rapport porteuse sur densité de bruit C/N_0^k obtenu en utilisant l'approche proposée avec le rapport porteuse sur densité de bruit C/N_0^r fourni par le récepteur GNSS OEM7 NovAtel. Nous calculons l'estimation de C/N_0^k en utilisant l'équation (10), où les amplitudes des signaux sont fournies par le filtre de Kalman toutes

les 1 ms. Nous montrons sur la Figure 4, les estimations de C/N_0^r fournies chaque seconde et les estimations de C/N_0^k fournies chaque milliseconde pour différents satellites. Nous rapportons également les observations du rapport porteuse sur densité de bruit C/N_0^o obtenues chaque milliseconde en utilisant les amplitudes dérivées de l'équation (23).

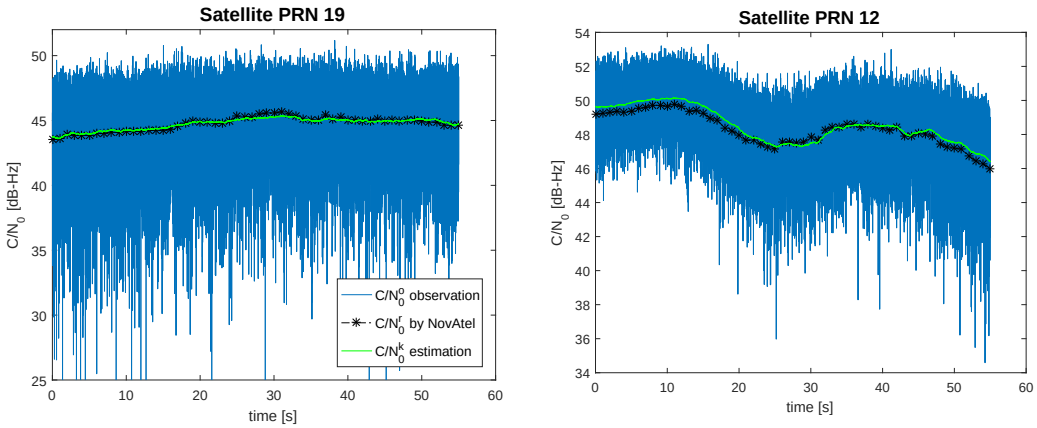

FIGURE 4: Évaluation de l'estimation du rapport C/N_0.

Les résultats obtenus montrent un bon accord entre le rapport porteuse sur densité de bruit C/N_0^r fourni par le récepteur GNSS NovAtel et le rapport C/N_0^k estimé par notre approche dans différents scénarios. Par conséquent, nous concluons que notre approche peut fournir une précision similaire à celle du récepteur GNSS de NovAtel. Cependant, le modèle proposé fournit des estimations de C/N_0 à un taux beaucoup plus élevé (1000 Hz) que le récepteur GNSS NovAtel (1 Hz).

3 Segmentation des signaux GNSS

3.1 Modèle de transition

Les amplitudes des signaux GNSS réfléchis sont directement proportionnelles à la réflectivité de la première zone de Fresnel de réflexion des signaux satellitaires. Un modèle de transition est adapté pour caractériser les ruptures d'amplitudes des signaux GNSS réfléchis associées au déplacement des empreintes des satellites d'un type de surface à un autre. Nous montrons sur la Figure 5, le modèle de signal dans la fenêtre de travail.

Dans ce modèle, lorsque la réflexion se produit sur un premier type de surface, la valeur moyenne de l'amplitude du signal GNSS est égale à m_1. La

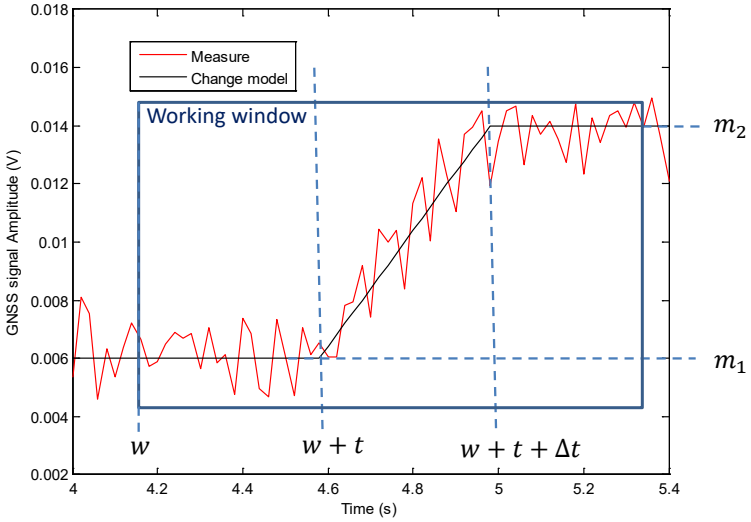

FIGURE 5: Modèle de signal dans une fenêtre de travail.

valeur moyenne de l'amplitude du signal GNSS atteint ensuite la valeur m_2 à mesure que la réflexion passe sur un deuxième type de surface.

3.2 Système de détection de rupture en ligne/hors ligne

3.2.1 Détection et localisation de rupture

Une approche Kalman CUSUM est utilisée pour détecter les ruptures en ligne en utilisant l'innovation du filtre [190]. Le détecteur CUSUM, cependant, ne détecte une rupture qu'après sa position réelle. Nous proposons un estimateur de localisation par maximum de vraisemblance (MLLE) pour un géo-positionnement précis des bords des surfaces scannées. L'estimation proposée est proche de l'optimalité car nous maximisons les tailles des fenêtres de travail dans lesquelles les ruptures détectées sont localisés.

Selon le modèle de signal de la Figure 5 et en supposant que le bruit additif est un bruit blanc gaussien de moyenne nulle, nous dérivons une estimation du maximum de vraisemblance de t, l'instant de départ de la transition, et de Δt, la durée de la transition. Les estimations sont traitées avec les observations des amplitudes des signaux GNSS dans la fenêtre de travail $(\tilde{x}_{\hat{n}^e_{i-1}}, \ldots, \tilde{x}_{\hat{t}^a_{i+1}})$. Les observations de l'amplitude GNSS $\tilde{x}_k$ sont obtenues à l'aide de l'expression (23). $\hat{n}^e_i$ est la localisation de la i^{ime} rupture pour le satellite l et $\hat{t}^a_i$ est le i^{ime} instant de rupture fourni par le détecteur CUSUM. N est le nombre d'échantillons dans la fenêtre de travail définie entre n^e_{i-1} et t^a_{i+1}. Pour estimer l'instant de rupture localisé n^e_i, nous définissons la fonction de vraisemblance comme suit :

$$
\begin{aligned}
f(\tilde{X}_{n_{i-1}^e}, \ldots, \tilde{X}_{t_{i+1}^a}) \quad = \quad & \frac{1}{(\sigma_1\sqrt{2\pi})^t} \exp\left(-\frac{\sum_{n=n_{i-1}^e}^{n_{i-1}^e+t-1}(\tilde{x}_n - m_1)^2}{2\sigma_1^2}\right) \\
& \frac{1}{(\sigma_f\sqrt{2\pi})^{\Delta t}} \exp\left(-\frac{\sum_{n=n_{i-1}^e+t}^{n_{i-1}^e+t+\Delta t-1}(\tilde{x}_n - f_n)^2}{2\sigma_f^2}\right) \\
& \frac{1}{(\sigma_2\sqrt{2\pi})^{N-t-\Delta t+1}} \exp\left(-\frac{\sum_{n=n_{i-1}^e+t+\Delta t}^{t_{i+1}^a}(\tilde{x}_n - m_2)^2}{2\sigma_2^2}\right)
\end{aligned} \tag{27}
$$

m_1 et m_2 sont les valeurs moyennes de l'amplitude du signal GNSS avant et après la rupture, respectivement. f_n est une droite échantillonnée qui modélise la croissance de la réflectivité entre $(n_{i-1}^e + t, m_1)$ et $(n_{i-1}^e + t + \Delta t, m_2)$. En pratique, les paramètres de la fonction de vraisemblance logarithmique sont estimés à l'aide de l'estimation empirique du maximum de vraisemblance. Les estimations empiriques du maximum de vraisemblance $\hat{t}$ et $\widehat{\Delta t}$ sont dérivées de la somme pondérée du log de l'écart type à chaque segment, par :

$$
(\hat{t}, \widehat{\Delta t}) = \underbrace{Argmin}_{t,\Delta t} \left\{ t \ \log(\hat{\sigma}_1) + \Delta t \ \log(\hat{\sigma}_f) + (N - t - \Delta t + 1) \log(\hat{\sigma}_2) \right\} \tag{28}
$$

D'après le modèle, la position réelle de la frontière entre deux zones différentes est supposée se trouver en $n_i^e = n_{i-1}^e + \hat{t} + \frac{\widehat{\Delta t}}{2}$.

3.2.2 Fusion de segments

En présence de bruit, l'algorithme CUSUM sursegmente les mesures d'amplitude GNSS. Nous proposons un algorithme de fusion des segments qui utilise leurs propriétés statistiques afin de diminuer le nombre de fausses alarmes dans les ruptures détectées. Nous montrons sur la Figure 6 l'architecture de l'algorithme de segmentation qui intègre l'étape de traitement de fusion.

Le processus de fusion proposé commence par définir l'intervalle de confiance de l'estimation de la moyenne m pour chaque segment de signal. Dans notre cas, la moyenne suit une distribution t de Student puisque l'écart type réel σ n'est pas connu. La Figure 7 représente les 3 différents cas d'intervalles de confiance considérés dans notre algorithme de fusion.

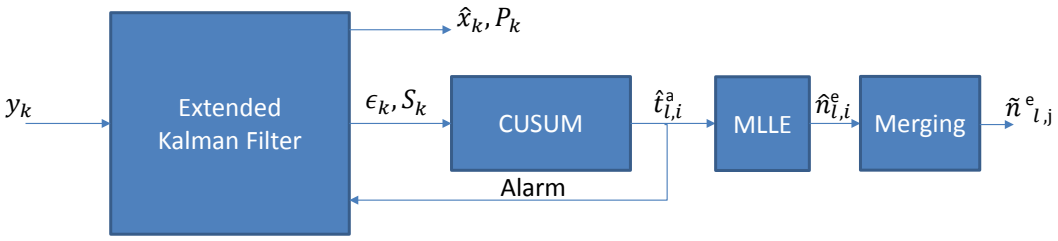

FIGURE 6: Architecture de l'algorithme de rupture avec fusion.

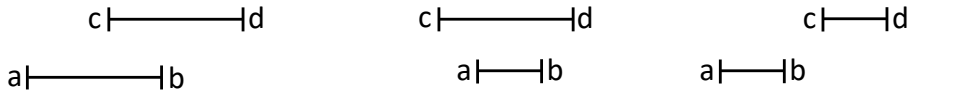

(a) Chevauchement (b) Inclusion (c) Non chevauchement

FIGURE 7: Positions relatives possibles des intervalles de confiance.

Dans le cas du chevauchement, nous calculons le pourcentage de chevauchement et s'il dépasse un seuil, nous fusionnons les segments. Dans le cas de l'inclusion, nous comparons la différence de moyenne entre les segments avec un seuil de symétrie pour déterminer si la fusion doit être mise en œuvre. Enfin, la moyenne des segments est recalculée après fusion.

3.3 Segmentation des mesures GNSS aéroportées réelles

Nous montrons sur la Figure 8 les mesures de réflectivité associées aux réflexions sur le sol et sur des plans d'eau obtenues avec notre récepteur GNSS-R, embarqué sur un autogire. Le signal de réflectivité augmente avec la teneur en eau des surface scannées.

Les ruptures dans les mesures de réflectivité sont détectées en ligne dans la première étape en utilisant l'approche Kalman-CUSUM (Figure 8a). Dans la deuxième étape, nous localisons ces ruptures à l'aide de l'approche MLLE proposée (Figure 8b). Ensuite, le signal est segmenté en segments stationnaires associés à différents niveaux de réflectivité moyenne. Nous montrons en bleu l'intervalle de confiance associé à chaque segment. Nous observons sur la Figure 8c un phénomène de sur-segmentation résultant de fausses alarmes dans la détection de rupture par l'approche CUSUM. Nous intégrons le processus de fusion et nous segmentons à nouveau le signal (Figure 8d). Nous remarquons une diminution significative du nombre de fausses alarmes.

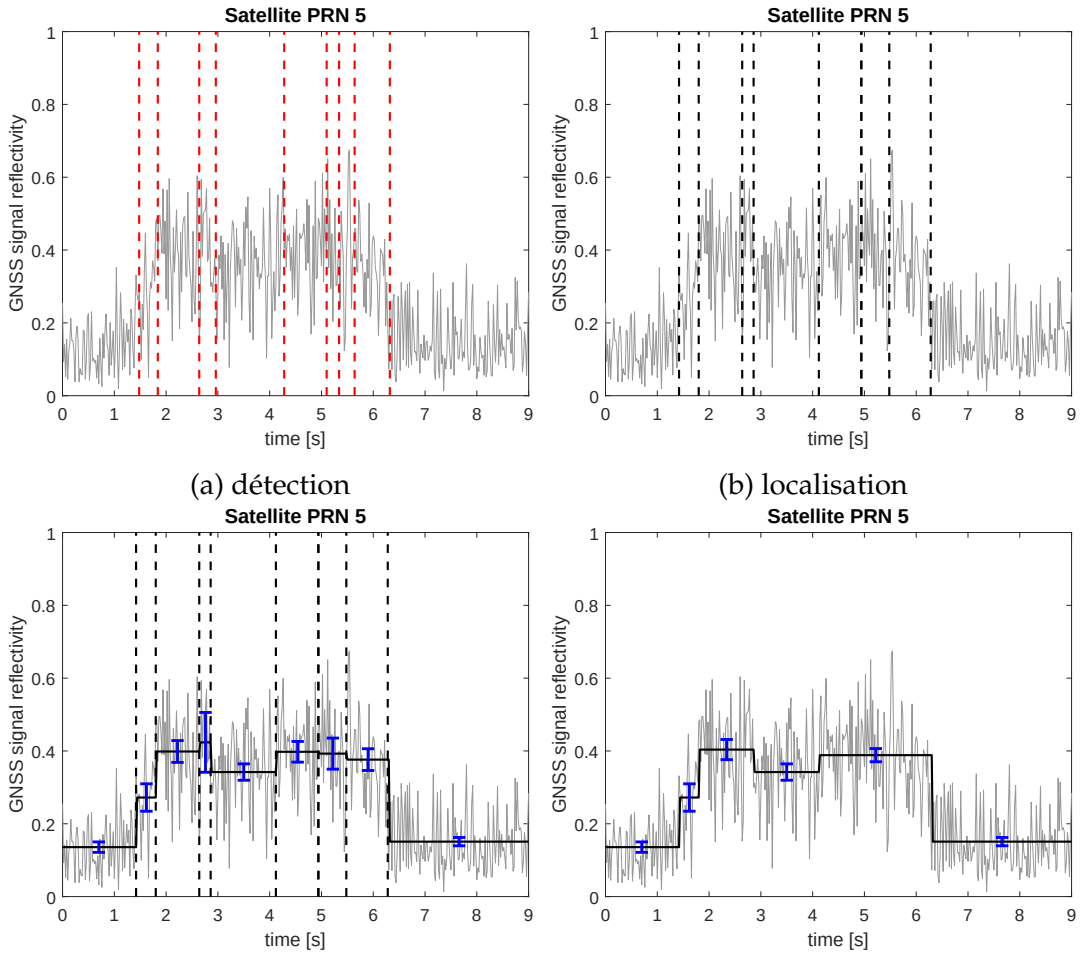

(a) détection

(b) localisation

(c) sur-segmentation (sans fusion)

(d) segmentation (avec la fusion)

FIGURE 8: Différentes étapes de la segmentation.

4 Réflectométrie GNSS aéroportée pour la détection de plans d'eau

4.1 Configuration GNSS-R bi-statique aéroportée

Le GNSS-R consiste à utiliser les signaux GNSS reçus sur Terre directement des satellites GNSS ainsi qu'après une réflexion sur la surface terrestre. Dans notre implémentation, nous utilisons la géométrie à double antenne GNSS-R décrite dans la Figure 9. Les signaux GNSS directs sont perçus par une antenne à polarisation circulaire droite (RHCP), et les signaux GNSS réfléchis sont perçus par une antenne à polarisation circulaire gauche (LHCP) après diffusion spéculaire depuis les différentes surfaces scannées le long de la trajectoire de vol.

Dans ce travail, nous traitons les amplitudes des signaux d'antenne RHCP

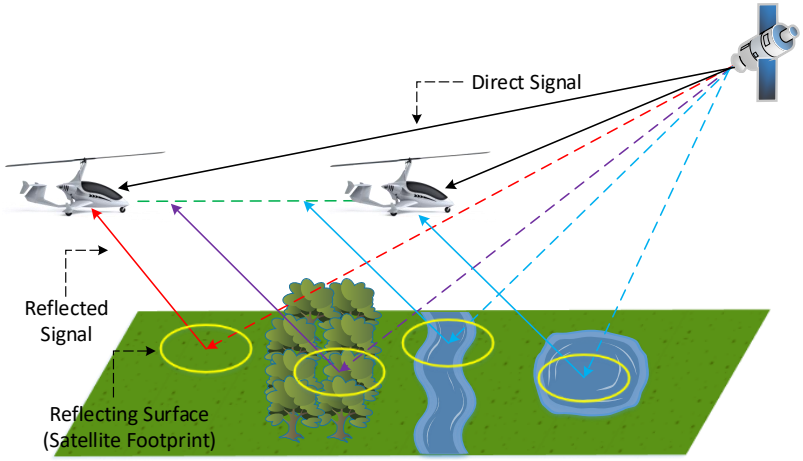

FIGURE 9: Géométrie du système GNSS-R aéroporté

et LHCP toutes les 20 *ms* afin de mesurer la réflectivité de la surface. Les mesures de réflectivité à 20 *ms* sont définies comme le rapport des amplitudes des signaux d'antenne LHCP réfléchis A^r_{LHCP} sur les signaux directs RHCP A^d_{RHCP} comme indiqué ci-dessous :

$$\Gamma(t) = \frac{A^r_{LHCP}(t)}{A^d_{RHCP}(t)} \tag{29}$$

Nous associons cette mesure à la localisation du point spéculaire à un taux de 20 *ms*.

4.2 Configuration matérielle du GNSS-R aéroporté

Un système GNSS-R a été conçu pour ce travail pour être embarqué à bord d'un autogire, de taille et de poids réduits. Une antenne RHCP est intégrée au nez de l'autogire et une antenne LHCP est fixée sous l'autogire. Une carte de vol de drone est également utilisée afin d'enregistrer la position de l'autogire par rapport au temps GPS. La Figure 10 montre l'autogire utilisé, équipé des différents capteurs intégrés.

L'autogire est également équipé d'élements utilisés pour la collecte des données GNSS-R autres que les antennes. Le système GNSS-R utilise un numériseur L1-L5 conçu spécialement pour ce travail par l'entreprise Syntony GNSS, une bobine de fibre optique, de diviseurs/combineurs de signaux et de batteries d'alimentation. La bobine de fibre optique introduit un retard supplémentaire au signal de l'antenne LHCP avant qu'il ne soit combiné au signal de l'antenne RHCP. Il s'agit d'une distinction importante de ce travail

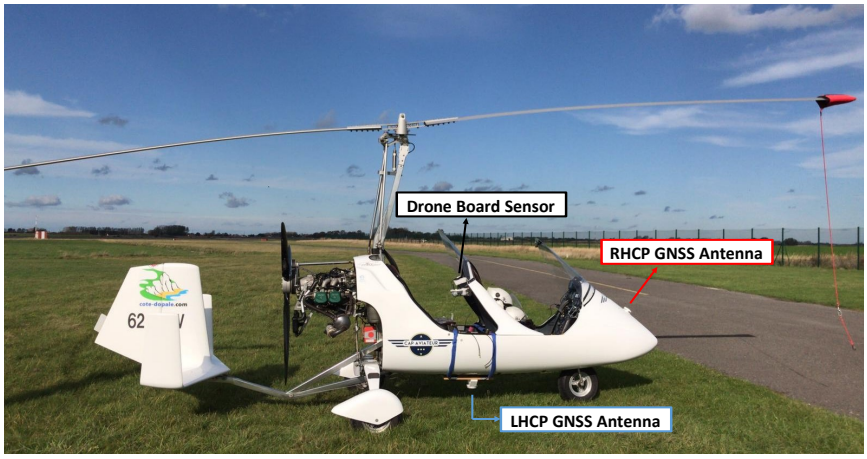

FIGURE 10: Autogire utilisé pour l'expérimentation, équipé des différents capteurs.

thèse, car cette ligne à retard permet un traitement séparé des signaux direct et réfléchis en utilisant un récepteur monocanal avec une synchronisation parfaite.

4.3 Système logiciel GNSS-R aéroporté

Nous présentons dans la Figure 11 le système logiciel GNSS-R utilisé dans notre expérimentation aéroportée.

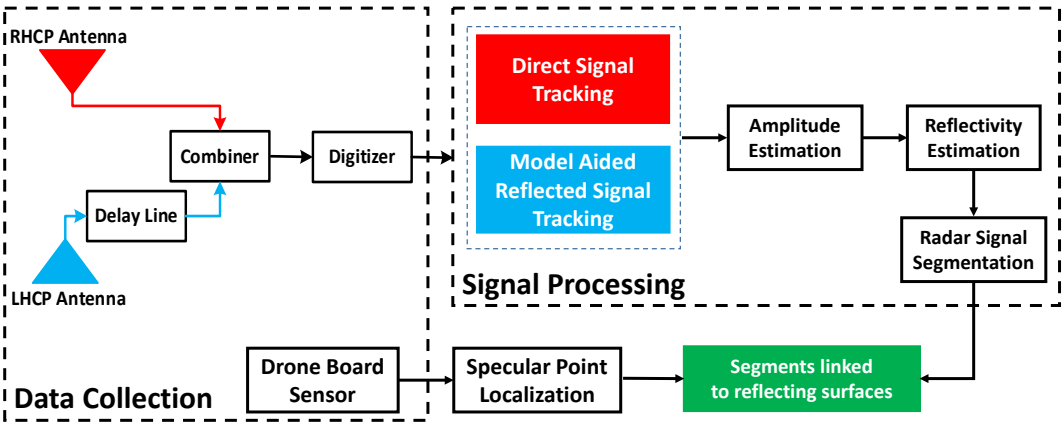

FIGURE 11: Système GNSS-R aéroporté

Après avoir collecté les données GNSS brutes, des techniques de traitement des signaux GNSS dédiées sont mises en œuvre dans notre récepteur logiciel GNSS pour l'extraction des données GNSS requises. Le traitement des signaux GNSS se fait dans une configuration maître/esclave. Il en résulte des observations GNSS liées aux signaux directs et réfléchis.

Les données GNSS fournies par les boucles de poursuite des signaux directs et réfléchis sont utilisées afin d'observer les amplitudes des signaux GNSS. Ensuite, les mesures de réflectivité sont dérivées des amplitudes des signaux GNSS en fonction du temps GPS. Les signaux GNSS sont segmentés en intervalles stationnaires à partir du détecteur de rupture et de la technique de segmentation développés dans ce travail. Ces segments sont associés à différentes zones de réflexions représentées par la localisation des points spéculaires.

4.4 Expérimentation en vol

4.4.1 Trajectoire de vol

Le vol a eu lieu dans le Nord de la France et a débuté à 14h45 UTC, le 19 Octobre 2020 et a duré 45 min. Nous avons scanné une large zone qui borde la Manche sur une trajectoire de $\sim$ 71 *km* entre Calais, Escalles et Ardres. La Figure 12 représente les traces des premières ellipses de Fresnel des empreintes des satellites d'angles d'élévation supérieurs à 50° le long de la trajectoire de vol, tracées sur fond de carte IGN à l'aide du logiciel QGIS.

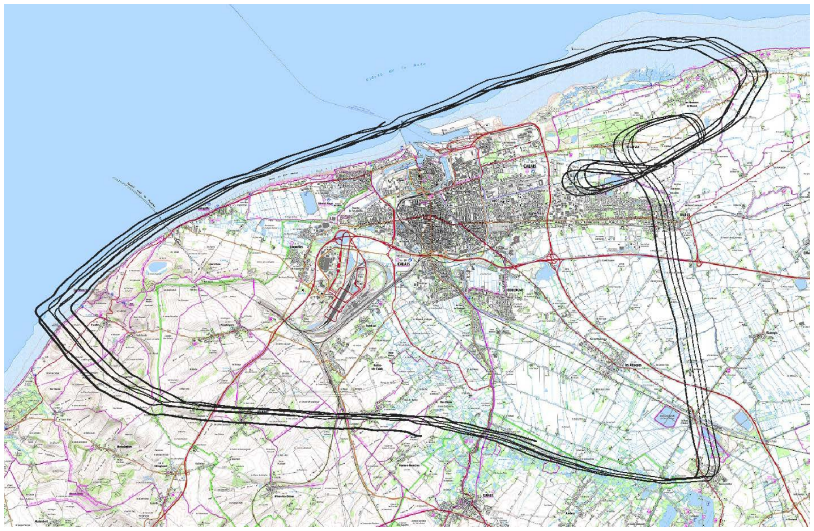

FIGURE 12: Traces d'empreintes satellitaires d'angles d'élévation élevés le long de la trajectoire de vol (fond de carte IGN).

4.4.2 Segmentation des signaux radar

Nous montrons sur la Figure 13, la segmentation automatique des mesures GNSS par la technique radar proposée. Les traces satellites sont représentées par les lieux des points de réflexion spéculaires, projetés sur Google

Earth. Le modèle de segmentation divise les signaux en segments stationnaires en fonction des mesures de réflectivité obtenues pour les différents signaux satellites. Lorsque les réflexions se font sur des plans d'eau, la réflectivité augmente, permettant leur détection par l'approche proposée, associée à une coloration bleue des segments et des points de réflexion spéculaires correspondants.

4.4.3 Détection des plans d'eau

La technique radar proposée est d'abord appliquée à la détection de plans d'eau à l'intérieur des terres. Nous comparons dans le Tableau 1 le nombre de surfaces de plans d'eau indiquées par les cartes IGN le long des traces satellitaires ainsi que le pourcentage de détection de ces plans d'eau par l'approche proposée.

TABLE 1: Résultats de l'inspection manuelle appliquée entre les cartes IGN et notre technique radar.

Plans d'eau	Nombre utilisant les cartes IGN	Pourcentage détecté par notre approche
Lacs/ Grands Marécages	20	100 %
Étangs/Marécages/Zones Humides	17	94 %
Rivières/Canaux	4	100 %
Ruisseaux	6	83 %
Totale	**47**	**96 %**

Nous montrons dans le Tableau 1 que notre technique radar détecte 96% des surfaces de plans d'eau intérieurs (c'est-à-dire 45 surfaces sur 47) le long des traces satellitaires par rapport aux informations fournies par les cartes IGN. Cela démontre l'importance d'une haute résolution spatio-temporelle pour la surveillance de tels plans d'eau.

4.4.4 Localisation des bords des plans d'eau

Le système de segmentation du signal radar est également appliqué à la localisation des bords des plans d'eau. Pour cela, nous comparons une localisation manuelle des bords via Google Earth avec la localisation automatique des bords obtenue par la technique radar proposée. Au total, 65 surfaces de plans d'eau ont été détectées le long des traces des trois satellites étudiés. La Figure 14 montre le nombre total de localisations parfaites (pour lesquelles

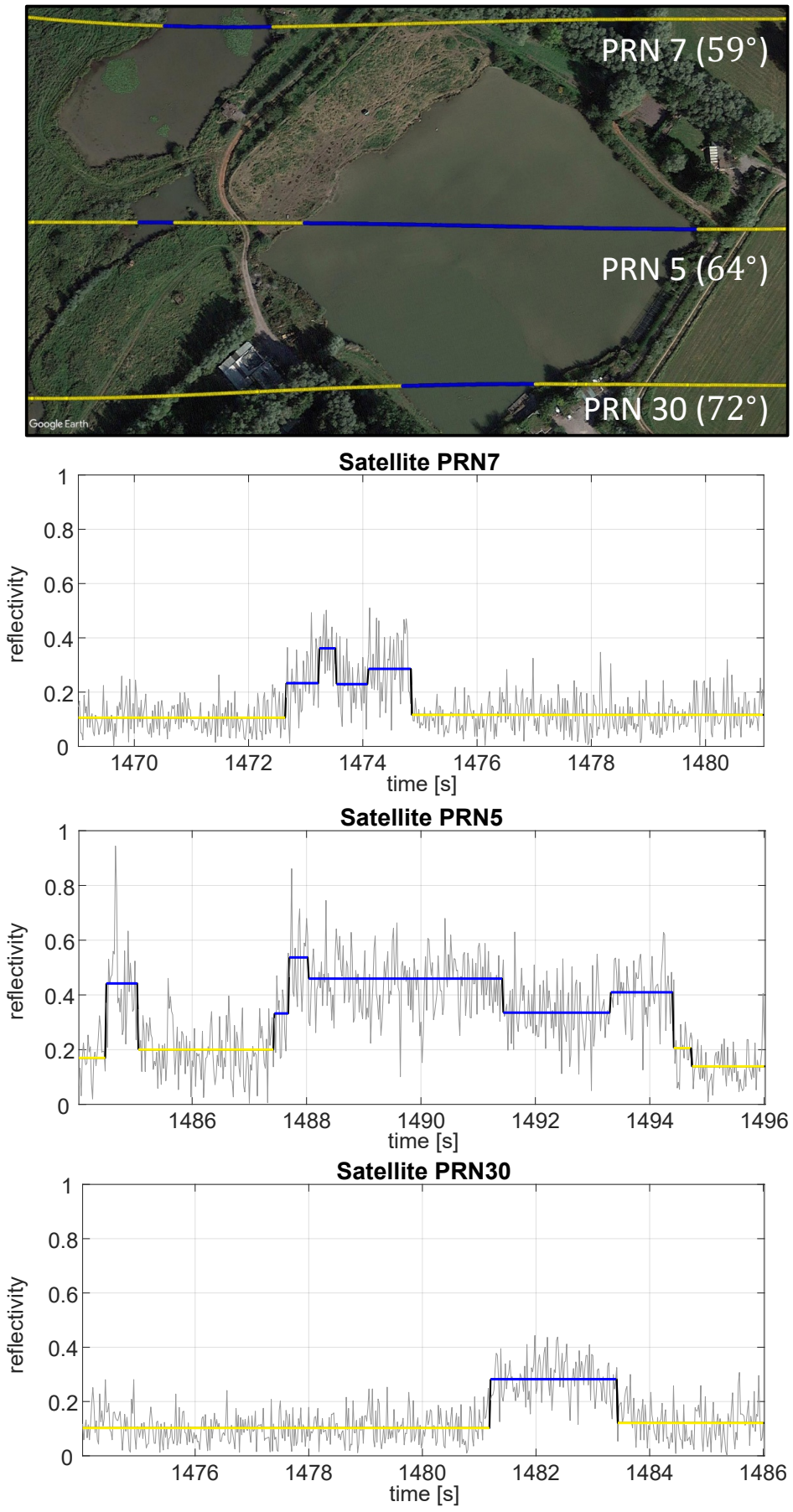

FIGURE 13: Segmentation automatique des mesures GNSS par la technique radar proposée.

la localisation automatique par notre approche est identique à la localisation manuelle) et imparfaites, ainsi que le nombre total de bords localisés pour les différentes surfaces de zones d'eau.

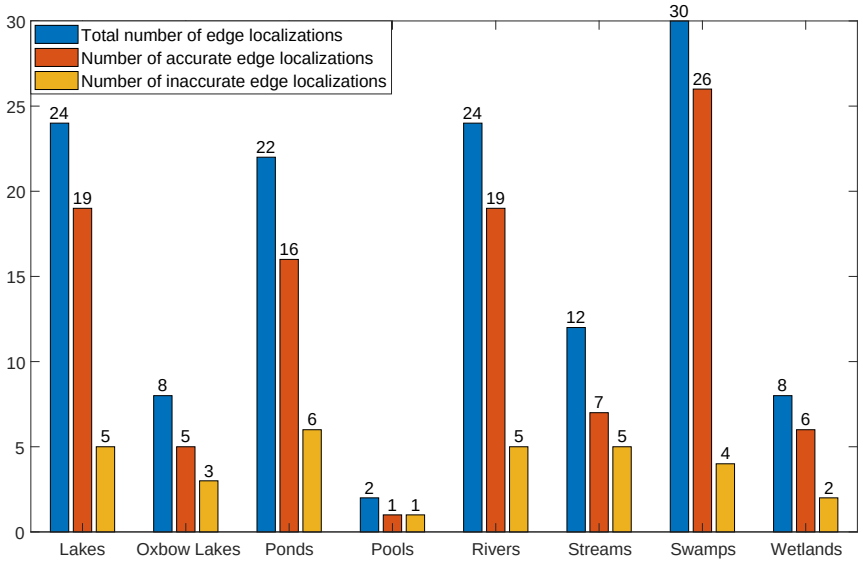

FIGURE 14: Statistiques de localisation des bords des plans d'eau par la technique radar proposée suivant leurs types.

D'après l'histogramme de la Figure 14, la technique radar proposée atteint un pourcentage total de localisation parfaite des bords de $76,2\%$, c'est-à-dire 99 localisations parfaites sur 130. De plus, l'analyse de la précision de la localisation des bords des plans d'eau révèle une erreur moyenne totale de localisation de $0,96\ m$ et un écart type total de la différence de localisation de $0,9\ m$. Par conséquent, nous concluons que notre approche de localisation automatique permet d'atteindre une précision de l'ordre du mètre.